Technical Physics, Vol. 47, No. 3, 2002, pp. 281–285. Translated from Zhurnal Tekhnicheskoĭ Fiziki, Vol. 72, No. 3, 2002, pp. 1–6.

ATOMS, SPECTRA, RADIATION

Atomic Hydrogen Cooling under Adiabatic Expansion in a Magnetic Trap

V. F. Ezhov*, E. K. Izrailov, G. B. Krygin*, M. M. Nesterov***, and V. L. Ryabov***

** Konstantinov Institute of Nuclear Physics, Russian Academy of Sciences, Gatchina, Leningrad oblast, 188350 Russia*

e-mail: krygin@pnpi.spb.ru

*** Mendeleev All-Russia Research Institute of Metrology, St. Petersburg, 198005 Russia*

**** St. Petersburg Institute of Information Science and Automation, Russian Academy of Sciences, Chetyrnadtsataya liniya, St. Petersburg, 199178 Russia*

Received May 18, 2001

Abstract—A new method for cooling atomic hydrogen down to 100 μK or below is suggested. The method exploits the unique properties of atomic hydrogen, which are the following: atomic hydrogen does not condense at temperatures as low as 20 μK and cannot be heated by IR radiation in the absence of atom–wall collisions. Therefore, the most efficient and well-known gas cooling technique can be employed, namely, the adiabatic expansion of the volume occupied by the gas (this approach is used in a gas-expansion machine). It is suggested to adiabatically expand the volume of a magnetic trap containing atomic hydrogen. © *2002 MAIK "Nauka/Interperiodica".*

INTRODUCTION

Atomic hydrogen is the simplest well-studied quantum system, which allows us to precisely verify the predictions of various theories of fundamental interactions. A most vivid example is the investigation of the Lamb dip in quantum electrodynamics. At present, topical problems of the physics of fundamental interactions studied with atomic hydrogen include the verification of the conventional model of electroweak interaction, the study of Bose–Einstein condensation, the creation of a hydrogen frequency standard, precise measurements of the fundamental constants, and the improvement of the Lamb dip measurement accuracy. These problems cannot be tackled if reliable methods for cooling atomic hydrogen down to 10 μK on a laboratory table, not in a cryostat, are absent.

The unique property of atomic hydrogen is that it can be heated and, accordingly, excited only by UV radiation. Therefore, when stored in Ioffe–Pritchard magnetic traps, which prevent atom–wall collisions [1, 2], polarized atomic hydrogen basically does not require additional thermal insulation. Yet, to cool atomic hydrogen to ultralow temperatures, researchers use sophisticated devices inside He^3-in-He^4 dilution cryostats. In these devices, atomic hydrogen is first precooled via atom–wall collisions. The walls are covered by an antirecombination superfluid helium film and are cooled down to 10 mK. The subsequent cooling of atomic hydrogen takes place by evaporating the fastest atoms (with an energy much higher than the magnetic barrier of the trap) from the atomic hydrogen gas "hanging" near the trap axis. These particles are certain to be generated because of atom-atom collisions. The temperature distribution of the atoms inside the trap is Maxwellian but truncated by the trap barrier height on the high-temperature side.

To date, the lowest temperatures have been obtained in experiments on the Bose–Einstein condensation of atomic hydrogen. It is generally believed that the condensation occurs at temperatures near 320 μK and a density of about 10^{14} cm^{-3}. Using this method, Masuhara *et al.* [3] have reached a density of 6×10^{13} cm^{-3} at a temperature 100 μK. Cesar *et al.* [4], using this source of atomic hydrogen, have performed one of the most accurate measurement of the $1S \longrightarrow 2S$ two-photon transition frequency. However, experiments with dilution cryostats are extremely complex. Therefore, it is of great importance that ultracold atomic hydrogen be much easier to access in experiments.

In this work, hydrogen atoms cool down (lose energy and momentum) when colliding with a receding magnetic barrier inside a magnetic trap. In this case, dilution cryostats become unneeded, and magnetic traps can be made of nonsuperconducting materials. Moreover, the cold atomic hydrogen gas becomes readily accessible for experimentalists.

In the first approximation, the temperature reduction expected can be estimated in terms of thermodynamics by considering the adiabatic expansion of the volume:

$$T_\mathrm{f} = T_\mathrm{i}(V_\mathrm{i}/V_\mathrm{f})^{2/3}\exp(S_\mathrm{i} - S_\mathrm{f}).$$

Here, T_i and V_i are the initial gas temperature and trap volume, respectively; T_f and V_f are the respective final

values; and $(S_i - S_f)$ is the change in the entropy. If the process is totally adiabatic, the entropy does not change and the temperature reduction depends only on the change in the volume. To provide the adiabatic conditions, it is necessary that the velocity of the barrier be much lower than the mean velocity of the atoms in the gas. This is readily achieved down to temperatures about several tens of microkelvins (the hydrogen atom velocity is on the order of 1m/s in this case).

Below, we calculate the parameters characterizing the state of atomic hydrogen in an Ioffe–Pritchard magnetic trap, as well as describe our experimental setup.

THERMODYNAMIC ANALYSIS

The thermodynamic consideration of the gas behavior in the trap will be performed in terms of the energy equation and the conservation equation for the number of particles. We will use the approach developed in [5]. Let N be the initial total number of polarized atoms in the trap with a barrier height ε_t. Elastic atom–atom collisions cause the evaporation of the number N_{ev} of the atoms with an energy E_{ev}. Because of dipole relaxation during the atom collisions, the number of the atoms N_{rel} with an energy E_{rel} is lost due to depolarization. The energy also changes because of the work done on or by the atoms during the adiabatic change in the trap volume.

An Ioffe–Pritchard trap is a magnetic quadrupole (or sextupole) producing a reflecting barrier in the radial direction and two solenoids at the ends of the quadrupole that produce reflecting gradients along the quadrupole axis near its end faces. The potential energy of the atoms in the trap is given by

$$U(\mathbf{r}) = \sqrt{\alpha^2 r^2 + (U_0 + \beta z^2)^2} - U_0,$$

where

$$\alpha^2 = \mu^2(c_1^2 - b_0 b_2), \quad \beta = |\mu| b_2, \quad U_0 = |\mu| b_0,$$

$$b_0 = \mu_0 I_c \frac{R_c^2}{(R_c^2 + A^2)^{3/2}},$$

$$b_2 = 3b_0 \frac{4A^2 - R_c^2}{2(A^2 + R_c^2)^2},$$

$$c_1 = 2\mu_0 \frac{I_b}{\pi R_b^2}.$$

Here, μ is the magnetic moment of the atom; I_b and I_c are the currents in the quadrupole and the solenoids, respectively; A is the distance between the trap center and the solenoid; R_c is the solenoid radius; and R_b is the distance between the trap axis and quadrupole pole.

The total energy of the atoms in the trap is the sum of the kinetic and potential energies:

$$E = \left(\frac{3}{2} + \gamma\right) NkT.$$

It has been shown [6] that the potential energy of the atoms in a magnetic trap with a barrier H_{max} is

$$\gamma = \left(\frac{T}{V_e}\right)\left(\frac{\partial V_e}{\partial T}\right)_\theta,$$

where V_e is the effective volume of the atoms in the trap.

Let θ be a parameter characterizing the properties of the trap (the current in the quadrupole or in the solenoids in our case). Then, the time variation of the energy can be written as

$$\dot{E} = \left(\frac{3}{2} + \gamma\right) kT\dot{N} + \left(\frac{\partial \gamma}{\partial \theta}\right)_T NkT\dot{\theta} + C\dot{T}.$$

Here, the first term is the energy variation due to relaxation and evaporation, the second one arises because of the changes in the trap parameters, and the third term reflects the temperature variation. The specific heat capacity is given by

$$C \equiv \left(\frac{\partial E}{\partial T}\right)_{N,\vartheta} = \left(\frac{3}{2} + \gamma + T\frac{\partial \gamma}{\partial T}\right) kN.$$

Eventually, we arrive at the set of equations

$$\begin{aligned} \dot{N} &= \dot{N}_{ev} + \dot{N}_{rel}, \\ C\dot{T} &= \dot{E}_{ev} + \dot{E}_\theta + \dot{E}_{rel} - \left(\frac{3}{2} + \gamma\right) kT\dot{N} - \left(\frac{\partial \gamma}{\partial \theta}\right)_T NkT\dot{\theta}. \end{aligned} \quad (1)$$

The change in the number of the atoms due to evaporation is

$$\begin{aligned} \dot{N}_{ev} &= -n_0^2 \sigma \bar{v} e^{-\eta} V_{ev}, \\ \dot{E}_{ev} &= \dot{N}_{ev}\left(\eta + \frac{W_{ev}}{V_{ev}}\right) kT. \end{aligned} \quad (2)$$

Here, N_0 is the atomic density at the trap axis, σ is the elastic collision cross section, $\bar{v} = \sqrt{8kT/\pi m}$ is the mean velocity of the atoms, $\eta = \varepsilon_t/kT$, and V_{ev} and W_{ev} are the effective volumes of elastic collisions [6]. The change in the trap parameter θ (for example, current) causes the energy change

$$\dot{E}_\vartheta = -\frac{NkT}{V_e}\left(\frac{\partial V_e}{\partial \theta}\right)_T \dot{\theta}. \quad (3)$$

In describing the gas state, it is also imperative to take into account inelastic atom–atom collisions. In our case, the basic inelastic process is spin relaxation, the degree of which is expressed as

$$\dot{N}_{rel} = -n_0^2 G V_{2e}, \quad (4)$$

$$\dot{E}_{\text{rel}} = \left(\frac{3}{2} + \gamma_2\right) kT\dot{N}_{\text{rel}}. \quad (5)$$

It is known from experiments [7] that the constant G in expression (4) depends on the magnetic field insignificantly and does not depend on the temperature at all. The effective volume of double collisions and the parameter γ_2 are given by

$$V_{2e} = \int d^3r[n(r)/n_0]^2, \quad (6)$$

$$\gamma_2 = \left(\frac{T}{2V_{2e}}\right)\frac{\partial V_{2e}}{\partial T}. \quad (7)$$

It is obvious that the cooling of the gas only by adiabatic expansion can be estimated if the effect of evaporation and spin relaxation is ignored in (1). In this case, the total number of the atoms in the trap will remain constant all the time and the dependence of the gas temperature on the current in the quadrupole will become fairly simple:

$$C\dot{T} = -\frac{T}{V_e}\left(\frac{\partial V_e}{\partial I_b}\right)_T \dot{I}_b. \quad (8)$$

Here, I_b is the current in the quadrupole and the effective volume V_e for the Ioffe–Pritchard trap can be calculated by the formula [5]

$$V_e = 6A_{IQ}\Lambda^3(kT)^4\left(P(4,\eta) + \frac{2}{3}\frac{U_0}{kT}P(3,\eta)\right), \quad (9)$$

$$P(a,\eta) = \frac{1}{\Gamma(a)}\int_0^\eta t^{a-1}e^{-t}dt, \quad (10)$$

$$\gamma = -\frac{3}{2} + \frac{12P_5kT + 6P_4U_0}{3P_4kT + 2P_3U_0}. \quad (11)$$

As follows from calculations, the dependence of the gas temperature on the current in the quadrupole can be written in the form

$$\frac{T}{T_0} = \left(\frac{I_0}{I}\right)^{-0.625}, \quad (12)$$

which is consistent with the estimate given in the Introduction and indicates the validity of the starting assumptions.

The set of equations (1) was solved for the trap with $R_c = 10$ cm, $R_b = 10$ cm, and $A = 10$ cm. The initial values of the currents I_b and I_c were taken such that the magnetic induction in the quadrupole and in the blocking solenoids was 1 and 0.5 T, respectively. The spin relaxation constant G was set equal to 10^{-21} m^3/s.

The results of the calculations are shown in Figs. 1–4.

Figure 1 demonstrates the results for cooling by evaporation, by evaporation with subsequent adiabatic

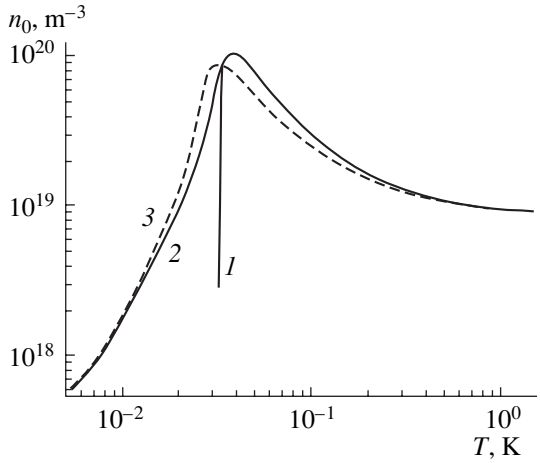

Fig. 1. Hydrogen cooling under different conditions: (*1*) without adiabatic expansion, (*2*) with expansion starting from the highest-density point, and (*3*) simultaneous evaporation and adiabatic expansion.

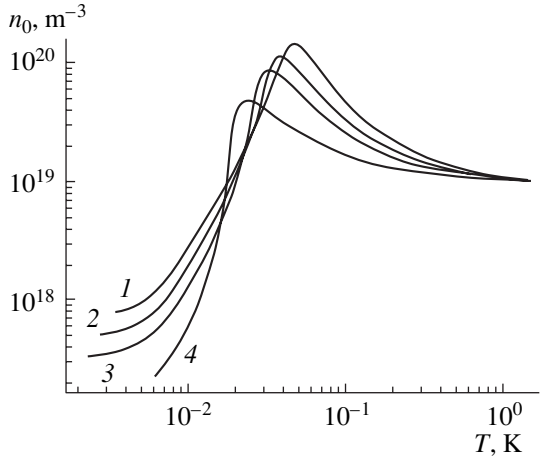

Fig. 2. Cooling at various initial heights of the trap barrier. B = (*1*) 1.3, (*2*) 1.0, (*3*) 0.75, and (*4*) 0.4 T.

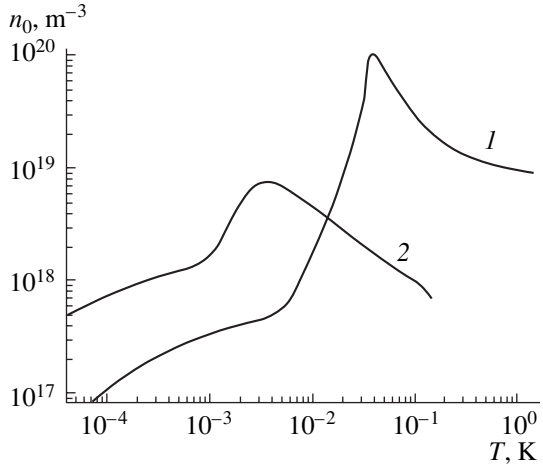

Fig. 3. Cooling efficiency vs. initial temperature. T_0 = (*1*) 1.5 and (*2*) 0.15 K.

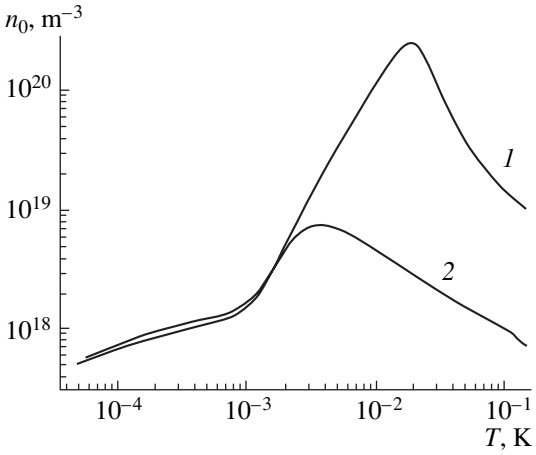

Fig. 4. Cooling efficiency vs. trap diameter. D = (*1*) 20 and (*2*) 10 cm.

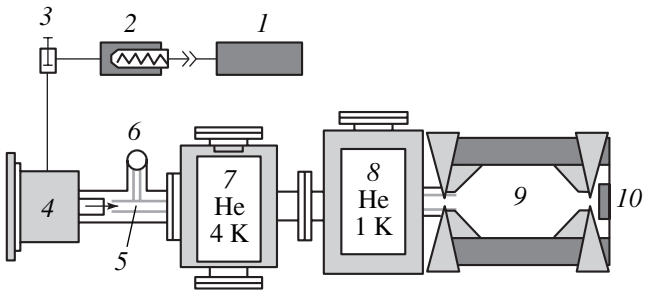

Fig. 5. Experimental setup. *1*, molecular hydrogen source; *2*, Pd filter; *3*, valve; *4*, hydrogen dissociation unit; *5*, Teflon tube; *6*, cooling the Teflon tube to ≈100 K; *7*, first helium cryostat; *8*, second helium cryostat with vapor pumping; *9*, Ioffe–Pritchard trap; and *10*, detector.

expansion, and by evaporation and adiabatic expansion proceeding simultaneously. In all of the cases, the initial temperature was 1.5 K and the radial barrier height, 1 T. At the early stage, cooling is basically due to evaporation. Once the gas temperature has decreased to 20–30 mK, becoming much less than the barrier height, evaporation virtually ceases. The sharp drop in the density in the absence of the expansion is the result of relaxation losses, which prevail in the absence of the evaporation.

Figure 2 compares the efficiencies of the cooling process when evaporation is followed by adiabatic expansion at various initial barrier heights, with the initial temperature being 1.5 K in all of the cases.

Figure 3 illustrates the increase in the hydrogen cooling efficiency when the initial temperature is decreased to 10 mK in the trap with a barrier height of 1 T.

Finally, Fig. 4 compares the cooling processes in the traps with various diameters but with the same lengths and barrier heights. It is seen that the final result depends on the trap diameter only slightly but significantly depends on the magnetic barrier height.

EXPERIMENTAL SETUP

Our experimental setup consists of three units, where three basic stages of atomic hydrogen cooling proceed. At the first stage, molecular hydrogen dissociates, producing atomic hydrogen. At the second stage, the atomic hydrogen is precooled. At the final stage, it is cooled to a desired temperature by adiabatically expanding in a magnetic trap. The basic point here is that the magnetic trap is made of a nonsuperconducting material. On the one hand, this allows us to vary the current in the trap windings with any rate and by any law. On the other hand, cryostats at the final stage of cooling become unnecessary, which greatly simplifies experiments with atomic hydrogen.

The setup, whose block diagram is depicted in Fig. 5, operates as follows. Molecular hydrogen from source *1* is purified in a Pd filter *2* and enters rf dissociation unit *4* through valve *3*. Further, it passes through the precooling duct, cooling first to nitrogen temperature in nitrogen refrigerator *6* and then subsequently to 4 and 1 K in refrigerators *7* and *8*. Refrigerator *7* is a helium cryostat; refrigerator *8*, a cryostat with helium vapor pumping. Having been precooled, the atomic hydrogen enters magnetic trap *9*, built around a quadrupole lens. The lens can generate a magnetic field with an induction of no less than 1 T in the radial direction. The basic difficulty associated with this trap is to block the end faces of the lens. We found that a solenoid with an inner diameter of 20 cm and an induction of 0.5 T is impossible to create with conventional technologies. Therefore, the entrance and exit apertures of the lens should be diminished. For this purpose, it is suggested to use additional pole pieces on the quadrupole.

The general view of the trap and the magnetic field configuration calculated in its two cross sections are shown in Fig. 6. The additional pole pieces do not change the field configuration in the radial direction. They can be made of magnetically soft materials, and the magnetic induction at the poles will not change.

Thus, the entrance and exit apertures of the lens can be decreased to 2 or 3 cm. Solenoids of such an inner diameter can be prepared. For example, a solenoid with an outer diameter of 30 cm, an inner diameter of 3 cm, and a thickness of 3 cm provides a magnetic induction of 0.5 T in the longitudinal direction if the current density in it is 1000 A/cm^2.

The atomic hydrogen in the magnetic trap is cooled in several steps. First, the hydrogen is delivered to the trap. At this step, the current in the first blocking solenoid decreases and hydrogen atoms fill the trap. Then, the current in the solenoid is raised and the hydrogen is blocked in the trap, where it is cooled by evaporation. As the gas cools, the evaporation rate decreases and the density n_0 rises. This process continues until the relax-

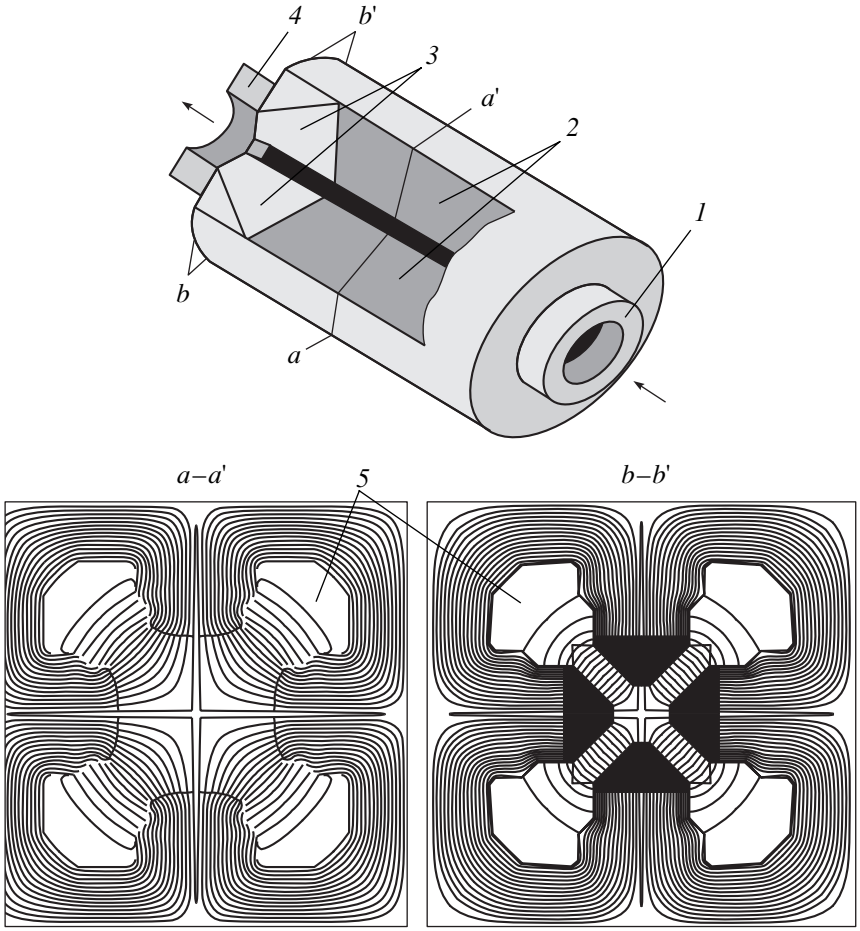

Fig. 6. Magnetic trap built around a quadrupole lens and the magnetic field configuration in its two cross sections (the current in the solenoids is switched off): *1* and *4*, blocking solenoids; *2*, quadrupole lens poles; *3*, additional pole pieces; and *5*, quadrupole lens windings.

ation losses dominate over the evaporation. The trap is so designed that the evaporation is a one-dimensional process, since the solenoid-induced barrier along the axis is half as high as in the radial direction. At the second step, the current in the trap windings decreases and the gas adiabatically expands.

As was noted above, the adiabatic conditions are easy to keep at temperatures down to several tens of microkelvins (the hydrogen atom velocity is about 1m/s in this case).

At the final step, the current in the second blocking solenoid is decreased and the intensity vs. barrier height is recorded. The cooling effect is estimated from two measurements: with and without the adiabatic expansion of the hydrogen volume in the trap.

ACKNOWLEDGMENTS

We thank M.I. Groshev, V.A. Knyaz'kov, and N.N. Dmitriev for their assistance and valuable comments. We are also indebted to V.A. Nazarenko for his constant interest in this work.

This work was supported by the Russian Foundation for Basic Research (grant no. 99-02-17378).

REFERENCES

1. T. H. Bergeman, P. McNicholl, J. Kycia, *et al.*, J. Opt. Soc. Am. B **6**, 2249 (1989).
2. T. H. Bergeman, G. Erez, and H. Metcalf, Phys. Rev. A **35**, 1535 (1987).
3. N. Masuhara, J. M. Doyle, *et al.*, Phys. Rev. Lett. **61**, 935 (1988).
4. C. L. Cesar, D. J. Fried, *et al.*, Phys. Rev. Lett. **77**, 255 (1996).
5. P. W. H. Pinkse, A. Mosk, A. Weidemüller, *et al.*, Phys. Rev. A **57** (6), 4747 (1998).
6. O. J. Luiten, M. W. Reynolds, and J. T. M. Walraven, Phys. Rev. A **53** (1), 381 (1996).
7. A. Lagendijk, I. F. Silvera, and B. J. Verhaar, Phys. Rev. B **33** (1), 626 (1986).

Translated by V. Isaakyan

Technical Physics, Vol. 47, No. 3, 2002, pp. 286–290. Translated from Zhurnal Tekhnicheskoĭ Fiziki, Vol. 72, No. 3, 2002, pp. 7–10.

GASES AND LIQUIDS

On the Motion of a Uniformly Heated Drop in a Viscous Liquid under Gravity

N. V. Malaĭ

Belgorod State University, Belgorod, Russia

e-mail: malay@bsu.edu.ru

Received February 20, 2001; in final form, May 19, 2001

Abstract—The motion of a uniformly heated spherical drop under gravity is theoretically studied within the Stokes approximation. The Stokes and Hadamard–Rybchinsky formulas are generalized so that the temperature dependence of the viscosity can be found in a wide temperature range. Also, the drag force and the velocity of gravity fall are calculated for an arbitrary temperature difference between the surface of the drop and distant points. © *2002 MAIK "Nauka/Interperiodica".*

STATEMENT OF THE PROBLEM

We consider the motion of a uniformly heated hydrosol drop (particle) with a surface temperature T_s in a viscous incompressible liquid under gravity. The liquid occupies the entire space, does not mix with the drop, and is at rest at infinity. A particle is considered to be heated (cooled) if its surface temperature differs from the temperature far away from it. Uniform heating can be associated with heat liberation during chemical reactions on its surface, the radioactive decay of the material, external effects, etc. If, for example, the particle is subjected to a monochromatic radiation of wavelength λ_0 and intensity I_0, it absorbs energy $\pi R^2 I_0 K_n$ (where R is the radius of the drop and K_n is the absorption factor [1, 2]), which is uniformly distributed over its volume. This statement is valid if the thermal conductivity of the drop is much higher than that of the environment and $\lambda_0 \gg R$. All the processes in the drop-liquid medium system are quasi-stationary, because the thermal relaxation time of the system is small.

The heated surface of the drop influences the thermal physical characteristics of the surrounding liquid and, eventually, the velocity and pressure fields in its neighborhood.

Unlike [3–6], the author generalizes the Stokes and Hadamard–Rybchinsky formulas for the case of a uniformly heated spherical drop steadily moving in a viscous incompressible liquid. The temperature difference between the surface of the drop and distant sites, as well as the temperature dependence of the viscosity of the liquid, is assumed to be arbitrary.

Among all the parameters of liquid transport, the viscosity depends on temperature to the greatest extent, exponentially decreasing with growing temperature [7, 8]. The review of the available semi-empirical formulas and experimental data shows that the temperature dependence of the liquid viscosity μ in a wide temperature range and with any desired accuracy can be described by the formula

$$\mu_e = \mu_\infty \left[1 + \sum_{n=1}^{\infty} F_n \left(\frac{T_e}{T_\infty} - 1 \right)^n \right] \exp\left\{ -A\left(\frac{T_e}{T_\infty} - 1 \right) \right\}, \quad (1)$$

where A and F_n are constants, $\mu_\infty = \mu_e(T_\infty)$, and T_∞ is the liquid temperature far away from the particle (at $F_n = 0$, this formula reduces to the well-known Reynolds expression [7]). Hereafter, the subscripts e and i refer to the viscous liquid and heated particle, respectively; the subscript ∞ designates the parameters of the undisturbed flow at infinity; and the subscript s refers to the parameters taken at the mean surface temperature T_s. For water, $A = 5.779$, $F_1 = 2.318$, and $F_2 = 9.118$ with an accuracy of 2% or higher at temperatures between 273 and 363 K ($T_\infty = 273$ K).

It is assumed that the densities, thermal conductivities, and specific heat capacities of the liquid and the drop are constant. The drop moves slowly (small Reynolds and Peclet numbers) and retains the spherical shape. The latter statement is valid if the surface tension forces at the drop–environment interface far exceed the drag forces, which tend to distort the sphere. Analytically, the shape conservation condition is written as the inequality [9] $\sigma/R \gg \mu_e|\mathbf{U}_e|/R$, where σ is the surface tension coefficient at the drop–environment interface and $\mathbf{U}_e$ is the velocity of the particle. This inequality holds true for most liquids.

It is appropriate to relate the frame of reference to the center of the moving particle (the problem is reduced to the analysis of an infinite parallel flow with a velocity $\mathbf{U}_\infty$ to be determined over the particle). The velocity and temperature distributions are symmetric about the 0z axis, which passes through the center of the particle and has the same direction as the incoming flow velocity. Therefore, we use the spherical coordinate

1063-7842/03/4702-0286$22.00 © 2002 MAIK "Nauka/Interperiodica"

system where the radius r is counted from the center of the drop and the angle Θ, from the incoming flow direction.

In the spherical coordinate system r, Θ, φ with regard for our assumptions, the equations and the boundary conditions for the velocities $\mathbf{U}$, pressures P, and temperatures T_e outside and inside the drop in the Stokes approximation are written in the form [5, 10]

$$\nabla P_e = \mu_e \nabla^2 \mathbf{U}_e + 2(\nabla \mu_e)(\nabla \mathbf{U}_e) + (\nabla \mu_e) \times (\nabla \times \mathbf{U}_e) + \mathbf{F}_g,$$

$$\mathrm{div}\mathbf{U}_e = 0, \tag{2}$$

$$\mu_i \Delta \mathbf{U}_i = \nabla P_i, \quad \mathrm{div}\mathbf{U}_i = 0, \tag{3}$$

$$\Delta T_e = 0, \tag{4}$$

$$r = R, \quad U_r^e = U_r^i = 0, \quad U_\Theta^e = U_\Theta^i, \quad T_e = T_s, \tag{5}$$

$$r \longrightarrow \infty, \quad \mathbf{U_e} \longrightarrow U_\infty \cos\Theta \mathbf{e}_r - U_\infty \sin\Theta \mathbf{e}_\Theta, \quad T_e \longrightarrow T_\infty, \quad P_e \longrightarrow P_\infty, \tag{6}$$

$$r \longrightarrow 0, \quad |\mathbf{U}_i| \neq \infty, \quad P_i \neq \infty. \tag{7}$$

Here, U_r and U_Θ are the radial and tangential components of the mass velocity $\mathbf{U}$ of the liquid in the spherical coordinate system; $\mathbf{F}_g$ is the vector of the gravitational forces; $U_\infty = |\mathbf{U}_\infty|$; U_∞ is the incoming flow velocity, which is to be determined from the condition of vanishing the total force acting on the particle (i.e., U_∞ and $|\mathbf{F}_g|$ should be so related that the total force acting on the particle vanishes); $\mathbf{e}_r$ and $\mathbf{e}_\Theta$ are the unit vectors in the spherical coordinate system; T_s is the mean surface temperature of the drop; ∇ is the del operator; Δ is Laplacian; and $(\nabla \mathbf{U}_e)$ is the scalar product.

Conditions (5) on the surface of the drop imply the impermeability and continuity conditions for the normal and tangential components of the mass velocity, respectively, as well as the constancy of the surface temperature of the particle. As the boundary conditions at infinity, i.e., far away from the particle, we take conditions (6), and the finiteness of the physical quantities characterizing the particle at $r \longrightarrow 0$ is included by (7).

To state the problem in closed form, the boundary conditions on the surface of a uniformly heated drop must be complemented by the continuity conditions for the stress tensor (normal and tangential) components [9, 10]

$$-P_e + 2\mu_e \frac{\partial U_r^e}{\partial r} = -P_i + 2\mu_i \frac{\partial U_r^i}{\partial r} + 2\frac{\sigma}{R}, \tag{8}$$

$$\mu_e\left(\frac{1}{r}\frac{\partial U_r^e}{\partial \Theta} + \frac{\partial U_\Theta^e}{\partial r} - \frac{U_\Theta^e}{r}\right) = \mu_i\left(\frac{1}{r}\frac{\partial U_r^i}{\partial \Theta} + \frac{\partial U_\Theta^i}{\partial r} - \frac{U_\Theta^i}{r}\right). \tag{9}$$

VELOCITY AND TEMPERATURE FIELDS. DRIFT VELOCITY OF THE DROP

To find the rate of fall of the uniformly heated drop, one should know the temperature, velocity, and pressure distributions in its vicinity. The general solution of heat conduction equation (4) that satisfies the appropriate boundary conditions has the form

$$t_e = 1 + \frac{\gamma}{y}, \quad \gamma = (T_s - T_\infty)/T_\infty, \tag{10}$$

where $y = r/R$ is the dimensionless radial coordinate, $t_e = T_e/T_\infty$, and γ is the dimensional parameter that characterizes the temperature difference between the surface of the particle and distant points.

Substituting (10) into (1) yields the expression for the dynamic viscosity

$$\mu_e = \mu_\infty\left[1 + \sum_{n=1}^{\infty} F_n \frac{\gamma^n}{y^n}\right]\exp\left\{-A\frac{\gamma}{y}\right\}. \tag{11}$$

Formula (11) will further be used to find the velocity and pressure fields near the uniformly heated drop. Boundary conditions (5)–(9) admit the separation of variables upon solving the hydrodynamic equations. The components of the mass velocity and pressure were found in the form

$$U_r(r, \Theta) = U_\infty G(r)\cos\Theta,$$

$$U_\Theta(r, \Theta) = -U_\infty g(r)\sin\Theta, \quad P(r, \theta) = P_0 + h(r)\cos\Theta,$$

where $G(r)$, $g(r)$, and $h(r)$ are arbitrary functions depending on the radial coordinate r.

From the continuity equation, a relation between the functions $G(r)$ and $g(r)$ were determined. Finally, all the parameters and relations found were substituted into the appropriate Stokes equations. Eventually, we obtained the fourth-order ordinary differential equation for the function $G(r)$ that is similar to that derived in [11]. Its solution was sought in the form of generalized power series. For the components of the mass velocity and pressure, we found

$$U_r^e(y, \Theta) = U_\infty \cos\Theta[1 + A_1 G_1(y) + A_2 G_2(y)], \tag{12}$$

$$U_\Theta^e(y, \Theta) = -U_\infty \sin\Theta[1 + A_1 G_3(y) + A_2 G_4(y)], \tag{13}$$

$$P_e(y, \Theta) = P_\infty + \frac{\mu_e U_\infty}{R}\cos\Theta[A_1 G_5 + A_2 G_6], \tag{14}$$

$$U_r^i(y, \Theta) = U_\infty \cos\Theta(A_3 + A_4 y^2), \tag{15}$$

$$U_\Theta^i(y, \Theta) = -U_\infty \sin\Theta(A_3 + 2A_4 y^2), \tag{16}$$

$$P_i(y, \Theta) = P_0 + 10\frac{\mu_i U_\infty}{R} A_4 \cos\Theta. \tag{17}$$

Here,

$$G_1(y) = -\frac{1}{y^3}\sum_{n=0}^{\infty}\frac{\Delta_n^{(1)}}{(n+3)y^n}, \quad G_3(y) = G_1(y) + \frac{1}{2}yG_1^I,$$

$$G_2(y) = -\frac{1}{y}\sum_{n=0}^{\infty}\frac{\Delta_n^{(2)}}{(n+1)y^n}$$

$$-\frac{\alpha}{y^3}\sum_{n=0}^{\infty}\left[(n+3)\ln\frac{1}{y}-1\right]\frac{\Delta_n^{(1)}}{(n+3)^2y^n},$$

$$G_5(y) = \frac{1}{2}yG_1^{III} + y\left(3+\frac{1}{2}\sum_{n=0}^{\infty}s_n\frac{\gamma^n}{y^n}\right)G_1^{II}$$

$$+\left(2+\sum_{n=0}^{\infty}s_n\frac{\gamma^n}{y^n}\right)G_1^I,$$

$$G_6(y) = \frac{1}{2}yG_2^{III} + y\left(3+\frac{1}{2}\sum_{n=0}^{\infty}s_n\frac{\gamma^n}{y^n}\right)G_2^{II}$$

$$+\left(2+\sum_{n=0}^{\infty}s_n\frac{\gamma^n}{y^n}\right)G_2^I,$$

$$s_n = AF_{n-1} - nF_n - \sum_{k=1}^{n}s_{n-k}F_k, \quad F_0 = 1,$$

and $G_4(y) = G_2(y) + \frac{1}{2}yG_2^I$, G_1^I, G_1^{II}, G_1^{III}, G_2^I, G_2^{II}, and G_2^{III} are the respective first, second, and third derivatives with respect of y. Also,

$$\Delta_n^{(1)} = -\frac{1}{n(n+5)}\sum_{k=1}^{n}[(n+4-k) \tag{18}$$

$$\times(\alpha_k^{(1)}(n+5-k)-\alpha_k^{(2)})+\alpha_k^{(3)}]\gamma^k\Delta_{n-k}^{(1)} \ (n\geq 1),$$

$$\Delta_n^{(2)} = -\frac{1}{(n+3)(n-2)}\left[-6\alpha_n^{(4)}\gamma^n + \sum_{k=1}^{n}[(n+2-k)\right.$$

$$\times\{(n+3-k)\alpha_k^{(1)}-\alpha_k^{(2)}\}+\alpha_k^{(3)}]\gamma^k\Delta_{n-k}^{(2)} \tag{19}$$

$$\left.+\alpha\sum_{k=0}^{n}[(2n+5-2k)\alpha_k^{(1)}-\alpha_k^{(2)}]\gamma^k\Delta_{n-k-2}^{(1)}\right] (n\geq 3).$$

In calculating the coefficients $\Delta_n^{(1)}$ and $\Delta_n^{(2)}$, it is necessary to take into account that

$$\Delta_0^{(1)} = -3, \quad \Delta_0^{(2)} = -1, \quad \Delta_2^{(2)} = 1,$$

$$\alpha_0^{(1)} = \alpha_0^{(4)} = 1, \quad \alpha_0^{(2)} = 4, \quad \alpha_0^{(3)} = -4,$$

$$\alpha_n^{(1)} = F_n, \quad \alpha_n^{(2)} = (4-n)F_n + AF_{n-1},$$

$$\alpha_n^{(3)} = 2AF_{n-1} - 2(2+n)AF_n,$$

$$\alpha_n^{(4)} = A^n/n!,$$

$$\alpha = -\frac{\gamma}{15}\{6\gamma^2\alpha_2^{(4)} - [3(4\alpha_1^{(1)}-\alpha_1^{(2)})+\alpha_1^{(3)}]\Delta_1^{(2)}$$

$$+[2(3\alpha_2^{(1)}-\alpha_2^{(2)})+\alpha_2^{(3)}]\gamma\},$$

$$\Delta_1^{(2)} = -\frac{\gamma}{4}[6\alpha_1^{(4)} + 2(3\alpha_1-\alpha_1^{(2)})+\alpha_1^{(3)}].$$

The constants of integration A_1, A_2, A_3, and A_4, which enter expressions (13)–(17), are determined by substituting them into the corresponding boundary conditions on the surface of the drop. Once they have been found, the force acting on the particle is found by integrating the stress tensor over the surface of the particle [12]:

$$\mathbf{F} = \int_{(S)}(-P_e\cos\Theta + P_{rr}\cos\Theta - P_{0r}\sin\Theta) \tag{20}$$

$$\times r^2\sin\Theta d\Theta d\varphi\mathbf{n}_z,$$

where

$$P_{rr} = 2\mu_e\frac{\partial U_r^e}{\partial r}, \quad P_{r\Theta} = \mu_e\left(\frac{\partial U_\Theta^e}{\partial r} + \frac{1}{r}\frac{\partial U_r^e}{\partial\Theta} - \frac{U_\Theta^e}{r}\right)$$

are the stress tensor components in the spherical coordinates and $\mathbf{n}_z$ is the unit vector directed along the z axis of the Cartesian coordinates.

Substituting (13) and (14) into (20) and integrating yields

$$\mathbf{F} = 4\pi R\mu_\infty U_\infty A_2\exp\{-A\gamma\}\mathbf{n}_z, \tag{21}$$

where

$$A_2 = -\left(N_3 + N_4\frac{\mu_e^s}{3\mu_i^s}\right)\Big/\left(N_1 + N_2\frac{\mu_e^s}{3\mu_i^s}\right),$$

$$N_1|_{y=1} = [G_1G_2^I - G_2G_1^I],$$

$$N_2|_{y=1} = [G_2(2G_1^I + G_1^{II}) - G_1(2G_2^I + G_2^{II})],$$

$$N_3|_{y=1} = -G_1^I,$$

$$N_4|_{y=1} = [2G_1^I + G_1^{II}].$$

Substituting the coefficient A_2 into (21), we find the expression for the drag (viscous) force acting on a uniformly heated drop moving under gravity:

$$\mathbf{F} = -6\pi R\mu_\infty U_\infty f_\mu\mathbf{n}_z, \tag{22}$$

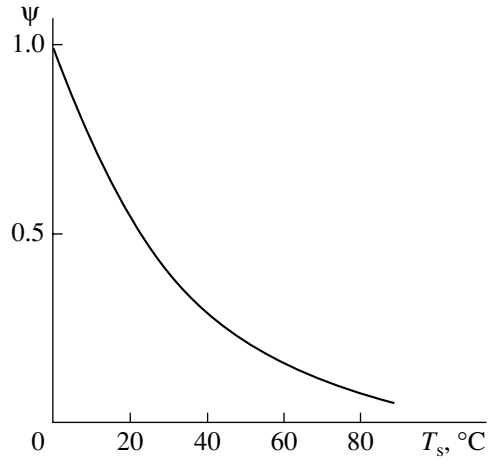

Fig. 1. ψ vs. mean surface temperature T_s.

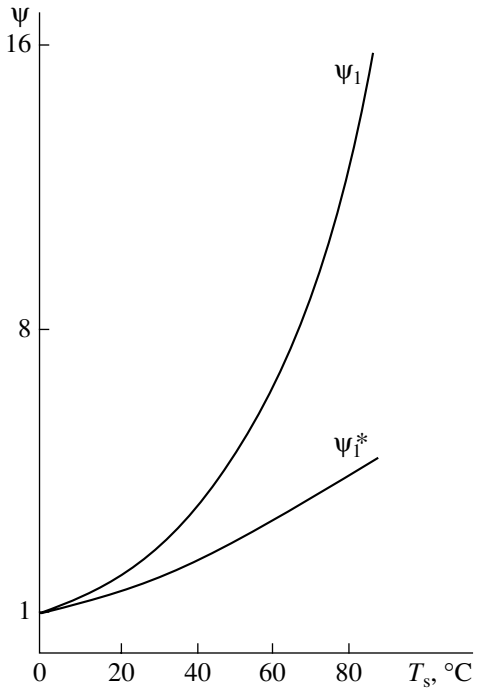

Fig. 2. ψ_1 and ψ_1^* vs. mean surface temperature T_s.

where

$$f_\mu = \frac{2}{3}\exp\{-A\gamma\}\left(N_3 + N_4\frac{\mu_e^s}{3\mu_i^s}\right)\Big/\left(N_1 + N_2\frac{\mu_e^s}{3\mu_i^s}\right).$$

Ultimately, a spherical drop moving under gravity in a liquid with viscosity acquires a constant velocity; that is, the gravity force is balanced out by the hydrodynamic forces. With regard for the buoyancy force, the gravity force acting on the particle is given by

$$\mathbf{F} = (\rho_i - \rho_e)g\frac{4}{3}\pi R^3\mathbf{n}_z, \qquad (23)$$

where g is the free-fall acceleration.

Equating (22) to (23), we obtain the rate of fall of a uniformly heated spherical drop (an analog of the Hadamard–Rybchinsky formula):

$$\mathbf{U}_e = h_\mu\mathbf{n}_z \quad \left(h_\mu = \frac{2}{9}R^2\frac{\rho_i - \rho_e}{\mu_\infty f_\mu}g\right). \qquad (24)$$

If $\mu_e^s/\mu_i^s \longrightarrow 0$ in (22), we come to the formula for the drag force acting on a uniformly heated solid particle (an analog of the Stokes formula).

If the surface of the drop is heated insignificantly, i.e., if the mean surface temperature of the drop differs from the environmental temperature at infinity only slightly [$\gamma = (T_s - T_\infty)/T_\infty \longrightarrow 0$], the temperature dependence of the dynamic coefficient viscosity can be neglected. Then, $G_1 = -1/3$, $G_1^I = 1$, $G_1^{II} = -4$, $G_1^{III} = 20$, $G_2 = -1$, $G_2^I = 1$, $G_2^{II} = -2$, $G_2^{III} = 6$, $N_1 = 2/3$, $N_2 = 2$, $N_3 = -1$, and $N_4 = -2$. In this case, formula (22) turns to the well-known expressions for a sphere that were obtained by Hadamard and also by Rybchinsky and Stokes [10].

The effect of heating the drop on the drag force and the rate of fall of the drop [i.e., the effect of the temperature dependence of the viscosity, formula (1)] is illustrated in Figs. 1 and 2. They plot, respectively, $\psi = f_\mu/f_\mu|_{T_s = 273\ \mathrm{K}}$ and $\psi_1 = h_\mu/h_\mu|_{T_s = 273\ \mathrm{K}}$ against T_s for large mercury drops of radius $R = 2 \times 10^{-5}$ m moving in water at $T_\infty = 273$ K. The curve ψ_1^* was constructed for small temperature differences ($\gamma \longrightarrow 0$) [10], but the molecular transport coefficients were taken for $T_e = T_s$. As follows from the curves, heating considerably affects both the drag force and the rate of gravity fall.

Thus, we generalized the Stokes and Hadamard–Rybchinsky expressions for the case of the steady-state motion of a uniformly heated solid spherical particle (drop) in an incompressible liquid under gravity at arbitrary temperature differences between the surface of the particle and distant points. In the analysis, the temperature dependence of the viscosity is represented as an exponential-power series.

REFERENCES

1. C. F. Bohren and D. R. Huffman, *Absorption and Scattering of Light by Small Particles* (Wiley, New York, 1983; Mir, Moscow, 1986).
2. A. V. Kuzikovskiĭ, Izv. Vyssh. Uchebn. Zaved., Fiz., No. 5, 89 (1970).
3. A. Acrivos and T. D. Taylor, Phys. Fluids **5** (4), 387 (1962).
4. D. R. Kassoy, T. S. Adamson, and A. F. Messiter, Phys. Fluids **9** (4), 7671 (1966).
5. A. M. Golovin and V. V. Fominykh, Izv. Akad. Nauk SSSR, Mekh. Zhidk. Gaza, No. 1, 38 (1983).

6. V. I. Naĭdenov, Prikl. Mat. Mekh. **38**, 162 (1974).
7. St. Bretsznajder, *Properties of Gases and Liquids. Engineering Methods of Calculation* (Wydawnictwo Naukowo-Techniczne, Warsaw, 1962; Khimiya, Moscow, 1966), translated from Polish.
8. N. B. Vargaftik, *Tables of the Thermophysical Properties of Liquids and Gases* (Nauka, Moscow, 1971; Halsted Press, New York, 1975).
9. V. G. Levich, *Physicochemical Hydrodynamics* (Fizmatgiz, Moscow, 1959).
10. J. Happel and H. Brenner, *Low Reynolds Number Hydrodynamics* (Prentice-Hall, Englewood Cliffs, 1965; Mir, Moscow, 1976).
11. N. V. Malaĭ, M. A. Amatov, and E. R. Shchukin, in *Collection of Scientific Works* (Ryazans. Gos. Pedagog. Univ., Ryazan, 1995), pp. 102–112.
12. L. D. Landau and E. M. Lifshitz, *Course of Theoretical Physics*, Vol. 6: *Fluid Mechanics* (Nauka, Moscow, 1986; Pergamon, New York, 1987).

Translated by V. Isaakyan

Technical Physics, Vol. 47, No. 3, 2002, pp. 291–298. Translated from Zhurnal Tekhnicheskoĭ Fiziki, Vol. 72, No. 3, 2002, pp. 24–30.

GASES AND LIQUIDS

The Effect of Volatility on the Thermophoretic Motion of a High-Viscosity Sphere in a Binary Gaseous Mixture with Regard for Thermodiffusion and Stefan Effects

S. N. D'yakonov*, L. V. Kotlyarova*, and Yu. I. Yalamov**

** Orel State University, Orel, 302015 Russia*

e-mail: UA3ECF@ORYOL.ORG

*** Moscow Pedagogical University, ul. Radio 10a, Moscow, 107005 Russia*

Received March 23, 2001; in final form, July 12, 2001

Abstract—The effect of the evaporation coefficient of a large aerosol particle on the velocity of its thermophoretic motion in a binary gaseous mixture is studied. The thermodiffusion of the mixture components and Stefan phenomena are taken into consideration. The results of this study are more general than those obtained previously. The conventional theories of thermophoresis, as applied to a volatile high-viscosity liquid drop, are extended for the cases of weak and moderately intense diffusive evaporation. © *2002 MAIK "Nauka/Interperiodica".*

INTRODUCTION

To date, the dynamics of individual particles in viscous gaseous media that are nonuniform in temperature and concentration has been studied at great length. Extensive references are given in related books (see, e.g., [1, 2]). In the limiting case when the effect of the nonuniform evaporation of the condensed phase on the reactive part of the momentum acting on the particle is negligible, the conventional theories for nonvolatile and volatile particles give the same results. Physically, however, such an approach seems to be rather formal, since the absence of volatility is not specifically indicated. Therefore, it is of interest to estimate the effect of the evaporation rate of an aerosol particle on thermophoresis and diffusive phoresis.

STATEMENT OF THE PROBLEM

A volatile high-viscosity spherical particle with an evaporation coefficient α is immersed in an unbounded stationary nonuniformly heated binary gas mixture with a constant temperature gradient $\mathbf{A}_T$. It is assumed that one of the components of the gaseous mixture undergoes the phase transition on the surface with a radius of curvature of R. Molecules of the condensed phase evaporate or condense at Mach numbers much less than unity and produce the first (volatile) component of the gaseous mixture. For molecules of the second component (carrier), the interface is impermeable.

The thermal creep of the gas over the interface causes the particle to move in the gaseous medium. In the laboratory frame of reference, directional uniform transfer with creep is characterized by a thermophoretic velocity $\mathbf{U}_T$. The high-viscosity sphere is subjected to the thermophoretic force, $\mathbf{F}_{\text{TP}}$, diffusive phoretic force, $\mathbf{F}_{\text{DP}}$, and reactive force, $\mathbf{F}_\alpha$, which tend to balance the viscous force $\mathbf{F}_\mathbf{V}$. The desired velocity $\mathbf{U}_T$ is established when the resultant force vanishes.

The problem is solved in the spherical coordinate system (r, Θ, φ). The origin is rigidly related to the geometric center of the sphere $r = R$, and the axis $0z$ is directed along the vector $\mathbf{A}_T = \nabla T_\infty$, where ∇ is the del operator. In this frame of reference, the center of mass of the external medium has the velocity $\mathbf{U} = -\mathbf{U}_T$.

The binary gaseous mixture is assumed to be incompressible, viscous, isotropic, and continuous, and the Knudsen number is relatively small:

$$\text{Kn} = \frac{\lambda}{R} \ll 1; \quad \lambda = \max(\lambda_1, \lambda_2),$$

where λ_i is the mean free path of gas molecules of the ith sort.

Relative changes in the temperature and concentration are also assumed to be small. The molecular transfer coefficients are assumed to be constant if the temperature T_0, relative concentration C_0 of the volatile component, and pressure p_0 are undisturbed. The parameters are undisturbed at the former geometric center of the particle when it is absent (the value of C_0 is found through the concentrations n_{10} and n_{20} of the gas molecules of the first and second sort). Our theoretical model ignores the time variation of T_0 and temperature drops associated with heat release due to viscous friction. Heat sources inside and in the vicinity of the aerosol particle are absent.

We consider the case of small Reynolds numbers: nonlinear terms in the equation of motion and the equa-

tion of heat and mass transfer are omitted. External mass forces do not act. Material circulation inside the drop and the surface tension force are not considered. The "solid" volatile aerosol particle retains the spherical shape during the thermophoretic motion.

Let the times of hydrodynamic, concentration, and thermal relaxations be small compared with the characteristic time of sphere transfer. Then, the state of the gaseous medium is hydrodynamically analyzed in the quasi-stationary approximation. This means that the vector field of velocities $\mathbf{v}(\mathbf{r})$; the distributions of the pressure $p(\mathbf{r})$ and relative concentration $C(\mathbf{r})$ of the volatile in the binary gaseous mixture; and the scalar temperature fields $T(\mathbf{r})$ and $T'(\mathbf{r})$ outside and inside the particle, respectively, are assumed to be stationary at any time instant and obey the axisymmetric Stokes equations, Laplace equations, and the continuity equation:

$$\eta_0 \Delta \mathbf{v} = \nabla p, \quad \mathrm{div}\mathbf{v} = 0,$$

$$\Delta C = 0, \quad \Delta T = 0, \quad \Delta T' = 0,$$

where Δ is the Laplacian.

At infinity and at the interface, the following conditions are valid:

$$r \longrightarrow \infty: \mathbf{v} = U\mathbf{i}_z, \quad T = T_0 + A_T z, \quad C = C_0;$$

$$r = R: n_1 v_r - \frac{(n_1 + n_2)^2 m_2}{\rho} D\{\nabla_r C + K_{TD}\nabla_r(\ln T)\}$$
$$= \alpha\nu(n_1 + n_2)\{C_s(T') - C\},$$

$$n_2 v_r + \frac{(n_1 + n_2)^2 m_1}{\rho} D\{\nabla_r C + K_{TD}\nabla_r(\ln T)\} = 0,$$

$$v_\Theta = K'_{TSL}\nabla_\Theta T + K'_{DSL}\nabla_\Theta C, \quad T = T',$$

$$-\kappa_0 \nabla_r T + \kappa'_0 \nabla_r T' = -Lm_1\alpha\nu(n_1 + n_2)\{C_s(T') - C\},$$

$$E_z = 0,$$

$$\rho = m_1 n_1 + m_2 n_2,$$

$$C = \frac{n_1}{n_1 + n_2}, \quad C_s(T') = \frac{n_{1s}(T')}{n_1 + n_2}, \quad \nu = \left(\frac{kT}{2\pi m_1}\right)^{\frac{1}{2}},$$

$$\eta_0 = \eta(T_0, C_0, p_0), \quad \kappa_0 = \kappa(T_0, C_0, p_0),$$

$$\kappa'_0 = \kappa'(T_0, p_0).$$

Here, n_1 and n_2 are the concentrations of the gas molecules of the first and second sort with respective masses of m_1 and m_2; D is the coefficient of interdiffusion for the gas mixture components; L is the heat of evaporation of the liquid; κ and κ' are the thermal conductivities of the gas phase and the condensed phase, respectively; k is the Boltzmann coefficient; and the subscript s refers to the saturated vapor of the volatile.

The above conditions have the following physical meaning. At infinity, the axisymmetric flux of the external medium is uniform and has the velocity $\mathbf{U}$, which is directed along the positive branch of the $0z$ axis. The temperature field $T(\mathbf{r})$ and the distribution of the relative concentration $C(\mathbf{r})$ of the volatile component are undisturbed.

The normal flow of the first (volatile) component at the interface is represented as the normal outflow of the volatile vapor from the surface through the Knudsen layer and is proportional to the evaporation coefficient α. The surface of the aerosol particle is impermeable for its carrier.

The shear component of the velocity of the external medium is the sum of the velocities of the thermal and diffusive creeps, which are proportional to the local shear gradients $\nabla_\Theta T$ and $\nabla_\Theta C$, respectively. The proportionality coefficients,

$$K'_{TSL} = K_{TSL}\frac{\eta_0}{\rho_0 T_0}, \quad K'_{DSL} = K_{DSL}D,$$

are determined by mathematical methods used in the kinetic theory of gases.

Since the Knudsen number is small, the isothermal creep, having the near-zero (KnU) velocity is neglected [1, 3]. The temperature and the normal heat flux with regard for the phase transition are continuous.

The resultant force $\mathbf{F}$, acting on the volatile drop on the side of the incoming flow of the external medium, equals zero.

At the interface, the normal flux

$$\alpha\nu(n_1 + n_2)m_1\{C_s(T') - C\}$$

of the volatile material and the difference between the normal heat fluxes outside and inside the drop have opposite signs.

In the left-hand sides of the first and second boundary conditions, the thermodiffusion force neglects the barodiffusion term and the term with the other forces, since they do not act on the gas molecules. The right-hand side of the first equality is obtained from simple statistical considerations that the evaporation coefficient and the coefficient of vapor condensation equal each other.

Let the gas molecules in the Knudsen layer of thickness $l \sim \lambda$ obey the Maxwell distribution and let ν designate one quarter of the mean absolute thermal velocity of vapor molecules. We assume that molecular exchange in the Knudsen layer is free, as in free space. Then, the rate of evaporation from unit surface area is $\alpha\nu(T')(n_1 + n_2)C_s(T')$. Since the diffusion equation is valid only outside the Knudsen layer, the rate of vapor condensation on unit surface area is $\alpha\nu(T)(n_1 + n_2)C$, where C is the relative concentration of the vapor molecules at a distance l from the particle. On a slightly curved surface, $T = T'$ and $\nu = \nu(T) = \nu(T')$, so that the rate of evaporation from this surface is given by

$$\alpha\nu(n_1 + n_2)\{C_s(T') - C(T)\}.$$

This expression coincides with the right-hand side of the first boundary condition if the Knudsen layer formally tends to disappear (Kn $\longrightarrow$ 0). The above expression for the normal vapor flow out of the surface remains valid if the direct effect of volatility on the diffusive phoresis of isolated large spherical high-viscosity drops is taken into account [4].

The partial pressure p_{1s} and the concentration n_{1s} of the saturated vapor of a neutral volatile particle depend on the absolute temperature T' and the radius of curvature of the interface (Kn $\ll$ 1). Let the state of the saturated vapor be far from critical, the vapor be approximated by perfect gas, and the saturation vapor pressure be nearly the same as the flat-surface pressure. Then, for the dynamic equilibrium of the condensed phase and the gaseous phase of the pure volatile, the approximate integral of the Clapeyron–Clausius equation can be written as

$$p_{1s}(T') = p_{1s}(T_\omega)\exp\left\{\frac{L\mu}{R_g T_\omega}\frac{T'-T_\omega}{T'}\right\},$$

$$p_{1s}(T') = n_{1s}(T')kT'.$$

Here, T_ω is the mean temperature on the surface of the volatile sphere (determined from the solution of the problem), R_g is the gas constant, and μ is the molar mass of the condensate. The temperature dependence

$$C_s(T') = C_s(T_\omega)\frac{T_\omega}{T'}\exp\left\{\frac{L\mu}{R_g T_\omega}\left(1-\frac{T_\omega}{T'}\right)\right\}$$

is expanded into the Taylor series in $(T' - T_\omega)$. If the nonisothermality of the aerosol particle is small, only the first two terms of the series are left and the estimator of the function $C_s(T')$ at the point $T' = T_\omega$ has the form

$$\left.\frac{\partial C_s}{\partial T'}\right|_{T'=T_\omega} = \frac{T_0}{T_\omega^2}C_s(T_0)\left(\frac{L\mu}{R_g T_\omega}-1\right)\times\exp\left\{\frac{L\mu}{R_g T_\omega}\frac{T_\omega-T_0}{T_0}\right\}.$$

This expression is applied in the numerical analysis of the results what follow.

The solution of the axisymmetric hydrodynamic problem will be represented in terms of the stream function Ψ. In the coordinate system (r, Θ, φ), the velocity component and the z projection of the resultant force acting on the sphere $(r = R)$ in the Stokes approximation are defined through the function $\Psi = \Psi(r, \Theta)$ as follows [3]:

$$v_r = -\frac{1}{r^2\sin\Theta}\frac{\partial\Psi}{\partial\Theta},\quad v_\Theta = \frac{1}{r\sin\Theta}\frac{\partial\Psi}{\partial r},\quad v_\varphi = 0,$$

$$F_z = \pi\eta_0\int_0^\pi r^4\sin\Theta\frac{\partial}{\partial r}\left\{\frac{E^2\Psi}{r^2}\right\}d\Theta,$$

$$E^2 = \frac{\partial^2}{\partial r^2}+\frac{\sin\Theta}{r^2}\frac{\partial}{\partial\Theta}\left\{\frac{1}{\sin\Theta}\frac{\partial}{\partial\Theta}\right\}.$$

In the dimensionless form, the physical quantities involved in the equation of hydrodynamics, equation for heat and mass transfer, and boundary conditions are expressed as

$$\tilde r = \frac{r}{R},\quad \tilde v_r = \frac{v_r}{U},\quad \tilde v_\Theta = \frac{v_\Theta}{U},\quad \tilde\Psi = \frac{\Psi}{UR^2},$$

$$\tilde T = \frac{T-T_0}{A_T R},\quad \tilde T' = \frac{T'-T_0}{A_T R},\quad \tilde F_z = \frac{F_z}{6\pi\eta_0 RU}.$$

Later on, the tilde is omitted and the problem is stated in the following linearized form:

$$E^4\Psi = 0,\quad \Delta T = 0,\quad \Delta T' = 0,\quad \Delta C = 0, \tag{1}$$

$$E^2 = \frac{\partial^2}{\partial r^2}+\frac{1-\zeta^2}{r^2}\frac{\partial^2}{\partial\zeta^2},$$

$$\Delta = \frac{1}{r^2}\frac{\partial}{\partial r}\left(r^2\frac{\partial}{\partial r}\right)+\frac{1}{r^2}\frac{\partial}{\partial\zeta}\left\{(1-\zeta^2)\frac{\partial}{\partial\zeta}\right\}; \tag{2}$$

$$r\longrightarrow\infty:\ \Psi = -\frac{1}{2}r^2(1-\zeta^2),\quad T = z,\quad C = C_0;$$

$$r = 1:\left\{C_0+(1-C_0)\frac{m_2}{m_1}\right\}Uv_r = \alpha\nu\left\{C_s(\tau)+\left.\frac{\partial C_s}{\partial T}\right|_{T=\tau}(T'-\tau)-C\right\}, \tag{3}$$

$$(1-C_0)\left\{C_0+(1-C_0)\frac{m_2}{m_1}\right\}Uv_r + \frac{D}{R}\left\{\frac{\partial C}{\partial r}+K_{TD}\varepsilon\frac{\partial T}{\partial r}\right\} = 0, \tag{4}$$

$$U = \frac{v_\Theta}{\sqrt{1-\zeta^2}} = -K_{TSL}\frac{\eta_0}{\rho_0 T_0}A_T\frac{\partial T}{\partial\zeta}-K_{DSL}\frac{D}{R}\frac{\partial C}{\partial\zeta}, \tag{5}$$

$$T = T', \tag{6}$$

$$-\frac{\kappa_0}{\kappa_0'}\frac{\partial T}{\partial r}+\frac{\partial T'}{\partial r} = -\frac{Lm_1\alpha\nu n_0}{A_T\kappa_0'}$$
$$\times\left\{C_s(\tau)+\left.\frac{\partial C_s}{\partial T}\right|_{T=\tau}(T'-\tau)-C\right\}, \tag{7}$$

$$F_z = 0,$$
$$n_0 = n_{10}+n_{20}, \quad \rho_0 = m_1n_{10}+m_2n_{20},$$
$$-1\le\zeta = \cos\Theta\le+1, \quad \tau = \frac{T_\omega-T_0}{A_TR}\ll 1, \tag{8}$$
$$\varepsilon = \frac{A_TR}{T_0}\ll 1.$$

If the liquid drop is covered by a thin film of a contaminant, it is considered to be nonvolatile ($\alpha \longrightarrow 0$) and the surface of the condensate becomes impermeable for the external phase; that is, the normal component at the interface $r = 1$ vanishes.

DETERMINATION OF THE THERMOPHORESIS VELOCITY

The general solutions of Eq. (1) have the form of infinite series in *n*th-order ultraspherical polynomials of degree ±0.5:

$$J_n(\zeta) = C_n^{-\frac{1}{2}}(\zeta), \quad P_n(\zeta) = C_n^{+\frac{1}{2}}(\zeta),$$
$$\Psi(r,\xi)$$
$$= \sum_{n=2}^{\infty}\{A_nr^n+B_nr^{-n+1}+C_nr^{n+2}+D_nr^{-n+3}\}J_n(\zeta),$$
$$v_r(r,\zeta)$$
$$= -\sum_{n=2}^{\infty}\{A_nr^{n-2}+B_nr^{-n-1}+C_nr^n+D_nr^{-n+1}\}P_{n-1}(\zeta),$$
$$v_\Theta(r,\zeta) = \sum_{n=2}^{\infty}\{nA_nr^{n-2}-(n-1)B_nr^{-n-1}$$
$$+(n+2)C_nr^n-(n-3)D_nr^{-n+1}\}\frac{J_n(\zeta)}{\sqrt{1-\zeta^2}},$$
$$\begin{matrix}T\\T'\end{matrix}(r,\zeta) = \sum_{n=0}^{\infty}\left\{\begin{matrix}E_n\\G_n\end{matrix}r^n+\begin{matrix}F_n\\H_n\end{matrix}r^{-n-1}\right\}P_n(\zeta),$$
$$C(r,\zeta) = \sum_{n=0}^{\infty}\{K_nr^n+L_nr^{-n-1}\}P_n(\zeta).$$

Taking into account conditions (2) at infinity and the finiteness of the temperature at the center of the particle, we can supplement expressions (3)–(8) by the expansions

$$\Psi(r,\zeta) = -r^2J_2(\zeta)+\sum_{n=2}^{\infty}\{B_nr^{-n+1}+D_nr^{-n+3}\}J_n(\zeta),$$
$$T(r,\zeta) = r\zeta+\sum_{n=0}^{\infty}F_nr^{-n-1}P_n(\zeta),$$
$$T'(r,\zeta) = \sum_{n=0}^{\infty}G_nr^nP_n(\zeta),$$
$$C(r,\zeta) = C_0+\sum_{n=0}^{\infty}L_nr^{-n-1}P_n(\zeta).$$

Properties (A2), (A3) and orthogonality conditions (A5), (A6) for ultraspherical polynomials allow us to write the expressions for the constants of integration ($n \ge 2$):

$$C_s(\tau)-C_0+\left.\frac{\partial C_s}{\partial T}\right|_{T=\tau}(G_0-\tau)-L_0 = 0, \tag{3a}$$

$$-\left\{C_0+(1-C_0)\frac{m_2}{m_1}\right\}U(-1+B_2+D_2)$$
$$= \alpha\nu\left\{\left.\frac{\partial C_s}{\partial T}\right|_{T=\tau}G_1-L_1\right\}, \tag{3b}$$

$$-\left\{C_0+(1-C_0)\frac{m_2}{m_1}\right\}U(B_{n+1}+D_{n+1})$$
$$= \alpha\nu\left\{\left.\frac{\partial C_s}{\partial T}\right|_{T=\tau}G_n-L_n\right\}, \tag{3c}$$

$$L_0+\varepsilon K_{TD}F_0 = 0, \tag{4a}$$

$$(1-C_0)\left\{C_0+(1-C_0)\frac{m_2}{m_1}\right\}U(-1+B_2+D_2)$$
$$+\frac{D}{R}\{2L_1+\varepsilon K_{TD}(-1+2F_1)\} = 0, \tag{4b}$$

$$(1-C_0)\left\{C_0+(1-C_0)\frac{m_2}{m_1}\right\}U(B_{n+1}+D_{n+1})$$
$$+(n+1)\frac{D}{R}\{L_n+\varepsilon K_{TD}F_n\} = 0, \tag{4c}$$

$$U(2 + B_2 - D_2) = 2K_{\mathrm{TSL}}\frac{\eta_0}{\rho_0 T_0}A_T(1 + F_1) + 2K_{\mathrm{DSL}}\frac{D}{R}L_1, \tag{5a}$$

$$U\{nB_{n+1} + (n-2)D_{n+1}\} = \left\{K_{\mathrm{TSL}}\frac{\eta_0}{\rho_0 T_0}A_T F_n + K_{\mathrm{DSL}}\frac{D}{R}L_n\right\}n(n+1), \tag{5b}$$

$$F_0 = G_0, \quad 1 + F_1 = G_1, \quad F_n = G_n, \tag{6a–6c}$$

$$\frac{\kappa_0}{\kappa_0'}F_0 = -\frac{Lm_1\alpha\nu n_0}{A_T\kappa_0'} \times\left\{C_3(\tau) - C_0 + \left.\frac{\partial C_3}{\partial T}\right|_{T=\tau}(G_0 - \tau) - L_0\right\}, \tag{7a}$$

$$\frac{\kappa_0}{\kappa_0'}(-1 + 2F_1) + G_1 = -\frac{Lm_1\alpha\nu n_0}{A_T\kappa_0'}\left\{\left.\frac{\partial C_s}{\partial T}\right|_{T=\tau}G_1 - L_1\right\}, \tag{7b}$$

$$\frac{\kappa_0}{\kappa_0'}(n+1)F_n + nG_n = -\frac{Lm_1\alpha\nu n_0}{A_T\kappa_0'}\left\{\left.\frac{\partial C_s}{\partial T}\right|_{T=\tau}G_n - L_n\right\}. \tag{7c}$$

From relationships (3a), (4a), (6a), and (7a), we find

$$F_0 = G_0 = L_0 = 0. \tag{8}$$

With property (A4) and condition (8), the integration of the expression for F_z yields

$$F_z = \frac{1}{6}\int_{-1}^{+1} r^4\frac{\partial}{\partial r}\left\{\frac{E^2\Psi}{r^2}\right\}d\zeta = \frac{2}{3}D_2,$$

$$D_2 = 0.$$

From Eqs. (3b) and (5a) in view of (6b), we find

$$3\left\{C_0 + (1 - C_0)\frac{m_2}{m_1}\right\}U = 2\left\{C_0 + (1 - C_0)\frac{m_2}{m_1}\right\}K_{\mathrm{TSL}}\frac{\eta_0}{\rho_0 T_0}A_T(1 + F_1) + 2\left\{C_0 + (1 - C_0)\frac{m_2}{m_1}\right\}K_{\mathrm{DSL}}\frac{D}{R}L_1 + \alpha\nu\left\{\left.\frac{\partial C_s}{\partial T}\right|_{T=\tau}(1 + F_1) - L_1\right\}.$$

From Eqs. (3b), (4b), and (7b) in view of (6b), we have

$$\left\{(1 - C_0)\frac{\alpha\nu R}{D}\left.\frac{\partial C_s}{\partial T}\right|_{T=\tau} - 2\varepsilon K_{\mathrm{TD}}\right\}(1 + F_1) - \left\{2 + (1 - C_0)\frac{\alpha\nu R}{D}\right\}L_1 = -3\varepsilon K_{\mathrm{TD}}, \tag{9}$$

$$\left\{\frac{Lm_1\alpha\nu n_0}{A_T\kappa_0'}\left.\frac{\partial C_s}{\partial T}\right|_{T=\tau} + 1 + 2\frac{\kappa_0}{\kappa_0'}\right\}(1 + F_1) - \frac{Lm_1\alpha\nu n_0}{A_T\kappa_0'}L_1 = 3\frac{\kappa_0}{\kappa_0'}. \tag{10}$$

The solution of the set of equations (9) and (10) yields

$$1 + F_1 = 3\frac{\Delta'}{\Delta}, \quad L_1 = 3\frac{\Delta''}{\Delta},$$

$$\Delta = \left(1 + 2\frac{\kappa_0}{\kappa_0'}\right)\left\{2 + (1 - C_0)\frac{\alpha\nu R}{D}\right\} + 2\frac{Lm_1\alpha\nu n_0}{A_T\kappa_0'}\left\{\left.\frac{\partial C_s}{\partial T}\right|_{T=\tau} + \varepsilon K_{\mathrm{TD}}\right\},$$

$$\Delta' = \frac{\kappa_0}{\kappa_0'}\left\{2 + (1 - C_0)\frac{\alpha\nu R}{D}\right\} + \varepsilon K_{\mathrm{TD}}\frac{Lm_1\alpha\nu n_0}{A_T\kappa_0'},$$

$$\Delta'' = \frac{\kappa_0}{\kappa_0'}(1 - C_0)\frac{\alpha\nu R}{D}\left.\frac{\partial C_s}{\partial T}\right|_{T=\tau} + \varepsilon K_{\mathrm{TD}}\left\{\frac{Lm_1\alpha\nu n_0}{A_T\kappa_0'}\left.\frac{\partial C_s}{\partial T}\right|_{T=\tau} + 1\right\}.$$

Eventually, for the velocity $\mathbf{U} = -\mathbf{U}_T$, we obtain

$$U = 2K_{\mathrm{TSL}}\frac{\eta_0}{\rho_0 T_0}A_T\frac{\Delta'}{\Delta} + 2K_{\mathrm{DSL}}\frac{D}{R}\frac{\Delta''}{\Delta} + \frac{\alpha\nu}{C_0 + (1 - C_0)\dfrac{m_2}{m_1}}\left\{2\frac{\kappa_0}{\kappa_0'}\left.\frac{\partial C_s}{\partial T}\right|_{T=\tau} - \varepsilon K_{\mathrm{TD}}\right\}\frac{1}{\Delta}. \tag{11}$$

The set of equations (3c), (4c), (5b), (6c), and (7c) has the trivial solution $B_{n+1} = D_{n+1} = F_n = G_n = L_n = 0$ at any $n \geq 2$. The mean reduced temperature τ at the interface is found by solving the transcendental algebraic equation

$$C_s(\tau) - C_0 - \left.\frac{\partial C_s}{\partial T}\right|_{T=\tau} \tau = 0.$$

ANALYSIS OF THE RESULTS

In formula (11), the first and second terms stand for the thermal and diffusive creeps, respectively. The third one is associated with the phase transition and describes the action of the reactive part of the momentum on the particle. The temperature dependence of the relative concentration of the volatile component vapor and the volume thermal diffusion effects in the gaseous mixture cause nonuniform evaporation from the condensed phase boundary and, accordingly, the reactive effect.

In the limit case $\alpha \longrightarrow 0$ and $K_{TD} \longrightarrow 0$, the thermophoresis velocity of a solid nonvolatile aerosol particle is given by [1]

$$U' = K_{TSL}\frac{\eta_0}{\rho_0 T_0}\frac{2\frac{\kappa_0}{\kappa_0'}}{1+2\frac{\kappa_0}{\kappa_0'}}A_T.$$

In the limit case of a large volatile spherical single-component high-viscosity aerosol drop, the theory of thermophoresis in a binary gaseous mixture (neglecting thermodiffusion effects) [5] gives the following formula (in our designations):

$$U'' = 2K_{TSL}\frac{\eta_0}{\rho_0 T_0}(1-C_0)\frac{\kappa_0}{\kappa_0'}\frac{1}{\Omega}A_T + 2K_{DSL}\frac{D}{R}(1-C_0)\frac{\kappa_0}{\kappa_0'}\left.\frac{\partial C_s}{\partial T}\right|_{T=\tau}\frac{1}{\Omega} + \frac{2}{C_0+(1-C_0)\frac{m_2}{m_1}}\frac{D}{R}\frac{\kappa_0}{\kappa_0'}\left.\frac{\partial C_s}{\partial T}\right|_{T=\tau}\frac{1}{\Omega},$$

$$\Omega = \left(1+2\frac{\kappa_0}{\kappa_0'}\right)(1-C_0) + 2\frac{Lm_1n_0}{A_T\kappa_0'}\left.\frac{\partial C_s}{\partial T}\right|_{T=\tau}\frac{D}{R}.$$

This formula also includes the heat flux due to the convective transfer of the volatile on the surface of the drop.

It should be noted that the limit case of a nonvolatile drop [5],

$$\left.\frac{\partial C_s}{\partial T}\right|_{T=\tau} \longrightarrow 0$$

does not mean that volatility as a phenomenon is absent. This limit merely indicates that the reactive effect disappears in the linear approximation.

If thermodiffusion is neglected and the high-viscosity drop intensely evaporates in the diffusion regime,

$$C_0 \ll 1, \quad \frac{\alpha\nu R}{D} \gg 1,$$

expression (11) gives an estimate of the center-of-mass velocity U'' of the gas. Therefore, expression (11) is the most general.

The condensation (evaporation) coefficient is usually defined as the probability that a vapor molecule striking (leaving) the surface will not leave (return to) it. The disadvantage of such a definition is that the associated coefficient is found indirectly, for example, by measuring the rate of condensation growth (evaporative shrinkage) of the drop. The condensation (evaporation) coefficient is difficult to find experimentally. The literature data on this point are rather contradictory. For example, the coefficient α for water drops measured by a variety of techniques reviewed in [6, 7] was found to be both low, $\alpha \approx 0.01$ [8, 9], and high, $\alpha \approx 1$ [10, 11]. From expression (11), it follows that if

$$\left.\frac{\partial C_s}{\partial T}\right|_{T=\tau} > 0, \quad K_{TD} = 0$$

the drop tends to move toward colder regions of the gaseous medium by virtue of the first and third terms ("positive" factors). The effect of the second term on the velocity $\mathbf{U}_T$ of thermophoresis depends on the coefficient K_{DSL}: if $m_1 > m_2$ ($K_{DSL} < 0$), the directions of the vector $\mathbf{A}_T$ and the drop coincide; otherwise ($m_1 < m_2$; $K_{DSL} > 0$), the directions are opposite.

The effect of volatility on the thermodiffusion fields and thermophoresis can be neglected if the evaporation of the drop is sufficiently weak and the thermodiffusion effects are pronounced:

$$0 < \frac{\alpha\nu R}{D} \ll 1,$$

$$0 < \left.\frac{\partial C_s}{\partial T}\right|_{T=\tau} \ll \varepsilon|K_{TD}| < 1,$$

$$0 < \varepsilon|K_{TD}|\frac{Lm_1\alpha\nu n_0}{A_T\kappa_0'} \ll \frac{\kappa_0}{\kappa_0'}\frac{\alpha\nu R}{D} < 1.$$

From these inequalities, we have

$$\Delta \longrightarrow 2\left(1+2\frac{\kappa_0}{\kappa_0'}\right), \quad \Delta' \longrightarrow 2\frac{\kappa_0}{\kappa_0'}, \quad \Delta'' \longrightarrow \varepsilon K_{TD},$$

$$U \longrightarrow K_{TSL}\frac{\eta_0}{\rho_0 T_0}A_T\frac{2\frac{\kappa_0}{\kappa_0'}}{1+2\frac{\kappa_0}{\kappa_0'}} + K_{DSL}\frac{D}{T_0}A_T\frac{K_{TD}}{1+2\frac{\kappa_0}{\kappa_0'}}.$$

Combining the above inequalities with the estimate

$$\left.\frac{\partial C_s}{\partial T}\right|_{T=0} = \varepsilon C_s(0)\left(\frac{L\mu}{R_g T_0} - 1\right)$$

we obtain the conditions when the effect of volatility can be disregarded:

$$\frac{\alpha\nu R}{D} \ll 1, \quad \left|\frac{L\mu}{R_g T_0} - 1\right| \ll |K_{TD}|, \quad |K_{TD}|\frac{Lm_1 n_0 D}{\kappa_0 T_0} \ll 1.$$

The distributions $T(\mathbf{r})$, $T'(\mathbf{r})$, and $C(\mathbf{r})$ are nearly independent of the thermal conductivity of the gaseous mixture if that of the volatile drop is high. The drop gains the unbalanced momentum primarily through thermodiffusion:

$$\Delta' \longrightarrow \varepsilon K_{TD}\frac{Lm_1\alpha\nu n_0}{A_T\kappa_0'},$$

$$\Delta'' \longrightarrow \varepsilon K_{TD}\left\{\frac{Lm_1\alpha\nu n_0}{A_T\kappa_0'}\left.\frac{\partial C_s}{\partial T}\right|_{T=\tau} + 1\right\},$$

$$\Delta \longrightarrow 2 + (1 - C_0)\frac{\alpha\nu R}{D}$$

$$+ 2\frac{Lm_1\alpha\nu n_0}{A_T\kappa_0'}\left\{\left.\frac{\partial C_s}{\partial T}\right|_{T=\tau} + \varepsilon K_{TD}\right\}.$$

Also of interest is the dependence $U = U(\alpha)$:

$$\frac{dU}{d\alpha} = 2\nu\Phi(\kappa_0, \kappa_0')\left\{2\frac{\kappa_0}{\kappa_0'}\left.\frac{\partial C_s}{\partial T}\right|_{T=\tau} - \varepsilon K_{TD}\right\}\frac{1}{\Delta^2},$$

$$\Phi(\kappa_0, \kappa_0') = -2K_{TSL}\frac{Lm_1 n_0 \nu_0}{\kappa_0' T_0 \rho_0}$$

$$+ K_{DSL}\left\{(1 - C_0)\left(1 + 2\frac{\kappa_0}{\kappa_0'}\right) + 2K_{TD}\frac{Lm_1 n_0 D}{\kappa_0' T_0}\right\}$$

$$+ \frac{1}{C_0 + (1 - C_0)\dfrac{m_2}{m_1}}\left(1 + 2\frac{\kappa_0}{\kappa_0'}\right).$$

The function $U(\alpha)$ is monotonically decreasing or increasing. It does not depend on the rate of evaporation if

$$\Phi(\kappa_0, \kappa_0') = 0,$$

$$2\frac{\kappa_0}{\kappa_0'}\left.\frac{\partial C_s}{\partial T}\right|_{T=\tau} - \varepsilon K_{TD} = 0.$$

Here, the first and second relationships between the physical quantities characterizing the state of the media outside and inside high-viscosity aerosol drops are valid for drops with a low and high thermal conductivity, respectively.

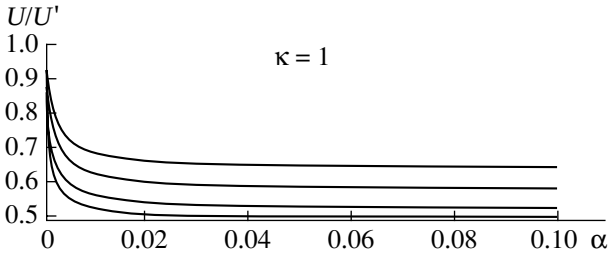

Fig. 1.

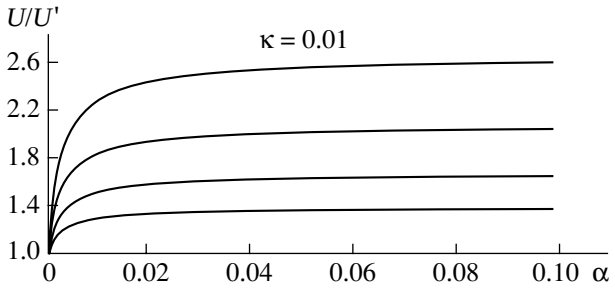

Fig. 2.

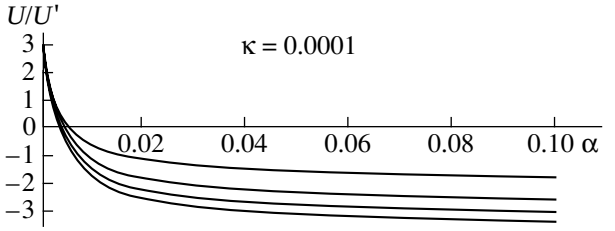

Fig. 3.

Figures 1–3 plot the ratio U/U' against the evaporation coefficient α for a water drop (R = 100 μm) in the steam-air mixture for the undisturbed temperatures T_0 = 293, 303, 313, and 323 K; $n_0 = 2.70 \times 10^{25}$ m^{-3}; and $C_0 = 0.01$. $\kappa = \kappa_0/\kappa_0' = 1$ (Fig. 1), 0.01 (Fig. 2), and 0.0001 (Fig. 3). Necessary reference data were taken from [1, 2, 12].

When α is small, the thermophoresis velocity depends on α very strongly. This dependence is extremely weak at $\alpha \geq 0.05$. At not-very-high temperatures, water volatility changes the velocity of thermophoretic transfer several fold in comparison with U'. This is consistent with the results obtained in [13].

APPENDIX

$$J_n(\xi) = \frac{P_{n-2}(\zeta) - P_n(\zeta)}{2n - 1}, \quad n \geq 2, \qquad \text{(A1)}$$

$$\frac{dJ_n(\zeta)}{d\zeta} = -P_{n-1}(\zeta), \quad n \geq 1, \qquad \text{(A2)}$$

$$(1-\zeta^2)\frac{dP_n(\zeta)}{d\zeta} = n(n+1)J_{n+1}(\zeta), \quad n \geq 0, \quad \text{(A3)}$$

$$\int_{-1}^{+1} J_n(\zeta)d\zeta = \begin{cases} 2 & \text{for } n = 0 \\ \frac{2}{3} & \text{for } n = 2 \\ 0 & \text{for } n \neq 0; 2, \end{cases} \quad \text{(A4)}$$

$$\int_{-1}^{+1} \frac{J_m(\zeta)J_n(\zeta)}{1-\zeta^2}d\zeta = \begin{cases} 0 & \text{for } m \neq n \\ \frac{2}{n(n-1)(2n-1)} & \text{for } m = n, \end{cases} \quad \text{(A5)}$$

$$\int_{-1}^{+1} P_m(\zeta)P_n(\zeta)d\zeta = \begin{cases} 0 & \text{for } m \neq n \\ \frac{2}{2n+1} & \text{for } m = n. \end{cases} \quad \text{(A6)}$$

Orthogonality conditions like (A5) require that $m \neq 0, 1$ and $n \neq 0, 1$.

REFERENCES

1. Yu. I. Yalamov and V. S. Galoyan, *Dynamics of Drops in Inhomogeneous Viscous Media* (Luĭs, Yerevan, 1985).
2. E. R. Shchukin, Yu. I. Yalamov, and Z. L. Shulimanova, *Selected Problems of Physics of Aerosols* (MPU, Moscow, 1992).
3. J. Happel and H. Brenner, *Low Reynolds Number Hydrodynamics* (Prentice-Hall, Englewood Cliffs, 1965; Mir, Moscow, 1976).
4. Yu. I. Yalamov, Available from VINITI, No. 4120-V 90 (Moscow, 1990).
5. Yu. I. Yalamov and A. V. Chermoshentsev, Available from VINITI, No. 1555-V 90 (Moscow, 1990).
6. B. Paul, Am. Rocket Soc. J. **32**, 1321 (1962).
7. A. I. Neizvestnyĭ, *Results of Experimental Determination of Water Condensing Coefficient* (VNIIGMI MTsD, Obninsk, 1976).
8. A. M. Sinnarwalla, D. J. Alots, and J. C. Carstens, J. Atmos. Sci. **32**, 592 (1975).
9. M. A. Vietti and B. G. Schuster, J. Chem. Phys. **58**, 434 (1973).
10. L. V. Ivanchenko, Tr. Ukr. Nauchno-Issled. Gidrometeorol. Inst., No. 156, 58 (1977).
11. A. I. Neizvestnyĭ, G. V. Kotov, and L. I. Onishchenko, Izv. Akad. Nauk SSSR, Fiz. Atmos. Okeana **15**, 74 (1979).
12. N. B. Vargaftik, *Tables of the Thermophysical Properties of Liquids and Gases* (Nauka, Moscow, 1972; Halsted Press, New York, 1975).
13. S. P. Bakanov, Izv. Akad. Nauk, Mekh. Zhidk. Gaza, No. 5, 181 (1995).

Translated by V. Isaakyan

Technical Physics, Vol. 47, No. 3, 2002, pp. 299–305. Translated from Zhurnal Tekhnicheskoĭ Fiziki, Vol. 72, No. 3, 2002, pp. 17–23.

GASES AND LIQUIDS

On the Interaction between a Charged Drop and an External Acoustic Field

A. I. Grigor'ev, A. P. Gaibov, and S. O. Shiryaeva

Demidov Yaroslavl State University, Sovetskaya ul. 14, Yaroslavl, 150000 Russia

e-mail: grig@uniyar.ac.ru

Received April 17, 2001

Abstract—An interaction between capillary oscillations of a charged drop and an external acoustic field is investigated under conditions in which nonlinear components of the acoustic pressure on the drop surface may be neglected. It is shown that equations describing the temporal evolution of modes of the capillary waves in this case may be either the Mathieu–Hill equations or ordinary inhomogeneous equations of the second order describing forced oscillations. In both cases, the drop instability (of a parametric or resonance type) may result in its disintegration due to deformation caused by the acoustic field at its own drop charge, subcritical in the sense of the Rayleigh criterion. © *2002 MAIK "Nauka/Interperiodica".*

1. Investigation of the interaction between an acoustic wave and a charged liquid drop is of interest in connection with numerous applications in geophysics, physics of aerosols, physics of thunderstorm electricity, acoustic levitation of drops in experiments aimed at producing high-purity materials (see, for example, [1–7] and the references therein), and other fields. However, some aspects of the excitation of capillary oscillations of a drop by acoustic waves are still insufficiently understood. For example, the stability of a charged drop exposed to an acoustic wave, as well as the effect on the energy transfer from the wave to the drop of the wave intensity, drop size, and its viscosity have not yet been investigated, though it was suggested that acoustic waves can affect disintegration and coalescence of charged drops, and conditions for rain precipitation [3]. Most of the early investigations dealt with the force acting on a drop of in an acoustic field produced for the purpose of ultrasonic dispersal of fogs and clouds [1, 4] or acoustic levitation [2, 3, 5–7]; therefore, the acoustic field was assumed very intensive, thus limiting the variety of possible interactions.

2. Consider a problem of dissipation of a plane sound wave by a drop of an ideal incompressible electroconductive liquid of a radius R having a density ρ_1 and surface tension γ carrying an electrical charge Q. The ambient is assumed to be ideal and compressible with a permitivity $\varepsilon = 1$ and density ρ_2.

The plane sound wave propagates from $-\infty$ along the z axis, partially dissipating as it passes around the liquid drop, experiencing thermal vibrations about its equilibrial spherical shape, and travels away toward $+\infty$. The potential of the velocity field in the ambient produced by the plane acoustic wave has the form

$$\varphi(\mathbf{r}, t) = \varphi_0 \exp(ikz - i\omega t), \qquad (1)$$

where φ_0 is the amplitude of the acoustic wave, k is the wave number, ω is the oscillation frequency, and i is the imaginary unit.

An equation of the ambient-drop interface (drop surface) perturbed by the capillary wave motion in a spherical coordinate system with the origin at the drop center of mass can be written in the form

$$r(\Theta, t) = R + \xi(\Theta, t),$$

where $\xi(\Theta, t)$ is a small perturbation of the drop equilibrium spherical surface caused by the thermal motion of the molecules of the drop and the ambient; $|\xi| \ll R$; and the angle Θ is reckoned from the propagation direction of the plane acoustic wave.

The resulting wave motions in the drop and its environment are of the potential type, with potentials $\psi_1(\mathbf{r}, t)$ and $\psi_2(\mathbf{r}, t)$, respectively.

An expression for the pressure exerted by the acoustic field on the drop surface has the form [8]

$$p = \rho_2 \frac{\partial \psi_2}{\partial t} + \frac{\rho_2}{2V^2}\left(\frac{\partial \psi_2}{\partial t}\right)^2 - \frac{1}{2}\rho_2 (\mathrm{grad}\,\psi_2)^2, \qquad (2)$$

where V is the speed of sound in the ambient.

As mentioned above, in most of the earlier investigations on the effect of an acoustic field on a drop (see, for example [2, 3, 5–7] and the references therein), the expression for the field pressure on the drop surface was averaged over the period of the acoustic wave. As a result, the pressure component linear in ψ_2 vanished and in the subsequent analysis only terms quadratic in ψ_2 were kept. In a more general case of the interaction of an acoustic wave with capillary drop oscillations, the term linear in ψ_2 should not be discarded, assuming that this term is of either zero or first order with respect to $|\xi|/R$. Below, situations are considered in which the

1063-7842/03/4702-0299$22.00

term of the acoustic pressure linear in ψ_2 plays a determining role, while the terms quadratic in ψ_2 are negligible.

Let the potential $\psi_2(\mathbf{r}, t)$ of the velocity field of the ambient be

$$\psi_2(\mathbf{r}, t) = \varphi(\mathbf{r}, t) + \varphi^{(1)}(\mathbf{r}, t) + \varphi^{(2)}(\mathbf{r}, t), \quad (3)$$

where $\varphi^{(1)}$ is the potential of the velocity field of the acoustic wave dissipated by the unperturbed drop surface; $\varphi^{(2)}$ is an additional dissipation of the acoustic wave caused by its interaction with the drop surface oscillations.

In the problem considered there is a small parameter $|\xi|/R \ll 1$, which is defined by the amplitude of the capillary drop oscillations. One more small parameter, $kR \ll 1$, may be of importance if the incident sound wavelength λ is much less than the drop characteristic size R (see Appendix).

Let φ_0 be of zero order of smallness with respect to $|\xi|/R$. The potential ψ_1 of the liquid velocity field in a drop is a harmonic function of the first order of smallness with respect to $|\xi|/R$ [9]. The additional term $\varphi^{(2)}$ due to the interaction between the acoustic field and the perturbation $\xi(\Theta, t)$ of the equilibrium spherical surface of the drop is naturally assumed to be of an order of smallness not lower than $|\xi|/R$. Mathematical formulation of the problem considered has the form

$$\Delta\psi_1 = 0, \quad (4)$$

$$\frac{1}{V^2}\frac{\partial^2\psi_2}{\partial t^2} = \Delta\psi_2, \quad (5)$$

$$r = R + \xi(\Theta, t): \quad \frac{\partial\psi_1}{\partial r} = \frac{\partial\psi_2}{\partial r}, \quad (6)$$

$$\frac{\partial\xi}{\partial t} = \frac{\partial\psi}{\partial r}, \quad (7)$$

$$\Delta p - \rho_1\frac{\partial\psi_1}{\partial t} + \rho_2\frac{\partial\psi_2}{\partial t} + \frac{\rho_2}{2V^2}\left(\frac{\partial\psi_2}{\partial t}\right)^2 - \frac{1}{2}\rho_2(\mathrm{grad}\psi_2)^2 + F_q(\Theta, t) = \gamma\left[\frac{2}{R} - \frac{1}{R^2}(2 + \hat{L})\xi\right]; \quad (8)$$

$$r = 0: \quad |\psi_1| < \infty, \quad (9)$$

where Δp is the differential of the constant pressure components in the drop and the ambient; $F_q(\Theta, t)$ is the pressure on the drop surface of the electric field due to its own drop charge; and $\hat{L}$ is the angular component of the Laplacian operator in a spherical coordinate system.

In addition, we postulate that the potential $\psi_2(\mathbf{r}, t)$ satisfies the Zommerfeld radiation condition at infinity [10]

$$r \longrightarrow \infty: \quad \frac{\partial\psi_2}{\partial r} - ik\psi_2 = 0\left(\frac{1}{r}\right). \quad (10)$$

Due to periodicity of the potential $\psi_2(\mathbf{r}, t)$ in time, $\psi_2 \sim \exp(-i\omega t)$, Eq. (5) transforms into the Helmholtz equation

$$\Delta\psi_2 + \frac{\omega^2}{V^2}\psi_2 = 0. \quad (11)$$

It is obvious that the incident plane acoustic wave is a solution of this equation. Substituting (1) into (11) gives a dispersion relation $k^2 \equiv (\omega/V)^2$.

Let us expand boundary conditions (6)–(8) in the vicinity of the unperturbed drop surface at $r = R$ in the small parameter $|\xi|/R$ keeping only the terms linear in $|\xi|/R$:

$$r = R: \quad \frac{\partial\psi_2}{\partial r} \equiv \frac{\partial\varphi}{\partial r} + \frac{\partial\varphi^{(1)}}{\partial r} + \frac{\partial\varphi^{(2)}}{\partial r} + \frac{\partial^2\varphi}{\partial r^2}\xi + \frac{\partial^2\varphi^{(1)}}{\partial r^2}\xi = \frac{\partial\psi_1}{\partial r}, \quad (6a)$$

$$\frac{\partial\xi}{\partial t} = \frac{\partial\psi_1}{\partial r}, \quad (7a)$$

$$\Delta p - \rho_1\frac{\partial\psi_1}{\partial t} + \rho_2\left[\frac{\partial\psi_2}{\partial t}\right] + \frac{\rho_2}{2V^2}\left(\frac{\partial\psi_2}{\partial t}\right)^2 - \frac{1}{2}\rho_2(\mathrm{grad}\psi_2)^2 + F_q(\Theta, t) = \gamma\left[\frac{2}{R} - \frac{1}{R^2}(2 + \hat{L})\xi\right], \quad (8a)$$

$$\frac{\partial\psi_2}{\partial t} \equiv \frac{\partial\varphi}{\partial t} + \frac{\partial\varphi^{(1)}}{\partial t} + \frac{\partial\varphi^{(2)}}{\partial t} + \frac{\partial^2\varphi}{\partial r\partial t}\xi + \frac{\partial^2\varphi^{(1)}}{\partial r\partial t}\xi.$$

Let us analyze the problem formulated in (1)–(5) and (6a)–(8a) to an accuracy of the zero and first orders of smallness with respect to $|\xi|/R$.

3. From boundary condition (6) it follows that in the zero approximation with respect to $|\xi|/R$ the normal component of the velocity field of the ambient becomes zero at the unperturbed drop surface:

$$\frac{\partial\varphi}{\partial r} + \frac{\partial\varphi^{(1)}}{\partial r} = 0. \quad (6b)$$

This condition means that the acoustic wave does not interact with the capillary oscillations of a drop and that dissipation of the incident acoustic wave by the drop in the zero approximation with respect to $|\xi|/R$ occurs in the same way as by a rigid sphere. The problem of dissipation of a plane wave by a rigid sphere is formulated by an equation similar to (11) with boundary conditions (6b) and (10) for the potential ψ_2. Thus, in the zero approximation with respect to $|\xi|/R$, the potential $\varphi^{(1)}$ of the dissipated acoustic wave is found by solving the problem

$$\Delta\varphi^{(1)} + k^2\varphi^{(1)} = 0,$$

$$r \longrightarrow \infty: \quad \frac{\partial \varphi^{(1)}}{\partial r} - ik\varphi^{(1)} = 0\left(\frac{1}{r}\right)$$

with boundary condition (6b) at the drop surface. The potential $\varphi(\mathbf{r}, t)$ of the incident plane wave satisfies the Helmholtz equation (11) and radiation condition (10) automatically.

We shall seek $\varphi^{(1)}$ in the form

$$\varphi^{(1)} = \sum_{n=0}^{\infty} D_n h_n^{(1)}(kr) P_n(\mu) \exp(-i\omega t), \qquad \mu \equiv \cos\Theta, \tag{12}$$

where $h_n^{(1)}(kr)$ are the Hankel spherical functions of the first kind and $P_n(\mu)$ are the Legendre polynomials.

Expanding the plane wave in a series in $P_n(\mu)$ we obtain

$$\varphi(\mathbf{r}, t) = \varphi_0 \sum_{n=0}^{\infty} i^n (2n+1) j_n(kr) P_n(\mu) \exp(-i\omega t). \tag{13}$$

Here, $j_n(kr)$ is the Bessel spherical function. Substituting (12) and (13) into (6b) we find unknown coefficients D_n in expansion (12), which now takes the form

$$\varphi^{(1)} = -\sum_{n=0}^{\infty} \left[\frac{\varphi_0 i^n (2n+1)(\partial j_n/\partial r)}{\partial h_n^{(1)}/\partial r}\right]_{r=R} \times h_n^{(1)}(kr) P_n(\mu) \exp(-i\omega t). \tag{14}$$

The zero-order component with respect to $|\xi|/R$ in the dynamic boundary condition defines an equilibrial shape of the drop (see, for example, [11]), which is spherical in the problem considered. Note that the pressure of the acoustic field (2) on the drop surface averaged over the period of the incident acoustic wave [5–7] does not contribute to dynamic boundary condition (8) in the zero approximation with respect to $|\xi|/R$ at $kR \ll 1$: for the plane wave (1), the sum of nonlinear terms in (2) vanishes and the rest of the components of nonlinear terms, $V^{-2}(\partial\varphi^{(1)}/\partial t)^2$, $V^{-2}(\partial\varphi/\partial t)(\partial\varphi^{(1)}/\partial t) \sim (\omega/V)^2\varphi\varphi^{(1)} \equiv k^2\varphi\varphi^{(1)}$, $(\nabla\varphi)(\nabla\varphi^{(1)})$, and $(\nabla\varphi^{(1)})^2$, are of an order of smallness not lower than $\sim(kR)^2$, which can be easily demonstrated by expanding the cylindrical functions in (13) and (14) and the reduced products of derivatives in series in kR in a region where $kR \ll 1$.

4. In the Appendix, it is shown that according to (13) and (14), at $r = R$ the module of the ratio of amplitudes of the dissipated and incident partial waves, by an order of magnitude, is of $\sim(kR)^0$ for $n \geq 1$, and $\sim(kR)^2$ for $n = 0$. To simplify the following computations for $kR \ll 1$, we confine the consideration to the case of dissipation by the drop of only the zero partial wave in expansion (13); that is, we assume that

$$\varphi = \varphi_0 \frac{\sin(kr)}{kr} \exp(-i\omega t). \tag{13a}$$

Then, from (14) for $\varphi^{(1)}$, it follows that

$$\varphi^{(1)} = -\varphi_0 \left[\frac{(\partial j_0/\partial r)}{\partial h_0^{(1)}/\partial r}\right]_{r=R} h_0^{(1)}(kr) \exp(-i\omega t), \tag{14a}$$

and at $r \longrightarrow R$ we have $\varphi^{(1)} \sim (kR)^2$.

We assume for definiteness that the small parameters kR and $|\xi|/R$ are related as $(kR)^2 \sim |\xi|/R$. Then, in the first approximation with respect to $|\xi|/R$, we deal with a problem formulated by (4) and (11) with the boundary conditions

$$r = R: \quad \frac{\partial \varphi^{(2)}}{\partial r} + \frac{\partial^2 \varphi}{\partial r^2}\xi + \frac{\partial^2 \varphi^{(1)}}{\partial r^2}\xi = \frac{\partial \psi_1}{\partial r}, \tag{6c}$$

$$\frac{\partial \xi}{\partial t} = \frac{\partial \psi_1}{\partial r}, \tag{7c}$$

$$-\rho_1 \frac{\partial \psi_1}{\partial t} + \rho_2 \left[\frac{\partial \varphi^{(2)}}{\partial t} + \frac{1}{2V^2}\left(\frac{\partial \varphi}{\partial t}\right)^2 + \frac{\partial \varphi^{(1)}}{\partial t}\right] + F_q^{(1)}(\Theta, t) = -\gamma \frac{1}{R^2}(2 + \hat{L})\xi, \tag{8c}$$

where $F_q^{(1)}(\Theta, t)$ is the pressure of the electric field of the drop own charge in the approximation of the first order of smallness with respect to $|\xi|/R$.

Components of the acoustic pressure in (8c) (the second and the third terms in brackets) at $r = R$ are functions of time only; therefore, they can be eliminated by redetermining the velocity field potential $\psi_1(\mathbf{r}, t)$ [9]. The component of the acoustic pressure $\sim(\nabla\psi_2)^2$ vanishes due to condition (6b). The other terms of the acoustic pressure are of a higher order of smallness with respect to $|\xi|/R$ than the first term.

We shall seek the potential $\varphi^2(\mathbf{r}, t)$, which must satisfy the Helmholtz equation (11), in the form

$$\varphi^{(2)}(\mathbf{r}, t) = \sum_{n=0}^{\infty} B_n h_n^{(1)}(kr) P_n(\mu) \exp(-i\omega t). \tag{15}$$

Excluding from the consideration radial oscillations of the drop, which are impossible in an incompressible liquid, and the translational motion of its center of mass because the origin of the coordinate system coincides with the center of mass by definition [9], we represent the sought for potential of the velocity field $\psi_1(\mathbf{r}, t)$ inside the drop and the perturbation $\xi(\Theta, t)$ of the drop

equilibrium spherical surface in the form of an expansion in Legendre polynomials:

$$\psi_1(\mathbf{r}, t) = \sum_{n=2}^{\infty} A_n(t) r^n P_n(\mu), \tag{16}$$

$$\xi(\theta, t) = \sum_{n=2}^{\infty} a_n(t) P_n(\mu). \tag{17}$$

We borrow from [12] an expression for the pressure of the electrical field due to the charge residing on the drop surface in the linear approximation with respect to $|\xi|/R$:

$$F_q^{(1)}(\Theta, t) = \frac{Q^2}{4\pi\varepsilon} \sum_{n=2}^{\infty} a_n(t)(n-1) P_n(\mu). \tag{18}$$

Substituting (13a), (14a), and (15)–(18) into boundary conditions (6c)–(8c), we obtain a set of equations describing the temporal evolution of the amplitudes $a_n(t)$ of capillary oscillations of the drop:

$$\frac{d^2 a_n}{dt^2} + E_n \cos(\omega t) \frac{da_n}{dt} + [\omega_{n0}^2 - \omega E_n \sin(\omega t)] a_n = 0,$$

$$E_n \equiv \mathrm{Re}\left[\frac{\varphi_0 \rho_2 n h_n^{(1)}}{\rho_1 R G_n(kR)} (f_{0n}(k, R) - x_{0n}(k, R))\right],$$

$$G_n(kR) \equiv \mathrm{Re}\left[1 - \frac{\rho_2 n h_n^{(1)}(kR)}{\rho_1 n h_n^{(1)}(kR) - \rho_1 kR h_{n+1}^{(1)}(kR)}\right],$$

$$f_{0n}(k, R) \equiv \left[\frac{\partial^2 j_0(kr)}{\partial r^2} \Big/ \frac{\partial h_n^{(1)}(kr)}{\partial r}\right]_{r=R}, \tag{19}$$

$$x_{0n}(k, R) \equiv \left[\frac{\partial j_0(kr)}{\partial r} \Big/ \frac{\partial h_0^{(1)}(kr)}{\partial r}\right]_{r=R} \times \left[\frac{\partial^2 h_0^{(1)}(kr)}{\partial r^2} \Big/ \frac{\partial h_n^{(1)}(kr)}{\partial r}\right]_{r=R},$$

$$\omega_{n0}^2 \equiv \frac{\gamma n(n-1)}{\rho_1 R^3 G_n(kR)} ((n+2) - W), \quad W \equiv \frac{Q^2}{4\pi\varepsilon R^3 \gamma}.$$

Set (19) is an infinite set of the independent Mathieu–Hill equations. With the help of the substitution

$$a_n(t) = \zeta(t) \exp\left(\frac{-E_n}{2\omega} \sin(\omega t)\right)$$

this set can be reduced to a simpler form [14]

$$\frac{d^2\zeta}{dt^2} + \left[\frac{1}{2} E_n^2 \cos^2(\omega t) - \frac{1}{2} E_n \omega \sin(\omega t) + \omega_{n0}^2\right] \zeta(t) = 0. \tag{20}$$

For further consideration we assume that $(\rho_2/\rho_1) \sim 10^{-3}$, while φ_0, R, and k are such that E_n is a small quantity: that is, $E_n \ll 1$. Then, neglecting the term $\sim E_n^2$ in (20) we reduce the equation obtained to the classic form of parametric oscillations, which is convenient for analysis [13]

$$\frac{d^2\zeta}{dt^2} + \omega_{n0}^2 [1 - h \sin(\omega t)] \zeta(t) = 0, \quad h \equiv E_n \omega / 2\omega_{n0}^2 \ll 1. \tag{21}$$

It is known [14] that parametric resonance may take place in a drop when the frequency of an external stimulus ω becomes close enough to twice one of the natural frequencies ω_{n0} of the capillary drop oscillations. Therefore, we assume that $\omega = 2\omega_{n0} + \varepsilon$, where $\varepsilon \ll \omega_{n0}$, and then seek a solution of Eq. (21) by a method of variation of arbitrary constants, as it was done in detail in [13]. As a result we find that the parametric resonance at the frequency ω_{n0} will take place in the system under consideration if a small additional term ε satisfies the set of inequalities

$$-h\omega_{n0}/2 < \varepsilon < h\omega_{n0}/2. \tag{22}$$

In this case, the interaction of an acoustic wave with a vibrating drop is accompanied by the parametric buildup of the drop oscillations at the frequency ω_{n0}. If the drop's own charge is close to the critical one in the sense of the Rayleigh criterion ($W \longrightarrow 4$), then the drop can disintegrate as described in [15].

According to (22), the frequency bandwidth of the external force in the vicinity of $\omega = 2\omega_{n0}$, in which the parametric resonance is realized, is proportional to h and the parametric instability factor η_n is of the same order as h [13]:

$$\eta_n = \frac{1}{2}\left[\left(\frac{h\omega_{n0}}{2}\right)^2 - \varepsilon^2\right]^{1/2}.$$

The above consideration has been carried out in the framework of a model of ideal liquid when the parametric buildup of oscillations takes place at an arbitrary small amplitude of the acoustic wave. If the liquid viscosity is taken into account, causing damping of the drop vibrations in a compressible medium with the damping rate [14]

$$\chi_n = \frac{\nu}{R^2}(2n+1)(n-1) G_n^{-1},$$

where ν is the coefficient of kinematic viscosity, then the frequency bandwidth (22), in which the parametric instability is realized, is reduced as follows:

$$-\left[\left(\frac{h\omega_{n0}}{2}\right)^2 - 4\chi_n^2\right]^{1/2} < \varepsilon < \left[\left(\frac{h\omega_{n0}}{2}\right)^2 - 4\chi_n^2\right]^{1/2}.$$

However, a more important consequence of taking into account the viscosity of a real liquid is that the parametric buildup of capillary waves can now be realized starting only at a certain finite (threshold) amplitude $h = h_*$ (or $\varphi_0 = \varphi_{0*}$) of the acoustic field [13, 14]:

$$h_* = 4\chi_n/\omega_{n0}. \quad (23)$$

From (23) it is easy to obtain a condition directly related to the amplitude range of the acoustic signal in which the parametric instability is realized:

$$\varphi_0 \geq \varphi_{0*} = 4\frac{\nu\rho_1\omega_{n0}}{R\rho_2\omega}(2n+1)(n-1)$$
$$\times\left\{\mathrm{Re}\left[y_0(k,R) - \frac{1}{2}f_{n0}(k,R)h_n^{(1)}(kR)\right]\right\}^{-1}.$$

From the relationship obtained it follows that in the approximation used, $kR \ll 1$ at $\rho_1/\rho_2 \gg 1$, the amplitude threshold for the parametric instability of an acoustic wave due to viscosity is very large even if the viscosity is low.

Note that, in a more general case than discussed in this section, dissipation by a drop not of the zero partial wave but of partial waves with a higher number or the whole plane wave (13), a set of the Mathieu–Hill equations for amplitudes of capillary drop oscillations turns out to be to involved and its analytical analysis becomes difficult. This is the reason why the consideration here is restricted to the case of dissipation of the zero partial wave.

5. Now, we assume that $kR \sim 1$ and the potentials φ and $\varphi^{(1)}$ are of the first order of smallness with respect to $|\xi|/R$; that is, we consider the dissipation of acoustic waves of a very small amplitude by a drop of a radius comparable with the oscillation wavelength. The hydrodynamic potential of the velocity field of the ambient accurate to the first order of smallness with respect to $|\xi|/R$ has the form

$$\psi_2(\mathbf{r}, t) = \varphi(\mathbf{r}, t) + \varphi^{(1)}(\mathbf{r}, t).$$

Then, within an accuracy of the first order of smallness with respect to $|\xi|/R$, we arrive at the problem formulated in (4) and (9)–(11) with boundary conditions (6)–(8) at the unperturbed drop surface; that is, at $r = R$,

$$\frac{\partial\psi_1}{\partial r} = \frac{\partial\psi_2}{\partial r} \equiv \frac{\partial\psi}{\partial r}, \quad (6d)$$

$$\frac{\partial\xi}{\partial t} \approx \frac{\partial\psi}{\partial r}, \quad (7d)$$

$$-\rho_1\frac{\partial\psi_1}{\partial t} + \rho_2\frac{\partial\psi_2}{\partial t} + F_1(\Theta, t) = -\frac{\gamma}{R^2}(2+\hat{L})\xi. \quad (8d)$$

We will seek the potential $\psi_1(\mathbf{r}, t)$ of the velocity field in the drop in the form (16), the perturbation $\xi(\Theta, t)$ of the equilibrium spherical drop in the form (17), the potential $\varphi^{(1)}(\mathbf{r}, t)$ of the velocity field of the dissipated acoustic wave in form (12), and the dissipated plane acoustic wave will be taken in the form (13). Now, we substitute (12), (13), (16), and (17), taking into account (18), into (6d)–(8d) and obtain a set of independent inhomogeneous ordinary differential equations of the second order with constant coefficients describing the temporal evolution of amplitudes a_n of the modes of capillary drop oscillations for $n \geq 2$

$$\frac{d^2a_n}{dt^2} + \omega_{n0}^2 a_n = \omega S_n\exp(-i\omega t), \quad n \geq 2,$$
$$S_n \equiv \varphi_0(2n+1)nk\mathrm{Re} \quad (24)$$
$$\times\left\{\frac{i^{n+1}\rho_2[h_{n+1}^{(1)}(kR)j_n(kR) - h_n^{(1)}(kR)j_{n+1}(kR)]}{G_n(kR)\rho_1[kRh_{n+1}^{(1)}(kR) - nh_n^{(1)}(kR)]}\right\}.$$

Partial spherical acoustic waves with $n = 0$ and 1 in the approximation assumed do not interact with the drop capillary oscillations and are dissipated as by a rigid sphere.

The general solution of Eq. (24) is easily obtained using a conventional technique [13]:

$$a_n = C_n\exp(-i\omega_{n0}t) + \frac{\omega}{\omega_{n0}^2 - \omega^2}S_n\exp(-i\omega t).$$

In the case of resonance, when the external field frequency ω is close to one of the natural frequencies ω_{n0} of the drop oscillations we assume that $\omega = \omega_{n0} + \varepsilon$, where $\varepsilon \ll \omega_{n0}$. Then the solution can be represented in the form

$$a_n = (C_n + N_n\exp(-i\varepsilon t))\exp(-i\omega_{n0}t),$$
$$N_n \equiv \frac{\omega}{\omega_{n0}^2 - \omega^2}S_n.$$

The term in brackets does not change much over the oscillation period due to the smallness of ε, and the oscillations have a variable amplitude $L_n(t)$ close to the resonance. We can write

$$a_n = L_n(t)\exp(i\omega_{n0}t),$$
$$L_n(t) = |C_n + N_n\exp(i\varepsilon t)|$$
$$= \sqrt{C_n^2 + N_n^2 + 2C_nN_n\cos^2(\varepsilon t)}.$$

The constant C_n is defined by the amplitude of the nth mode of the drop natural oscillations at the initial instant.

From the expressions obtained above it is seen that as the frequency of the incident acoustic wave approaches the natural frequency of the nth mode of the drop free vibrations (at $\varepsilon \longrightarrow 0$), the amplitude of this mode rises unboundedly and varies periodically with time with the frequency ε. The unboundedness of the amplitude growth arises from neglecting in the model

the influence of the energy dissipation of the oscillations. In a real physical situation, the viscosity of the liquid limits the amplitude growth.

To take into account the liquid viscosity, assuming it to be small, one should add a velocity-dependent term to (24) [9, 13]:

$$F_T = 2\frac{\nu}{R^2}(2n+1)(n-1)G_n^{-1}\frac{da}{dt}.$$

From an analysis of the obtained equation for the drop forced vibrations as is done, for example, in [13], it is easy to find that if the viscosity is taken into account, the amplitude of forced oscillations does not become infinite, as is the case for an inviscid liquid, but tends to that given by the expression

$$a_n^* = \frac{\omega S_n}{2\omega_{n0}\chi_n}, \quad \chi_n = \frac{\nu}{R^2}(2n+1)(n-1)G_n^{-4},$$

which defines the amplitude of steady-state resonance oscillations. It is easy to see that the steady-state amplitude is of an order of the amplitude of the acoustic wave $\varphi_0\chi_n^{-1}$ (since $S_n \sim \varphi_0 \sim |\xi|/R$). In other words, in comparison with thermal oscillations of the drop, the amplitude of forced oscillations is as large by a factor of χ_n^{-1}. This means that at $\chi_n \ll 1$ the drop may become unstable as a result of considerable deformation even if its own charge is slightly lower than an order of magnitude corresponding to the Rayleigh limit [16].

CONCLUSION

An external acoustic field is capable of causing steady oscillations of the drop surface, both of the forced and parametric types, with the amplitude determined by the drop internal parameters: charge, radius, surface tension, viscosity, as well as the amplitude and frequency of the acoustic field. For a certain ratio between the frequency of an acoustic wave and that of the natural frequencies of drop oscillations, a resonant growth of the amplitude of the corresponding mode of the drop oscillations is observed. When the oscillation amplitude is great enough, the drop surface may become unstable with respect to its own charge even at subcritical values of the Rayleigh parameter *W*.

APPENDIX

Estimation of the Intensity of an Acoustic Wave Dissipated by a Drop in Comparison with the Intensity of the Incident Wave

1. Assuming that the drop radius *R* is much less than the wavelength λ of an incident acoustic wave interacting with the drop, we find that the dimensionless argument of the spherical cylindrical functions is small ($kR \ll 1$). In this connection, to sort hydrodynamic terms of the equations describing an acoustic wave interacting with capillary oscillations of a drop in accordance with their orders of smallness, it is reasonable to compare the orders of smallness of the intensities of the incident and dissipated acoustic waves. According to (13) and (14), the ratio between the amplitudes of partial waves at $r = R$ is defined by the expression

$$B_n \equiv \left|\frac{\partial j_n(kR)/\partial(kR)}{\partial h_n^{(1)}(kR)/\partial(kR)}\right|\left|\frac{h_n^{(1)}(kR)}{j_n(kR)}\right|. \tag{A1}$$

To evaluate the magnitude of B_n we apply a recurrent relation for the derivatives of spherical cylindrical functions that are valid both for j_n and $h_n^{(1)}$ [17]:

$$\frac{d}{dz}f_n(z) = f_{n+1}(z) + \frac{n}{z}f_n(z), \tag{A2}$$

where $f_n(z)$ symbolizes functions $j_n(z)$ and $h_n^{(1)}(z)$.

Now, we take into account that $kR \ll 1$ and apply an asymptotic representation for spherical cylindrical functions for a small argument value [17]:

$$z \longrightarrow 0\colon\ j_n(z) \longrightarrow \frac{z^n}{(2n+1)!!}, \tag{A3}$$

$$h_n^{(1)}(z) \longrightarrow \frac{z^n}{(2n+1)!!} - i\frac{(2n-1)!!}{z^{n+1}}, \tag{A4}$$

where

$$(2n+1)!! \equiv 1\cdot 3\cdot 5\cdot 7\cdot \ldots \cdot (2n+1);\ \ n = 0, 1, 2, \ldots.$$

By substituting (A3) and (A4) into (A1) and taking into account (A2), it is easy to find that for a small *kR* the amplitude ratio B_n is minimal at $n = 0$ when $B_0 \sim (kR)^2$, and $B_n \sim (kR)^0$ at $n \geq 1$. The relationships obtained define the order of smallness with respect to *kR* at $r = R$ of the dissipated acoustic wave as compared with the incident one.

2. To estimate the order of smallness of the parameter *kR*, we note that in problems associated with the dissipation of acoustic waves in liquid drop systems of natural origin, the characteristic size *R* of the drops varies from a few micrometers (in a fog) to a few millimeters (for raindrops), while the wavelength of the dissipated waves varies from a few fractions of a millimeter upward to ten meters [1, 4]. This means that a range of possible variation of the parameter *kR* in various concrete situations is between 10^{-5} and 10^2.

In the interaction between acoustic waves and capillary oscillations of a drop, a substantial role is played by the small parameter $|\xi|/R$ characterizing the amplitude of the capillary drop oscillations. Assuming that the amplitude of the drop thermal oscillations is defined by the expression

$$\xi \sim (kT/\gamma)^{1/2},$$

where k is the Boltzmann constant and T is the liquid temperature, it is not difficult to obtain $\xi \sim 10^{-8}$ cm. Then, in terms of the problems discussed, the parameter $|\xi|/R$ varies from 10^{-7} to 10^{-5}.

Thus, the parameters kR and $|\xi|/R$ may be either of the same or different orders of smallness, which should be taken into account for a correct statement of the problems of interaction between an acoustic field and capillary oscillations of a drop.

ACKNOWLEDGMENTS

The work was supported by a grant from the President of the Russian Federation (grant no. 00-15-9925).

REFERENCES

1. H. L. Green and W. R. Lane, *Particulate Clouds: Dusts, Smokes, and Mists* (Spon, London, 1964; Khimiya, Leningrad,1969).
2. Ph. L. Marston, J. Acoust. Soc. Am. **67**, 15 (1980).
3. M. P. Foster and J. C. Pflaum, J. Geophys. Res. D **93**, 747 (1988).
4. L. G. Kachurin, *Physical Principles of Interaction on Atmospheric Processes* (Gidrometeoizdat, Leningrad, 1990).
5. C. P. Lee, A. V. Anilkumar, and T. G. Wang, Phys. Fluids A **3**, 2497 (1991).
6. E. H. Trinh, R. G. Holt, and D. B. Thiessen, Phys. Fluids **8**, 43 (1996).
7. Z. C. Feng and Y. H. Su, Phys. Fluids **9**, 519 (1997).
8. L. V. King, Proc. R. Soc. London, Sect. A **147**, 212 (1934).
9. L. D. Landau and E. M. Lifshitz, *Mechanics of Continuous Media* (Gostekhteorizdat, Moscow, 1953).
10. A. N. Tikhonov and A. A. Samarskii, *Equations of Mathematical Physics* (Gostekhteorizdat, Moscow, 1951; Pergamon, Oxford, 1964).
11. A. I. Grigor'eva, S. O. Shiryaeva, and E. I. Belavina, Zh. Tekh. Fiz. **59** (6), 27 (1989) [Sov. Phys. Tech. Phys. **34**, 602 (1989)].
12. S. O. Shiryaeva, A. I. Grigor'ev, and I. D. Grigor'eva, Zh. Tekh. Fiz. **65** (2), 1 (1995) [Tech. Phys. **40**, 117 (1995)].
13. L. D. Landau and E. M. Lifshitz, *Course of Theoretical Physics*, Vol. 1: *Mechanics* (Nauka, Moscow, 1988; Pergamon, New York, 1988).
14. A. I. Grigor'ev, Izv. Akad. Nauk SSSR, Mekh. Zhidk. Gaza, No. 1, 50 (1989).
15. A. I. Grigor'ev, Zh. Tekh. Fiz. **70** (5), 22 (2000) [Tech. Phys. **45**, 543 (2000)].
16. V. A. Koromyslov, Yu. D. Rakhmanova, and S. O. Shiryaeva, Pis'ma Zh. Tekh. Fiz. **23** (14), 40 (1997) [Tech. Phys. Lett. **23**, 553 (1997)].
17. *Handbook of Mathematical Functions*, Ed. by M. Abramowitz and I. A. Stegun (National Bureau of Standards, Washington, 1964; Nauka, Moscow, 1979).

Translated by N. Mende

Technical Physics, Vol. 47, No. 3, 2002, pp. 306–312. Translated from Zhurnal Tekhnicheskoĭ Fiziki, Vol. 72, No. 3, 2002, pp. 11–16.

GASES AND LIQUIDS

The Effect of the Evaporation Coefficient on the Thermophoresis of a Volatile Single-Component Drop in a Binary Gas Mixture

S. N. D'yakonov, É. V. Efremov, and A. A. Morozov

Orel State University, Orel, 302015 Russia

e-mail: ua3ecf@esc.private.oryol.su

Received March 19, 2001; in final form, July 12, 2001

Abstract—A theory of the uniform thermophoretic motion of a liquid volatile spherical drop in a binary gas mixture is developed based on hydrodynamic analysis. One of the components undergoes the phase transition on the surface. The solution of the problem makes it possible to estimate the effect of the evaporation rate on the rate and direction of thermophoresis, as well as on the distributions of the velocity, temperature, and concentration of the volatile component. The thermal diffusion of the gas mixture, together with Stefan and capillary phenomena, is taken into account. The velocity of thermophoretic transport is expressed through the evaporation coefficient of the drop by the formula that generalizes the known results of the conventional theories for the cases of weak and moderately intense diffusive evaporation of a liquid drop. © *2002 MAIK "Nauka/Interperiodica".*

STATEMENT OF THE PROBLEM

This work generalizes the study [1], performed for small Reynolds numbers, by including internal motion in a volatile spherical single-component drop and thermocapillary effects. The theory is constructed in the spherical coordinate system (r, Θ, φ). The origin is rigidly related to the geometric center of the drop, and the 0z axis is aligned with the vector $\mathbf{A}_T = (\nabla T)_\infty$, where ∇ is the del operator.

The drop of radius R experiences the action of thermophoretic ($\mathbf{F}_{TP}$), diffusion phoretic ($\mathbf{F}_{DP}$), reactive ($\mathbf{F}_\alpha$), and thermocapillary ($\mathbf{F}_\sigma$) forces, which tend to balance the viscous force $\mathbf{F}_\mathbf{v}$ of the gas mixture. The desired thermophoretic velocity $\mathbf{U}_T = -\mathbf{U}$ of the liquid sphere is established when the resultant force vanishes:

$$\mathbf{F} = \mathbf{F}_{TP} + \mathbf{F}_{DP} + \mathbf{F}_\alpha + \mathbf{F}_\sigma + \mathbf{F}_\mathbf{v} = 0.$$

Volatility affects the thermophoretic motion of a liquid body in two ways. First, because of the change in the temperature distributions inside and outside the drop, an extra creep of the gas mixture over the interface arises and the tangential thermocapillary force due to the variable surface tension σ changes. Second, the environment is saturated by the vapor of volatiles and the volume thermal diffusion of the components of the gas mixture is enhanced.

The media are described in the quasi-stationary approximation (the vector fields $\mathbf{v}(\mathbf{r})$ and $\mathbf{v}'(\mathbf{r})$, pressure distributions $p(\mathbf{r})$ and $p'(\mathbf{r})$, scalar temperature fields $T(\mathbf{r})$ and $T'(\mathbf{r})$ outside and inside the drop, respectively, as well as the relative concentration $C(\mathbf{r})$ of the volatile component in the binary gas mixture, are assumed to be steady-state at any time instant) by the Stokes–Laplace axisymmetric differential continuity equations

$$\eta_0\Delta\mathbf{v} = \nabla p, \quad \mathrm{div}\mathbf{v} = 0, \quad \eta_0'\Delta\mathbf{v}' = \nabla p', \quad \mathrm{div}\mathbf{v}' = 0,$$

$$\Delta T = 0, \quad \Delta T' = 0, \quad \Delta C = 0,$$

where Δ is the Laplacian.

At infinity and at the interface, the linearized equations are valid:

$$r \longrightarrow \infty\colon \mathbf{v} = U\mathbf{i}_z,$$

$$T = T_0 + A_T z, \quad C = C_0, \quad p = p_0;$$

$$r = R\colon n_{10}v_r - \frac{n_0^2 m_2}{\rho_0}D\left(\nabla_r C + \frac{K_{TD}}{T_0}\nabla_r T\right)$$

$$= \alpha\nu n_0\{C_s(T') - C\},$$

$$n_{20}v_r + \frac{n_0^2 m_1}{\rho_0}D\left(\nabla_r C + \frac{K_{TD}}{T_0}\nabla_r T\right) = 0,$$

$$n_0'v_r' = n_{10}v_r - \frac{n_0^2 m_2}{\rho_0}D\left(\nabla_r C + \frac{K_{TD}}{T_0}\nabla_r T\right),$$

$$v_\Theta - v_\Theta' = K_{TSL}\frac{\eta_0}{\rho_0 T_0}\nabla_\Theta T + K_{DSL}D\nabla_\Theta C,$$

$$\tau_{rr} - \tau_{rr}' - \frac{2\sigma}{R} = 0, \quad \tau_{r\Theta} - \tau_{r\Theta}' + \nabla_\Theta\sigma = 0,$$

$$T = T',$$

$$-\kappa_0\nabla_r T + \kappa_0'\nabla_r T' = -Lm_1\alpha\nu n_0\{C_s(T') - C\},$$

1063-7842/03/4702-0306$22.00

$$\tau_{rr} = -p + 2\eta_0\frac{\partial v_r}{\partial r}, \quad \tau'_{rr} = -p' + 2\eta'_0\frac{\partial v'_r}{\partial r},$$

$$\tau_{r\Theta} = \eta_0\left(\frac{1}{r}\frac{\partial v_r}{\partial \Theta} + \frac{\partial v_\Theta}{\partial r} - \frac{v_\Theta}{r}\right),$$

$$\tau'_{r\Theta} = \eta'_0\left(\frac{1}{r}\frac{\partial v'_r}{\partial \Theta} + \frac{\partial v'_\Theta}{\partial r} - \frac{v'_\Theta}{r}\right),$$

$$C_s(T') = C_s(T_W) + \left.\frac{\partial C_s}{\partial T'}\right|_{T' = T_W}(T' - T_W),$$

$$\sigma(T') = \sigma(T_W) + \left.\frac{\partial \sigma}{\partial T'}\right|_{T' = T_W}(T' - T_W),$$

$$\nabla_{\Theta\sigma} = \frac{1}{R}\left.\frac{\partial \sigma}{\partial T'}\right|_{T' = T_W}\frac{\partial T'}{\partial \Theta},$$

$$C = \frac{n_1}{n_1 + n_2}, \quad C_s = \frac{n_{1s}}{n_1 + n_2}, \quad \nu = \left(\frac{R_g T}{2\pi\mu}\right)^{\frac{1}{2}},$$

$$n_0 = n_{10} + n_{20}, \quad \rho_0 = m_1 n_{10} + m_2 n_{20}, \quad \rho'_0 = m_1 n'_0,$$

$$\eta_0 = \eta(T_0, C_0, p_0), \quad \eta'_0 = \eta'(T_0, p'_0),$$

$$\kappa_0 = \kappa(T_0, C_0, p_0), \quad \kappa'_0 = \kappa'(T_0, p'_0).$$

Here, n_1 and n_2 are the concentrations of the gas molecules of the first and second sort with respective masses of m_1 and m_2; C_s is the relative concentration of the saturated vapor of the volatile; D is the coefficient of interdiffusion for the gas mixture components; L and μ are the heat of evaporation and the molar mass of the material of the drop, respectively; (ρ_0, ρ'_0), (η_0, η'_0), and (κ_0, κ'_0) are the densities, coefficients of dynamic viscosity, and thermal conductivities of the gas medium and the condensed phase, respectively; ν is one quarter of the mean thermal velocity for the molecules of the first sort; R_g is the gas constant; $(\tau_{rr}, \tau_{t\Theta})$ and $(\tau'_{rr}, \tau'_{r\Theta})$ are the components of the viscous stress tensors in incompressible media (outside and inside the drop); T_W is the mean temperature on the surface of the drop (which is determined by solving the problem); and p'_0 is the pressure inside the drop when it is weighed in an isothermal gas at a temperature T_0 (external mass forces are absent):

$$p'_0 - p_0 = \frac{2\sigma(T_0)}{R}.$$

The above conditions have the following physical meaning. At infinity, the axisymmetric flux of the external medium is uniform and has the velocity U along the $0z$ axis. The scalar temperature field $T(\mathbf{r})$, the distribution of the relative concentration $C(\mathbf{r})$ of the first component, and the pressure $p(\mathbf{r})$ are undisturbed. The normal flow of the volatile molecules at the interface is continuous. It can be represented as the normal outflow of the gas molecules of the first sort from the surface through the Knudsen layer and is proportional to the evaporation coefficient α. The surface of the aerosol particle is impermeable for its carrier. The normal and shear components of the total stress tensor are discontinuous, while the temperature and the normal heat flux are continuous (with regard for the phase transition).

The gas mixture and the condensed phase do not mix. Then, if the drop moves with a constant velocity, each of its surface elements is in equilibrium and the acting forces are balanced. If the surface element is considered in the frame of reference where it is at rest, the stress produced by either of the media is defined as the associated momentum flux (the normal to the interface is outer). In addition, each of the elements is subjected to an additional force due to the surface tension:

$$\mathbf{f} = -\mathbf{i}_r\frac{2\sigma}{R} + \mathbf{i}_\Theta\nabla_\Theta\sigma.$$

The state of the saturated vapor of the volatile liquid is far from critical, so the perfect gas approximation applies. When the liquid and gaseous phases of the volatile are in dynamic equilibrium, we have the estimate [1]

$$\left.\frac{\partial C_s}{\partial T}\right|_{T = T_W} = \frac{1}{T_W}C_s(T_W)\left(\frac{L\mu}{R_g T_W} - 1\right),$$

$$C_s(T_W) = C_s(T_0)\frac{T_0}{T_W}\exp\left\{\frac{L\mu}{R_g T_W}\left(\frac{T_W}{T_0} - 1\right)\right\}.$$

For incompressible media, the general solution of the axisymmetric hydrodynamic problem is given in terms of the stream function (Ψ, Ψ'):

$$\begin{matrix} v_r \\ v'_r \end{matrix} = -\frac{1}{r^2\sin\Theta}\frac{\partial}{\partial\Theta}\begin{matrix}\Psi \\ \Psi'\end{matrix},$$

$$\begin{matrix} v_\Theta \\ v'_\Theta \end{matrix} = \frac{1}{r\sin\Theta}\frac{\partial}{\partial r}\begin{matrix}\Psi \\ \Psi'\end{matrix}, \quad \begin{matrix} v_\varphi \\ v'_\varphi \end{matrix} = 0.$$

In the dimensionless form, the physical quantities involved in the equations of hydrodynamics, in the equations for heat and mass transfer, and in the boundary conditions have the form

$$r = R\tilde{r}, \quad \begin{matrix} v \\ v' \end{matrix} = U\begin{matrix}\tilde{v} \\ \tilde{v}'\end{matrix}, \quad \begin{matrix}\Psi \\ \Psi'\end{matrix} = UR^2\begin{matrix}\tilde{\Psi} \\ \tilde{\Psi}'\end{matrix},$$

$$\begin{matrix} p \\ p' \end{matrix} = \begin{matrix} \eta_0\left(\frac{U}{R}\right)\tilde{p} + p_0 \\ \eta'_0\left(\frac{U}{R}\right)\tilde{p}' + p'_0 \end{matrix}, \quad \begin{matrix} T \\ T' \end{matrix} = A_T R\begin{matrix}\tilde{T} \\ \tilde{T}'\end{matrix} + T_0.$$

Later on, the tilde is omitted and the problem is stated as follows:

$$E^4\Psi(r, \xi) = 0, \quad E^4\Psi'(r, \xi) = 0, \qquad (1)$$

$$\frac{\partial p}{\partial r} = \frac{1}{r^2}\frac{\partial}{\partial \xi}(E^2\Psi), \quad (1-\xi^2)\frac{\partial p}{\partial \xi} = -\frac{\partial}{\partial r}(E^2\Psi), \quad (2)$$

$$\frac{\partial p'}{\partial r} = \frac{1}{r^2}\frac{\partial}{\partial \xi}(E^2\Psi'), \quad (1-\xi^2)\frac{\partial p'}{\partial \xi} = -\frac{\partial}{\partial r}(E^2\Psi'), \quad (3)$$

$$\Delta T(r,\xi) = 0, \quad \Delta T'(r,\xi) = 0, \quad \Delta C(r,\xi) = 0, \quad (4)$$

$$E^2 = \frac{\partial^2}{\partial r^2} + \frac{1-\xi^2}{r^2}\frac{\partial}{\partial \xi^2},$$

$$\Delta = \frac{1}{r^2}\frac{\partial}{\partial r}\left(r^2\frac{\partial}{\partial r}\right) + \frac{1}{r^2}\frac{\partial}{\partial \xi}\left\{(1-\xi^2)\frac{\partial}{\partial \xi}\right\}, \quad (5)$$

$$r \longrightarrow \infty: \Psi = -\frac{1}{2}r^2(1-\xi^2),$$

$$T = z, \quad C = C_0, \quad p_0 = 0,$$

$$r = 1: \left\{C_0 + (1-C_0)\frac{m_2}{m_1}\right\}U\nu_r = \alpha\nu\left\{C_s(\tau) + \left.\frac{\partial C_s}{\partial T'}\right|_{T'=\tau}(T'-\tau) - C\right\}, \quad (6)$$

$$(1-C_0)\left\{C_0 + (1-C_0)\frac{m_2}{m_1}\right\}U\nu_r + \frac{D}{R}\left\{\frac{\partial C}{\partial r} + K_{TD}\varepsilon\frac{\partial T}{\partial r}\right\} = 0, \quad (7)$$

$$U\nu_r' = \alpha\nu\frac{n_0}{n_0'}\left\{C_s(\tau) + \left.\frac{\partial C_s}{\partial T'}\right|_{T'=\tau}(T'-\tau) - C\right\}, \quad (8)$$

$$U(\nu_\Theta - \nu_\Theta') = -K_{TSL}\frac{\eta_0}{\rho_0 T_0}A_T\sqrt{1-\xi^2}\frac{\partial T}{\partial \xi} - K_{DSL}\frac{D}{R}\sqrt{1-\xi^2}\frac{\partial C}{\partial \xi}, \quad (9)$$

$$-\frac{\eta_0' U}{R}\left(\frac{\eta_0}{\eta_0'}p - p'\right) - (p_0 - p_0') + 2\frac{\eta_0' U}{R}\left(\frac{\eta_0}{\eta_0'}\frac{\partial \nu_r}{\partial r} - \frac{\partial \nu_r'}{\partial r}\right) - \frac{2}{R}\left\{\sigma(\tau) + \left.\frac{\partial \sigma}{\partial T'}\right|_{T'=\tau}(T'-\tau)\right\} = 0, \quad (10)$$

$$\eta_0 U\left\{\frac{1}{r}\sqrt{1-\xi^2}\frac{\partial \nu_r}{\partial \xi} - \frac{\partial \nu_\Theta}{\partial r} + \frac{\nu_\Theta}{r}\right\} - \eta_0' U\left\{\frac{1}{r}\sqrt{1-\xi^2}\frac{\partial \nu_r'}{\partial \xi} - \frac{\partial \nu_\Theta'}{\partial r} + \frac{\nu_\Theta'}{r}\right\} + \sqrt{1-\xi^2}\left.\frac{\partial \sigma}{\partial T'}\right|_{T'=\tau}\frac{\partial T'}{\partial \xi} = 0, \quad (11)$$

$$T = T', \quad -\frac{\kappa_0}{\kappa_0'}\frac{\partial T}{\partial r} + \frac{\partial T'}{\partial r} = -\frac{Lm_1\alpha\nu n_0}{A_T\kappa_0'}\left\{C_s(\tau) + \left.\frac{\partial C_s}{\partial T'}\right|_{T'=\tau}(T'-\tau) - C\right\}, \quad (12)$$

$$\tau = \frac{T_W - T_0}{A_T R}, \quad \varepsilon = \frac{A_T R}{T_0}, \quad -1 \le \xi = \cos\Theta \le +1.$$

If the aerosol particles are nonvolatile ($\alpha = 0$), the interface is impermeable for the gas molecules: the normal velocity components of the gas and the condensed phase vanish on the spherical surface of radius $r = 1$.

DETERMINATION OF THE THERMOPHORESIS VELOCITY

The solutions of Eqs. (1)–(4) have the general form [2]

$$\begin{matrix}\Psi \\ \Psi'\end{matrix}(r,\xi) = \sum_{n=1}^{\infty}\left\{\begin{matrix}A_n r^n + B_n r^{-n+1} \\ A_n' \quad\quad B_n'\end{matrix} + \begin{matrix}C_n r^{n+2} + D_n r^{-n+3} \\ C_n' \quad\quad D_n'\end{matrix}\right\}J_n(\xi),$$

$$\begin{matrix}p \\ p'\end{matrix}(r,\xi) = -2\sum_{n=1}^{\infty}\left\{\frac{1}{n}(2n+3)\begin{matrix}C_{n+1} r^n \\ C_{n+1}'\end{matrix} + \frac{1}{n+1}(2n-1)\begin{matrix}D_{n+1} r^{-n-1} \\ D_{n+1}'\end{matrix}\right\}P_n(\xi),$$

$$T(r,\xi) = \sum_{n=0}^{\infty}\{G_n r^n + H_n r^{-n-1}\}P_n(\xi),$$

$$T'(r,\xi) = \sum_{n=0}^{\infty}\{G_n' r^n + H_n' r^{-n-1}\}P_n(\xi),$$

$$C(r,\xi) = \sum_{n=0}^{\infty}\{K_n r^n + L_n r^{-n-1}\}P_n(\xi).$$

Then, in view of the conditions at infinity and taking into account the finiteness of the velocity, pressure, and temperature at the center of the drop, we expand bound-

ary conditions (6)–(13) into the series:

$$v_r(r,\xi) = P_1(\xi) - \sum_{n=1}^{\infty}\{B_{n+1}r^{-n-2} + D_{n+1}r^{-n}\}P_n(\xi),$$

$$v_\Theta(r,\xi) = -2\frac{J_2(\xi)}{\sqrt{1-\xi^2}}$$

$$-\sum_{n=2}^{\infty}\{(n-2)B_n r^{-n-1} + (n-3)D_n r^{-n+1}\}\frac{J_n(\xi)}{\sqrt{1-\xi^2}},$$

$$v'_r(r,\xi) = -\sum_{n=1}^{\infty}\{A'_{n+1}r^{n-1} + C'_{n+1}r^{n+1}\}P_n(\xi),$$

$$v'_\Theta(r,\xi) = \sum_{n=2}^{\infty}\{nA'_n r^{n-2} + (n+2)C'_n r^n\}\frac{J_n(\xi)}{\sqrt{1-\xi^2}},$$

$$p(r,\xi) = -2\sum_{n=1}^{\infty}\frac{1}{n+1}(2n-1)D_{n+1}r^{-n-1}P_n(\xi),$$

$$p'(r,\xi) = -2\sum_{n=1}^{\infty}\frac{1}{n}(2n+3)C'_{n+1}r^n P_n(\xi),$$

$$T(r,\xi) = r\xi + \sum_{n=0}^{\infty}H_n r^{-n-1}P_n(\xi),$$

$$T'(r,\xi) = \sum_{n=0}^{\infty}G'_n r^n P_n(\xi),$$

$$C(r,\xi) = C_0 + \sum_{n=0}^{\infty}L_n r^{-n-1}P_n(\xi).$$

Properties (A1) and (A2), as well as orthogonality conditions like (A3) and (A4) for the ultraspherical nth-order polynomials of degree ±0.5,

$$J_n(\xi) = C_n^{-\frac{1}{2}}(\xi), \quad P_n(\xi) = C_n^{+\frac{1}{2}}(\xi)$$

yield the following algebraic equations ($n \le 2$):

$$C_s(\tau) - C_0 + \left.\frac{\partial C_s}{\partial T'}\right|_{T'=\tau}(G'_0 - \tau) - L_0 = 0, \qquad (6a)$$

$$-\left\{C_0 + (1-C_0)\frac{m_2}{m_1}\right\}U(-1 + B_2 + D_2) = \alpha\nu\left\{\left.\frac{\partial C_s}{\partial T'}\right|_{T'=\tau}G'_1 - L_1\right\}; \qquad (6b)$$

$$-\left\{C_0 + (1-C_0)\frac{m_2}{m_1}\right\}U(B_{n+1} + D_{n+1}) = \alpha\nu\left\{\left.\frac{\partial C_s}{\partial T'}\right|_{T'=\tau}G'_n - L_n\right\}; \qquad (6c)$$

$$-L_0 - \varepsilon K_{TD}H_0 = 0, \qquad (7a)$$

$$-(1-C_0)\left\{C_0 + (1-C_0)\frac{m_2}{m_1}\right\}U(-1 + B_2 + D_2) - \frac{D}{R}\{2L_1 + \varepsilon K_{TD}(1+2H_1)\} = 0, \qquad (7b)$$

$$-(1-C_0)\left\{C_0 + (1-C_0)\frac{m_2}{m_1}\right\}U(B_{n+1} + D_{n+1}) - (n+1)\frac{D}{R}\{L_n + \varepsilon K_{TD}H_n\} = 0, \qquad (7c)$$

$$-U(A'_2 + C'_2) = \alpha\nu\frac{n_0}{n'_0}\left\{\left.\frac{\partial C_s}{\partial T'}\right|_{T'=\tau}G'_1 - L_1\right\}, \qquad (8a)$$

$$-U(A'_{n+1} + C'_{n+1}) = \alpha\nu\frac{n_0}{n'_0}\left\{\left.\frac{\partial C_s}{\partial T'}\right|_{T'=\tau}G'_n - L_n\right\}, \qquad (8b)$$

$$U(2 + B_2 - D_2 + 2A'_2 + 4C'_2) = 2K_{TSL}\frac{\eta_0}{\rho_0 T_0}A_T(1+H_1) + 2K_{DSL}\frac{D}{R}L_1, \qquad (9a)$$

$$U\{-nB_{n+1} - (n-2)D_{n+1} - (n+1)A'_{n+1} - (n+3)C'_{n+1}\} = -K_{TSL}\frac{\eta_0}{\rho_0 T_0}A_T n(n+1)H_n - K_{DSL}\frac{D}{R}n(n+1)L_n, \qquad (9b)$$

$$-(p_0 - p'_0) - \frac{2}{R}\left\{\sigma(\tau) + \left.\frac{\partial\sigma}{\partial T'}\right|_{T'=\tau}(G'_0 - \tau)\right\} = 0, \qquad (10a)$$

$$3\eta_0 U(2B_2 + D_2) - 6\eta'_0 UC'_2 - 2\left.\frac{\partial\sigma}{\partial T'}\right|_{T'=\tau}G'_1 = 0, \qquad (10b)$$

$$2\eta_0 U\left\{(n+2)B_{n+1} + \frac{n^2+3n-1}{n+1}D_{n+1}\right\} + 2\eta'_0 U\left\{(n-1)A'_{n+1} + \frac{1}{n}(n^2-n-3)C'_{n+1}\right\} - 2\left.\frac{\partial\sigma}{\partial T'}\right|_{T'=\tau}G'_n = 0, \qquad (10c)$$

$$3\eta_0 UB_2 - 3\eta_0' UC_2' - \left.\frac{\partial\sigma}{\partial T'}\right|_{T'=\tau} G_1' = 0, \tag{11a}$$

$$2\eta_0 U\{n(n+2)B_{n+1} + (n^2-1)D_{n+1}\} - 2\eta_0' U\{(n^2-1)A_{n+1}' + n(n+2)C_{n+1}'\} - \left.\frac{\partial\sigma}{\partial T'}\right|_{T'=\tau} n(n+1)G_n' = 0, \tag{11b}$$

$$H_0 = G_0', \quad \frac{\kappa_0}{\kappa_0'}H_0 = -\frac{Lm_1\alpha\nu n_0}{A_T\kappa_0'} \times\left\{C_s(\tau) - C_0 + \left.\frac{\partial C_s}{\partial T'}\right|_{T'=\tau}(G_0' - \tau) - L_0\right\}, \tag{12a}$$

$$1 + H_1 = G_1', \quad \frac{\kappa_0}{\kappa_0'}(-1 + 2H_1) + G_1' = -\frac{Lm_1\alpha\nu n_0}{A_T\kappa_0'}\left\{\left.\frac{\partial C_s}{\partial T'}\right|_{T'=\tau} G_1' - L_1\right\}, \tag{12b}$$

$$H_n = G_n', \quad \frac{\kappa_0}{\kappa_0'}(n+1)H_n + nG_n' = -\frac{Lm_1\alpha\nu n_0}{A_T\kappa_0'}\left\{\left.\frac{\partial C_s}{\partial T'}\right|_{T'=\tau} G_n' - L_n\right\}. \tag{12c}$$

In our problem, the concentration, $C(\mathbf{r})$, and temperature, $T(\mathbf{r})$ and $T'(\mathbf{r})$, fields do not depend on the internal motion in the drop and thermocapillary phenomena and have the form given in [1].

Jointly solving Eqs. (6b), (7b), (8a), (9a), (10b), (11a), and (12b), we come to the expression for the center-of-mass velocity of the gaseous media relative to the drop:

$$U = 6K_{TSL}\frac{\eta_0}{\rho_0 T_0}A_T\left(3 + 2\frac{\eta_0}{\eta_0'}\right)^{-1}\frac{\Delta'}{\Delta} + 6K_{DSL}\frac{D}{R}\left(3 + 2\frac{\eta_0}{\eta_0'}\right)^{-1}\frac{\Delta''}{\Delta} + \frac{2}{\eta_0'}\left(3 + 2\frac{\eta_0}{\eta_0'}\right)^{-1}\left.\frac{\partial\sigma}{\partial T'}\right|_{T'=\tau}\frac{\Delta'}{\Delta} + 3\alpha\nu\left(2\frac{n_0}{n_0'} + \frac{1 + 2\dfrac{\eta_0}{\eta_0'}}{C_0 + (1-C_0)\dfrac{m_2}{m_1}}\right)\left(3 + 2\frac{\eta_0}{\eta_0'}\right)^{-1} \times\left\{2\frac{\kappa_0}{\kappa_0'}\left.\frac{\partial C_s}{\partial T'}\right|_{T'=\tau} - \varepsilon K_{TD}\right\}\frac{1}{\Delta}, \tag{13}$$

$$\Delta = \left(1 + 2\frac{\kappa_0}{\kappa_0'}\right)\left\{2 + (1-C_0)\frac{\alpha\nu R}{D}\right\} + 2\frac{Lm_1\alpha\nu n_0}{A_T\kappa_0'}\left\{\left.\frac{\partial C_s}{\partial T'}\right|_{T'=\tau} + \varepsilon K_{TD}\right\},$$

$$\Delta' = \frac{\kappa_0}{\kappa_0'}\left\{2 + (1-C_0)\frac{\alpha\nu R}{D}\right\} + \varepsilon K_{TD}\frac{Lm_1\alpha\nu n_0}{A_T\kappa_0'},$$

$$\Delta'' = \frac{\kappa_0}{\kappa_0'}(1-C_0)\frac{\alpha\nu R}{D}\left.\frac{\partial C_s}{\partial T'}\right|_{T'=\tau} + \varepsilon K_{TD}\left\{\frac{Lm_1\alpha\nu n_0}{A_T\kappa_0'}\left.\frac{\partial C_s}{\partial T'}\right|_{T'=\tau} + 1\right\}.$$

The mean reduced temperature τ on the surface of the volatile drop is found from the solution of the transcendental algebraic equation

$$C_s(\tau) - C_0 - \left.\frac{\partial C_s}{\partial T'}\right|_{T'=\tau}\tau = 0.$$

The set of Eqs. (6c), (7c), (8b), (9b), (10c), (11b), and (12c) has the trivial solution $B_{n+1} = D_{n+1} = A_{n+1}' = C_{n+1}' = H_n = G_n' = L_n = 0$ for any $n \geq 2$.

ANALYSIS OF THE RESULTS

In (13), the first two terms stand for the thermal and diffusive creeps of the gaseous media. The third one is related to the variable surface tension acting on the surface of the drop. The fourth term describes the reactive part of the momentum that acts on the particle and is associated with the phase transition. For a solid volatile particle ($\eta_0' \longrightarrow \infty$), we obtain the result of [1].

For a single-component spherical drop of a volatile liquid in a binary gaseous mixture, the conventional theory of thermophoresis [3] gives (in terms of the above designations and upon neglecting thermal diffusion and the effect of the Knudsen layer)

$$U = 6K_{TSL}\frac{\eta_0}{\rho_0 T_0}A_T\left(3 + 2\frac{\eta_0}{\eta_0'}\right)^{-1}\frac{\kappa_0}{\kappa_0'}(1-C_0)\frac{1}{\Omega} + 6K_{DSL}\frac{D}{R}\left(3 + 2\frac{\eta_0}{\eta_0'}\right)^{-1}\frac{\kappa_0}{\kappa_0'}(1-C_0)\left.\frac{\partial C_s}{\partial T'}\right|_{T'=\tau}\frac{1}{\Omega} + \frac{2}{\eta_0'}\left(3 + \frac{\eta_0}{\eta_0'}\right)^{-1}\frac{\kappa_0}{\kappa_0'}(1-C_0)\left.\frac{\partial\sigma}{\partial T'}\right|_{T'=\tau}\frac{1}{\Omega} + \frac{6}{C_0 + (1-C_0)\dfrac{m_2}{m_1}R}\frac{D}{R}\left(2\frac{n_{10}}{n_0} + 1 + 2\frac{\eta_0}{\eta_0'}\right) \times\left(3 + 2\frac{\eta_0}{\eta_0'}\right)^{-1}\frac{\kappa_0}{\kappa_0'}\left.\frac{\partial C_s}{\partial T'}\right|_{T'=\tau}\frac{1}{\Omega},$$

$$\Omega = \left(1 + 2\frac{\kappa_0}{\kappa_0'}\right)(1 - C_0) + 2\frac{Lm_1n_0D}{\kappa_0'A_TR}\left.\frac{\partial C_s}{\partial T'}\right|_{T' = \tau}.$$

The derivation of this expression also takes into account the heat flux on the surface of the drop that is due to the convective transfer of a mass being evaporated.

Formula (13) is the most general and coincides with the result of [3] if the diffusive evaporation of the drop is intense:

$$C_0 \ll 1 \ll \frac{\alpha\nu R}{D}.$$

In other words, formula (13) is also valid for the cases of weak and moderately intense drop evaporation due to diffusion. This formula implies that if

$$\left.\frac{\partial C_s}{\partial T'}\right|_{T' = \tau} > 0, \quad \left.\frac{\partial \sigma}{\partial T'}\right|_{T' = \tau} < 0, \quad K_{TD} = 0,$$

the drop tends to move toward colder regions of the gaseous medium by virtue of the first and fourth terms ("positive" factors). The effect of the second term on the velocity of thermophoresis depends on the coefficient K_{DSL}: if $m_1 > m_2$ ($K_{DSL} < 0$), the directions of the vector $\mathbf{A}_T$ and the drop coincide; otherwise ($m_1 < m_2$; $K_{DSL} > 0$), the directions are opposite. Since the surface tension is variable, the third term describes thermocapillary effects and tends to increase the temperature of the gaseous environment.

If the effect of the thermal diffusion phenomena is appreciable and the evaporation rate of the drop is sufficiently low, volatility affects the thermal diffusion fields insignificantly and the velocity of thermophoresis is negligible [1]. In this case,

$$U \longrightarrow 3K_{TSL}\frac{\eta_0}{\rho_0T_0}A_T\left(3 + 2\frac{\eta_0}{\eta_0'}\right)^{-1}\frac{2\dfrac{\kappa_0}{\kappa_0'}}{1 + 2\dfrac{\kappa_0}{\kappa_0'}}$$

$$+ 3K_{DSL}\frac{D}{T_0}A_T\left(3 + 2\frac{\eta_0}{\eta_0'}\right)^{-1}\frac{K_{TD}}{1 + 2\dfrac{\kappa_0}{\kappa_0'}}$$

$$+ \frac{1}{\eta_0'}\left(3 + 2\frac{\eta_0}{\eta_0'}\right)^{-1}\left.\frac{\partial \sigma'}{\partial T'}\right|_{T' = \tau}\frac{2\dfrac{\kappa_0}{\kappa_0'}}{1 + 2\dfrac{\kappa_0}{\kappa_0'}}.$$

If the thermal conductivity of the drop is high, the distributions of the temperature and of the relative concentration of the volatile are almost independent of the thermal conductivity of the gaseous medium [1].

Of interest is the dependence $U = U(\alpha)$. After rearrangements, we come to

$$\frac{\partial U}{\partial \alpha} = -2\nu\left(3 + 2\frac{\eta_0}{\eta_0'}\right)^{-1}\Phi(\kappa_0, \kappa_0')$$

$$\times\left\{2\frac{\kappa_0}{\kappa_0'}\left.\frac{\partial C_s}{\partial T'}\right|_{T' = \tau} - \varepsilon K_{TD}\right\}\frac{1}{\Delta^2},$$

$$\Phi(\kappa_0, \kappa_0') = 6K_{TSL}\frac{\eta_0}{\rho_0T_0}\frac{Lm_1n_0}{\kappa_0'}$$

$$- 3K_{DSL}\left\{(1 - C_0)\left(1 + 2\frac{\kappa_0}{\kappa_0'}\right) + 2K_{TD}\frac{Lm_1n_0D}{T_0\kappa_0'}\right\}$$

$$- 3\left(2\frac{n_0}{n_0'} + \frac{1 + 2\dfrac{\eta_0}{\eta_0'}}{C_0 + (1 - C_0)\dfrac{m_2}{m_1}}\right)\left(1 + 2\frac{\kappa_0}{\kappa_0'}\right)$$

$$+ \frac{2}{\eta_0'}\left.\frac{\partial \sigma}{\partial T'}\right|_{T' = \tau}\frac{Lm_1n_0}{A_T\kappa_0'}.$$

The function $U(\alpha)$ is monotonically decreasing or increasing. The rate of thermophoretic transport does not depend on the evaporation coefficient if the physical quantities characterizing the state of the media outside and inside the high-viscosity drop obey the conditions

$$\Phi(\kappa_0, \kappa_0') = 0, \quad 2\frac{\kappa_0}{\kappa_0'}\left.\frac{\partial C_s}{\partial T'}\right|_{T' = \tau} - \varepsilon K_{TD} = 0.$$

The first and second conditions are valid for aerosol particles with a low and high thermal conductivity, respectively.

The numerical analysis shows that the velocity of thermophoresis depends on the coefficient α very strongly if the diffusive evaporation of the water drop is weak ($\alpha < 0.05$). At usual temperatures, the volatility of water increases the rate of thermophoresis two- or threefold and thermocapillary effects prevail.

APPENDIX

$$\frac{dJ_n(\xi)}{d\xi} = -P_{n-1}(\xi), \quad n \geq 1, \tag{A1}$$

$$(1 - \xi^2)\frac{dP_n(\xi)}{d\xi} = n(n + 1)J_{n+1}(\xi), \quad n \geq 0, \tag{A2}$$

$$\int_{-1}^{+1} \frac{J_m(\xi)J_n(\xi)}{1-\xi^2} = \begin{cases} 0, & m \neq n \\ \dfrac{2}{n(n-1)(2n-1)}, & m = n, \end{cases} \quad \text{(A3)}$$

$$m \neq 0; 1, \quad n \neq 0; 1,$$

$$\int_{-1}^{+1} P_m(\xi)P_n(\xi)d\xi = \begin{cases} 0, & m \neq n \\ \dfrac{2}{2n+1}, & m = n. \end{cases} \quad \text{(A4)}$$

REFERENCES

1. S. N. D'yakonov, L. V. Kotlyarova, and Yu. I. Yalamov, Zh. Tekh. Fiz. **72** (3), 24 (2002) [Tech. Phys. **47**, 291 (2002)].
2. J. Happel and H. Brenner, *Low Reynolds Number Hydrodynamics* (Prentice-Hall, Englewood Cliffs, 1965; Mir, Moscow, 1976).
3. Yu. I. Yalamov and A. V. Chermoshentsev, Available form VINITI, No. 1555-V (Moscow, 1990).

Translated by V. Isaakyan

Technical Physics, Vol. 47, No. 3, 2002, pp. 313–319. Translated from Zhurnal Tekhnicheskoĭ Fiziki, Vol. 72, No. 3, 2002, pp. 31–37.

GAS DISCHARGES, PLASMA

Probe Measurements in a Discharge with Liquid Nonmetallic Electrodes in Air at Atmospheric Pressure

Yu. A. Barinov and S. M. Shkol'nik

Ioffe Physicotechnical Institute, Russian Academy of Sciences, St. Petersburg, 194021 Russia

e-mail: shkolnik@vas.pti.spb.su

e-mail: Yury@pop.ioffe.rssi.ru

Received August 1, 2001

Abstract—Discharges with liquid nonmetallic electrodes of much interest for applications are investigated. It is found that a dc discharge between two streams of tap water in air at atmospheric pressure is stable at a current of $40 \le I \le 100$ mA. The discharge exists in the diffuse (volume) form with a relatively low current density (~0.2 A/cm^2) and a high (above one kilovolt) voltage drop across the air gap (~1 cm) between the water electrodes. The current density and voltage depend only slightly on the discharge current. Probe measurements show that three regions can be distinguished in the discharge: two electrode regions (1–2 mm in length) and a discharge column with a constant electric field of ≈0.8 kV/cm (i.e., $E/N \approx 20$ Td, because the gas in the discharge is heated up to 1500–2000 K). The average electric field strength near the electrodes is $E \approx 2$–3×10^3 V/cm ($E/N \approx 60$–80 Td). The charged particle density in the column is $n \sim 10^{12}$ cm^{-3}. The probe measurements of n agree with the previous microwave absorption measurements. The water vapor concentration in the column is also estimated from probe measurements. © *2002 MAIK "Nauka/Interperiodica".*

1. Electric discharges in which nonmetallic liquids (e.g., water solutions of various salts or bases or industrial or tap water) are used as electrodes possess unique properties. Under certain conditions, self-sustained high-pressure (up to atmospheric pressure or higher) dc discharges of this type in various gases (including molecular gases) can exist in the volume (diffuse) form.

In contrast to arc discharges, discharges with liquid nonmetallic electrodes (DLNMEs) are excited at a relatively high voltage $U \ge 10^3$ V and a low current density $j \approx 10^{-1}$–1 A/cm^2. The discharge parameters can be controlled over a wide range by varying the composition and concentration of electrolytes. The discharge duration, which, for metal electrodes, is usually limited by their erosion, is almost unlimited for DLNMEs. DLNMEs are widely used, e.g., to treat metal surfaces and to deposit special-purpose coatings [1]. On the other hand, the DLNME properties listed above, as well as its other features (e.g., that the discharge spectrum contains the spectral lines of elements dissolved in liquid electrodes [2] and that the discharge plasma is strongly nonequilibrium, in particular, in discharges excited in high-pressure molecular gases [3]), make this type of discharges promising for various technological applications in plasma chemistry (in particular, for treating polluted gas flows), spectral analysis [4], etc. We also point out an advantageous feature of DLNMEs as compared to barrier discharges [5] that presently attract much interest as generators of a high-pressure nonequilibrium plasma. Whereas the barrier discharge requires an ac power supply at a frequency of $f \sim 10^3$ Hz or higher, the DLNME is also stable with a dc power supply. However, DLNMEs are still poorly studied. The main results refer to a discharge with only one liquid electrode (cathode) [6].

This paper is devoted to the study of the electric potential and charged particle distributions in a discharge in which a low-conductivity liquid (namely, tap water) is used as electrodes. The discharge was excited in air at atmospheric pressure.

2. The design of the discharge unit used in our experiment is shown schematically in Fig. 1. A discharge was excited in air between two tap water streams (water electrodes). Water flowed downward along two ceramic chutes deflected at a small angle from the vertical direction. The chutes were 15 mm wide, and their sidewalls were 5 mm high. The chutes had two opposite holes in which two stainless-steel conductors 0.3 mm in diameter were mounted so that their ends were flush with the chute bottom, which was covered by water.

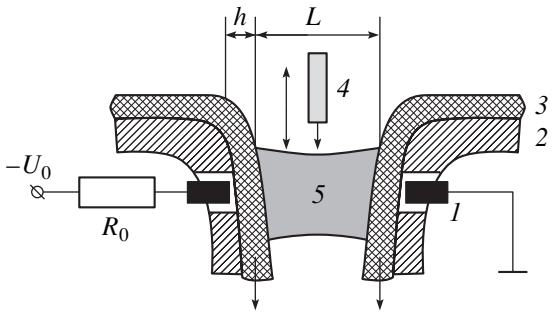

Fig. 1. Design of the discharge unit: (*1*) metal current supply conductors, (*2*) ceramic chutes, (*3*) water streams, (*4*) movable probe, and (*5*) discharge plasma.

1063-7842/03/4702-0313$22.00

The water flow rate was stabilized and adjusted so that the high-voltage diffuse discharge mode was achieved at a minimum flow rate. Experiments showed that, to achieve the high-voltage mode, it was necessary that the thickness h of the water layer covering the metal conductors exceed a certain minimum value h_{min}. Otherwise, water breakdown occurred, contracted erosion attachments appeared at the conductors, and the discharge transformed into a low-voltage arc with a high current density inside the contracted channel. The interelectrode gap (the air gap between the opposite water surfaces) could be up to $L \approx 10$ mm.

The discharge was powered by a high-voltage source producing a current of $I \leq 2$ A at a voltage of $U_0 \leq 10$ kV. The source consisted of a step-up transformer and a bridge rectifier. An RC filter was connected to the rectifier output, so that pulsations did not exceed 1%. The positive pole of the source was grounded. A ballast resistor R_0 was connected in series to the discharge unit, thus limiting the current in the case of the breakdown of the water electrode. The discharge was excited when opening the circuit after the interelectrode gap was closed for a short time with a special metal conductor.

3. The experiments were carried out at currents in the range $40 \leq I \leq 100$ mA. A diffuse discharge mode in this current range was achieved by adjusting the values of the supply voltage U_0, the ballast resistance R_0, and the water layer thickness h. At $U_0 \approx -4$ kV and $R_0 = 10$ kΩ, the minimum water layer thickness ensuring prevention from breakdown was $h_{min} \approx 4$ mm. In this case, the water flow velocity, which was estimated from the water flow rate, was $v \approx 1$ m/s.

Under these conditions, the discharge voltage (i.e., the voltage between the metal current conductors) was at a level of $U \approx -3$ kV and depended slightly on the current. The total voltage drop U was the sum of the voltage drops across the water electrodes, U_1, and across the plasma in the interelectrode gap, U_2. The value of U_1 was measured in separate experiments without a discharge. Thin stainless-steel disks with diameters equal to the diameters of the discharge attachments to the surface of the water electrodes were prepared. The diameters of the cathode and anode attachments, which were determined from discharge photographs, were close to each other. The attachment diameter increased with increasing current. Typically, for $I \approx 60$–70 mA, the attachment diameter was $D \approx 0.6$–0.7 cm. The disks were brought into contact with the water electrodes, and the voltage drop between the current supply conductors and the disks in the current range under study was measured. The experiments showed that nearly one-half of the voltage applied to the current supply conductors dropped across the water electrodes. For example, for the thickness of the water layers covering the cathode and anode conductors equal to $h \approx 5$ mm, a discharge current of $I \approx 65$ mA, an interelectrode gap of $L \approx 6$ mm, and a voltage at the current supply conductors of $U \approx -2.9$ kV, the voltage drop across the water electrodes was $U_1 \approx -1.6$ kV.

The water electrode conductivity estimated from these measurements is equal to $\sigma \approx 10^{-4}$ $(\Omega\ \text{cm})^{-1}$, which is only several times higher than the conductivity of distilled water [7]. This shows that, apparently, there are no specific conduction mechanisms in the water electrodes (partial discharges, etc.), because the difference from the data of [7] falls within the limits expected for tap water without additional filtering.

The discharge current and voltage signals were significantly corrupted by noise over a wide frequency range. We also observed distinct low-frequency oscillations in the discharge voltage with an amplitude of up to several tens of volts. For example, at $L = 6$ mm, the main frequency of these oscillations was $f \approx 60$ Hz.

The procedure of probe measurements will be described below. Here, we only mention that the measurements with the help of auxiliary probes located one above the other in the center of the interelectrode gap at the periphery of the current channel (one located under the discharge and the other located above it) allowed us to establish the reasons for low-frequency voltage oscillations. As the gas in the discharge is heated, the current channel "floats up," in which case its length and, accordingly, the voltage somewhat increases. Then, the channel returns to its original position. The vertical displacement of the discharge in the center of the interelectrode gap is ≤0.5 mm. The previous spectroscopic measurements [8] showed that air in the discharge is heated to $T_g \approx 1500$–2000 K.

4. Probe measurements were carried out with a cylindrical probe 0.3 mm in diameter and 1.5 mm in length and with a flat single-sided probe 0.33×1.2 mm in size. The probes were made of molybdenum. The nonoperating surfaces of the probes were insulated with BeO ceramics. The operating surface of the probe was oriented perpendicular to the discharge axis and could be facing the cathode or anode. In dry air, molybdenum begins to oxidize only at $T \geq 700$ K; however, in the presence of water vapor, it oxidizes even at $T \geq 520$ K [9]. To prevent the probe from substantial oxidation, it should be inserted into the discharge for a short time. Estimates show that, at a gas temperature of $T_g \approx 2000$ K, the probe temperature increases by $\Delta T \approx 50$ K in a time $t \approx 10^{-1}$ s. For this reason, the time interval during which the probe can stay in the plasma is limited by $\Delta t \leq 0.5$ s. The probe was inserted into the discharge from above (Fig. 1). The spring-supported probe could be displaced along or transverse to the axis of the discharge unit. The probe was inserted to a given depth in the plasma for a short time with the help of an electromagnet or manually. From time to time, the operating surface of the probe was mechanically cleaned to avoid measurement errors introduced by oxide films [10].

5. Figure 2 shows a block diagram of the probe measurements. The probe circuit was fed from a stabilized dc voltage source, whose output voltage could be con-

tinuously varied in the range from 0 to –2.5 kV. Resistors R_1, R_2, and R_3 = 150 MΩ, as well as a limiting resistor R_4 = 100 kΩ, were connected in series to the probe. The values of R_1 and R_2 were chosen depending on the current range in which the measurements were carried out. Under the conditions described above, the probe measurements were complicated by two circumstances: first, the necessity of measuring low (down to a fraction of a microampere) currents at a high (one kilovolt or higher) voltage and, second, the repulsion of the discharge from the probe and the above-mentioned "floating-up" of the discharge.

The first of these circumstances prohibits the use of resistive dividers for measuring the probe current, because, under the conditions described above, the measurements with the use of such dividers do not ensure the required accuracy. For this reason, we designed a device that provided the measurement of small probe currents, as well as the galvanic insulation of the measurement circuit from recording devices. This device allowed us to measure input signals below 0.3 V at an applied voltage of up to 10 kV. To overcome the second of the above problems, the probe current and its floating potential were measured at close instants. This was achieved by switching the resistor R_3 (and also R_2) with the help of an electronic switch. This switch was controlled by a meandering signal with a period of ≈1 ms. The output signal from the galvanic insulation device, along with signals proportional to the probe voltage and the discharge voltage, were digitized by a multichannel 11-digit analog-to-digital converter and were stored in a computer. The recording cycle duration was chosen to be about 0.5 s. The measurements were repeated many times. Simultaneously, we visually checked that the probe fell into the discharge channel. Then, we changed the probe voltage and made the next series of measurements. In fact, the probe measurements were performed at a distance of ≈1 mm from the discharge axis, because when the probe fell onto the axis, the discharge was repelled from the probe.

After the measurements were finished, the entire data file was processed using a special program selecting subsequent (no less than two) values of the probe current and probe floating potential such that they differed by no more than 10% and corresponded to close values of the discharge voltage ($\Delta U \le \pm 6$ V). The selected data were then processed statistically and averaged.

6. The probe measurements were conducted at I = 65–70 mA and $L \approx 6$ mm. The results of the measurements of the probe floating potential U_f are shown in Fig. 3. Closed circles indicate the results obtained when the probe was inserted into water near the surface of the water electrode. Note that these results agree well with the results of the above measurements, in which the voltage drop across the water electrodes was measured with the help of disk electrodes.

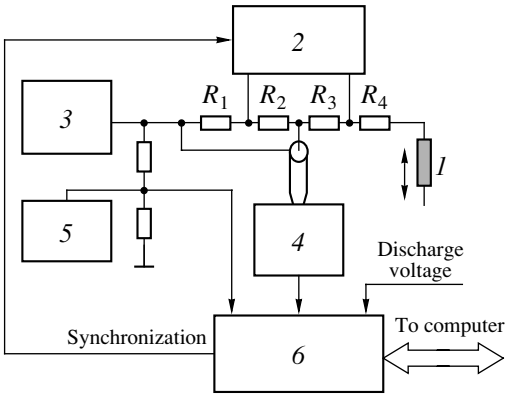

Fig. 2. Block diagram of probe measurements: (*1*) movable probe, (*2*) electronic switch, (*3*) voltage source, (*4*) high-voltage galvanic insulation device, (*5*) digital voltmeter, and (*6*) multichannel analog-to-digital converter.

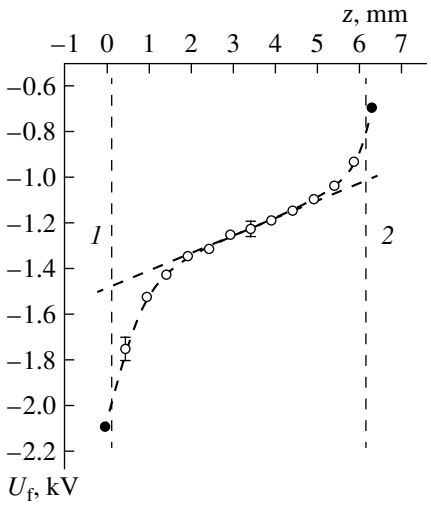

Fig. 3. Profile of the probe floating potential across the interelectrode gap at $I \approx 65$ mA and $L \approx 6$ mm (cylindrical probe): (*1*) water cathode and (*2*) water anode.

It is seen in Fig. 3 that, in the discharge, two electrode regions and a discharge column with an almost constant electric field can be distinguished. As will be shown below, the probe floating potential can be identified with the plasma potential accurate to $\sim kT_e/e$, where T_e is the characteristic electron energy (the electron "temperature"). As follows from the data in Fig. 3, the electric field in the column is equal to $E_c \approx 7$–8×10^2 V/cm. Note that visual observations and discharge photographs, as well as the results of spectroscopic measurements [3], show that the column is not uniform: it is slightly narrowed on the cathode side and broadens toward the anode. In this paper, the most attention is concentrated on investigation of the discharge column.

Figure 4 shows the current-voltage (I–V) characteristics of the plane probe near the cathode and anode ends of the plasma column (the potential U_p is counted

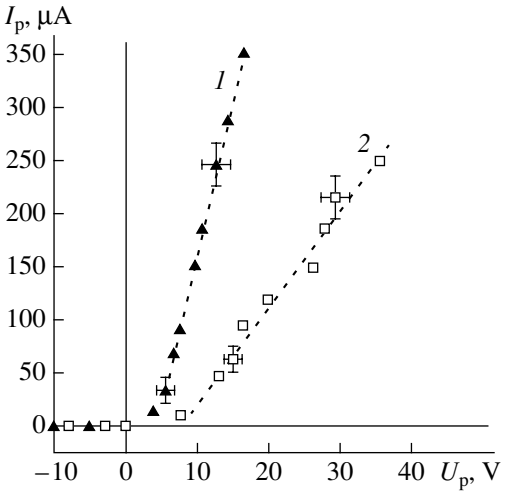

Fig. 4. Plane probe characteristics for a probe facing the cathode at $I \approx 65$ mA and z = (*1*) 2.5 and (*2*) 4.5 mm.

from the probe floating potential). The shape of the *I–V* characteristic allows us to conclude that the electrons are the main current carriers in the discharge under study. The characteristic feature of the *I–V* characteristic is the linear dependence of the current on the probe potential in the transition region at $U_p \geq 10$ V. The linear segment in the *I–V* characteristic of the probe was also observed previously in various experiments with a weakly ionized plasma at atmospheric pressure [11–13].

Figure 5 shows the results of measurements of the ion branches of the *I–V* characteristic at higher values of R_1 and R_2. It is seen in Fig. 5a that the probe ion current (similarly to the electron current) depends on the probe position in the column. When the probe is positioned at the cathode end of the column, we cannot notice any dependence on its orientation within the data scatter (Fig. 5b). At the anode end of the column, the measurements with the probe facing the anode seem unreasonable, because the distance between the probe and anode is close to the probe size and the probe significantly perturbs the plasma in this region.

7. Let us consider the conditions under which the probe collects the current. According to [8], the gas temperature is equal to $T_{gc} \approx 2000$ K at the cathode end of the column and $T_{ga} \approx 1400$ K at the anode end, and the molecule densities near the cathode and anode are equal to $N_{gc} \approx 3.5 \times 10^{18}$ and $N_{ga} \approx 5.3 \times 10^{18}$ cm^{-3}, respectively. The parameter E/N varies along the column from ≈20 Td at the cathode end to ≈15 Td at the anode end. It follows from the results presented in [3] that the characteristic electron energy (or the "temperature") can be estimated as $T_e \approx 3500$–4000 K and it varies only slightly along the column. From microwave absorption measurements [14], the average electron density in the column can be estimated as $n_e \approx 5 \times 10^{11}$ cm^{-3}. For estimates, we take $n_e = 10^{12}$ cm^{-3} near the axis. The main positive charge carriers in an air plasma at relatively low temperatures are NO^+ ions. The negative ion density is small compared to the electron density [15] (note, however, that [15] gives the composition of a dry air plasma in thermodynamic equilibrium). Hence, we may assume that $n_e \approx n_i = n$, where n_i is the positive ion density.

The water vapor concentration in the discharge column is an important parameter, because the drift velocity of electrons and their characteristic energies in humid and dry air at $E/N < 20$ Td differ by more than one order of magnitude [16]. Depending on the temperature and humidity of air, up to several percent of water vapor can be contained in the atmosphere. In view of the low ion current density (~10^{-1} A/cm^2) and low ion energy (~10^2 eV), the sputtering of the water cathode cannot substantially increase the water vapor concentration. The humidity can increase due to water heating by the current flowing between the plasma and the metallic current supply conductor.

Water is heated by the volume Joule heating and the heat flux transferred through the discharge attachments to the surface. Taking into account that the water flow velocity is $v \approx 10^2$ cm/s and the typical diameter of the electrode attachments is $D \approx 0.7$ cm, we obtain that the

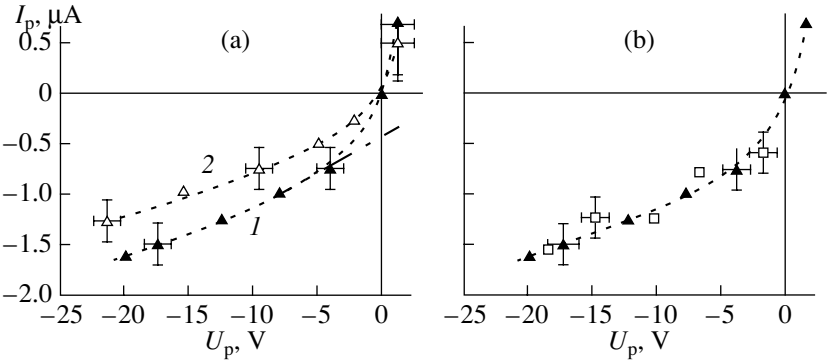

Fig. 5. Ion branches of the plane probe characteristics at $I \approx 65$ mA for (a) a probe facing the cathode at z = (*1*) 2.5 and (*2*) 4.5 mm and (b) for a probe facing the cathode (triangles) and anode (squares) at $z = 2.5$ mm.

duration of the heat sources is $t_0 \approx 7 \times 10^{-3}$ s. Over this time, Joule heating is as low as a few degrees. Let us estimate the surface heating. We consider the cathode attachment, in which most of the energy is released. We assume that the energy W released in the cathode plasma region, in which the voltage drops by ≈600 V (Fig. 3) at a current density of ≈(0.20–0.25) A/cm^2, is totally transferred onto the water electrode and neglect the cooling of the latter. Since we have $l \sim (at_0)^{1/2} \approx 3 \times 10^{-3}$ cm $\ll D$ (where $a = \lambda/C_p\rho$), λ is the thermal conductivity, C_p is the specific heat, and ρ is the water mass density), the surface heating can be estimated from the expression [17] $T_s = T_0 + (2W/\lambda)(at_0/\pi)^{1/2}$, where T_0 is the temperature of the flow before entering the discharge region. For $T_0 = 285$–290 K, we obtain $T_s \approx 320$–330 K. This is the maximum temperature that can be reached on the water-flow surface at the exit from the discharge region. This temperature corresponds to a saturation vapor pressure of $p_w \le 2 \times 10^{-1}$ atm. In addition, the discharge generates small drops (this problem was not examined). When heated in the plasma, these drops can also contribute to water vapor concentration. Apparently, water vapor concentration in the discharge can be substantially higher than that in ambient air.

8. Let us choose a method for treating the measurement results. For this purpose, we estimate the characteristic lengths of the region disturbed by the probe for dry air and then consider the effect of humidity. At the given plasma density and electron temperature, the Debye length is equal to $l_D \approx 3 \times 10^{-4}$ cm. The gas temperature near the probe is close to the temperature of its surface, $T_g \approx 500$–600 K. At such temperatures, the ion mean free path is $l_i \sim 10^{-5}$ cm and the electron mean free path is $l_e \sim 10^{-4}$ cm. The electron energy relaxation length is equal to $l_\varepsilon = \delta^{-1/2} l_e \sim 10^{-3}$ cm (where δ is the parameter characterizing the energy exchange efficiency), so that $l_\varepsilon E_c \sim 1$ eV $> T_e$. Taking into account the relatively high humidity of air changes the estimate for l_e; as a result, we obtain the inverse inequality. Hence, we can assume that the electron distribution function in the plasma column is close to Maxwellian. Under these conditions, the dominant recombination mechanism is associated with dissociation. The recombination length of NO^+ ions is equal to $L_r = D_a/(\alpha n)^{1/2} \approx 4 \times 10^{-3}$ cm, where $D_a = D_i(1 + T_e/T_i)$ is the ambipolar diffusion coefficient, D_i is the ion diffusion coefficient, and α is the recombination coefficient. The values of D_i and α are taken from [18].

The above estimates show that the following inequalities hold: $l_i \ll l_D \sim l_e \ll l_\varepsilon \ll L_r \ll b$, where b is the characteristic probe size. Under these conditions, the plasma region of size $\sim b$, which is in the ionization equilibrium state and from which the probe current is collected, makes the main contribution to the difference between the probe and unperturbed plasma potentials in the transition region of the *I–V* characteristic. The probe floating potential coincides with the plasma potential accurate to $\sim kT_e/e$. The probe current in the transition region of the *I–V* characteristic is described by the expression [11]

$$I_p = 4\pi c \sigma_\infty U_p, \qquad (1)$$

where c is the probe electric capacitance and σ is the unperturbed plasma conductivity.

The ion current toward the plane probe is described by the expression [19]

$$I_p = 3^{-1/2} e n_\infty^{3/2} (D_a \alpha)^{1/2} (1 + b_i/b_e) S_0, \qquad (2)$$

where n_∞ is the unperturbed plasma density; b_i and b_e are the ion and electron mobilities, respectively; and S_0 is the area of the space charge sheath.

The theories of [11, 19] were developed assuming that the external field is low as compared to the ambipolar one. The opposite case was considered in [20], where it was shown that, in this case, the *I–V* characteristic has no linear segment. The shape of the *I–V* probe characteristic is determined by the probe shape; e.g., the spherical probe current in the transition region of the *I–V* characteristic is proportional to the square of the probe potential. Under our experimental conditions, the ambipolar field is estimated as $E_a \sim 10^3$ V/cm $\sim E_c$. For expression (1) to be applicable, it is also required that the field in the unperturbed plasma be low as compared to the field produced by the probe in the current collection region. Estimates show that, for $U_p \ge 20$ V, the field produced by the probe exceeds that existing in the unperturbed plasma. The shape of the *I–V* characteristic allows us to suggest that, without large errors, we can use expressions (1) and (2) to process these characteristics. The applicability of the corresponding theories at $E_a \sim E_c$ will be checked by comparing their predictions with the results of noncontact measurements [14].

It should also be noted that expression (2) for the probe current is valid if the density and temperature of neutral particles near the probe do not depend on the coordinates. In our experiments, the probe temperature is lower than the gas temperature, so that there are the temperature and density gradients near the probe. As was shown in [21], in the case of a plane probe, this can be taken into account by correcting the probe current for the value on the order of the ratio between the probe and gas temperatures.

9. The plasma density was determined from the ion branch of the *I–V* characteristic in accordance with expression (2) and was corrected for the difference between the probe and gas temperatures. The probe temperature was assumed to be ≈500 K. The ion current was determined by extrapolating the *I–V* characteristic to $U_p \approx 0$ (Fig. 5a). We obtained the following estimates for the density: $n_c \approx 1.5$–2.0×10^{12} cm^{-3} at the cathode end of the plasma column and $n_a \approx 0.9$–$1.2 \times$

10^{12} cm^{-3} at the anode end. The density in the column decreases slightly toward the anode.

The plasma conductivity was determined from the transition region of the *I–V* characteristic by using expression (1). In this case, the probe capacitance was specified as the capacitance of a single-sided plane disk with the same area ($c \approx 10^{-2}$ cm). The conductivity can be estimated as $\sigma \approx 2\text{–}3 \times 10^{-4}$ (Ω cm)$^{-1}$ at the cathode end of the column and $\sigma \sim 10^{-4}$ (Ω cm)$^{-1}$ at the anode end. Equation (1) was also derived assuming that, in the largest part of the current collection region, the gas temperature is constant and equal to the gas temperature in the discharge. For this reason, the conductivity values presented here are somewhat lower than the unperturbed plasma conductivity.

Estimating the plasma density from the results of conductivity measurements and comparing it to the values obtained from the ion current measurements, we can also estimate the water vapor concentration in the column. Indeed, the difference between the ion mobilities in dry and humid air is not as large as the difference between the electron mobilities. In addition, the plasma density, determined from expression (2), depends weakly (as a third root) on the ion diffusion coefficient. At the cathode end of the column, the plasma density estimated from the ion current measurements agrees satisfactorily with that estimated from the conductivity measurements, assuming that the humidity in the discharge is ~30–40%. When estimating the electron mobility, we used the data from [22]. Note that, at such a high humidity, the electron mobility is determined mostly by water vapor. To a high accuracy, the electron mobility in water vapor is constant up to $E/N \approx 30$ Td. This justifies the use of expression (1), derived assuming that the transport coefficients are independent of the electric field, and the expression $n_e = \sigma/eb_e$ when evaluating the electron density. Since we used underestimated values for the plasma conductivity, the obtained values of the water vapor concentration must be considered as an upper estimate.

10. The probe measurements in the interelectrode gap of a discharge with tap water electrodes in air have shown that a more or less homogeneous discharge column exists between the electrode regions. The electric field strength in the column amounts to ~700–800 V/cm, and the plasma density is ~$(1\text{–}2) \times 10^{12}$ cm^{-3} and decreases as approaching the anode end of the column by a factor of 1.5–2 in comparison to that at the cathode end. The probe measurements also allowed us to estimate the water vapor concentration in the column near the cathode. The concentration of water vapor substantially exceeds its concentration in ambient air.

The obtained values of the plasma density agree with the results of microwave absorption measurements of the average electron density in the column [14]. In [14], the processing of results under the assumption of dry air yielded $4 \times 10^{11} < n_e < 7 \times 10^{11}$ cm^{-3}. However, the processing of the data from [14] with allowance for the presence of water vapor shows that taking into account air humidity nearly doubles the average electron density, which satisfactorily agrees with the results of the probe measurements.

In conclusion, we note that, when estimating the average electric field near the cathode and anode from the data presented in Fig. 3, we obtain close values on the order of $(2\text{–}3) \times 10^3$ V/cm. Using this value and also the results of the gas temperature measurements [8], we can estimate the average value of the parameter E/N near the electrodes. Since the gas is heated more strongly near the cathode, the average value of E/N in this region is higher than near the anode by a factor of about 1.5 and amounts to 60–80 Td.

ACKNOWLEDGMENTS

We thank F.G. Baksht for his continuing interest in this work and helpful discussions.

REFERENCES

1. F. M. Gaĭsin and É. E. Son, in *Encyclopedia of Low-Temperature Plasma*, Ed. by V. E. Fortov (Nauka, Moscow, 2000), Vol. 2, p. 241.
2. F. M. Gaĭsin, F. A. Gizatullina, and R. R. Kamalov, Fiz. Khim. Obrab. Mater., No. 4, 58 (1985).
3. P. Andre, Yu. Barinov, G. Faure, *et al.*, in *Progress in Plasma Processing of Materials 1999: Proceedings of the 5th International Thermal Plasma Processes Conference, St. Petersburg, 1998*, Ed. by P. Fauchais and J. Amouroux (Begell Haouse, New York, 1999), p. 848.
4. T. Cserfalvi, P. Mezei, and P. Apai, J. Phys. D **26**, 2184 (1993).
5. V. G. Samoĭlovich, V. I. Gibalov, and K. V. Kozlov, *Physical Chemistry of Barrier Discharge* (Mosk. Gos. Univ., Moscow, 1989).
6. F. M. Gaĭsin and É. E. Son, *Electrophysical Processes in Discharges with Solid and Liquid Electrodes* (Ural'skiĭ Univ., 1989), p. 357.
7. *Tables of Physical Quantities*, Ed. by I. K. Kikoin (Atomizdat, Moscow, 1976).
8. G. Faure and S. M. Shkol'nik, J. Phys. D **31**, 1212 (1998).
9. W. Espe, *Werkstoffkunde der Hochvakuumtechnik* (Deutscher Verlag der Wissenschaften, Berlin, 1959; Gosénergoizdat, Moscow, 1962), Vol. 1.
10. Yu. A. Ivanov, Yu. A. Lebedev, and L. S. Polak, *Contact Diagnostics Techniques in Nonequilibrium Plasmochemistry* (Nauka, Moscow, 1981).
11. M. S. Benilov, G. G. Bochkarev, A. E. Buznikov, *et al.*, Izv. Akad. Nauk SSSR, Mekh. Zhidk. Gaza, No. 1, 150 (1983).
12. A. Anders, A. P. Ershov, K. Sh. Isaev, and I. B. Timofeev, Teplofiz. Vys. Temp. **25**, 743 (1987).
13. G. A. Batyrbekov, É. A. Belyaeva, M. S. Benilov, *et al.*, Fiz. Plazmy **17**, 114 (1991) [Sov. J. Plasma Phys. **17**, 64 (1991)].

14. Yu. A. Barinov, V. B. Kaplan, V. V. Rozhdestvenskiĭ, and S. M. Shkol'nik, Pis'ma Zh. Tekh. Fiz. **24** (23), 52 (1998) [Tech. Phys. Lett. **24**, 929 (1998)].
15. *Physics and Technology of Low-Temperature Plasma*, Ed. by S. V. Dresvin (Atomizdat, Moscow, 1972).
16. L. G. H. Huxley and R. W. Crompton, *The Diffusion and Drift of Electrons in Gases* (Wiley, New York, 1974; Mir, Moscow, 1977), Chap. 14.
17. A. V. Lykov, *Theory of Heat Conductivity* (Vysshaya Shkola, Minsk, 1967).
18. *Handbook of Physical Quantities*, Ed. by I. S. Grigoriev and E. Z. Meilikhov (Énergoatomizdat, Moscow, 1991; CRC Press, Boca Raton, 1997).
19. K. N. Ul'yanov, Zh. Tekh. Fiz. **40** (4), 790 (1970) [Sov. Phys. Tech. Phys. **15**, 613 (1970)].
20. Yu. S. Akishev and A. P. Napartovich, Dokl. Akad. Nauk SSSR **242**, 812 (1978) [Sov. Phys. Dokl. **23**, 736 (1978)].
21. K. N. Ul'yanov, Teplofiz. Vys. Temp. **16**, 492 (1978).
22. F. E. Spencer and A. V. Phelps, in *Proceedings of the 15th Symposium on the Engineering Aspects of Magnetohydrodynamics, Philadelphia, 1976*, p. IX-9.1.

Translated by N. Larionova

Technical Physics, Vol. 47, No. 3, 2002, pp. 320–324. Translated from Zhurnal Tekhnicheskoĭ Fiziki, Vol. 72, No. 3, 2002, pp. 38–42.

SOLIDS

The Non-Hooke's Behavior of Porous Zirconia Subjected to High-Rate Compressive Deformation

S. N. Kul'kov, V. I. Maslovskiĭ, S. P. Buyakova, and D. S. Nikitin

Institute of Strength Physics and Materials Science, Siberian Division, Russian Academy of Sciences, Akademicheskiĭ pr. 2/1, Tomsk, 634021 Russia

Received May 18, 2001

Abstract—The deformation of partially stabilized zirconia $ZrO_2(Y_2O_3)$ with various pore morphologies is studied. During the synthesis of bar and lamellar ceramic structures, an effect of mechanical instability is discovered. This effect, along with the purely elastic behavior of the ceramic and the accumulation of microdamages under high-rate compressive deformation, produces considerable strains in the porous structure without material failure and substantially extends the applications of porous ceramic materials. © *2002 MAIK "Nauka/Interperiodica".*

1. INTRODUCTION

At present, materials with a developed pore structure are attracting great interest because of their wide application as filters for fluid purification and separation, catalyst carriers, heat-insulating coatings, etc. [1, 2]. Nonmetal (ceramic) materials offer high chemical and corrosion resistance and, therefore, have advantages over metals and high-molecular compounds when used in porous structures operating in an aggressive environment or at elevated temperatures. Most ceramics are chemically inactive in biological media, so that associated porous products can be implanted into the human organism (bony tissue endoprostheses and medicinal preparation dispensers).

The synthesis of porous materials with desired properties calls for the detailed investigation of a correlation between the physicomechanical properties of the material and its structure. This is especially true for ceramic materials, because porosity, as a rule, leads to a catastrophic reduction of the mechanical strength. In ceramics, dislocations are hard to move, so that stress concentrators relax insignificantly under loading. Mechanisms behind the macroscopic deformation of ceramics with different pore morphologies are of particular interest.

Porous ceramics are a heterogeneous material. Depending on applications, the pore size and the integral porosity may vary in a very wide range. Therefore, their mechanical behavior is also of scientific interest.

Zirconia is among the materials that are promising for porous structures. It offers high strength, fracture toughness, and corrosion resistance. Also, zirconia is stable in aggressive media and does not react with human organism tissues. This ceramic, containing a controllable pore concentration, retains strength properties due to strain hardening [4].

In this work, we study the effect of pore morphology on the mechanical behavior of partially stabilized zirconia subjected to high-rate compressive deformation.

EXPERIMENTAL

The objects of investigation were ZrO_2 ceramic samples partially stabilized by Y_2O_3 (3 mol %). Their porosity ranged between 10 and 60%, and the mean pore size was comparable to or much larger (by several orders of magnitude) than the grain size. The samples were prepared by the power metallurgy method (pressing with the subsequent sintering of the ultrafine powder at temperatures of 1200–1600°C). In this way, samples with a pore size comparable to the grain size were obtained. Larger pores were produced by adding granulated admixtures that are easy to burn out, such as rosin or paraffin, into the powder.

Compression tests were carried out on an INSTRON-1185 machine with a constant loading rate of 3×10^{-4} s^{-1}. From stress–strain curves, we evaluated the strain and the ultimate strength of the material.

RESULTS AND DISCUSSION

Figure 1 shows stress–strain curves for the ceramics with different porosities. The mean pore size was comparable to or much larger than the mean grain size. It is seen that the increase in the pore volume causes multiple microdamages during the deformation, which are the greater, the higher the porosity. In the curves, this process shows up as sharp stress drops due to microcracking. After the microcracks have terminated at the pores, the material can elastically deform again. As the porosity grows, the range of microcracking shifts toward higher strains and expands. When the porosity exceeds 20%, the stress–strain curves become concave

1063-7842/03/4702-0320$22.00

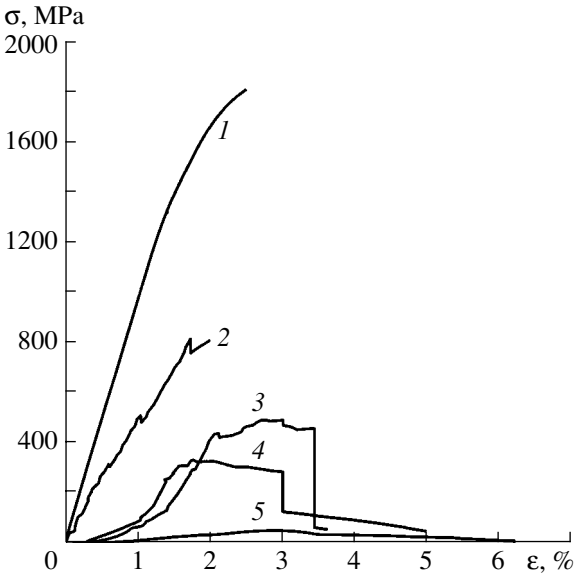

Fig. 1. Stress–strain curves for the ceramic: (*1*), (*2*), (*5*) pore size is comparable to the grain size and (*3*), (*4*) pore size is much larger than the pore size. The porosity is (*1*) 10, (*2*) 15, (*3*) 23, (*4*) 29, and (*5*) 60%.

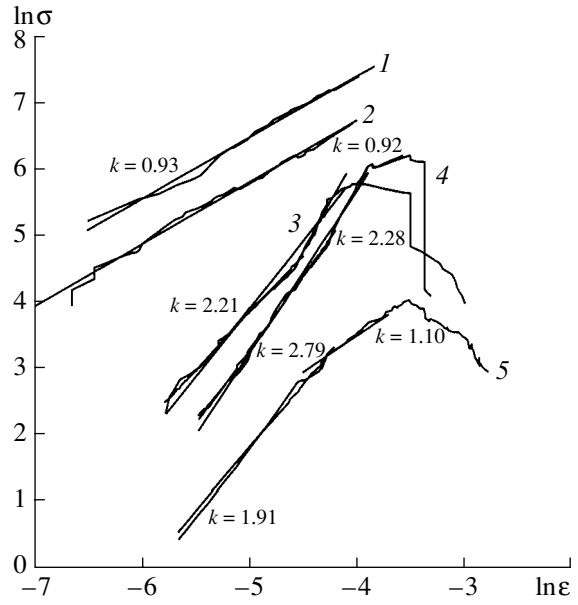

Fig. 2. Stress–strain curves in the log–log coordinates. Designations the same as in Fig. 1.

upward, which is totally untypical of the stress–strain curves for sintered materials.

At the stage of high-rate deformation (prior to microcracking), the general slope of the curves $\sigma = f(\varepsilon)$ varies with integral porosity. However, the slope varies also locally (within one curve), depending on the porosity type and pore size. Such dependences can be described by a power function like $Y = bX^k$ for both deformation- and pressing-related processes (the latter are also possible in this system). Here, the exponent k depends on which of the processes, pressing or plastic deformation, is governing. For purely elastic deformation, $k = 1$; for plastic deformation, $k < 1$; and for pressing, $k > 1$.

Figure 2 demonstrates the curves $\sigma = f(\varepsilon)$ in the log–log coordinates. For the ceramic of porosity higher than 20%, the curves take the form of several linear segments, which obviously have various slopes k. The higher the porosity, the larger the number of the linear segments.

In Fig. 3, the exponents k measured from the slopes of the linear segments are plotted against porosity for the ceramic where the mean pore diameter is comparable to the mean grain size. The data points for k are well fitted by three straight lines. There exists some critical porosity value at which the deformation of the porous material radically changes: the second exponent of the power function (much larger than that in the initial state) appears. Most likely, this is related to a change in the pore distribution: individual pores give way to the continuous pore distribution. In essence, the material is split into two subsystems, which deform in different ways under stressing.

For the high-porosity samples, the k vs. porosity dependence is different: the lower the porosity, the larger the exponent on the average. As follows from Fig. 4, k exponentially decreases with increasing porosity. Here, the values of k measured are distributed rather irregularly presumably because of the stochastic nature of microdamages in this material. In general, the values of k lie near the approximating exponentials.

The examination of the sample surface after the deformation indicates no signs of local pressing-related material displacement before microcracking. Moreover, at this stage, the stress–strain curves are reversible; that is, the deformation process is purely elastic, as demonstrated by direct metallographic studies. Figure 5, depicting the image of the ceramic structure, was obtained by superposing the micrographs taken before compressive stressing and after a strain of 1.5% had been achieved. The complete coincidence of the micrographs is obvious.

Thus, the experiments did not reveal the displacement of the material into the pore space. This means that the process of pressing was absent and the material deformed only elastically. However, the rather high values of k (from 1.4 to 7.8) obtained in the absence of traces of residual deformation seem to be very intriguing.

The above results characterize the response of our sample, which is a deformable system produced by pressing followed by sintering (i.e., consisting of many randomly shaped grains more or less bonded to their neighbors), to uniaxial stressing. The structural features of this material are responsible for the dependence $\sigma = f(\varepsilon)$ obtained in our experiments, which considerably differs from that for an isotropic elastic body. There-

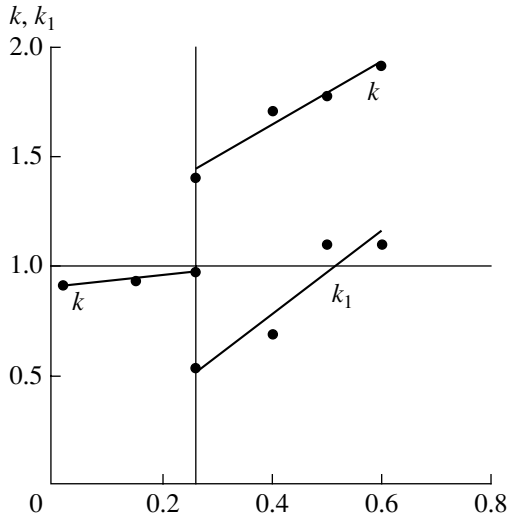

Fig. 3. Exponent k of the stress–strain law vs. porosity for the ceramic where the pore and grain sizes are roughly equal.

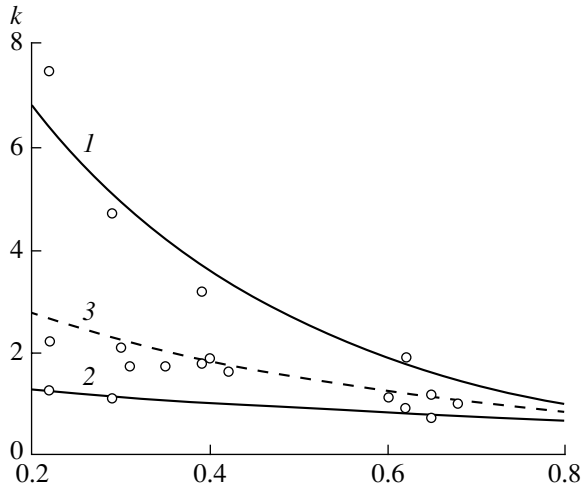

Fig. 4. k vs. porosity for the ceramic where the grain size far exceeds the pore size. Y = (*1*) $13\exp(-3.2X)$, (*2*) $1.5\exp(-1.04X)$, and (*3*) $4\exp(-1.97X)$.

fore, to explain the behavior of the zirconia-based ceramic sample as a whole, it is necessary to elucidate plausible mechanisms that deform its structure constituents.

At the initial stage of deformation of porous zirconia ceramic,

$$\frac{d\sigma}{d\varepsilon} < E \quad \text{and} \quad \frac{d^2\sigma}{d\varepsilon^2} > 0. \tag{1}$$

This means that the deformation response to a stress applied is associated with essentially nonlinear mechanisms. Among them is that relying on the well-known solution of the Hertz problem of two contacting homogeneous bodies [5, 6]. Extending the solution of this problem [5] for the case of arbitrary shaped bodies, we will have (in terms of conventional stresses)

$$\sigma \approx AE\varepsilon^{3/2}, \tag{2}$$

where A is a constant depending on the packing density of the contacting grains and their sizes.

For granular systems with a linear or lamellar structure or for those where grains are loosely bonded to neighbors along lines or planes, the bifurcation transition to the adjacent equilibrium state may take place. This transition is accompanied by reversible bending, which disappears when the generating reasons are removed. Such structures, which can be simulated by bars, may arise in high-porosity ceramics with a limited contact area between the grains. Because of small sizes of the grains produced by sintering and, accordingly, small contact areas, the bending stresses do not exceed the ultimate strength of the ceramic material (which is almost defect-free within a zirconia grain). To estimate the deformation response of such structures once they have lost stability (in the subcritical state, this response obeys the Hooke law), we will turn to the well-known Euler problem of elasticity considered in [7]. Omitting the basic statements of work [7], we note that the bending angle of a stability-losing hinged bar is found from the relationship

$$\Phi = \int_0^{\pi/2} \frac{d\varphi}{\sqrt{1 - m^2\sin^2\varphi}} = \frac{kl}{2}; \quad \left(\sin\frac{\Theta_0}{2} = m, \quad k = \sqrt{\frac{P}{EJ}}\right), \tag{3}$$

where P is the force applied to the bar, E is the shear modulus, and J is the moment of inertia of the cross section with a length l.

Considering the case of small m (the force applied is slightly above the critical value) and expanding the integrand in m up to fourth-order terms, we come to

$$(1 - m^2\sin^2\varphi)^{-1/2} \approx 1 + \frac{m^2}{4} + \frac{9}{64}m^4 - \frac{m^2}{4}\cos 2\varphi - \frac{3}{16}m^4\cos 2\varphi + \frac{3}{64}m^4\cos 4\varphi \tag{4}$$

and, accordingly, to the equation for m

$$\left(1 + \frac{m^2}{4} + \frac{9}{64}m^4\right)\pi = kl. \tag{5}$$

The solution of Eq. (5) is

$$m^2 \approx 4\left(\frac{kl - \pi}{\pi}\right). \tag{6}$$

Taking into account that the displacement of the free end of the rod is twice as large as that of its middle part [7], we find the strain of the rod in the above-critical range:

$$\Delta\varepsilon = 1 - \frac{2}{kl}(2\varepsilon - \Phi),$$

where

$$\varepsilon = \int_0^{\pi/2} \sqrt{1 - m^2 \sin\varphi}\, d\varphi. \quad (7)$$

Expanding the integrand and performing appropriate rearrangements, we arrive at

$$\frac{\Delta\bar{P}}{P_1} = \frac{\Delta\varepsilon}{2}, \quad \text{where} \quad \Delta P = P - P_1, \quad P_1 = \frac{\pi^2 EJ}{l^2} \quad (8)$$

or

$$\frac{\Delta P}{S} = \Delta\sigma = \frac{P_1}{2S}\Delta\varepsilon = \frac{\sigma_1}{2}\Delta\varepsilon, \quad (9)$$

where $\Delta\varepsilon$ is the extra above-critical bending strain and S is the cross-sectional area of the rod.

Writing (8) in the form

$$\Delta\sigma = E\frac{\varepsilon_1}{2}\Delta\varepsilon, \quad (10)$$

one can see that when the rod becomes unstable, the strain in the above-critical range is a linear function of the stress increment, being $2/\varepsilon_1$ times higher than Hooke's strain.

Let us estimate the likelihood of reversible elastic loss of stability occurring in bar ceramic structures in terms of their strength characteristics. Using the well-known approximations from the engineering theory of bars, we write the expression for the maximal stress arising in a rod under above-critical bending:

$$\sigma = \frac{P}{S} \pm \frac{M_{\max}}{W} = \frac{P}{S} \pm \frac{PY_{\max}}{W}. \quad (11)$$

Here, P is the force applied, S is the cross-sectional area of the rod, M is the bending moment, W is the modulus of twist, and $Y_{\max}$ is the maximal transverse deflection of the rod. With the expressions derived above and the expression for $Y_{\max}$ from [7], we find the stability conditions under compression:

$$\pm\frac{P^*}{F}\left(1 \pm \frac{2\sqrt{2l}}{\pi}\frac{E}{W}\sqrt{\Delta\bar{P}}\right) \le \sigma_b. \quad (12)$$

Let us assume that

$$\sigma_b = \frac{\sigma_{th}}{Z} = \frac{E}{\pi^2 Z}, \quad (13)$$

then, considering the rod as consisting of n particles of diameter D that agglomerate on areas of diameter d, we find the stability condition in the form

$$\pm\frac{\pi^4}{16}\left(V^2 \pm \frac{16\sqrt{2}}{\pi}V\sqrt{\bar{P}}\right) \le \frac{1}{Z}, \quad (14)$$

where

$$V = \frac{d}{nD}.$$

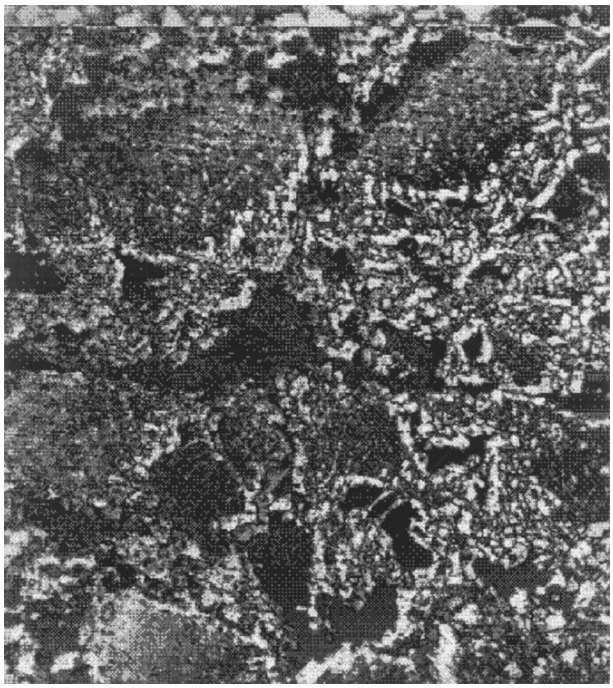

Fig. 5. $ZrO_2(Y_2O_3)$ ceramic with a porosity of 30%. The image was obtained by superposing the micrographs taken before compression and after a strain of 1.5% had been achieved.

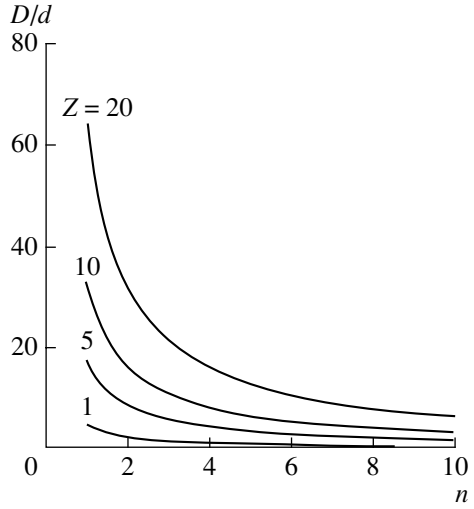

Fig. 6. Range of D/d where the sample exhibits mechanical instability vs. number of particles n in the rod. The above-critical strain $\Delta\varepsilon$ is 1%.

If the above-critical strain $\Delta\varepsilon$ is, for example, 1%, one can determine the range of D/d where the material deforms without failure but loses stability and the range of D/d where it fails. A family of curves that divide the plane (D/d, n) into associated regions for various Z is shown in Fig. 6. Here, the ranges (D/d, n) where the material remain intact lie above the curves. Below the curves, the material fails.

Thus, we see that even if the bars with small n (n = 2, 3, 4, …) become unstable, they as structure constituents may undergo substantial yet elastic macroscopic deformation provided that D/d is small, which is observed experimentally.

REFERENCES

1. *Porous Structural Ceramics*, Ed. by Yu. L. Krasulin (Metallurgiya, Moscow, 1980).
2. V. N. Antsiferov and S. N. Peshcherenko, Fiz. Mezomekh., No. 8, 66 (1999).
3. A. G. Evans and R. M. Cannon, Acta Metall. **34**, 761 (1986).
4. S. P. Buyakova, Han Wei, A. G. Mel'nikov, *et al.*, Pis'ma Zh. Tekh. Fiz. **25** (17), 44 (1999) [Tech. Phys. Lett. **25**, 695 (1999)].
5. L. D. Landau and E. M. Lifshitz, *Course of Theoretical Physics*, Vol. 7: *Theory of Elasticity* (Nauka, Moscow, 1987; Pergamon, New York, 1986).
6. Yu. A. Amen-Zade, *Theory of Elasticity* (Vysshaya Shkola, Moscow, 1971).
7. Yu. N. Rabotnov, *Mechanics of Deformed Solid* (Nauka, Moscow, 1979).

Translated by V. Isaakyan

Technical Physics, Vol. 47, No. 3, 2002, pp. 325–329. Translated from Zhurnal Tekhnicheskoĭ Fiziki, Vol. 72, No. 3, 2002, pp. 43–47.

SOLIDS

Properties of Nonstoichiometric Sodium Niobate

L. A. Reznichenko, L. A. Shilkina, O. N. Razumovskaya, I. V. Pozdnyakova, E. M. Kuznetsova, and S. I. Dudkina

Research Institute of Physics, Rostov State University, pr. Stachki 194, Rostov-on-Don, 344090 Russia

e-mail: klevtsov@ip.rsu.ru

Received June 27, 2001; in final form, August 7, 2001

Abstract—Stoichiometric and nonstoichiometric sodium niobate of the composition $Na_{1-x}NbO_{3-x/2}$ ($0 \le x \le 0.2$) is obtained by the two-stage solid-phase reaction technique. X-ray diffraction study reveals the homogeneity region for compositions below $x = 0.1$. At higher x, the samples become two-phase. The phase transition is found to occur at $x = 0.04$. It is accompanied by a change in the multiplicity of the monoclinic subcell of the sodium niobate rhombic unit cell, as well as by the anomalous behavior of its structural and electrophysical characteristics. From the study of the dielectric and piezoelectric properties of the material, it is concluded that the stability of the antiferroelectric phase is enhanced, whereas the ferroelectric phase becomes less stable, as the nonstoichiometry in terms of Na_2O increases. © *2002 MAIK "Nauka/Interperiodica".*

It is known that complex niobium oxides feature polymorphism, morphotropy, and nonstoichiometric composition [1]. These properties are the most pronounced in sodium niobate (SN), which is characterized by the largest number of phase transitions among octahedral oxygen compounds [2]. Moreover, SN can combine with other compounds (by virtue of the wide isomorphism [3]) to form solid solutions (SS) with numerous sequential morphotropic transitions of different nature [4] and has the extended homogeneity region [5, 6], where the electrophysical parameters may widely vary [7]. However, only a few works have been concerned with the influence of nonstoichiometry on the SN properties [5–10] and they mainly examine the structure and the dielectric properties of the material. However, our data [11] indicate that in the SN ceramics, where the "nonstoichiometry" index x in the formula $Na_{1-x}NbO_{3-x/2}$ ($0 \le x \le 0.2$) varies within wide limits, the long-lived metastable ferroelectric (FE) phase appears as the result of polarization. Its presence shows up in the distinct piezoelectric effect related to the piezoresonant dispersion of the permittivity. The dispersion arises when the sample passes from the mechanically free to the mechanically squeezed state. This fact, along with dielectric hysteresis loops observed in [11–13], allows us to conclude that polar microdomains (FE clusters), whose dimensions may increase with the polarization of the ceramic [11], appear in the antiferroelectric (AFE) phase of stoichiometric and nonstoichiometric SN. It was suggested to use SN of composition $Na_{1-x}NbO_{3-x/2}$ in nondestructive testing, where the high anisotropy of the piezoelectric coefficients, typical of SN, is an advantage. This study follows our study on nonstoichiometric SN undertaken in [10, 11].

Analytical-grade Na_2CO_3 and extra-pure- and commercial-grade Nb_2O_5 (with differing impurity contents and compositions) were used to prepare stoichiometric and nonstoichiometric SN of composition $Na_{1-x}NbO_{3-x/2}$, where $0 \le x \le 0.2$ and $\Delta x = 0.2$–0.025. The niobates were synthesized using the solid-phase reaction, including two-stage firing at temperatures of 800–850°C with a holdup time of 4 h at either stage. The components were mixed in alcohol to avoid hydrolysis. Grinding was carried out in water. Two lots of samples were prepared. The powders from the first lot were not granulated, while those from the second one were granulated to make them free-flowing. The granulation, resulting in the considerable increase in the density of the ceramic samples, was performed by rubbing the pressed blocks first through a sieve with the mesh size 0.7–0.9 mm and then, after keeping the material for more than 4 h in a closed vessel, through a sieve with a mesh of 0.25–0.3 mm. A 5% aqueous solution of polyvinyl alcohol was used as a binder. Double-ended powder pressing under a pressure of 20 MPa was used to form pellets 12 mm in diameter and 2.5 mm thick. Sintering was carried out by the usual ceramic technique in a closed alundum boat at temperatures of 1220–1240°C for 2 h.

To choose the optimal sintering temperatures T_s, the structural characteristics of the compound with $x = 0.02$ were analyzed for annealing temperatures varying from 800 to 1240°C (Table 1; I_{rel} is the ratio of the intensities of impurity-related reflections to the intensity of the 110 SN reflection). As is seen from Table 1, impurity-free SN forms at 1220–1240°C and is characterized by the least values of the unit cell parameters and strains δ. A further increase in T_s does not improve the quality of the ceramic.

1063-7842/03/4702-0325$22.00 © 2002 MAIK "Nauka/Interperiodica"

Table 1. Structural characteristics of SN with $x = 0.02$

T_s, °C	I_{rel} for impurity phase reflections	$a = c$, Å	b, Å	β, deg	V, Å^3	$\bar{a}$, Å	δ	a/b
800	6($Na_2Nb_4O_{11}$)	3.9173	3.8809	90.63	59.55	3.9050	0.0087	1.0094
950	6($Na_2Nb_4O_{11}$)	3.9160	3.8823	90.67	59.53	3.9047	0.0088	1.0087
1150	<1($NaNb_3O_8$)	3.9160	3.8815	90.63	59.52	3.9044	0.0085	1.0089
1200	Traces 1 ($NaNb_3O_8$)	3.9134	3.8834	90.65	59.47	3.9033	0.0082	1.0077
1220	Pure	3.9135	3.8854	90.65	59.50	3.9040	0.0081	1.0072
1240	Pure	3.9135	3.8853	90.65	59.50	3.9040	0.0081	1.0072

Table 2. X-ray diffraction data and measured densities for both lots of stoichiometric and nonstoichiometric sodium niobate of composition $Na_{1-x}NbO_{3-x/2}$

Lot number	x	I_{rel}	Unit cell symmetry	Parameters of reduced monoclinic subcell						ρ_r, g/cm^3	ρ_m, g/cm^3	ρ_{rel}
				$a = c$, Å	b, Å	β, deg	V, Å^3	$\bar{a}$, Å	δ			
1	0	0	*RII*(*M*4)	3.9135	3.8854	90.65	59.503	3.9040	0.0081	4.60	3.1	0.702
2		0	*RII*(*M*4)	3.9121	3.8841	90.70	59.4388	3.9026	0.0085	4.605	4.31	0.936
1	0.02	2	*RII*(*M*4)	3.9129	3.8825	90.67	59.440	3.9026	0.0084	4.587	4.27	0.931
2		5	*RII*(*M*4)	3.9128	3.8849	90.64	59.4730	3.9034	0.0080	4.585	4.25	0.927
1	0.04	0	*RII*(*M*4)	3.9187	3.8890	90.45	59.719	3.9087	0.0065	4.548	4.16	0.915
2		1	*RII*(*M*4 + *M*2)	3.9128	3.8845	90.65	59.4576	3.9032	0.0081	4.568	4.38	0.959
1	0.06	3	*RII*(*M*4 + *M*2)	3.9134	3.8813	90.62	59.438	3.9026	0.0082	4.553	4.18	0.918
2		2	*RII*(*M*4 + *M*2)	3.9127	3.8854	90.63	59.4780	3.9035	0.0078	4.549	4.28	0.941
1	0.08	3	*RII*(*M*4 + *M*2)	3.9124	3.8837	90.64	59.444	3.9027	0.0081	4.535	4.08	0.899
2		5	*RII*(*M*4 + *M*2)	3.9126	3.8863	90.63	59.4902	3.9037	0.0077	4.531	4.15	0.916
1	0.10	7	*RII*(*M*4 + *M*2)	3.9125	3.8822	90.64	59.425	3.9023	0.0082	4.519	3.74	0.828
2		2	*RII*(*M*4 + *M*2)	3.9121	3.8860	90.64	59.4695	3.9033	0.0078	4.515	4.35	0.963
1	0.12	16	*RII*	3.9127	3.8849	90.64	59.471	3.9033	0.0080	4.498	3.09	0.687
1	0.14	19	*RII*	3.9135	3.8827	90.65	59.462	3.9031	0.0083	4.481	3.4	0.759
1	0.16	25	*RII*	3.9124	3.8852	90.64	59.467	3.9032	0.0079	4.463	3.18	0.713
1	0.18	26	*RII*	3.9125	3.8844	90.63	59.457	3.9030	0.0079	4.447	3.18	0.715
1	0.20	28	*RII*	3.9132	3.8851	90.63	59.490	3.9037	0.0079	4.427	3.4	0.768

The electrodes were conventionally fabricated by firing-in silver paste. The samples were polarized in PÉS-5 polyethylene siloxane liquid in the following way: first, they were placed into the chamber at room temperature and then the temperature smoothly rose to 140°C for 15–20 min. The temperature rise was accompanied by an increase in the polarizing field from 0 to 4.5 kV/cm. Under these conditions, the samples were kept for 20–25 min and then were cooled down to 60°C for no less than 20 min without removing the field.

X-ray diffraction studies were carried out using a DRON-3 diffractometer (Fe_{K_α} radiation, Mn filter) on the powder objects (ground ceramic samples). We identified the impurity phases and the unit cell symmetry, as well as measured the parameters of the reduced perovskite subcell, the size of coherent scattering areas (CSAs) D_{100}, and the microstrains $\Delta d/d_{100}$. The relative permittivity of the nonpolarized samples, $\varepsilon/\varepsilon_0$, as a function of temperature was determined with an E8-2 ac bridge at a frequency of 20 kHz. The piezoelectric modulus $d_{33}^{qu.stat}$ was found by the quasi-static technique.

The X-ray diffraction data and the measurements of the density for both lots of the stoichiometric and nonstoichiometric (containing extra-pure-grade Nb_2O_5) SNs are presented in Table 2. Here, I_{rel} is the ratio of the 430 reflection intensity from the $NaNb_3O_8$ impurity compound, forming during the synthesis (and observed also in [5, 6]), to the intensity of the $NaNbO_3$ 110 reflection. When commercial-grade Nb_2O_5 is used, the $NaNb_2O_5F$ compound can also appear as an impurity,

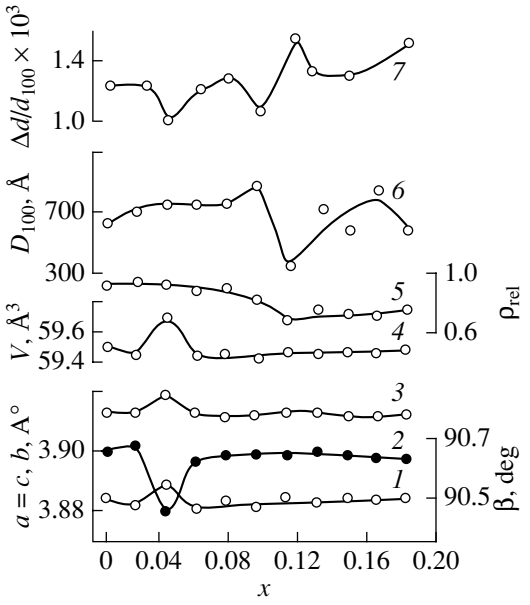

Fig. 1. Relative density (ρ_{rel}) and structural characteristics of stoichiometric and nonstoichiometric sodium niobate of composition $Na_{1-x}NbO_{3-x/2}$ as a function of x. (*1*) b, (*2*) β, (*3*) $a = c$, (*4*) V, (*5*) ρ_{rel}, (*6*) D_{100}, and (*7*) $\Delta d/d_{100}$.

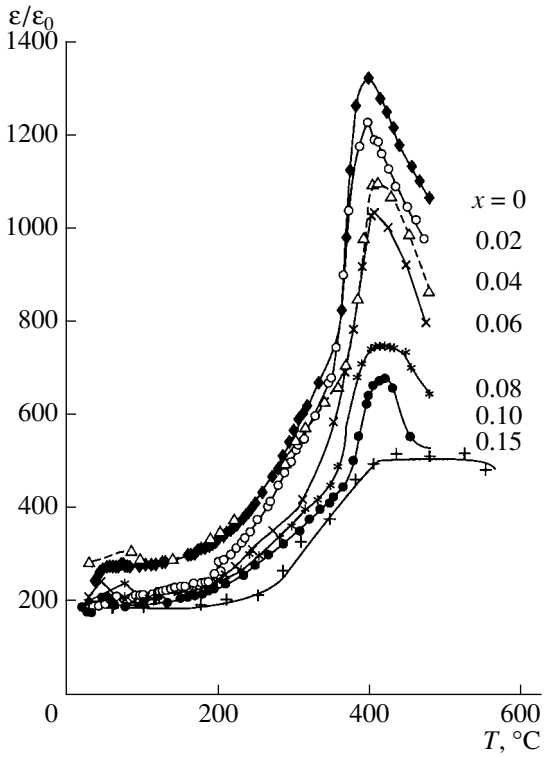

Fig. 2. Temperature dependences of the relative permittivity for stoichiometric and nonstoichiometric sodium niobate of composition $Na_{1-x}NbO_{3-x/2}$ taken at a frequency of 20 kHz.

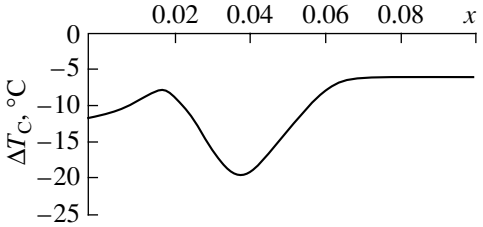

Fig. 3. Curie temperature shift ΔT_C in $Na_{1-x}NbO_{3-x/2}$ under the action of the electric field 1 kV/cm.

which is difficult to distinguish from $NaNb_3O_8$, since the most intense reflections from both compounds used for the impurity identification have the same or very close interplanar spacings.

The experimental data indicate that practically "pure" samples with the perovskite-like structure are obtained at $x < 0.1$. The minor content of the $NaNb_3O_8$ impurity (and, probably, of $NaNb_2O_5F$) observed in this range of x is related to the previously discovered [14] effect of crystallographic shift [15] in SN. Because of this effect, some of *AO* sites [16] disappear, which is responsible for an excess of Na. The range of SN homogeneity ($0 \le x \le 0.1$) found by us agrees with data reported in [5, 6]. Outside this range, the impurity content abruptly grows with x and the system becomes essentially two-phase. The samples from both lots have close lattice parameters. As was expected, the relative density of the samples from the second lot turned out to be higher than for the samples from the first lot. As we noted in [11], this strongly affects the permittivity and the elastic modulus of the ceramics: both parameters considerably increase with increasing density. At the same time, a marked influence of the density on the piezoelectric properties was not observed: a decrease in the porosity (an increase in the density) diminished the electromechanical coupling coefficient K_p of the plane vibrational mode only slightly and scarcely affects the value of the electromechanical coupling coefficient K_t for the thickness vibrational mode [11].

For $x \le 0.04$, SN has the rhombic symmetry (*RII* [17]) with the monoclinic (*M*) perovskite subcell *R*(*M*4); i.e., the symmetry is the same as in stoichiometric SN. The parameters of the unit *R* cell are related to those of the reduced *M* subcell as follows: $A = 2a_0\cos\beta/2$, $B = 4b_0$, and $C = 2a_0\sin\beta/2$ (where a_0, b_0, and β are the parameters of the *M* subcell). SN with $x > 0.04$ is characterized by the coexistence of *R* phases with different multiplicities, namely, *R*(*M*4) and *R*(*M*2) (with $B = 2b_0$). In the region $x \ge 0.12$, the multiplicity was not determined because of the high impurity content in the samples. Figure 1 shows the x dependences of the *M* subcell parameters, D_{100} and $\Delta d/d_{100}$, and the relative density of the samples from the first lot. In the homogeneity range $x = 0.04$, the structural characteristics experience anomalies observed previously [10] in these compounds near the same values of x. The transition between two AFE *R* phases was anticipated to take

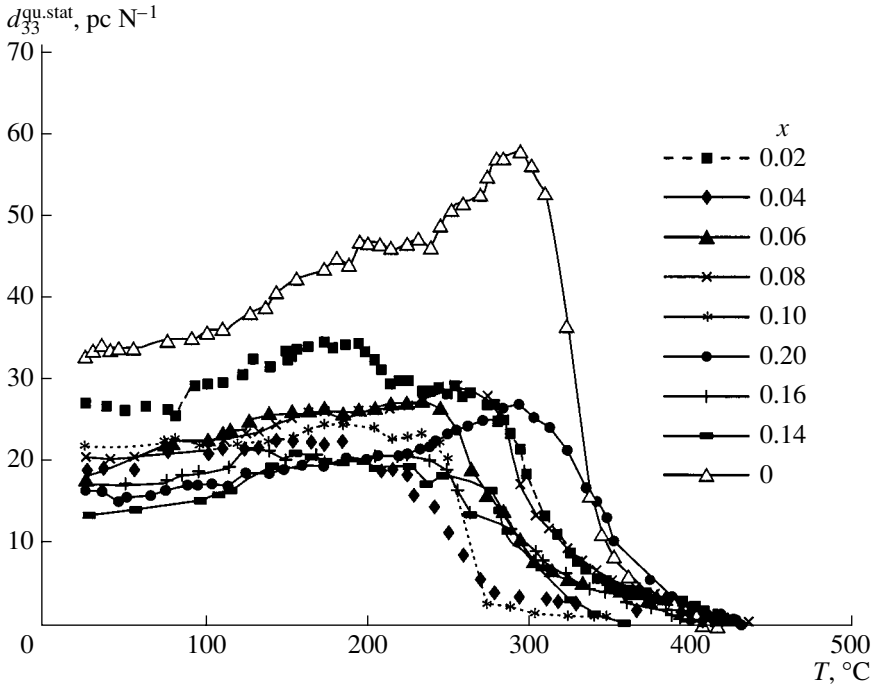

Fig. 4. Temperature dependence of the quasi-static piezomodule $d_{33}^{qu.stat}$ for stoichiometric and nonstoichiometric sodium niobate of composition $Na_{1-x}NbO_{3-x/2}$.

place in this range [10]. It was noted that the appearance of an extra anomaly in the curves $\varepsilon(T)$ in the range 280–330°C at high x, as well as the disappearance of the endoeffects [6] corresponding to high-temperature phase transitions in the thermograms of the samples with $x \geq 0.08$, indicate the difference in the properties of these phases. Our data relate this transition primarily to the change in the M subcell multiplicity, as well as to the change in the compound type: at $x < 0.04$, the excess Na (≈4.4 at. % [14]) in stoichiometric SN is depleted, decreasing the overall Na content; at $x > 0.04$, Na leaves regular cubic and octahedral sites. The anomalies of the parameters at $x \approx 0.1$ are associated with the boundary of the homogeneity range and, at $x > 0.1$, with fluctuations of the chemical composition in the two-phase region. Note that the transition to the two-phase region is accompanied by the abrupt deterioration of the SN crystal perfection (CSA shrinkage and increased microstrains).

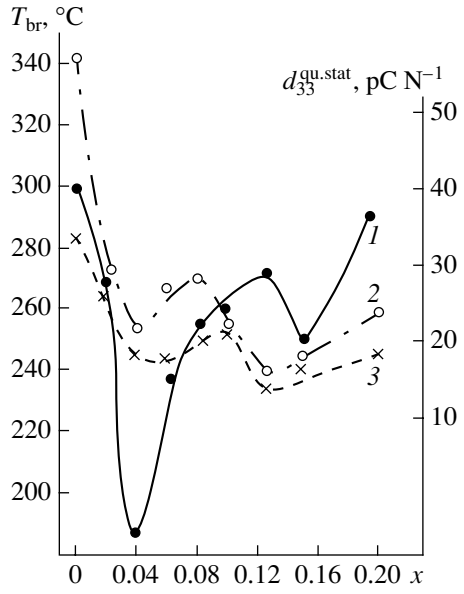

Fig. 5. x dependences of the (*1*) temperature of the piezoelectric activity breakage T_{br}, (*2*) corresponding values of the quasi-static piezoelectric modulus $d_{33_{T_{br}}}^{qu.stat}$, and (*3*) $d_{33_k}^{qu.stat}$ at room temperature for stoichiometric and nonstoichiometric sodium niobate of composition $Na_{1-x}NbO_{3-x/2}$.

Figure 2 demonstrates the temperature dependences of $\varepsilon/\varepsilon_0$ for a number of compositions. As x increases, so does the Curie temperature (T_C) (which is in agreement with data of [10]), approaching the temperature of transition (520°C) to the phase $T1$ [18], where the displacements of Nb^{5+} are entirely absent. The peak of $\varepsilon/\varepsilon_0$ diffuses, and its value decreases. The shape of the dependence $\varepsilon/\varepsilon_0(T)$ at $x = 0.15$ is close to the theoretical dependence of the permittivity for the nonferroelectric phase transition. Therefore, in the phenomenological description of SN with high nonstoichiometry, there is no need to consider the FE instability, which is typical of stoichiometric SN and compositions with $x < 0.15$. Thus, Na vacancies stabilize the AFE phase in SN,

which is consistent with the results of [19], where it was found by the electron microscopy method that the AFE state in SN monocrystals is observed mainly in the regions with Na deficiency.

The stabilization of the Na-deficient AFE phase is also supported by the following fact. For all the compositions studied, T_C decreases under the action of the external electric field, as in antiferroelectrics (Fig. 3). Starting from $x = 0.06$, the shift of T_C remains unchanged, about 6 K per 1 kV/cm. The minimum of ΔT_C at $x = 0.04$ is related, as before, to the transition $R(M4) \longrightarrow R(M4 + M2)$.

Throughout the range of x, SN takes on the piezoelectric properties after polarization. Figure 4 exhibits the dependences $d_{33}^{\text{qu.stat}}(T)$ for the stoichiometric and nonstoichiometric SN with the characteristic (for each of the compositions) "breakage" of the piezoelectric activity at the temperature T_{br}, which is 70–190°C lower than T_C. The nonmonotonic variations of T_{br}, $d_{33_{T_{\text{br}}}}^{\text{qu.stat}}$ corresponding to this temperature, and $d_{33_k}^{\text{qu.stat}}$ at room temperature with the deep minimum at $x = 0.04$ and minima near $x = 0.12$ and 0.14 (Fig. 5), reflect, as indicated above, the change in the multiplicity of the M subcell of the compound, as well as the transition (at $x = 0.10$) from the one- to the two-phase state. The fact that T_{br}, $d_{33_{T_{\text{br}}}}^{\text{qu.stat}}$, and $d_{33_K}^{\text{qu.stat}}$ for $x \neq 0$ are smaller than for the stoichiometric SN and decrease as x increases testifies that the FE phase in SN loses stability as the nonstoichiometry in terms of Na_2O arises. The experimental results obtained should be taken into account in producing SN-based piezoelectric ferroelectrics.

CONCLUSIONS

(1) The homogeneity range for sodium niobate of composition $Na_{1-x}NbO_{3-x/2}$ extends to $x = 0.10$. With a further increase in x, the material becomes two-phase.

(2) Within the homogeneity region (at $x = 0.04$), the multiplicity of the monoclinic subcell of the rhombic unit cell changes: $R(M4) \longrightarrow R(M4 + M2)$, which is accompanied by the anomalies in the structural and electrophysical characteristics.

(3) The antiferroelectric phase becomes more stable, while the ferroelectric phase loses stability, as the nonstoichiometry (x) increases.

(4) The experimental results obtained should be taken into account in producing sodium niobate-based piezoelectric ferroelectrics.

ACKNOWLEDGMENTS

This work was supported in part by the Russian Foundation for Basic Research (grant no. 99-02-17575).

REFERENCES

1. A. V. Voloshin, *Tantalum Niobate: Systematization, Crystal Chemistry, and Evolution of Mineral Formation in Granite Pegmatites* (Nauka, St. Petersburg, 1993).
2. H. D. Megaw, Ferroelectrics **7**, 87 (1974).
3. V. P. Sakhnenko, N. V. Dergunova, and L. A. Reznichenko, *Energy Crystal Chemistry of Solid Solutions of Octahedral Oxygen Compounds and Simulation of Piezoelectric Ceramics* (RGPU, Rostov-on-Don, 1999).
4. B. Jaffe, W. R. Cook, and H. Jaffe, *Piezoelectric Ceramics* (Academic, New York, 1971; Mir, Moscow, 1974).
5. Y. Bouilland, Soc. Chim. Fr., Bull., No. 1, 112 (1968).
6. Y. Bouilland, Bull. Soc. Fr. Mineral. Cristallogr. **92** (4), 347 (1969).
7. Z. I. Shapiro, V. K. Trunov, and V. V. Shishov, *Production and Physicochemical Properties of Lithium and Sodium Metaniobates* (NIITÉKhIM, Moscow, 1978).
8. M. Cosec and D. Kolar, Mater. Res. Bull. **10**, 335 (1975).
9. G. D. Yanson, I. S. Ziemele, and I. A. Gorbacheva, *Inorganic Glasses, Coatings, and Materials* (Zinatne, Riga, 1973), Vol. 1, pp. 214–219.
10. S. O. Lisitsyna, I. P. Raevskiĭ, L. A. Reznichenko, *et al.*, Izv. Akad. Nauk SSSR, Neorg. Mater. **21**, 997 (1985).
11. E. M. Kuznetsova, L. A. Reznichenko, A. V. Turik, *et al.*, in *Proceedings of the 2nd Rostov International Workshop on High-Temperature Superconductivity (IMHTS-2R), Rostov-on-Don, 2000*, p. 121.
12. R. H. Dungan and R. D. Golding, J. Am. Ceram. Soc. **47** (2), 73 (1964).
13. I. V. Pozdnyakova, L. A. Reznichenko, and V. G. Gavrilyachenko, Pis'ma Zh. Tekh. Fiz. **25** (18), 81 (1999) [Tech. Phys. Lett. **25**, 752 (1999)].
14. L. A. Reznichenko, L. A. Shilkina, S. V. Titov, *et al.*, in *Proceedings of the International Symposium "Orderings in Minerals and Alloys" (OMA-2000), Rostov-on-Don, 2000*, p. 111.
15. C. N. R. Rao and J. Gopalakrishnan, *New Directions in Solid State Chemistry* (Cambridge Univ. Press, Cambridge, 1986; Nauka, Novosibirsk, 1990).
16. A. G. Petrenko and V. V. Prisedskiĭ, *Structure Defects in Ferroelectrics* (UMK, Kiev, 1989).
17. E. G. Fesenko, *Perovskite Family and Ferroelectricity* (Atomizdat, Moscow, 1972).
18. A. M. Glazer and H. D. Megaw, Acta Crystallogr. A **29**, 489 (1973).
19. J. Chen and D. Feng, Phys. Status Solidi A **109**, 171 (1988).

Translated by M. Lebedev

Technical Physics, Vol. 47, No. 3, 2002, pp. 330–334. Translated from Zhurnal Tekhnicheskoĭ Fiziki, Vol. 72, No. 3, 2002, pp. 48–52.

RADIOPHYSICS

The Ultimate Sensitivity of a High-Temperature Microwave SQUID Magnetometer Operating in the Hysteresis Regime

O. G. Vendik* and I. S. Danilov**

** St. Petersburg State Electrotechnical University, ul. prof. Popova 5, St. Petersburg, 197376 Russia*

*** Universitaet Karlsruhe, Institut fuer Elektrotechnische Grundlagen der Informatik, 76187 Karlsruhe, Germany*

Received April 25, 2001

Abstract—A method for the determination of the noise spectral density in a high-temperature microwave SQUID operating in the hysteresis regime is developed. Under these conditions, the reflection coefficient serves as an output signal. It is shown that if a directional coupler used for extracting the reflected wave is placed as close to the SQUID loop as possible, the magnetometer can be designed as a microwave integrated circuit with a noise flux spectral density $S_\Phi^{1/2} < 10^{-5}\Phi_0/\text{Hz}^{0.5}$, where Φ_0 is the magnetic flux quantum. © *2002 MAIK "Nauka/Interperiodica".*

INTRODUCTION

The ultimate sensitivity of microwave SQUID-based measuring systems depends on the noise level. In SQUIDs, by noise we mean random oscillations of the magnetic flux. The theory of noise for a single-contact low-temperature SQUID, i.e., for a SQUID operating at liquid-helium temperature (T = 4.2 K) in the hysteresis regime, has been described in detail in [1, 2]. At low temperatures, it is customary to consider noise as the sum of the SQUID noise itself and the noise of the measuring system (preamplifier, oscillator, or feeders). The noise of the preamplifier at room temperature dominates in the low-temperature measuring systems [1–8].

The theory of a single-contact SQUID predicts that as the pumping frequency increases up to the critical frequency f_C of a Josephson junction, the noise level of the measuring system decreases. This has stimulated the advance to microwave pumping frequencies. Unfortunately, for microwave SQUIDs operating in the hysteresis regime, unlike the anhysteretic one [9, 10], a model for noise spectral density has not been developed by now. In the literature, it is "carefully" suggested to evaluate the noise level of a high-temperature superconducting (HTSC) single-contact microwave SQUID by extrapolating the theoretical results for a low-temperature SQUID to the HTSC range [8]. The recommendation is based on the assumption that the ratio between the noise from internal and external sources (the latter is, e.g., the preamplifier noise at room temperature), 1 : 20 at T = 4.2 K, does not change substantially in passing to the high-temperature range (T = 78 K). Such an assumption may be valid for SQUID magnetometers shown in Fig. 1a. Typically, these circuits include a *Y*-circulator, separating the incident and reflected waves. Even in the case of elaborate screening, the circulator should remote from the SQUID loop, because it generates stray magnetic fields. This leads, however, to an increase in the length of feed lines and, accordingly, their contribution to the noise [11–14].

In the microwave HTSC SQUID layout illustrated in Fig. 1b, the SQUID loop impedance is matched with external circuits using, for example, a slot-line-based quadripole [15, 16]. To separate the incident and reflected waves, one can use a directional coupler with isolated arms I–II and I–III that is arranged as close to the SQUID loop as possible. In this case, the device layout will differ from the traditional one. Moreover, if the first cascade of the low-noise amplifier is placed near the directional coupler, the contributions of each of the noise sources become of the same order of magnitude. Therefore, a model allowing more accurate calculations of the HTSC SQUID magnetometer ultimate sensitivity in the hysteresis regime has to be developed.

INTRINSIC NOISE OF THE MEASURING SYSTEM

Noise is characterized by the noise flux Φ_N, which can be described by statistical methods due to its random nature. An estimate of the least possible noise factor in device and ways of decreasing it are of practical importance. The noise factor is defined as

$$N = \frac{\langle \Phi^2 \rangle + \langle \Phi_N^2 \rangle}{\langle \Phi^2 \rangle}, \quad (1)$$

1063-7842/03/4702-0330$22.00

where $\langle\Phi^2\rangle$ is the averaged value of the squares of the magnetic flux measured and $\langle\Phi_N^2\rangle$ is the averaged value of the squares of the noise flux.

Two components of the total noise flux can be distinguished. The first component is caused by external noise sources; the other, by intrinsic sources of the measuring system. Below, we will consider the second component, i.e., the noise of the measuring system. The external sources are omitted, since they are effectively removed by properly screening the measuring channel and the residual noise (if any) characterizes the screen quality rather than the system noise. Note that in the literature, the oscillator and the amplifier are usually referred to as "external" noise sources. However, hereafter we are dealing with the noise of the measuring system and all its components are viewed as intrinsic noise sources.

Let us consider the microwave SQUID circuit shown in Fig. 1b more fully. Here, the elements (SQUID loops, matching quadripole, and the first amplifier cascade) are arranged very closely. This is achieved by using the directional coupler with the isolated arms I–II and I–III, instead of the circulator, to separate the incident and reflected waves, as well as by placing the first amplifier cascade (transistor) on the same substrate. For such a modification of the magnetometer, the model for noise calculation based on the approach described in [1–5] is given below.

The total noise Φ_N in the system is generated by different sources: (1) Josephson junction, (2) matching circuit (resonant circuit in the case of an rf SQUID), (3) conductors (waveguides and feeders) connecting the SQUID with the measuring equipment kept at room temperature, (4) preamplifier, (5) oscillator, (6) feedback loop [5], and (7) magnetometer case.

Assuming that all the noise sources are independent and the superposition condition is fulfilled, the averaged square of the noise flux is given by

$$\langle\Phi_N^2\rangle = \langle\Phi_{N1}^2\rangle + \langle\Phi_{N2}^2\rangle + \ldots + \langle\Phi_{Ni}^2\rangle, \qquad (2)$$

while the averaged product $\langle\Phi_{Ni}\Phi_{Nj}\rangle = 0$ for $i \neq j$. This assumption is not quite rigorous, because the superconducting ring influences the resonant circuit noises; however, the corresponding corrections can be neglected [17–19]. Therefore, first, the average square of the noise flux $\langle\Phi_N^2\rangle$ adjusted to the system input is determined for each of the sources and then the results are summed. Every partial contribution is calculated as the effective noise flux passing through the hole of the superconducting ring. Hence, a comparison between the total contribution from all the sources and the external magnetic flux Φ becomes possible.

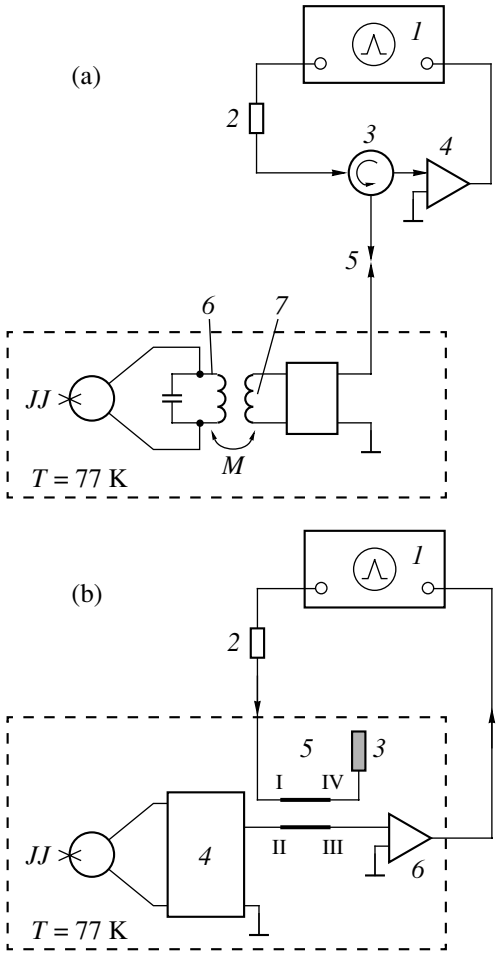

Fig. 1. Designs of microwave magnetometers. (a) Conventional design using a *Y* circulator: *1*, analyzer; *2*, attenuator; *3*, *Y* circulator; *4*, LNA; *5*, 50-Ω cable; *6*, resonance circuit; and *7*, pickup coil. (b) Planar design with a directional coupler placed close to the SQUID loop: *1*, analyzer; *2*, attenuator; *3*, matched load; *4*, matching quadripole; *5*, directional coupler; and *6*, LNA.

The results of simulation are conveniently represented in terms of the flux fluctuation spectral density for each of the sources:

$$S_{\Phi_i} = \frac{\langle\Phi_N^2\rangle}{\Delta f}, \qquad (3)$$

where Δf is the passband of the output filter.

The noise in the system can thus be expressed as the average square of the noise flux per unit frequency bandwidth:

$$S_{\Phi N} = (S_{\Phi 1} + S_{\Phi 2} + S_{\Phi 3} + \ldots). \qquad (4)$$

In the literature, it is the practice to express the final (numerical) result for the noise spectral density through $S_{\Phi N}^{1/2}/\Phi_0$, which gives a clear estimate in units of magnetic flux quantum.

NOISE IN MICROWAVE SQUIDs

In this section, we present an analytical description of noise in the measuring system of a microwave SQUID. The noise flux spectral density $S_{\Phi N}^{1/2}$ is expressed through typical parameters of a microwave circuit, such as reflection coefficient, transmission coefficient, etc. Let us consider each of the components of the noise spectrum separately. In the magnetometer circuit shown in Fig. 1, four noise sources can be distinguished: (1) SQUID loop closed by the Josephson contact, (2) amplifier, (3) feed lines, and (4) oscillator.[1] The feedback loop is not shown in Fig. 1, but its contribution can be assumed to be equal to that from the feed lines because the loop and the lines are traced in a similar way. Therefore, when calculating the noise in the circuit with a feedback loop, one must double the noise value due to the feed lines in the expression for the noise spectral density. It is also significant that we discuss thermal noise, i.e., that generated by temperature oscillations. For the amplifier, where the noise is caused by nonthermal effects, we introduce the notion of effective noise temperature T_N^{AMP} with the analytic approach remaining the same.

NOISE OF A JOSEPHSON JUNCTION

An expression for the noise flux of a Josephson junction can be found based on the uniform energy distribution over degrees of freedom. If the magnetic flux energy stored in the ring is equal to the thermal excitation energy, the average energy is

$$\frac{\Phi^2}{2L_S} = \frac{k_B T}{2}, \tag{5}$$

where k_B is the Boltzmann constant, $T = 78$ K, L_S is the SQUID loop inductance, and Φ is the total magnetic flux encircled by the SQUID loop.

From Eq. (5), the magnetic flux is

$$\Phi = k_B T L_S. \tag{6}$$

For unitary sampling, the magnetic flux Φ is a random quantity from the infinite statistical ensemble. Hence, to obtain a truer value, the sampling time, i.e., the time of measurement, should be more than the microwave oscillation period. If this condition is fulfilled, the spread of the random magnetic flux values $\Delta\Phi$, or, in essence, the magnetic flux noise in a band Δf, is given by

$$\Delta\Phi^2 = k_B T L_S \left(\frac{\omega_0}{2\pi\Delta f}\right)^{-1}, \tag{7}$$

where $(\omega_0/2\pi\Delta f)^{-1}$ is the number of samples for a time $\tau = 1/\Delta f$.

Dividing Eq. (7) by Δf, we obtain the expression for the spectral density of the Josephson contact noise flux:

$$S_{\Phi,1}^{1/2} = \left(k_B T L_S \frac{1}{f_0}\right)^{1/2}. \tag{8}$$

For rf SQUIDs, formulas for the spectral density of the Josephson contact noise can be found in the literature, e.g., in [8, 19]. However, Eq. (8) is based on the simple assumptions; has the simpler form; and, which is more important, gives a good fit to the experimental data for the rf range.

NOISE OF THE AMPLIFIER AND FEED LINES

At the early stage, the noise spectral densities of the amplifier, $S_{\Phi,2}^{1/2}$, and feed lines, $S_{\Phi,3}^{1/2}$, were calculated. The calculation procedure was as follows. First, the average microwave pump power reflected by the SQUID loop was determined. Then, a relationship for the noise fluxes caused by the above-mentioned sources was found. Further, using the Nyquist theorem, we obtained expressions for the noise power of the amplifier and feed lines. Finally, these expressions were converted to those for the noise spectral density. Let us start with the expression for the maximum pump (input) power incident on the SQUID loop:

$$P_{in} = \frac{1}{2} R_M I_C^2. \tag{9}$$

Here, I_C is the critical current of the Josephson contact, R_M is the sum of the contact-shunting impedance R_{SH} and the real component of the Josephson contact impedance at a fixed basic SQUID parameter β_L and a dc magnetic flux $\Phi_{x,DC}$ that is a multiple of half the magnetic flux quantum.

The microwave power reflected by the Josephson contact depends on the reflection coefficient, which, in its turn, depends on the magnetic flux $\Phi_{x,DC}$ by a sawtooth law:

$$P_{refl}(\Phi_{x,DC}) = P_{in}\left|\Gamma(\Phi_{x,DC})\right|^2. \tag{10}$$

In terms of the normalized values ($x = 2\Phi_{x,DC}/\Phi_0$), Eq. (10) in the range $0 \le x \le 1$ can be written as

$$P_{refl}(x) = P_{in}\left|\Gamma_{max}(1-x)^2\right|, \tag{11}$$

where Γ_{max} is the maximum value of the reflection coefficient.

To find the average power reflected by the SQUID loop, it is necessary to integrate the left-hand part of Eq. (11) over x in the range considered and to take into

[1] The preliminary calculation for the case noise showed that the noise flux is $\Phi_N = 0.02\Phi_0$ at a case perimeter of 8 cm and a wall thickness of 0.5 cm. In this situation, the effective noise flux adjusted to the SQUID loop input is negligibly small in comparison with the other sources, since it depends on the ratio between the SQUID loop area and the area outlined by the case. As a result, we obtain for the effective case noise flux $\Phi_N \le 10^{-8}\Phi_0$.

account the transmission coefficient of the line:

$$\langle P_{\text{refl}}\rangle = P_{\text{in}}\Gamma_{\max}\eta\int_0^1 (1-x)^2 dx. \quad (12)$$

Here, η is the fractional transmission coefficient:

$$\eta = \frac{1}{\exp(2\alpha l)}, \quad (13)$$

where l is the length of the lines, i.e., the distance between the SQUID loop and the preamplifier, and α is the damping coefficient of the lines that depends on the pumping frequency.

From the microwave SQUID designs shown in Fig. 1, it is obvious that the transmission coefficient is higher in the second modification (Fig. 1b). Equations (10) and (12) imply that

$$\langle P_{\text{refl}}\rangle = \frac{1}{6}R_M I_C^2 |\Gamma_{\max}|^2\eta. \quad (14)$$

Let us write the expression relating the noise power P_N and the noise magnetic flux Φ_N through the average reflected power. This relation has the quadratic form

$$\frac{P_N}{\langle P_{\text{refl}}\rangle} = \left(\frac{\Phi_N}{\langle \Phi_{x,\text{DC}}\rangle}\right)^2, \quad (15)$$

where $\langle\Phi_{x,\text{DC}}\rangle = \Phi_0/4$ is the average signal flux in the range $\Phi_{x,\text{DC}} = 0 \ldots \Phi_0/2$.

The noise flux can be expressed from Eq. (15) as

$$\Phi_N^2 = \left(\frac{\Phi_0}{4}\right)^2 \frac{P_N}{\langle P_{\text{refl}}\rangle}. \quad (16)$$

The only unknown in Eq. (16) is the combined noise power P_N of the amplifier and the feed lines. The value of P_N was sought with the Nyquist theorem, which states that the mean square of the noise voltage for a resistance R at a temperature T is given by the expression

$$\langle U_N^2\rangle = 4k_B TR\Delta f. \quad (17)$$

From Eq. (17), we can obtain the expression for the power of the sought noise:

$$P_N^{\text{AMP}} = 4k_B T_N^{\text{AMP}}\Delta f, \quad (18)$$

$$P_N^{\text{LINE}} = 4k_B T(1-\eta)\Delta f, \quad (19)$$

where P_N^{AMP} and P_N^{LINE} are the noise powers of the amplifier and the lines, respectively, and T_N^{AMP} is the noise temperature of the amplifier.

According to Eqs. (16), (18), and (19), we have

$$\Phi_{N,2}^2 = \left(\frac{\Phi_0}{4}\right)^2 \frac{4k_B T_N^{\text{AMP}}\Delta f}{\langle P_{\text{refl}}\rangle}, \quad (20)$$

$$\Phi_{N,3}^2 = \left(\frac{\Phi_0}{4}\right)^2 \frac{4k_B T(1-\eta)\Delta f}{\langle P_{\text{refl}}\rangle}. \quad (21)$$

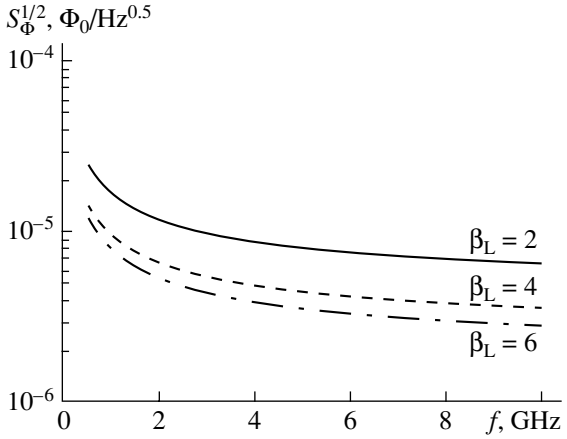

Fig. 2. Frequency dependences of the spectral density $S_\Phi^{1/2}$ of the noise flux for different values of the main SQUID parameter β_L at f_0 = 3 GHz, J_C = 5 μA, R_{SH} = 5 Ω, and L_S = 200 pH.

To obtain the final equation for the spectral density of the noise flux, both parts of Eqs. (20) and (21) should be divided by Δf:

$$S_{\Phi,2}^{1/2} = \frac{\Phi_0}{4}\left[\frac{4k_B T_N^{\text{AMP}}}{R_M I_C^2|\Gamma_{\max}|^2\eta/6}\right]^{1/2}, \quad (22)$$

$$S_{\Phi,3}^{1/2} = \frac{\Phi_0}{4}\left[\frac{4k_B T(1-\eta)}{R_M I_C^2|\Gamma_{\max}|^2\eta/6}\right]^{1/2}. \quad (23)$$

NOISE OF THE MICROWAVE OSCILLATOR

Microwave power sources should obey several general rules: the Q factor of the oscillator must be as high as possible, the power generated must be low, and the coupling with the oscillator must be weak [19]. If these requirements are fulfilled, the attainable values of the effective Q factor, which determines the signal-to-noise ratio, are more than 10^{12} for crystal oscillators and 10^{10} for LC oscillators [19]. The spectral density of the oscillator is given by

$$S_{P,\text{LO}}(\omega) = \frac{P_0}{\pi}\frac{\omega_0/Q}{(\omega_0/Q)^2 + (\omega-\omega_0)^2}, \quad (24)$$

where P_0 is the operating power of the oscillator.

The spectral power density at frequencies other than the resonant one is given by the expression

$$S_{P,\text{LO}}(\omega_0+\Omega) = \frac{P_0}{\pi}\frac{\omega_0/Q}{(\omega_0/Q)^2 + \Omega^2}, \quad (25)$$

where Ω is the modulation frequency.

In Eq. (25), the term $(\omega_0/Q)^2$ is a second-order infinitesimal if $\Delta\omega/\omega \approx 12/Q$ and $\Omega = 2\pi F_0$, where F_0 =

Table

$S_{\Phi,1}$, $\Phi_0/\mathrm{Hz}^{0.5}$	$S_{\Phi,2}$, $\Phi_0/\mathrm{Hz}^{0.5}$	$S_{\Phi,3}$, $\Phi_0/\mathrm{Hz}^{0.5}$	$S_{\Phi,4}$, $\Phi_0/\mathrm{Hz}^{0.5}$	$S_\Phi^{1/2}$, $\Phi_0/\mathrm{Hz}^{0.5}$
4.1×10^{-6}	5.6×10^{-6}	1.7×10^{-6}	3.8×10^{-6}	8.1×10^{-6}

100 kHz (which is valid for modern crystal oscillators). With regard for this, Eq. (25) takes the form

$$S_{\mathrm{P,LO}}(\omega_0 + \Omega) = \frac{P_0}{\pi}\frac{\omega_0}{Q\Omega^2}. \quad (26)$$

We should transform Eq. (26) to the general form, i.e., express the spectral density of the noise flux:

$$S_{\Phi,4}^{1/2} = \frac{\Phi_0}{4}\left[\frac{S_{\mathrm{P,N}}}{P_{\mathrm{in}}|\Gamma_{\max}|^2\eta/3}\right]^{1/2}. \quad (27)$$

Eventually, for the spectral density of the oscillator noise flux, we have

$$S_{\Phi,4}^{1/2} = \frac{\Phi_0}{4}\left[\frac{\omega_0}{Q\Omega^2}\frac{3}{\pi|\Gamma_{\max}|^2\eta}\right]^{1/2}. \quad (28)$$

Thus, we have found the equations for the spectral density of the noise flux for all the four noise sources.

To represent the final expression in the generally accepted form, it is necessary to sum the squares of Eqs. (8), (22), (23), and (28), take the root of this sum, and divide the result by the magnetic field quantum. Ultimately, for the spectral noise density expressed in units of magnetic flux quantum, we obtain

$$S_{\Phi,\mathrm{N}}^{1/2} = \left[\frac{k_\mathrm{B}TL_\mathrm{S}}{f\Phi_0^2} + \frac{3}{2}\frac{k_\mathrm{B}(T_\mathrm{N}^{\mathrm{AMP}} + T(1-\eta))}{R_M I_\mathrm{C}^2|\Gamma_{\max}|^2\eta} + \frac{3}{8}\frac{f}{Q\Omega^2|\Gamma_{\max}|^2\eta}\right]^{1/2}. \quad (29)$$

For typical parameters of the measuring system based on a high-temperature microwave SQUID, $S_\Phi^{1/2}$ as a function of f is shown in Fig. 2. Data for the center frequency $f_0 = 3$ GHz are given in the table.

CONCLUSION

The calculations of the spectral density of the noise flux for each of the sources showed the following. For the planar magnetometer design, where the losses due to long feed lines are absent and the preamplifier and the matching quadripole are integrated into one chip, the partial noise contributions are comparable by order of magnitude. This allows us to refine the ultimate sensitivity of the integrated systems by extrapolating theoretical results for low-temperature SQUIDs to the high-temperature range.

According to our method, the spectral noise density of a SQUID-based microwave measuring system decreases as the pumping frequency increases, which is well corroborated by the experimental data. The model is valid in the frequency range down to the critical frequency of the Josephson junction.

ACKNOWLEDGMENTS

We are grateful to prof. V. Yuttsi for the support.

REFERENCES

1. J. Kurkijarvi, Phys. Rev. B **6**, 832 (1972).
2. J. Kurkijarvi, J. Appl. Phys. **44**, 3729 (1973).
3. G. J. Ehnholm, J. K. Soini, and T. Wiik, J. Low Temp. Phys. **4**, 234 (1977).
4. J. N. Hollenhorst and R. P. Giffard, IEEE Trans. Magn. **15**, 474 (1978).
5. T. Ryhanen, H. Seppa, R. Ilmoniemi, and J. Knuutila, J. Low Temp. Phys. **6**, 87 (1989).
6. L. D. Jackel and R. A. Buhrman, J. Low Temp. Phys. **19**, 201 (1975).
7. R. P. Giffard, R. A. Webb, and J. C. Wheatly, J. Low Temp. Phys. **6**, 533 (1972).
8. D. Koelle, R. Kleiner, F. Ludwig, *et al.*, Rev. Mod. Phys. **71**, 631 (1999).
9. B. Chesca, J. Low Temp. Phys. **110**, 963 (1998).
10. B. Chesca, J. Low Temp. Phys. **112**, 165 (1998).
11. Y. Zhang, M. Muck, K. Hermann, *et al.*, Appl. Phys. Lett. **60**, 645 (1992).
12. Y. Zhang, U. Kriiger, R. Kutzen, *et al.*, Appl. Phys. Lett. **65**, 3380 (1994).
13. Y. Zhang, M. Muck, M. Bode, *et al.*, Appl. Phys. Lett. **60**, 2303 (1992).
14. K. K. Likharev, V. K. Kornev, and O. V. Snigirev, Radiotekh. Éektron. (Moscow) **26**, 2647 (1980).
15. O. G. Vendik and I. S. Danilov, Zh. Tekh. Fiz. **69** (11), 106 (1999) [Tech. Phys. **44**, 1360 (1999)].
16. O. G. Vendik, I. S. Danilov, and S. P. Zubko, Zh. Tekh. Fiz. **67** (9), 94 (1997) [Tech. Phys. **42**, 1068 (1997)].
17. A. V. Sutormin and I. S. Danilov, in *Proceedings of the 6th International Student Seminar on High Temperature Superconductors (HTS) at Microwaves, Oulu, Finland, 1999*, p. 17.
18. J. E. Carroll, *Hot-Electron Microwave Oscillators* (Arnold, London, 1970; Mir, Moscow, 1972).
19. O. Lounasmaa, *Experimental Principles and Methods Below 1 K* (Academic, London, 1974; Mir, Moscow, 1977).

Translated by M. Astrov

Technical Physics, Vol. 47, No. 3, 2002, pp. 335–342. Translated from Zhurnal Tekhnicheskoĭ Fiziki, Vol. 72, No. 3, 2002, pp. 53–60.

RADIOPHYSICS

Generation of Subnanosecond Microwave Pulses Based on the Cherenkov Superradiance Effect

N. S. Ginzburg*, I. V. Zotova*, A. S. Sergeev*, R. M. Rozental'*, V. G. Shpak, M. I. Yalandin**, A. D. R. Felps***, and A. V. Cross*****

** Institute of Applied Physics, Russian Academy of Sciences, ul. Ul'yanova 46, Nizhni Novgorod, 603600 Russia*

e-mail: ginzburg@appl.sci-nnov.ru

*** Institute of Electrophysics, Ural Division, Russian Academy of Sciences, Komsomol'skaya ul. 34, Yekaterinburg, 620049 Russia*

**** Strathclyde University, Glasgow, G4 0NG, United Kingdom*

Received July 18, 2001

Abstract—Experimentally observed Cherenkov superradiance produced by a subnanosecond electron bunch traveling through a partially filled waveguide is reported. 400-ps microwave pulses with a peak power of 2 MW are obtained. The experimental results are in good agreement with the theoretical analysis and numerical simulations performed with the help of the PIC code KARAT. *© 2002 MAIK "Nauka/Interperiodica".*

INTRODUCTION

Recently, considerable attention has been focused on the possibility of generating ultrashort electromagnetic pulses using the effect of superradiance of spatially localized 5- to 10-wavelength-long electron bunches [1–11]. The bunch as a whole can generate intense coherent radiation only if the process of bunching is completed. In extended electron bunches, the bunching mechanisms are similar to those observed in continuous flows. Nevertheless, the stimulated radiation of extended electron bunches has certain features associated primarily with energy withdrawal from the bunch. The result is the intrinsically pulsed nature of the radiation. Moreover, the radiation is coherent and its peak power is proportional to the number of particles in the bunch squared.

Naturally, the superradiance of classical electron ensembles can be associated with different elementary induced radiation mechanisms (bremsstrahlung, cyclotron radiation, Cherenkov radiation, etc.). To date, pioneering experiments on superradiance in electron bunches have been carried out [7–11]. Electromagnetic pulses with a peak power of up to 150 MW and as short as ~300 ps were generated at 39 GHz using an electron bunch moving along a rectilinear path in a slow-wave structure (the Cherenkov mechanism) [10, 11]. In this case, the radiation was produced by synchronous interaction between the particles and a slow electromagnetic wave traveling in the opposite direction. Cherenkov superradiance can also be produced by interaction with the wave traveling in the same direction, for example, when the electrons move rectilinearly in a waveguide partially filled with a dielectric.

This paper reports the theoretical and experimental study of Cherenkov superradiance in such systems. Section 1 analyzes the superradiance in terms of the averaged equations for the slowly varying amplitude of the wave. In Section 2, Cherenkov superradiance is simulated with the PIC code KARAT, which directly (without averaging) integrates the Maxwell equations combined with the equations of electron motion with allowance for the real geometry of the partially filled waveguide, the effect of space charge, dispersion, etc. In Section 3, we discuss early experiments on Cherenkov superradiance that have been performed on the RADAN subnanosecond accelerator. In these experiments, 400- to 500-ps-long microwave pulses with a peak power of 1–2 MW were generated.

1. ANALYSIS OF CHERENKOV SUPERRADIANCE BASED ON THE EQUATIONS FOR THE SLOWLY VARYING AMPLITUDE OF THE WAVE

In a partially filled waveguide (Fig. 1), electrons interact with the wave if the Cherenkov synchronism condition is met:

$$\omega = hV_{\parallel}, \tag{1}$$

where $V_{\parallel} = \beta_0 c$ is the undisturbed translational velocity of the electrons and h is the longitudinal wave number.

Figure 2 shows the dispersion diagram corresponding to the partially filled waveguide excited by the electron bunch of the TM_{01} mode. The dispersion relation

1063-7842/03/4702-0335$22.00 © 2002 MAIK "Nauka/Interperiodica"

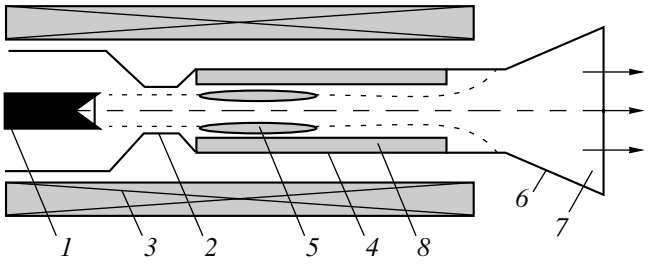

Fig. 1. Layout of the Cherenkov superradiance experiment: *1*, cathode; *2*, anode; *3*, solenoid; *4*, drift chamber; *5*, electron bunch; *6*, horn antenna; *7*, output aperture; and *8*, dielectric insert.

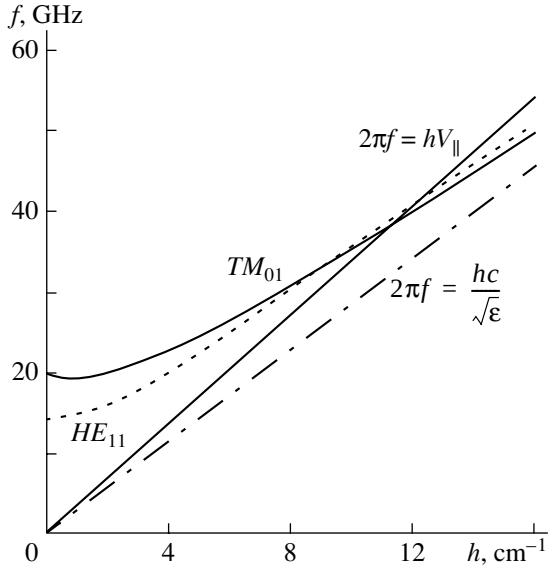

Fig. 2. Dispersion diagram for the TM_{01} and HE_{11} modes excited by the electron bunch in the partially filled waveguide.

for this mode can be written as

$$\frac{I_1(p(R-a))}{pI_0(p(R-a))} - \frac{\varepsilon}{g} \times \frac{N_0(gR)J_1(g(R-a)) - N_1(g(R-a))J_0(gR)}{J_0(g(R-a))N_0(gR) - N_0(g(R-a))J_0(gR)} = 0, \quad (2)$$

where R is the radius of the waveguide; a and ε are the thickness and permittivity of the dielectric insert; $g = \sqrt{k^2\varepsilon - h^2}$ and $p = \sqrt{h^2 - k^2}$ are the transverse wave numbers for the dielectric and free space, respectively; $k = \omega/c$; J_n is the Bessel function; N_n is the Neumann function; and I_n is the modified Bessel function.

Let us represent the field excited in the waveguide by an electron bunch following a rectilinear trajectory as

$$E_z = \mathrm{Re}\{E_z^s(\mathbf{r}_\perp)A(z,t)\}\exp[i\omega t - ihz],$$

where the function $E_z^s(\mathbf{r}_\perp)$ describes the transverse field distribution specified by the waveguide mode, ω is the carrier frequency corresponding to exact synchronism, and $A(z, t)$ is the slowly varying amplitude.

Using

$$Z = C\frac{\omega}{c}z, \quad \zeta = C\frac{\omega}{c}\left(t - \frac{Z}{V_\parallel}\right)\left(\frac{1}{V_{gr}} - \frac{1}{V_\parallel}\right)^{-1},$$

where V_{gr} is the group velocity of the wave, as independent variables, the stimulated radiation of an individual electron bunch can be described by the system of equations

$$\left[\frac{\partial}{\partial Z} + \frac{\partial}{\partial \zeta}\right]a = iJf(\zeta), \quad \frac{\partial^2\Theta}{\partial Z^2} = \mathrm{Im}(ae^{i\Theta}) \quad (3)$$

with the initial and boundary conditions

$$a|_{\zeta=0} = 0, \quad \Theta|_{Z=0} = \Theta_0 + r\cos\Theta_0,$$

$$\left.\frac{\partial\Theta}{\partial Z}\right|_{Z=0} = 0, \quad \Theta_0 \in [0, 2\pi].$$

Here,

$$J = \frac{1}{\pi}\int_0^{2\pi} e^{-i\Theta}d\Theta_0$$

is the amplitude of the rf electron current, $\Theta = \omega t - hz$ is the phase of the electron relative to the synchronous wave,

$$a = \frac{e}{mc\omega}C^{-2}\gamma_0^{-3}\beta_0^{-3}E_{s_z}(R_0)$$

is the dimensionless amplitude of the wave,

$$C = \left(\frac{1}{(2\pi)^3}\frac{eI}{mc^3}\frac{\lambda^3}{R^3}\frac{p^4R^4I_0^2(pR_0)}{n_s}\right)^{1/3}$$

is the gain parameter, I is the total current, $\lambda = 2\pi c/\omega$, R_0 is the injection radius,

$$n_s = Rhp^2\int_0^{R-a} I_1^2(pr)rdr + \frac{Rh\varepsilon p^4}{g^2}\frac{I_0^2(p(R-a))}{[N_0(gR)J_0(gd) - J_0(gR)N_0(gd)]^2} \times \int_{R-a}^{R}[J_0(gR)N_1(gr) - N_0(gR)J_1(gr)]^2rdr$$

is the norm of the TM_{01} mode, and $f(\zeta)$ is the bunch density distribution in the longitudinal direction. We further assume that the electrons are uniformly distributed

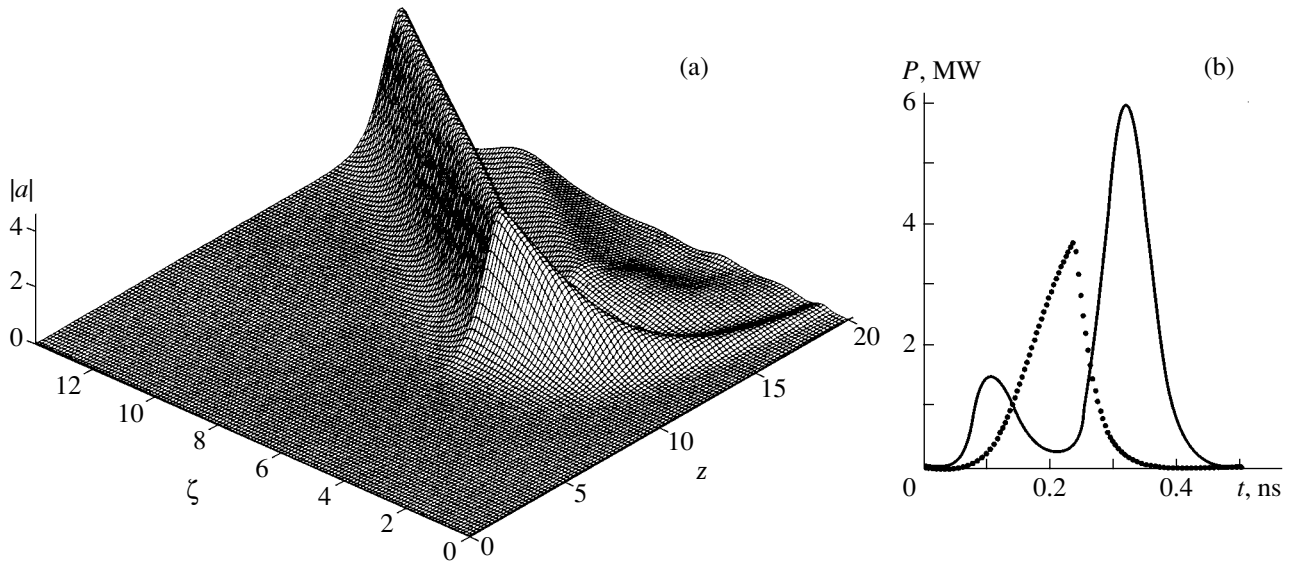

Fig. 3. (a) Evolution of the electromagnetic pulse amplitude distribution and (b) the amplitude of the superradiance pulse at $L = 14$ (solid line) and 11 (dotted line).

within the bunch; i.e., $f(\zeta) = 1$ for $\zeta \in [0, T]$, where

$$T = C\frac{\omega}{c}t_{\text{e.pulse}}\left(\frac{1}{V_{\text{gr}}} - \frac{1}{V_{\parallel}}\right)^{-1} \qquad (4)$$

is the normalized duration of the electron bunch.

The radiated power can be found from the expression

$$P = 2\pi^3\frac{m^2c^5}{e^2}\frac{n_s}{I_0^2(pR_0)}\frac{C^4\gamma^6\beta_0^6}{R\lambda^3p^4}|a|^2\big|_{Z=L}, \qquad (5)$$

where $L = Cl\omega/c$ is the dimensionless length of the interaction space.

Note that system of equations (3) coincides with that describing the superradiance of an electron bunch traveling in the periodic magnetic field of an undulator [1, 2].

System (3) was numerically simulated for the parameters of the electron bunch and slow-wave structure close to those used in the experiment: $R = 0.5$ cm, $R_0 = 0.15$ cm, $\varepsilon = 3$, $a = 0.2$ cm, $I = 200$ A, $\gamma = 1.4$, and $C = 0.057$. We considered the excitation of the TM_{01} mode, for which the group velocity at the resonance frequency 38 GHz is $V_{\text{gr}} = 0.5c$, as follows from the dispersion diagram (Fig. 2). The process was simulated at a normalized bunch duration $T = 6$, which corresponds, with the above parameters, to the ≈250-ps-long plateau of the electron pulse. The initial modulation $r = 0.0005$ was chosen so that the saturation was achieved when the system was longer than 30 cm (for the dimensionless length $L \geq 13$), according to the experimental conditions (Section 3).

Figure 3a shows the space–time distribution of the electric field amplitude, which illustrates the shaping of a short superradiance pulse in a sufficiently long interaction space. The pulse arises because of the grouping of electrons in the bunch and a slip of the wave relative to the electrons. The slip is associated with the difference between the group velocity of the wave and the particle velocity. As a result of the slip, individual portions of the electron bunch are synchronized. Figure 3b shows superradiance pulses for different normalized lengths of the interaction space: $L = 14$ and $L = 11$, which correspond to the nonlinear saturation mode and to the final stage of the linear mode, respectively. The minimum superradiance pulse duration is achieved in the saturation mode and equals ≈250 ps at a peak power of 6 MW. At the shorter length ($L = 11$), which is close to that used in the experiment, the pulse duration is ≈300 ps at a peak power of ≈4 MW.

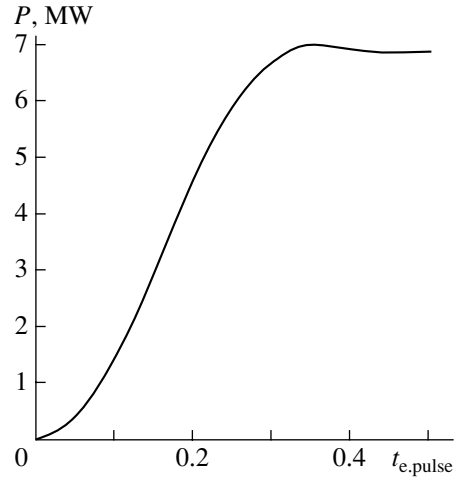

Fig. 4. Peak radiated power versus electron bunch duration.

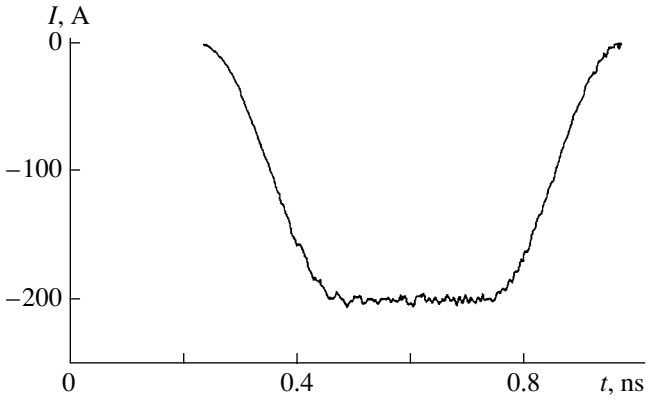

Fig. 5. Current pulse used in the KARAT code simulation.

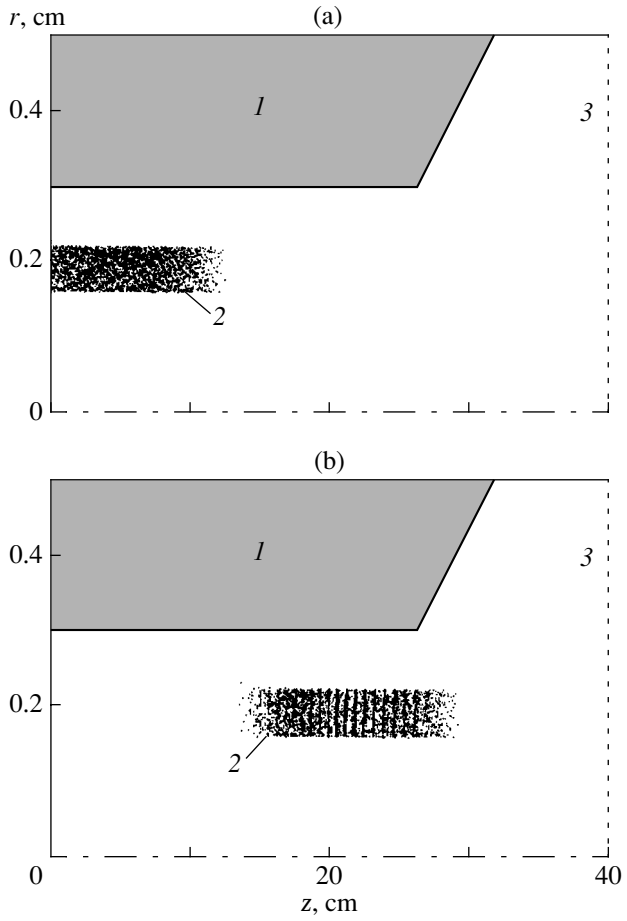

Fig. 6. Geometry of the interaction space and the positions of the electron bunch at time instants t = (a) 0.5 and (b) 1.5 ns. (*1*) Dielectric insert, (*2*) electron bunch, and (*3*) output aperture.

An important property of the superradiance process is the dependence of the peak power on the total number of particles or on the total bunch charge. Figure 4 shows the peak power versus pulse duration at a constant current and $L = 20$ (the saturation mode). As long as the electron pulse duration is shorter than 250 ps, the curve is nearly quadratic. This means that all particles of the bunch emit coherently under these conditions. When the duration of the electron bunch is greater than 300 ps, the peak power saturates, because the electron bunch becomes too long to radiate coherently from the entire volume.

2. SIMULATION OF CHERENKOV SUPERRADIANCE WITH THE KARAT CODE

To more fully cover factors affecting the real experiment, including the of space charge the bunch the dispersion of the electromagnetic pulse, etc., we simulated Cherenkov radiation in a partially filled waveguide, using the 2.5-dimensional version of the KARAT code. In this model, the electron motion is three-dimensional, while the fields are axisymmetric. We assume that an electron bunch with given current and energy of the electrons is injected along a uniform magnetic field directly into the interaction space, i.e., into a cylindrical waveguide with a dielectric insert. The current pulse used in the simulations is shown in Fig. 5. The geometry of the system meets actual experimental conditions and is illustrated in Fig. 6, where the position of the electron bunch at different time instants after the injection is also shown. As a result of the interaction, the initially uniform bunch density becomes strongly modulated, causing the longitudinal momentum modulation of the particles (Fig. 7).

Figure 8a plots the radiated power versus time at an electron energy of 200 keV and a peak current of 200 A. The radiation has the form of a short, ≈300 ps, pulse of peak power ≈2 MW. Note that the period-averaged pulse power is half the instantaneous power shown in Fig. 8a. The spectrum of the radiation (Fig. 8b) is wide. Its relative bandwidth is 15%. The center frequency meets Cherenkov synchronism condition (1) for the TM_{01} mode of the partially filled waveguide (Fig. 2). The transverse field distribution also corresponds to the TM_{01} mode excitation (Fig. 9).

The induced nature of the radiation can be illustrated by the dependence of the peak radiated power on the length of the interaction space (virtually, on the length of the dielectric insert), Fig. 10a. The peak power first exponentially increases and then saturates. The exponential growth of the radiated power with interaction length is associated with particle bunching. It should be noted that if we had dealt with conventional spontaneous radiation due to either density fluctuations in the electron bunch or current fronts, the exponential power versus interaction length dependence would have been absent. Our simulations show that, under the experimental conditions, the induced radiation prevails and the spontaneous radiation acts as a trigger. Depending on the experimental conditions, this trigger can be produced either by particle density fluctuations or by the radiation from the leading edge of the electron bunch.

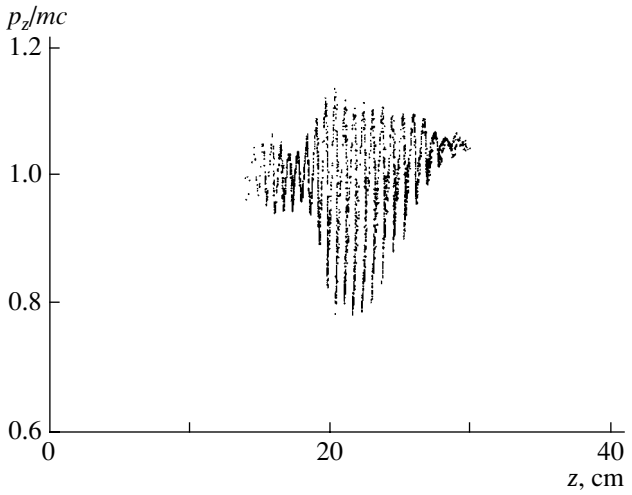

Fig. 7. Phase plane (p_z, z) showing the longitudinal momentum modulation of the electron bunch at t = 1.5 ns.

The simulations with the KARAT code also confirmed the quadratic peak power versus bunch particle number dependence. Here, the duration and the shape of the electron pulse were kept unchanged and the peak power was varied. The length of the dielectric insert was 36 cm, i.e., corresponded to the saturation mode. As follows from Fig. 10b, the peak radiated power is proportional to the number of particles in the bunch squared (i.e., all electrons of the bunch radiate coherently) as long as the peak current is below 100 A. When the current exceeds 100 A, the dependence is nonquadratic and saturates at currents stronger than 200 A. This can be attributed, in particular, to the effect of the space charge, which causes the bunch to diverge and, consequently, increases the dynamic spread in the longitudinal particle velocity.

Similarly to Fig. 4, the peak power is a square function of the pulse duration at a given current while the pulse is sufficiently short (in our simulations, at $t_{\text{e.pulse}} \leq$ 300 ps). It is important that an increase in the duration of the electron bunch with the shape of its leading edge and the peak current remaining unchanged creates additional (secondary) peaks of the electromagnetic radiation (Fig. 11a): i.e., the radiation takes the form of a train of electromagnetic pulses. As we noted in Section 2, this effect occurs because the bunch becomes too long [in terms of the cooperative duration $t_c = (\omega C)^{-1}(\beta_{\text{gr}}^{-1} - \beta_{\|}^{-1})$] to provide coherent radiation from its entire volume. As a result, the bunch splits into separate regions, which emit electromagnetic pulses virtually independently of each other. This mode is commonly called self-amplified spontaneous emission (SASE).

It should be noted that the generation of the secondary pulses (Fig. 11a), whose amplitude is almost the same as that of the first pulse, indicate that, for the simulation parameters (primarily, for the gain assumed),

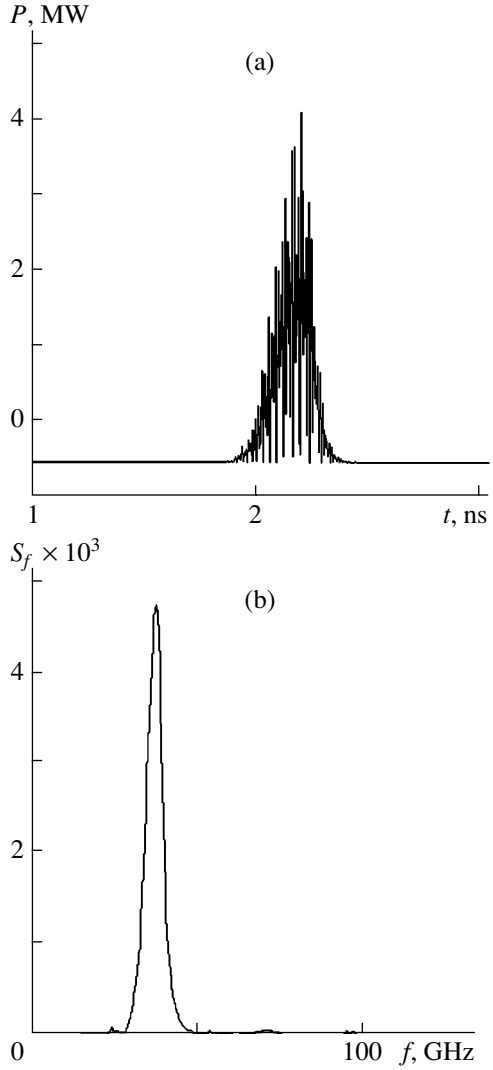

Fig. 8. (a) Cherenkov superradiance pulse and (b) its spectrum.

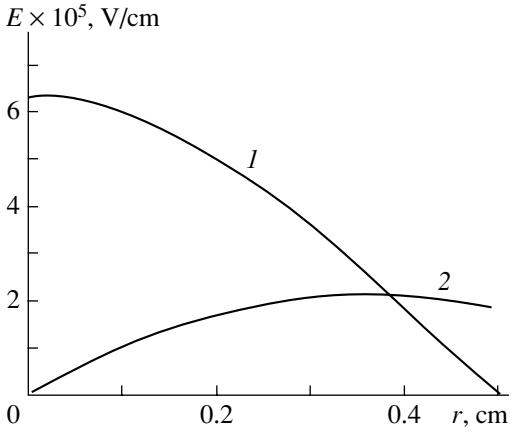

Fig. 9. Transverse distributions of the (*1*) E_z and (*2*) E_r at the exit from the interaction space (z = 33 cm).

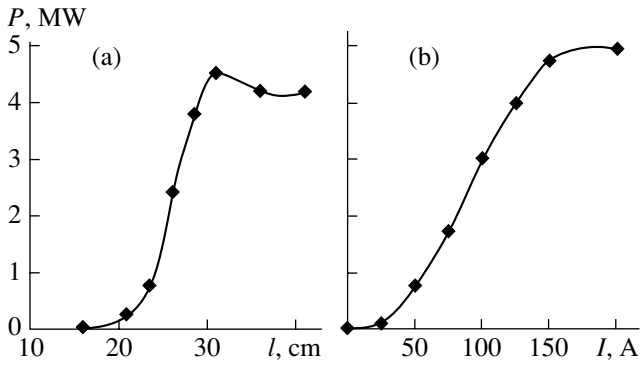

Fig. 10. Peak power of the superradiance pulse versus (a) length of the interaction space and (b) amplitude of the current at a fixed electron bunch duration.

the radiation is triggered by the fluctuation noise in the electron bunch. However, the situation where the emission is triggered by the coherent radiation of the leading edge of the current pulse is also quite possible. We simulated this situation by increasing the gap between the bunch and the slow-wave structure, thus decreasing the increments and simultaneously shortening the leading edge of the electron pulse to 30 ps. The output radiation generated in this situation by a 1.2-ns-long pulse is illustrated in Fig. 11b. In this case, it is concentrated mostly in the first pulse, which is initiated by the emission of the leading edge. After this pulse has passed, the amplitude of the initial fluctuations of the electron flow density is insufficient for the process to develop and the output signal decays almost to zero over the given interaction length. As a result, the effective duration of the pulse train radiated is found to be significantly smaller than the electron pulse duration.

3. EXPERIMENTAL STUDY OF CHERENKOV SUPERRADIANCE

The RADAN 303 accelerator with a subnanosecond sharpener was used as an injector of 1-kA pulses of 200- to 250-keV electrons [12, 13]. The pulses were 0.3–0.5 ns wide. They were generated by the explosive emission cathode of a coaxial vacuum diode with magnetic insulation. The average pulse radius was 0.15 cm.

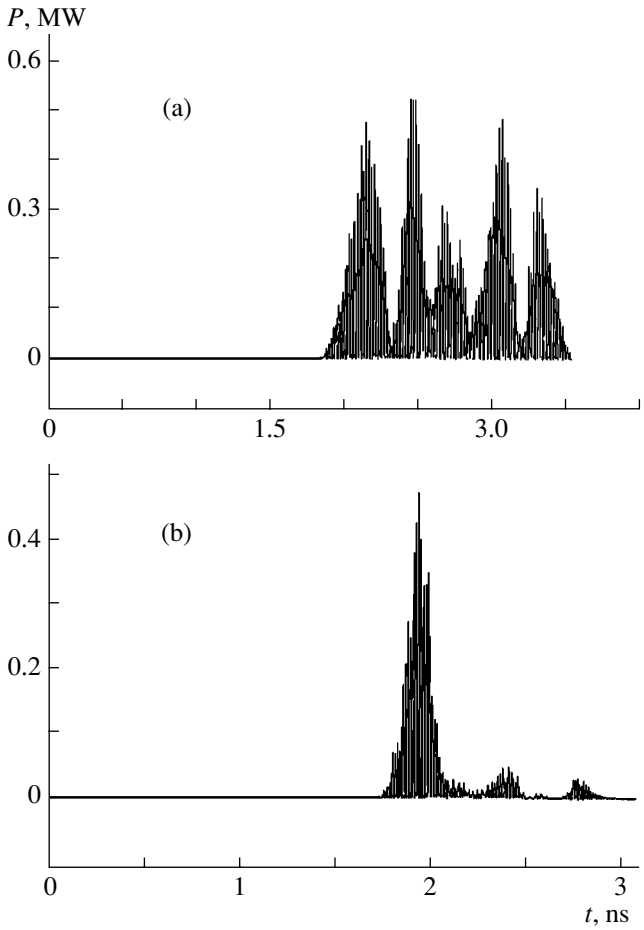

Fig. 11. Radiated power versus time for a long electron bunch. The radiation is triggered by (a) fluctuation noise and (b) emission of the leading edge of the electron pulse.

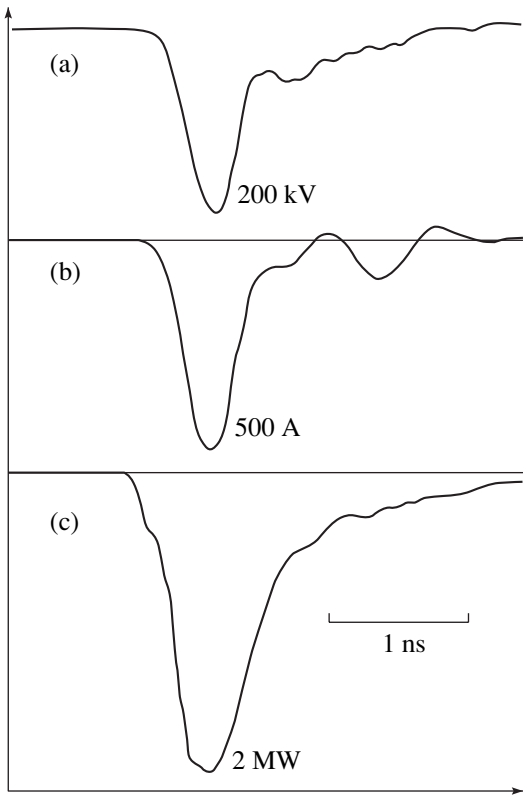

Fig. 12. Typical oscillograms of (a) the accelerating voltage, (b) electron current before entering the anode collimator, and (c) Cherenkov superradiance pulse.

Typical oscillograms of the accelerating voltage and of the electron current are shown in Figs. 12a and 12b, respectively. Note that, when the electron bunch enters the dielectric waveguide and also when it moves through it, the current is partially lost due to the collimating effect of the anode unit and adjustment errors. A 7-GHz-bandwidth Textronix 7250 oscilloscope was used to record subnanosecond pulses picked up by the voltage, current, and microwave power sensors. The transient period of the hot-carrier germanium diodes was 200 ps. The high-current electron bunches were transported through the interaction space in a uniform magnetic field of 13–14 kOe. The interaction space was a partially filled waveguide. Lavsan[1] and Teflon dielectric inserts with a permittivity of 2.5–3 were used. The best results were obtained with the multilayer dielectric insert made by winding a 0.05-mm-thick Lavsan film. For this case, typical 0.4- to 0.5-ns-long Cherenkov superradiance pulses with a peak current of 200 A at the exit from the interaction space are shown in Fig. 12c.

The spectra taken with a system of high-pass waveguide filters and metallic gratings with different meshes show that the center frequency is close to the theoretical value of ≈39 GHz. However, the width of the entire spectrum is found to be significantly larger than predicted (Fig. 8b), reaching 10 GHz. The broadening of the pulse spectrum can be attributed to the fact that the TM_{01} mode is excited along with the hybrid HE_{11} mode, whose dispersion characteristic also intersects the electron flow in the operating frequency band (Fig. 2). The higher modes of the partially filled waveguide could also be excited. The presence of several modes in the output radiation is also corroborated by the shape of the radiation pattern (Fig. 13), which lacks a deep dip at the center, which is typical of the TM_{01} mode.

Note that the initial spread in the longitudinal electron velocity and the variation of the average electron energy due to the time instability of the shape of the accelerating voltage pulse may also cause the broadening of the superradiance pulse spectrum. As a result, electron fractions with different translational velocities produce different resonance points in the dispersion characteristic.

The peak power radiated was estimated by integrating the radiation pattern constructed. At a current of 200 A, it was as high as 1–2 MW. The duration of the superradiance pulses measured (≈0.4 ns) was somewhat longer than that obtained in the simulation. The increase in the pulse duration can also be explained by the simultaneous excitation of several modes, which, in general, have different group velocities.

Figure 14 plots the experimental peak power against the length of the interaction space. The length of the interaction space was varied by depositing the electron bunch on the wall of the partially filled waveguide through successively switching off the coils generating the guiding magnetic field, with the field strength in the uniform portion of the solenoid kept unchanged. The initial portion of the curve is exponential. Further, the curve tends to saturation (cf. Fig. 10a), implying that the radiation is induced, i.e., arises be cause of particle bunching.

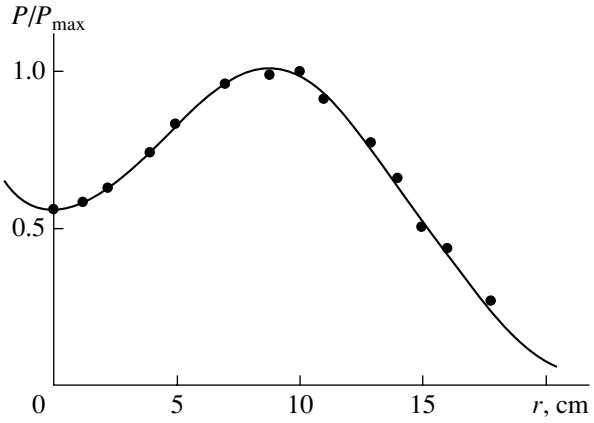

Fig. 13. Radiation pattern.

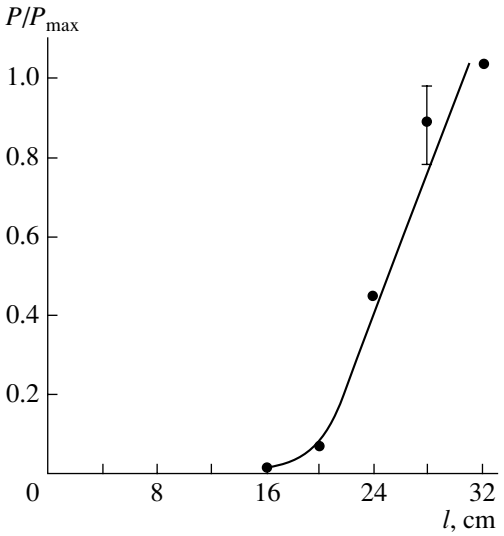

Fig. 14. Experimental dependence of the peak power on the length of the interaction space.

CONCLUSION

Thus, we first observed short-pulse Cherenkov radiation produced by a single electron bunch. Megawatt microwave pulses of subnanosecond duration corresponding to approximately 15 periods of the carrier frequency were generated. In accordance with the theoretical analysis and computer simulation, this radiation can be interpreted as the superradiance. It should be noted that in our experiments, the pulsed radiation was produced by a single subnanosecond electron bunch in

[1] Polyester fiber. Russian equivalent of Dacron.

contrast to the experiments [14], where the radiation was generated by a train of such pulses synchronized by an external feedback.

ACKNOWLEDGMENTS

This work was supported by the Russian Foundation for Basic Research (grant no. 98-02-17308).

REFERENCES

1. R. H. Bonifacio, C. Maroli, and N. Piovella, Opt. Commun. **68**, 369 (1988).
2. R. Bonifacio, N. Piovella, and B. W. J. McNeil, Phys. Rev. A **44**, 3441 (1991).
3. V. V. Zheleznyakov, V. V. Kocharovskiĭ, and Vl. V. Kocharovskiĭ, Izv. Vyssh. Uchebn. Zaved., Radiofiz. **29**, 1095 (1986).
4. N. S. Ginzburg, Pis'ma Zh. Tekh. Fiz. **14**, 440 (1988) [Sov. Tech. Phys. Lett. **14**, 197 (1988)].
5. N. S. Ginzburg, I. V. Zotova, and A. S. Sergeev, Pis'ma Zh. Éksp. Teor. Fiz. **60**, 501 (1994) [JETP Lett. **60**, 513 (1994)].
6. N. S. Ginzburg, Yu. V. Novozhilova, and A. S. Sergeev, Pis'ma Zh. Tekh. Fiz. **22** (9), 39 (1996) [Tech. Phys. Lett. **22**, 359 (1996)].
7. N. S. Ginzburg, A. S. Sergeev, I. V. Zotova, *et al.*, Phys. Rev. Lett. **78**, 2365 (1997).
8. D. A. Jaroszynski, P. Chaix, and N. Piovella, Phys. Rev. Lett. **78**, 1699 (1997).
9. N. S. Ginzburg, A. S. Sergeev, Yu. V. Novozhilova, *et al.*, Nucl. Instrum. Methods Phys. Res. A **393**, 352 (1997).
10. V. G. Shpak, M. I. Yalandin, N. S. Ginzburg, *et al.*, Dokl. Akad. Nauk **365**, 50 (1999) [Dokl. Phys. **44**, 143 (1999)].
11. N. S. Ginzburg, Yu. V. Novozhilova, A. S. Sergeev, *et al.*, Phys. Rev. E **60**, 3297 (1999).
12. G. A. Mesyats, V. G. Shpak, S. A. Shunailov, and M. I. Yalandin, in *Proceedings of the 9th IEEE International Pulsed Power Conference, Albuquerque, 1993*, Vol. 2, p. 835.
13. V. G. Shpak, S. A. Shunailov, M. R. Ulmaskulov, *et al.*, in *Proceedings of the 11th International Conference on High Power Particle Beams, Prague, 1996*, Vol. 2, p. 913.
14. F. Ciocci *et al.*, Phys. Rev. Lett. **66**, 699 (1991).

Translated by A. Khzmalyan

Technical Physics, Vol. 47, No. 3, 2002, pp. 343–349. Translated from Zhurnal Tekhnicheskoĭ Fiziki, Vol. 72, No. 3, 2002, pp. 61–68.

RADIOPHYSICS

The Effect of Metallic Screens on the Spectrum of Exchange Dipole Hybrid Electromagnetic-Spin Waves

V. E. Demidov*, B. A. Kalinikos*, and P. Edenhofer**

**St. Petersburg State Electrotechnical University,*
ul. prof. Popova 5, St. Petersburg, 197376 Russia
e-mail: eivt@eltech.ru
***Institute for High-Frequency Equipment, University of Bochum, D-44780 Bochum, Germany*
e-mail: edh@hf.ruhr-uni-bochum.de

Received August 6, 2001

Abstract—A theory of exchange dipole hybrid electromagnetic-spin waves is elaborated. The waves propagate in arbitrary magnetized five-layer screened structures where a ferromagnetic layer is separated from the metallic screens by two insulating layers on both sides, the layers having different permittivities. Within this theory, the effect of the screens on the hybrid surface wave spectrum in layered structures is analyzed. The structures consist of a ferromagnetic film that is applied on an insulating substrate and is in contact with a ferroelectric plate. © *2002 MAIK "Nauka/Interperiodica".*

In [1, 2], the idea of tuning microwave spin-wave devices by varying the permittivity of the ferroelectric film contacting with the ferromagnetic one has been put forward. Its implementation would greatly improve the parameters of such devices as electrically controlled spin-wave phase shifters, delay lines, resonators, etc. The control is accomplished by varying the constant electric field applied to the ferroelectric rather than the magnetizing field. With this approach, the need for electromagnets, usually used in electrically controlled spin-wave devices, is eliminated, so that the devices become smaller and lighter. In addition, such a tuning mechanism offers high speed and is not power-hungry.

To study layer structures containing ferromagnetic and ferroelectric films, a spin wave theory including electromagnetic delay should be elaborated. The magnetostatic approximation, which is usually used for characterizing spin waves, fails when the permittivity of the magnetic film or the insulating layers in contact with it is large. The spectrum and the dispersion characteristics of hybrid electromagnetic-spin waves with regard for electromagnetic delay have been considered for a number of specific cases [3–9]. For example, in [3], the theory of surface hybrid waves in a free ferromagnetic layer and in a ferromagnetic layer metallized on one side was constructed. In [4–6], the hybridization of surface and backward volume spin waves with electromagnetic waves was analyzed in ferromagnetic film–air gap–ferroelectric plate structures. In [7, 8], the theory of hybrid electromagnetic-spin waves in tangentially magnetized layer structures was developed for the case when the magnetization direction and the propagation direction make an arbitrary angle. In [7], a layer structure consisting of a ferromagnetic film separated from two metallic screens on both sides by two insulating layers was considered; in [8], a ferromagnetic layer metallized on one side was separated from a ferroelectric plate by an air gap. Finally, in [9], the dispersion properties of hybrid electromagnetic-spin waves in tangentially magnetized two-dimensional layer structures were studied by numerically solving the equations of electrodynamics. In all the works cited above, the hybrid wave spectrum was looked for with no regard for exchange interaction. With such an approximation, the results obtained in [3–9] cannot be extended for layer structures with thin ferromagnetic films. It is also essential that none of these works considered the optimization of the layer structure geometry for designing spin-wave structures that are tuned by applying a constant electric field.

The aims of this work are as follows.

(1) The construction of a general theory of exchange dipole electromagnetic-spin waves propagating in arbitrarily magnetized layer structures where the ferromagnetic film is separated from the metallic screens by four (two on either side) insulating layers of different permittivity.

(2) The study (within this theory) of the effect of the metallic screens on the degree of hybridization between the dispersion properties of the electromagnetic and surface spin waves.

(3) The analysis of controllability of the dispersion properties of the waves by varying the permittivities of the layers in order to find the optimal geometry of the layer structures for designing tunable spin-wave devices.

The geometry of the layer structure is shown in Fig. 1. It is unbounded in the plane $\eta\zeta$ and has an isotropic ferromagnetic layer of thickness L (hatched),

1063-7842/03/4702-0343$22.00

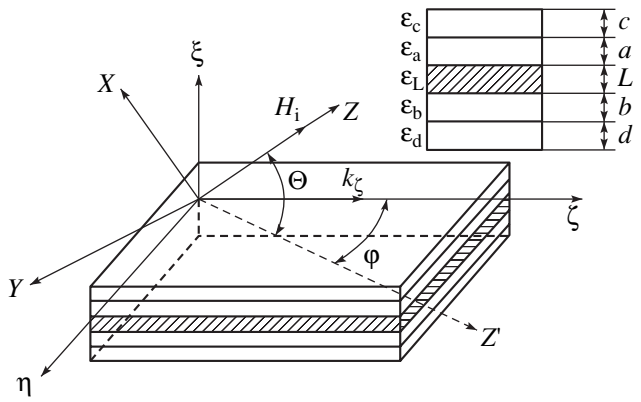

Fig. 1. Layer structure geometry. The inset shows the cross section of the structure.

permittivity ε_L, and saturation magnetization M_0. The ferromagnet is separated from perfectly conducting metallic screens by four (two on either side) insulating layers of thicknesses *a*, *b*, *c*, and *d* and respective permittivities ε_a, ε_b, ε_c, and ε_d. The origin is placed at the center of the ferromagnetic film. The ξ axis is assumed to be aligned with the direction of wave propagation. For convenience, we introduce the second coordinate system *XYZ* rotated about the system $\xi\eta\zeta$ so that the *Z* axis coincides with the direction of the permanent magnetic field $\mathbf{H}_i$ and the *Y* axis lies in the plane of the structure. The orientation of the two coordinate systems relative to each other is specified by the angle φ between the ζ axis and the projection of the *Z* axis onto the plane *Z*' of the structure and by the angle Θ between the *Z* and *Z*' axes.

A boundary-value problem for the equations of magnetization motion and the complete set of the Maxwell equations is solved by using Green's tensor function formalism for a planar-layer structure [10, 11]. Following this method, we first find relations between the distribution of the variable magnetic field and that of the variable magnetization across the layer structure, i.e., Green's tensor function of the Maxwell equations for the structure. Then, the resulting expressions are substituted into the linearized equation of magnetization, which is solved for two limiting exchange boundary conditions: fixed and free surface spins. The solution yields an implicit dispersion relation that relates the cyclic frequency ω of the waves to their longitudinal wave number k_ζ:

$$\det\hat{A}(\omega, k_\zeta) = 0. \qquad (1)$$

The matrix $\hat{A}$ is a block matrix consisting of four infinite matrices. For free surface spins,

$$\hat{A} = \begin{bmatrix} -A_{00}^{xx} + \Omega_{0k} & -A_{10}^{xx} & \cdots & A_{00}^{xy} + \omega & A_{10}^{xy} & \cdots \\ -A_{01}^{xx} & -A_{11}^{xx} + \Omega_{1k} & \cdots & A_{01}^{xy} & A_{11}^{xy} + \omega & \cdots \\ \vdots & \vdots & \ddots & \vdots & \vdots & \ddots \\ -A_{00}^{yx} + \omega & -A_{10}^{yx} & \cdots & -A_{00}^{yy} + \Omega_{0k} & -A_{10}^{yy} & \cdots \\ -A_{01}^{yx} & -A_{11}^{yx} + \omega & \cdots & -A_{01}^{yy} & -A_{11}^{yy} + \Omega_{1k} & \cdots \\ \vdots & \vdots & \ddots & \vdots & \vdots & \ddots \end{bmatrix}. \qquad (2)$$

For fixed surface spins, the indices of the matrix elements are numbered, starting from unity. The expressions for the matrix elements for free and fixed surface spins are given in the Appendix.

Dispersion relation (1) represents the exact spectrum of natural waves in an arbitrarily magnetized layer structure with regard for dipole–dipole and exchange interactions, electrodynamic and exchange boundary conditions, and electromagnetic delay. Thus, the dispersion relation obtained is a universal tool for studying the spectrum and the dispersion properties of hybrid electromagnetic-spin waves that propagate in arbitrarily magnetized layer structures. Our theory, taking into account exchange interaction, enables the analysis of layer structures incorporating both thin ferromagnetic films, where exchange interaction plays a major role in forming the spin wave spectrum, and thick films, where it has a minor effect on the dispersion properties up to very large ("exchange") values of the wave numbers of the spin waves. Moreover, the inclusion of electromagnetic delay in all the layers of the structure makes it possible to analyze waveguide structures containing both ferromagnetic and ferroelectric layers, as well as magnetodielectric layers, i.e., layers combining both ferromagnetic and ferroelectric properties.

Note that the matrix elements involved in (2) are complicated function of the natural frequency and the wave number of the hybrid waves. Because of this, dispersion relation (1) cannot be solved analytically without invoking numerical methods. In this case, the number of matrix elements that must be left in (2) depends on a specific geometry of the structure and on the angle between the hybrid wave propagation direction and the magnetization.

It has been shown [1, 2] that, surface hybrid electromagnetic-spin waves propagating at a right angle to the magnetization ($\Theta = 0$, $\varphi = -\pi/2$) in tangentially magnetized insulating substrate–thick ferromagnetic film–fer-

roelectric layer structures are the most appropriate for the implementation of microwave electric-field-tuned spin-wave devices. However, the works cited considered only layer structures screened on both sides. The dispersion relation derived in this work gives a chance to examine the structures of a similar geometry where the metallic screens are some distance away from the surfaces of the structure or are completely lacking. In this case, we can estimate the effect of the screens on the formation of the hybrid wave spectrum and optimize the geometry of the structure for the design of tunable spin-wave devices. We take, as the starting point, the geometry for which the best hybridization of spin and electromagnetic waves and the highest controllability were obtained: $a = b = 300$ μm, $\varepsilon_a = 1630$, $\varepsilon_b = 14$, $L = 20$ μm, and $\varepsilon_L = 14$ [2]. This structure resembles that consisting of a YIG film (layer L) grown on an insulating GGG substrate (layer b) that is in contact with a ferroelectric ceramic plate (layer a). Let us assume that the metallic screens are separated from the ferroelectric plate and insulating substrate by air gaps ($\varepsilon_c = \varepsilon_d = 1$) of thicknesses c and d, respectively.

Before quantitatively analyzing the effect of the metallic screens on the surface hybrid wave spectrum, we will describe its properties on a qualitative basis. From general considerations, it is obvious that the hybrid wave spectrum is a combination of the dispersion curves corresponding to fast electromagnetic and slow spin waves that are hybridized in those areas of the dispersion diagram where their phase velocities approach each other. Therefore, the formation of the complete spectrum of the waves propagating in a layer structure should be analyzed in two steps. At the first step, one considers the spectrum of the purely electromagnetic waves, neglecting the magnetic properties of the layer L; then, at the second stage, the magnetic properties are added into consideration and the complete spectrum is analyzed.

Following this approach, let us consider first the effect of the screens on the spectrum of the purely electromagnetic waves propagating in the above-mentioned structures. To do this, we will use dispersion relations that are easy to obtain when deriving Eq. (1) by eliminating the magnetization variable. For transverse electric (TE) waves, the dispersion relation has the form

$$\frac{N(\omega, k_\zeta)}{\gamma_L(\omega, k_\zeta)} = 0, \tag{3}$$

for transverse magnetic (TM) waves,

$$\gamma_L(\omega, k_\zeta) N^y(\omega, k_\zeta) = 0. \tag{4}$$

The expressions entering into dispersion relations (3) and (4) are given in the Appendix.

Figure 2 shows the spectra of the purely electromagnetic waves calculated with relations (3) and (4). They correspond to three limiting metallizations of the structure with the parameters $a = b = 300$ μm, $\varepsilon_a = 1630$, $\varepsilon_b =$

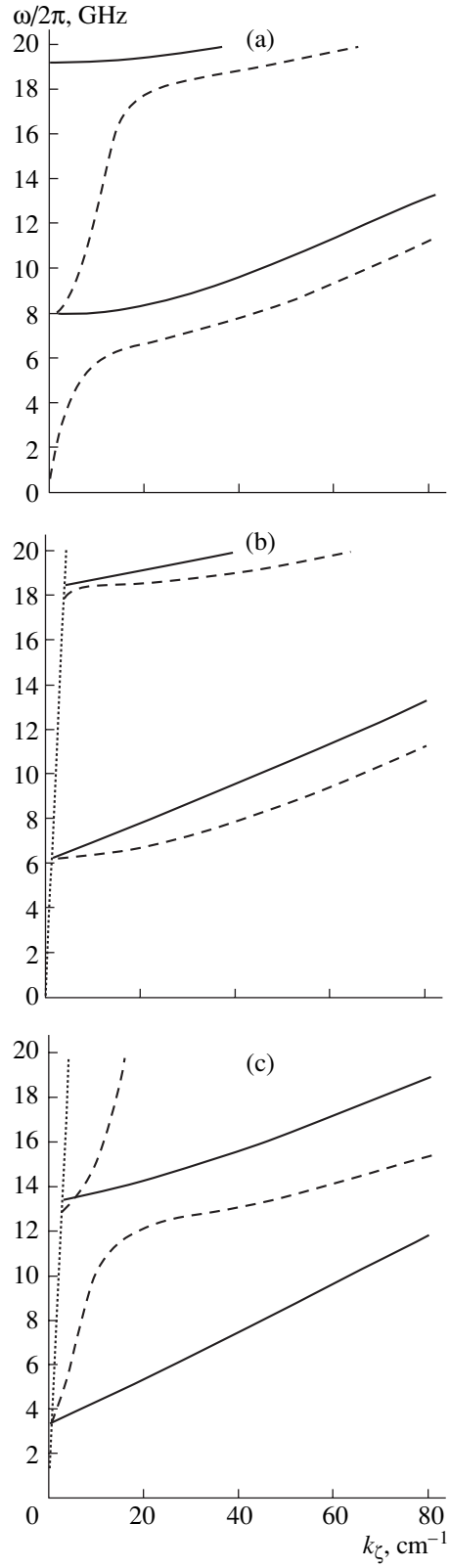

Fig. 2. Electromagnetic wave spectra in the dielectric waveguide structure in the absence of the magnetic properties of the layer L under different metallization conditions.

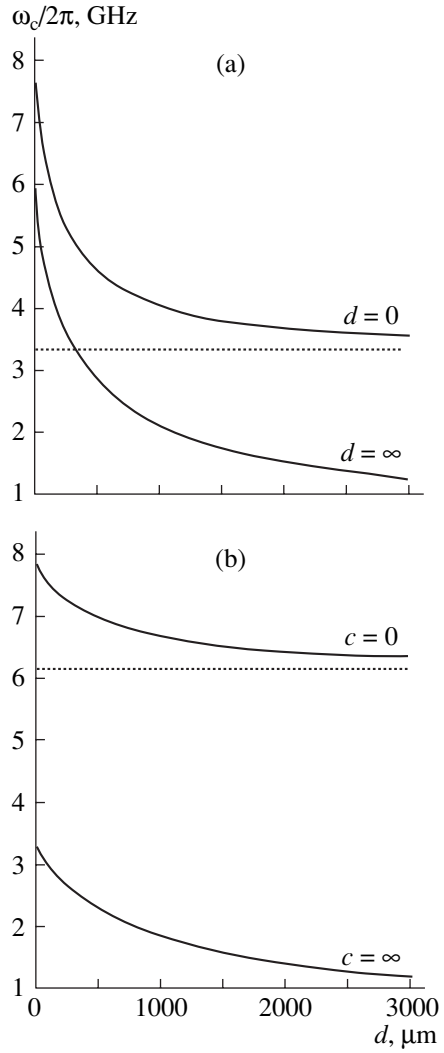

Fig. 3. Variation of the cutoff frequency of the TE_1 mode with spacing between the screens and the surfaces of the layer structure.

14, L = 20 μm, and ε_L = 14. In Fig. 2a, the waveguide structure is metallized on both sides ($c = d = 0$); in Fig. 2b, only on the side of the ferroelectric layer a ($c = 0$, $d = \infty$); and in Fig. 2c, on the side of the insulating substrate b ($c = \infty$, $d = 0$). The continuous and dashed lines in Fig. 2 are the dispersion curves for the TE and TM waves, respectively. The dotted line shows the boundary of the domain where the continuous spectrum of the waves exists. To the left of this line, the spectrum is continuous; to the right, it is discrete.

As follows from Fig. 2, the absence of either of the screens considerably modifies the electromagnetic wave spectrum, the spectra of the TE and TM waves changing in a different way. For the former, the elimination of the metal leads to a decrease in the cutoff frequencies of both branches and to an increase in the group velocities. This is because their fields partially penetrate into the low-permittivity regions. For the latter, the elimination of the metal drastically changes the form of the dispersion curves, because the electromagnetic fields of these waves are concentrated in the low-permittivity regions. It is essential that the curve corresponding to the fundamental mode of the TM waves shifts to the frequency domain above the cutoff frequency for the fundamental mode of the TE waves when the metal is removed.

As has been shown [1, 2], the efficiency of controlling the dispersion properties of the spin waves by varying the permittivity of the ferroelectric layer is high when the dispersion curves for the surface spin waves propagating normally to the magnetization in a tangentially magnetized layer structure and those for the electromagnetic TE_1 waves "repel" each other. The controllability is the highest when the cutoff frequency of the TE_1 mode is near the frequency range of exchangeless spin waves.

Figure 3 shows how the cutoff frequency of the TE_1 mode varies with distance c between the ferroelectric surface and the screen in the presence ($d = 0$) and absence ($d = \infty$) of the metallization on the side of the insulating substrate (Fig. 2a) and with distance d between the screen and the insulating substrate in the presence ($c = 0$) and absence ($c = \infty$) of the screen near the ferroelectric (Fig. 2b). The dotted lines indicate the frequencies to which the curves tend at $d \longrightarrow \infty$, $c = 0$ or $c \longrightarrow \infty$, $d = 0$. In the limit case of the absence of both screens ($c = \infty$, $d = \infty$), the cutoff frequency of the TE_1 mode goes to zero. It is seen that the removal of the screen from the ferroelectric surface affects the TE_1 cutoff frequency much stronger than when the screen is removed from the insulating substrate. The cutoff frequency changes most significantly when the distance to the screen is varied from 0 to 500 μm. Thus, varying the spacing between the screens and the surfaces of the layer structure, all other parameter being the same, one can vary the cutoff frequency of the TE_1 mode in wide limits.

Now we will consider the complete spectrum of the hybrid waves. The effect of the metallic screens on the hybridization of the dispersion curves for the electromagnetic (TE_1) and surface spin waves, as well as on the efficiency of controlling the dispersion properties of the spin waves by varying the permittivity of the ferroelectric, is demonstrated in Fig. 4. This figure refers to the layer structure with $a = b$ = 300 μm, ε_b = 14, L = 20 μm, and ε_L = 14. Three limit cases of metallization are considered: $c = d = 0$ (Fig. 4a); $c = 0$, $d = \infty$ (Fig. 4b); and $c = \infty$, $d = 0$ (Fig. 4c). The continuous lines show the dispersion curves of the hybrid surface waves for ε_a = 1630; dashed lines, the dispersion curves of the hybrid waves for ε_a = 1000; and dash-and-dot lines, the dispersion curves of the surface spin waves that were calculated in the magnetostatic approximation. The dotted lines indicate the boundaries of the frequency domain where exchangeless surface magneto-

static waves exist: $\sqrt{\omega_H(\omega_H + \omega_M)}$ is the lower boundary; $\omega_H + 0.5\omega_M$, the upper one. The dispersion curves for the TM modes and the domains of existence of the continuous spectrum are omitted lest the figure be encumbered.

Since the cutoff frequency of the TE_1 mode depends on the metallization conditions, the permanent magnetic field strength H_i for each of the cases shown in Fig. 4 was selected such that the cutoff frequency of the TE_1 mode coincided with the lower limit of the domain where exchangeless surface magnetostatic waves exist in a free ferromagnetic film. Therefore, the dispersion curves in Figs. 4a–4c were calculated for H_i = 2078, 1498, and 606 Oe, respectively. As follows from Fig. 4, the removal of either of the screens weakens the hybridization of the dispersion curves for the electromagnetic and spin waves. Moreover, when the metal is eliminated, the control of the dispersion curves by varying the permittivity of the ferroelectric becomes difficult. It is also significant that when the metal is removed from the insulating substrate (Fig. 4b), the cutoff frequency of the upper branch of the hybridized dispersion curves shifts downward, resulting in multimode propagation in the frequency range of hybridization. When the metal is removed from the ferroelectric (Fig. 4c), the dispersion curves become monotonic, which may be of importance for the practical use of the hybridization effect. In addition, single-mode propagation in a wide frequency range is typical of the latter case. However, the control efficiency here is lower than in the case of double-side metallization.

On way to improve the control efficiency is to make the ferroelectric film thinner. This would enhance the "overlap" between the electromagnetic fields of the TE waves and the fields of the surface spin waves. By way of example, Fig. 5 shows the dispersion curves for the hybrid waves in the layer structure metallized on the side of the insulating substrate ($c = \infty$, $d = 0$) when the ferroelectric layer is 66 μm thick. The other parameters are the same as before: b = 300 μm, ε_b = 14, L = 20 μm, ε_L = 14, and $\varepsilon_c = \varepsilon_d$ = 1. The magnetizing field strength is H_i = 2078 Oe. As in Fig. 4, the continuous curves correspond to ε_a = 1630; dashed curves, to ε_a = 1000; and dash-and-dot curves, to the magnetostatic approximation. As before, the parameters are taken in such a way that the cutoff frequency of the TE_1 mode coincides with the lower limit of the domain where exchangeless surface magnetostatic waves exist, $\sqrt{\omega_H(\omega_H + \omega_M)}$.

From Figs. 4a and 5, one can see that the thinning of the ferroelectric layer in the structure metallized only on the side of the substrate provides the control efficiency nearly the same as in the structure with double-side metallization. However, as was noted, the former case is characterized by the monotonic dispersion curves and single-mode propagation, which may be of importance for applications.

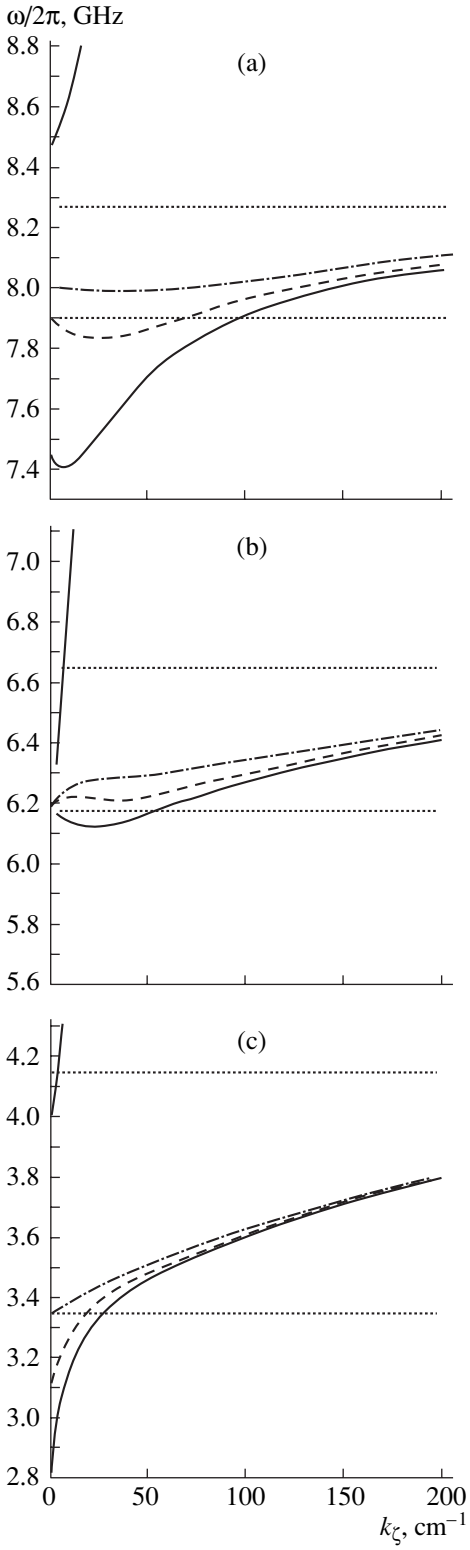

Fig. 4. Effect of the screens on the hybridization efficiency for the dispersion properties of the electromagnetic and surface spin waves.

From our analysis, some conclusion can be drawn. The removal of the metallic screens from the surfaces of the layer (insulating substrate–ferromagnetic film–

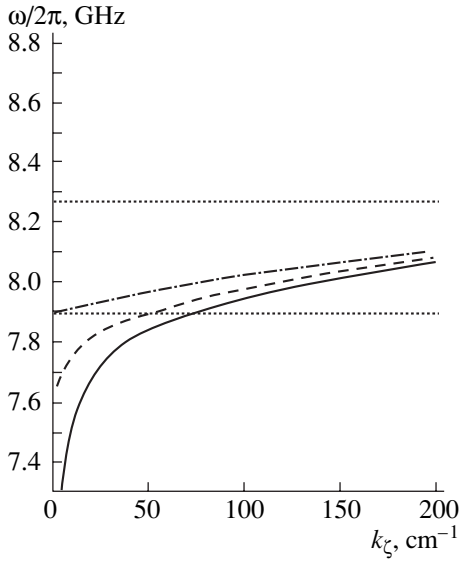

Fig. 5. Partial compensation for weak hybridization in the layer structure metallized on the side of the insulating substrate by thinning the ferroelectric.

ferroelectric plate) structure markedly weakens the hybridization of the dispersion curves for the electromagnetic and surface spin waves, as well as deteriorates the efficiency of controlling the dispersion properties by varying the permittivity of the ferroelectric. At the same time, varying the spacing between the metallic screen and the ferroelectric surface, one can effectively alter the cutoff frequency of the TE_1 mode of the electromagnetic waves. This frequency specifies the operating frequency range of microwave devices that could be based on the hybridization effect. Moreover, the removal of the screen on the side of the ferroelectric makes the dispersion curves of the hybrid waves monotonic. The degradation of the control efficiency observed in this case may partially be compensated for by thinning the ferroelectric layer.

The basic results obtained in this work are as follows. By jointly solving the complete set of the Maxwell equations and the equation of magnetization motion with regard for electrodynamic and exchange boundary conditions, we derived the universal dispersion relation, which allows us to calculate the complete spectrum of waves in tangentially magnetized layer structures including ferromagnetic and insulating (ferroelectric) layers. With this relation, we looked for the structure geometry optimal for the control of the dispersion properties of the hybrid waves by varying the permittivity of the ferroelectric. The structure screened on both sides has been shown to be optimal in this respect. That metallized on the side of the ferroelectric also offers a number of advantages but the controllability in this specific case is poorer.

ACKNOWLEDGMENTS

This work was supported by the Russian Foundation for Basic Research (grant no. 99-02-16370) and the INTAS Foundation (grant no. 99-1812).

APPENDIX

The expressions for the matrix elements involved in Eq. (1) are as the following:

$$A_{nm}^{xx} = A_{nm}^{\xi\xi}\cos^2(\Theta) - i(A_{nm}^{\xi\zeta} + A_{nm}^{\zeta\xi}) \times \cos(\varphi)\sin(\Theta)\cos(\Theta) + A_{nm}^{\eta\eta}\sin^2(\varphi)\sin^2(\Theta) + A_{nm}^{\zeta\zeta}\cos^2(\varphi)\sin^2(\Theta),$$

$$A_{nm}^{xy} = A_{nm}^{\xi\zeta}\sin(\varphi)\cos(\Theta) - i(A_{nm}^{\eta\eta} - A_{nm}^{\zeta\zeta})\sin(\varphi)\cos(\varphi)\sin(\Theta),$$

$$A_{nm}^{yx} = A_{nm}^{\zeta\xi}\sin(\varphi)\cos(\Theta) - i(A_{nm}^{\eta\eta} - A_{nm}^{\zeta\zeta})\sin(\varphi)\cos(\varphi)\sin(\Theta),$$

$$A_{nm}^{yy} = A_{nm}^{\eta\eta}\cos^2(\varphi) + A_{nm}^{\zeta\zeta}\sin^2(\varphi),$$

$$A_{nm}^{\xi\xi} = -\delta_{nm} + \frac{k_\zeta^2}{\gamma_L^2 + \kappa_m^2}\delta_{nm} - \frac{k_\zeta^2}{N\gamma_L}R_{nm}^1\begin{Bmatrix}F_{nm}^3\\F_{nm}^4\end{Bmatrix},$$

$$A_{nm}^{\xi\zeta} = R_{nm}^2 + \frac{k_\zeta}{N}R_{nm}^1\begin{Bmatrix}F_{nm}^2\\F_{nm}^1\end{Bmatrix},$$

$$A_{nm}^{\eta\eta} = \frac{k_{0L}^2}{\gamma_L^2 + \kappa_m^2}\delta_{nm} - \frac{k_{0L}^2}{N^y\gamma_L}R_{nm}^1\begin{Bmatrix}F_{nm}^5\\F_{nm}^6\end{Bmatrix},$$

$$A_{nm}^{\zeta\xi} = R_{nm}^2 + \frac{k_\zeta}{N}R_{nm}^1\begin{Bmatrix}F_{nm}^1\\F_{nm}^2\end{Bmatrix},$$

$$A_{nm}^{\zeta\zeta} = -\frac{\gamma_L^2}{\gamma_L^2 + \kappa_m^2}\delta_{nm} + \frac{\gamma_L}{N}R_{nm}^1\begin{Bmatrix}F_{nm}^4\\F_{nm}^3\end{Bmatrix},$$

$$R_{nm}^1 = \frac{1}{(\gamma_L^2 + \kappa_m^2)(\gamma_L^2 + \kappa_n^2)}\frac{2}{L}\begin{Bmatrix}\gamma_L^2/\sqrt{(1+\delta_{0n})(1+\delta_{0m})}\\-\kappa_n\kappa_m\end{Bmatrix},$$

$$R_{nm}^2 = \frac{k_\zeta[1-(-1)^{n+m}]}{(\gamma_L^2 + \kappa_m^2)(\kappa_m^2 - \kappa_n^2)}\frac{2}{L}\begin{Bmatrix}\kappa_m^2/\sqrt{(1+\delta_{0n})(1+\delta_{0m})}\\\kappa_n\kappa_m\end{Bmatrix},$$

$$F_{nm}^1 = -Q_{ac}Q_{bd}\sinh(\gamma_L L)(1-(-1)^{n+m}) - (\cosh(\gamma_L L) - (-1)^n)(S_{ac}Q_{bd} - S_{bd}Q_{ac}(-1)^{n+m}),$$

$$F^2_{nm} = -S_{ac}S_{bd}\sinh(\gamma_L L)(1-(-1)^{n+m})$$
$$+(\cosh(\gamma_L L)-(-1)^n)(S_{ac}Q_{bd}(-1)^{n+m}-S_{bd}Q_{ac}),$$
$$F^3_{nm} = S_{ac}S_{bd}(\cosh(\gamma_L L)-(-1)^n)(1+(-1)^{n+m})$$
$$+\sinh(\gamma_L L)(S_{ac}Q_{bd}(-1)^{n+m}+S_{bd}Q_{ac}),$$
$$F^4_{nm} = Q_{ac}Q_{bd}(\cosh(\gamma_L L)-(-1)^n)(1+(-1)^{n+m})$$
$$+\sinh(\gamma_L L)(S_{ac}Q_{bd}+S_{bd}Q_{ac}(-1)^{n+m}),$$
$$F^5_{nm} = Q^y_{ac}Q^y_{bd}(\cosh(\gamma_L L)-(-1)^n)(1+(-1)^{n+m})$$
$$+\sinh(\gamma_L L)(S^y_{ac}Q^y_{bd}+S^y_{bd}Q^y_{ac}(-1)^{n+m}),$$
$$F^6_{nm} = S^y_{ac}S^y_{bd}(\cosh(\gamma_L L)-(-1)^n)(1+(-1)^{n+m})$$
$$+\sinh(\gamma_L L)(S^y_{ac}Q^y_{bd}(-1)^{n+m}+S^y_{bd}Q^y_{ac}),$$
$$N = \sinh(\gamma_L L)(S_{bd}S_{ac}+Q_{ac}Q_{bd})$$
$$+\cosh(\gamma_L L)(S_{ac}Q_{bd}+S_{bd}Q_{ac}),$$
$$N^y = \sinh(\gamma_L L)(S^y_{bd}S^y_{ac}+Q^y_{ac}Q^y_{bd})$$
$$+\cosh(\gamma_L L)(S^y_{ac}Q^y_{bd}+S^y_{bd}Q^y_{ac}),$$
$$S_{bd} = 1+\frac{\gamma_b}{\gamma_d}\tanh(\gamma_d d)\tanh(\gamma_b b),$$
$$S_{ac} = 1+\frac{\gamma_a}{\gamma_c}\tanh(\gamma_c c)\tanh(\gamma_a a),$$
$$Q_{bd} = \frac{\gamma_L}{\gamma_d}\tanh(\gamma_d d)+\frac{\gamma_L}{\gamma_b}\tanh(\gamma_b b),$$
$$Q_{ac} = \frac{\gamma_L}{\gamma_c}\tanh(\gamma_c c)+\frac{\gamma_L}{\gamma_a}\tanh(\gamma_a a),$$
$$S^y_{bd} = 1+\frac{\varepsilon_b\gamma_d}{\varepsilon_a\gamma_b}\tanh(\gamma_d d)\tanh(\gamma_b b),$$
$$S^y_{ac} = 1+\frac{\varepsilon_a\gamma_c}{\varepsilon_c\gamma_a}\tanh(\gamma_c c)\tanh(\gamma_a a),$$
$$Q^y_{bd} = \frac{\varepsilon_L\gamma_d}{\varepsilon_d\gamma_L}\tanh(\gamma_d d)+\frac{\varepsilon_L\gamma_b}{\varepsilon_b\gamma_L}\tanh(\gamma_b b),$$
$$Q^y_{ac} = \frac{\varepsilon_L\gamma_c}{\varepsilon_c\gamma_L}\tanh(\gamma_c c)+\frac{\varepsilon_L\gamma_a}{\varepsilon_a\gamma_L}\tanh(\gamma_a a),$$
$$\Omega_{nk} = \omega_H+\omega_M\alpha(k_\zeta^2+\kappa_n^2),$$
$$\kappa_n = \frac{n\pi}{L},\quad \omega_H = |g|\mu_0 H_i,\quad \omega_M = |g|\mu_0 M_0,$$
$$k_{0a}^2 = \omega^2\varepsilon_0\mu_0\varepsilon_a,\quad \gamma_a^2 = k_\zeta^2-k_{0a}^2,$$
$$k_{0b}^2 = \omega^2\varepsilon_0\mu_0\varepsilon_b,\quad \gamma_b^2 = k_\zeta^2-k_{0b}^2,$$
$$k_{0c}^2 = \omega^2\varepsilon_0\mu_0\varepsilon_c,\quad \gamma_c^2 = k_\zeta^2-k_{0c}^2,$$
$$k_{0d}^2 = \omega^2\varepsilon_0\mu_0\varepsilon_d,\quad \gamma_d^2 = k_\zeta^2-k_{0d}^2,$$
$$k_{0L}^2 = \omega^2\varepsilon_0\mu_0\varepsilon_L,\quad \gamma_L^2 = k_\zeta^2-k_{0L}^2,$$

where $|g| = 1.76\times10^{11}$ C/kg is the gyromagnetic ratio for the electron spin and $\alpha$is the constant of nonuniform exchange interaction.

In the expressions for $A^{\xi\xi}_{nm}$, $A^{\xi\zeta}_{nm}$, $A^{\zeta\xi}_{nm}$, $A^{\zeta\zeta}_{nm}$, $A^{\eta\eta}_{nm}$, R^1_{nm}, and R^2_{nm}, the upper and lower rows in the braces stand for the boundary conditions on the ferromagnet surface that correspond to free and fixed surface spins, respectively.

REFERENCES

1. V. E. Demidov and B. A. Kalinikos, Pis'ma Zh. Tekh. Fiz. **26** (7), 8 (2000) [Tech. Phys. Lett. **26**, 272 (2000)].
2. V. E. Demidov and B. A. Kalinikos, Zh. Tekh. Fiz. **71** (2), 89 (2001) [Tech. Phys. **46**, 219 (2001)].
3. J. D. Gerson and J. S. Nadan, IEEE Trans. Microwave Theory Tech. **22**, 757 (1974).
4. V. B. Anfinogenov, T. N. Verbitskaya, Yu. V. Gulyaev, *et al.*, Radiotekh. Élektron. (Moscow) **34**, 494 (1989).
5. V. B. Anfinogenov, T. N. Verbitskaya, Yu. V. Gulyaev, *et al.*, Radiotekh. Élektron. (Moscow) **35**, 320 (1990).
6. V. B. Anfinogenov, T. N. Verbitskaya, P. E. Zil'berman, *et al.*, Zh. Tekh. Fiz. **60** (9), 114 (1990) [Sov. Phys. Tech. Phys. **35**, 1068 (1990)].
7. V. N. Ivanov, N. P. Demchenko, I. S. Nefedov, *et al.*, Izv. Vyssh. Uchebn. Zaved., Radiofiz. **32**, 764 (1989).
8. T. A. Smirnova and Yu. F. Filipov, Radiotekh. Élektron. (Moscow) **38**, 34 (1993).
9. G. S. Makeeva, Radiotekh. Élektron. (Moscow) **44**, 1308 (1999).
10. V. F. Dmitriev and B. A. Kalinikos, Izv. Vyssh. Uchebn. Zaved., Fiz. (1988).
11. B. A. Kalinikos, Izv. Vyssh. Uchebn. Zaved., Fiz. **24** (8), 42 (1981).

Translated by V. Isaakyan

Technical Physics, Vol. 47, No. 3, 2002, pp. 350–356. Translated from Zhurnal Tekhnicheskoĭ Fiziki, Vol. 72, No. 3, 2002, pp. 69–75.

ELECTRON AND ION BEAMS, ACCELERATORS

Focusing of an Intense Neutralized Proton Beam

V. I. Engelko*, H. Giese, V. S. Kuznetsov*, G. A. Viazmenova*, and S. Schalk****

** Efremov Research Institute of Electrophysical Equipment, St. Petersburg, 196641 Russia*
e-mail: engelko@niiefa.spb.su
*** Karlsruhe Research Center, 76021 Karlsruhe, Germany*

Received April 12, 2001

Abstract—An intense low-energy (15–20 keV) proton beam is focused in two stages: ballistic focusing is followed by magnetic compression. The beam is formed by an MAIS wide-aperture source, in which a plasma is generated by many discharge elements via a discharge over the polyethylene surface. In the presence of an external magnetic field, the beam turns out to be overneutralized by electrons coming from the cathode grids of the source and from the target. The maximal focusing efficiency (>70%) is observed within 10 μs after the pulse has been applied if the target is negatively biased. The degree of beam compression in terms of cross-sectional area is 1.6×10^3. The numerical simulation of the focusing agrees well with the results of measurement. © *2002 MAIK "Nauka/Interperiodica".*

INTRODUCTION

Intense pulsed low-energy proton beams of power density up to 10 MW/cm^2 are used for studying the behavior of materials of the first wall and divertor of a fusion reactor under anomalous modes of its operation. The necessary parameters of the beam are as follows: proton energy 10–30 keV, pulse duration ≈10 μs, and power density up to 10 MW/cm^2 (the respective current density 0.3–1.0 kA/cm^2). For a linear size of test samples of ≈1 cm, the total beam current must be ≈1 kA.

The scheme for the formation of a proton beam with the desired parameters has been considered in [1]. It includes two stages. The first one is the generation of the beam with a current density of ≈0.1 kA/cm^2 and a cross-sectional area of ~10^4 cm^2. The second one is beam focusing. The beam is first focused ballistically and then magnetically compressed over a length of ≈1.5 m in a longitudinal magnetic field increasing in the direction of beam propagation. The injection of the beam into the growing magnetic field is necessary not only for focusing but also for studying the erosion of the materials under typical operating conditions of the reactor, where the magnetic induction may be as high as 5 T. The feasibility of such an experimental scheme was tested with the PROFA installation [2]. Its dimensions allow the simulation of the beam-forming procedure for a beam with a diameter of ≈0.44 m in the emission region and for a focusing channel length of 1.2 m. Proton beams with a large cross-sectional area were generated with the special source. Its design and the parameters of the beams generated have been described in [3]. In this work, we analyze experimental data for proton beam focusing.

PROFA INSTALLATION

The schematic diagram of the experimental setup is shown in Fig. 1. It consists of a plasma source of ions, two cathode grids, the region of ballistic focusing, the region of magnetic compression, and a target chamber. The regions of ballistic focusing and magnetic compression are 0.6 m long. The magnetic field induction is 2×10^{-3} T in the emission region; 0.4 T at the ballistic focus; and 4.5 T at the target. The axial magnetic field distribution in the setup is demonstrated in Fig. 1. The flat part of voltage pulses from the high-voltage generator was about 30 μs long, and their amplitude was no higher than 30 kV. The potentials of the first and second cathode grids were, respectively, –1 kV and –100…–300 V. At such potentials, the beam current did not oscillate, so that the space charge of the beam was neutralized most efficiently. The residual gas pressure was 5×10^{-5} torr.

In the experiments, the accelerating voltage was determined with a voltage divider. The discharge current of the ion source, the current to the cathode grids, that to the focusing channel wall, and the ion current, all were measured with Rogowski loops. Finally, the ion current to the target was determined with a three-electrode probe (ThEP) consisted of an outer grounded electrode, a control electrode, and a Faraday cup. Both electrodes are cylindrical, and their entry apertures are covered by grids. The control electrode and the Faraday cup are biased. This sensor not only measures the ion current but also provides some information on the energy and concentration of electrons neutralizing the space charge of the beam while moving together with the ions. The method for gaining such information is based on taking the collector current vs. second-grid potential dependence (for details, see [4, 5]). The current density near the target was measured by a movable

1063-7842/03/4702-0350$22.00

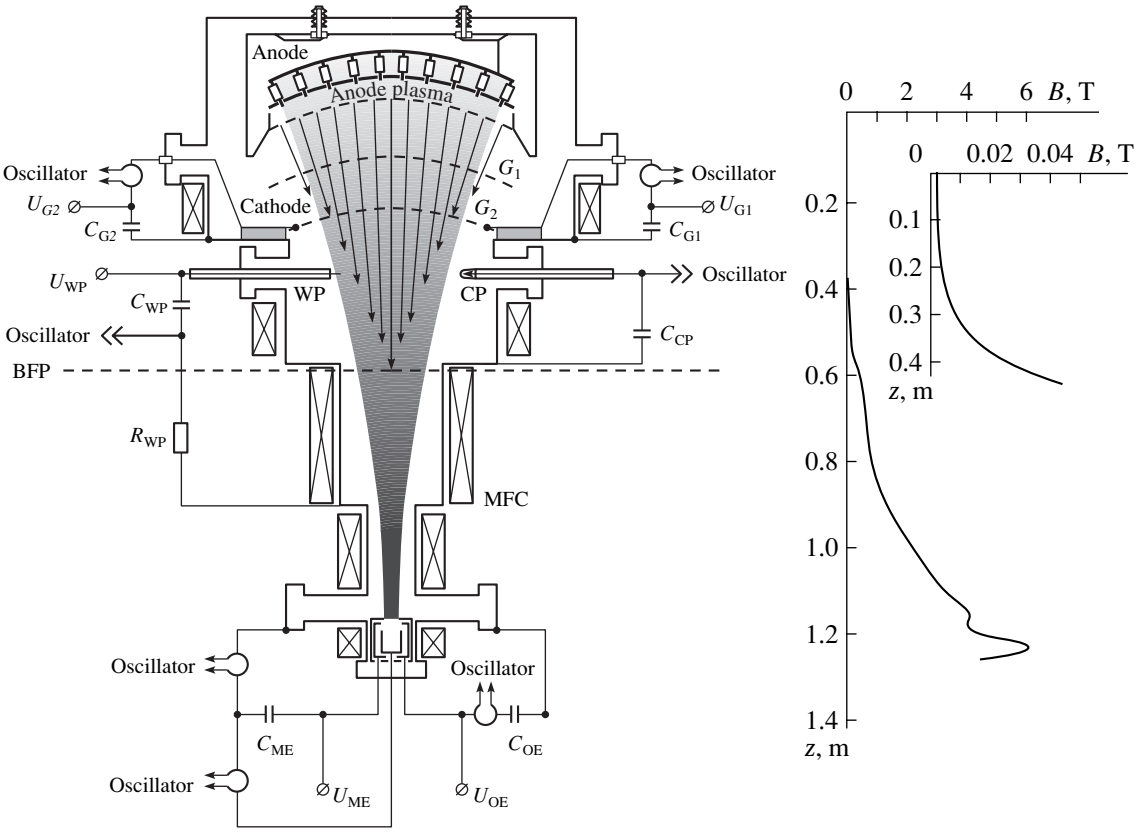

Fig. 1. Schematic diagram of the PROFA installation. BFP, ballistic focus plane; MFC, magnetic focusing coils; WP, wire probe; and CP, capacitive probe.

ThEP with an aperture diameter of 1 mm; the energy density distribution, by movable minicalorimeters. The current density at the entry to the focusing channel was determined with a ThEP moving over the second cathode grid at a distance of 7 cm from it. The current density distribution near the ballistic focus was taken with a movable ThEP and also with a sensor made up of circular electrodes placed behind the grid (the grid is under a negative potential to arrest secondary electrons). The potential of the focusing region was measured with a capacitive transducer. The dynamics of the space charge in the focusing channel was traced with capacitive and wire probes.

EXPERIMENTAL RESULTS

Beam Focusing without External Magnetic Field

Figure 2 shows the distribution of the ion current density measured with the ThEP moving over the second cathode grid. The center of ThEP angular displacement was coincident with the center of curvature of the grid, and the angular position β of the sensor was reckoned from the axis of the system. The data were obtained at an accelerating voltage $U_a \approx 20$ kV and a total ion current of 58 A. Curve *2* was constructed using the modified ion source, where an extra grid of transparency 35% are placed between the discharge electrode and the main grid. Dotted curve *3* corresponds to the Child–Langmuir law for $U = 20$ kV and an accelerating gap (between the anode and the first cathode grid) of 1.5 cm. Some decline at the edges is due to the nonideality of the grid geometry.

It is obvious that the extra grid considerably improves the ion beam. Unfortunately, the ion current markedly decreases in this case. We will be interested largely in the high-current mode of ion source operation (curve *1*). It is seen that the current density distribution at the entry to the focusing channel has the Gaussian shape. In the central part, the current density exceeds the Child–Langmuir values presumably because the plasma penetrates into the accelerating gap.

Figure 3 shows the current density distribution over the cross section of the ballistic crossover. The data were taken with the ThEP under the same conditions as curve *1* in Fig. 2.

Signals from the capacitive probe 40 cm distant from the anode grid and offset from the beam axis by 4 cm are depicted in Fig. 4. The steady-state distribution of the space charge in the beam is set roughly within 3 μs. The beam is underneutralized, the residual potential being about 100 V. At the edges of the transporting channel, the potential is negative. Thus, in the

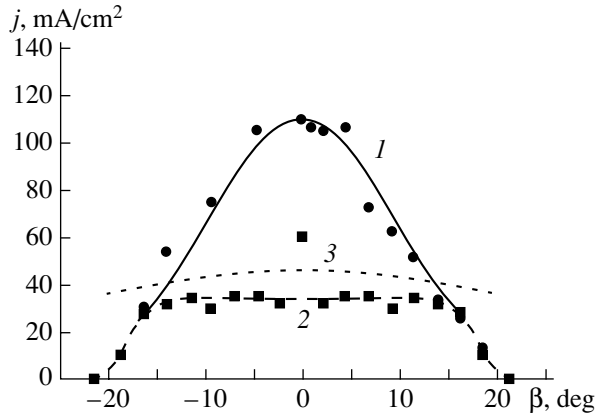

Fig. 2. Current density distribution at the exit from the source vs. ThEP angular position β.

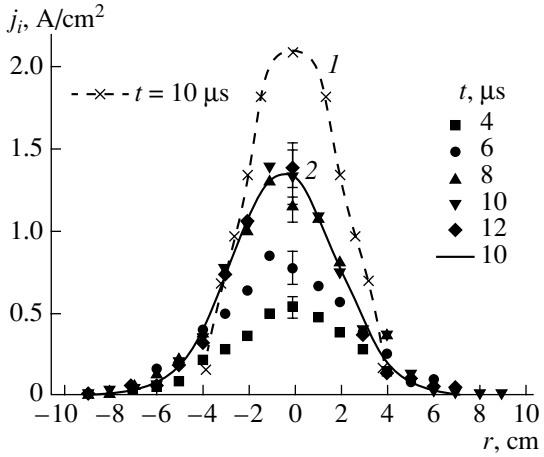

Fig. 3. Current density distribution in the ballistic focus plane (*1*) with and (*2*) without the external magnetic field.

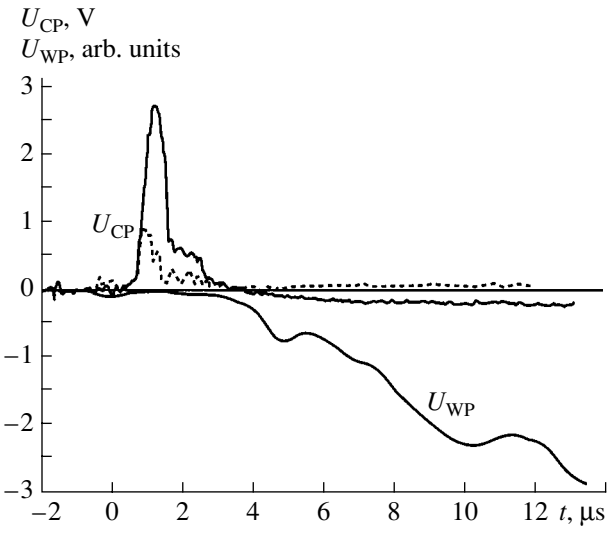

Fig. 4. Waveforms of the signals from the capacitive, U_{CP}, and wire, U_{WP}, probes in the presence (continuous curves) and absence (dashed curves) of the magnetic field.

absence of an external magnetic field, the radial potential distribution indicates the conventional distribution of the space charge in the focusing channel: an underneutralized ion flow surrounded by an "electron coat."

Electrons that neutralize the space charge of the ion beam are due to electron-ion emission from the cathode grids and focusing channel walls. From the waveforms of the current to the cathode grids, one can estimate the coefficients of electron-ion emission for the first and second grids at ν_1 =1.4 and ν_2 = 1.7, respectively. The electron temperature evaluated from the *I–V* characteristic of the ThEP is 20 eV.

Beam Focusing with an External Magnetic Field

The application of a magnetic field improves the beam focusing in the ballistic area. It follows from Fig. 3, where the current density distributions with and without the field are shown.

The signals from the capacitive and wire probes demonstrate the behavior of the space charge in the focusing channel (Fig. 4). The steady-state distribution is set within 3 or 4 μs. Within this time interval, the electrons are accumulated in the focusing channel, as indicated by the signals from the wire probe. In the steady state, the beam is overneutralized, the potential in the transporting channel being approximately –200 V. Information of the space charge evolution can also be gained from the current to the focusing channel wall, whose waveform is shown in Fig. 5. Once the steady-state potential has been established in the focusing channel, this current is negative, indicating the motion of the electrons across the magnetic field. In the presence of the field, the space charge of the beam is neutralized by secondary electrons emitted from the cathode grids. From the grid current waveforms, ν_1 = 1.4 and ν_2 = 1.6. The electron current from the cathode grids exceeds the ion current injected into the focusing channel. The electron temperature equals 100 eV.

The evolution of the space charge and the efficiency of ion beam focusing considerably depend on the target potential. This follows from Figs. 5 and 6, where the time dependences of the current to the focusing channel wall and of the beam focusing efficiency (the ratio between the current to the target and the total beam current) are shown for various target potentials. Two types of the targets were used: a planar aluminum disk of diameter 3 cm and a two-electrode probe (TwEP) with a grounded collector and a grid to which a negative bias is applied (the same as is applied to the planar target).

The disadvantage of the former target is that the current being measured may be affected by electron-ion emission if the negative target potential is sufficiently high. To estimate this effect, we used a TwEP as a target. The results are given in Fig. 6. The difference between the measurements with the TwEP and the planar target is observed only in the initial part of the pulse. Thus, it can be concluded that the secondary

electron emission from the target affects the process of space charge neutralization and the current to the target only within 5–6 μs. Subsequently, the electrons are delivered to the focusing channel primarily by the cathode grids.

The focusing efficiency is the lowest at positive target potentials. This fact is obvious, since the beam electrons are directed to the target in this case and the space charge neutralization becomes difficult. With the target grounded, this effect also takes place, but to a lesser extent compared with the case of a positive target potential. As was noted, under positive target potentials, the beam turns out to be overneutralized. The maximal efficiency of beam transport, 20%, is achieved within 7–8 μs after the pulse has been applied.

The beam focusing efficiency is the highest when the target potential is negative and equals or exceeds that of the second cathode grid. The maximal efficiency, 70%, is achieved within 10 μs after the application of the pulse. Clearly, the accumulation of the electrons in the focusing region proceeds faster in this case, since the target itself contributes to the accumulation process rather than extracts the electrons from the beam. Specifically, this follows from the waveform of the current to the focusing channel wall: at a negative target potential, this current becomes negative 2 μs early and has a larger value.

The focusing efficiency was also measured by the calorimetric method (Fig. 6). Here, the curves correlate well with the data obtained by integrating the waveforms of the beam current and accelerating voltage. This also indicates the reliability of the focusing efficiency measurements.

The energy profile of the ion beam constructed with an array of minicalorimeters is depicted in Fig. 7. The total diameter of the beam is 30 mm; the FWHM, 11 mm.

ANALYSIS OF THE MEASUREMENTS

The measurements were analyzed by numerical simulation. The goal was to elaborate a physical model of beam focusing that provides the best fit to experimental data. We considered several models differing in ways of space charge neutralization computation. The model of choice is as follows.

Electrons neutralizing the positive charge of the ion beam are generated by secondary ion–electron emission from the cathode grids and the target. If the grid and target potentials are the same, the resulting electrons oscillate along the magnetic field lines, providing their equipotentiality. The electrons leave the space occupied by the ion beam, diffusing across the magnetic field. Equating the rates of electron generation and electron diffusion to each other, one can find the electron concentration distribution and, hence, the degree of beam overneutralization. In [6], the problem of transporting an overneutralized ion beam in a uni-

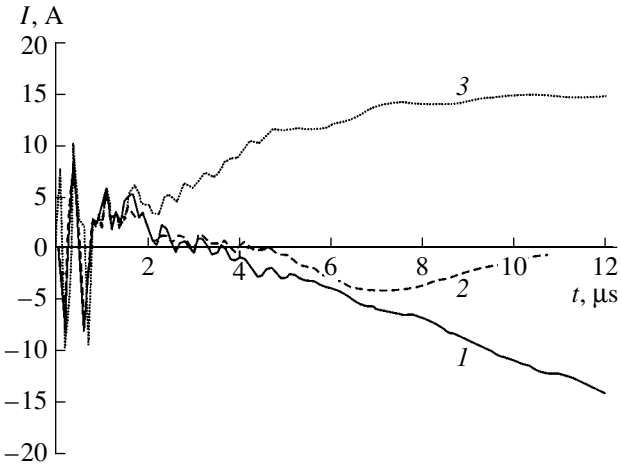

Fig. 5. Waveforms of the current to the focusing channel wall at a (*1*) negative, (*2*) zero, and (*3*) positive target potential.

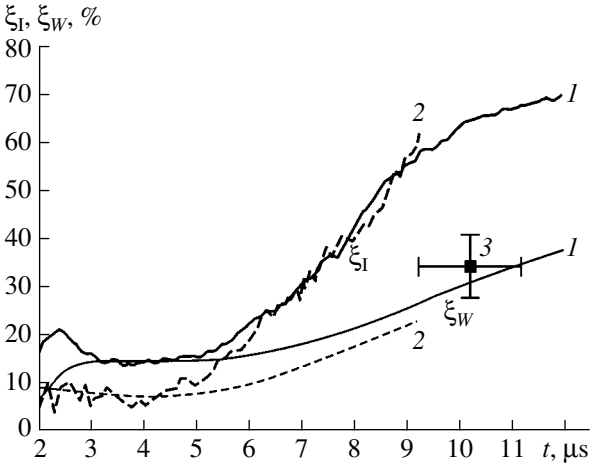

Fig. 6. Beam focusing efficiency in terms of current, ξ_I, and energy, ξ_W, obtained with the (*1*) planar target, (*2*) TwEP, and (*3*) calorimeter.

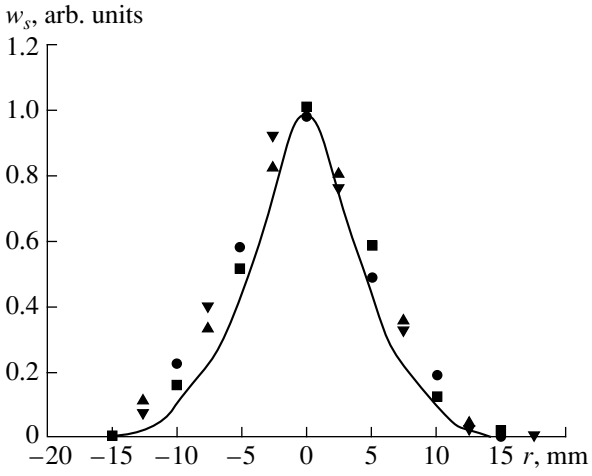

Fig. 7. Profile of the energy density w_s of the ion beam in the target plane normalized to the maximum value. Symbols, experiment; curve, simulation.

form magnetic field was considered for the uniform distribution of the ion current density over the cross section and the uniform transverse velocities of the ions. In our case, the ion beam has a spread in transverse velocities and propagates in the converging magnetic field. Thus, numerical simulation is necessary.

At the beginning of the pulse, the electrons are accumulated in the beam until the electric field changes the sign and the electrons leave the beam. This time interval is estimated from the formula

$$t_c = \frac{L}{V_z}\frac{\alpha_1\alpha_2}{(1-\alpha_1)\alpha_2\nu_1 + (1-\alpha_2)\alpha_1\nu_2}, \quad (1)$$

where L is the beam length; ν_1 and ν_2 are the coefficients of electron–ion emission from the first and second cathode grids, respectively; α_1 and α_2 are the transparencies of the grids; and V_z is the longitudinal ion velocity. For $\nu_1 = 1.4$, $\nu_2 = 1.6$, $\alpha_1 = 0.8$, $\alpha_2 = 0.9$, $L = 1.2$ m, and $V_z = 2 \times 10^6$ m/s, we have $t_c \approx 1$ μs. This is consistent with the experimentally found value.

The accumulation of the electrons ceases when the rate with which the electrons enter into the beam becomes equal to the rate of their diffusion across the magnetic field in the presence of the electric field; i.e.,

$$\nu I_i = -\int_0^L D\rho_e\left(\frac{e}{kT_e}\right)E_r 2\pi r\,dz, \quad (2)$$

where $\nu = (1-\alpha_1)\alpha_2\nu_1 + (1-\alpha_2)\alpha_1\nu_2 + \alpha_1\alpha_2\nu_t$ is the effective (combined) coefficient of electron–ion emission from the cathode grids and the target (ν_t is the coefficient of electron–ion emission from the negatively biased target), I_i is the ion beam current, D is the diffusion coefficient, ρ_e is the electron space charge density, kT_e is the thermal energy of the electrons, e is the charge of an electron, E_r is the radial component of the electric field, and r is the current value of the beam radius.

If the space charge density distribution in the beam is uniform, the electric field strength in terms of the space charge density is given by

$$E_r = \frac{1}{2\varepsilon_0}(\rho_i - \rho_e)r, \quad (3)$$

where ε_0 is the permittivity of free space and ρ_i is the ion space charge density. The Bohm coefficient of electron diffusion across the magnetic field is expressed as

$$D = \frac{1}{16}\frac{kT_e}{eB}, \quad (4)$$

where B is the current value of magnetic induction.

Assuming that the ratio ρ_e/ρ_i does not depend on the radius, we introduce the coefficient of ion beam neutralization

$$k_{ei} = 1 - \rho_e/\rho_i = 1 - Q_e/Q_i, \quad (5)$$

where Q_e and Q_i are the absolute values of the electron and ion charges per unit length.

If the beam is underneutralized (overneutralized), $k_{ei} > 0$ (< 0).

Note also that in a converging magnetic field,

$$B_0 r_0^2 = Br^2, \quad (6)$$

where B_0 and r_0 are the magnetic induction and the beam radius in the emission region.

Substituting (3)–(6) into (2) yields

$$\nu I_i = -\int_0^L \frac{k_{ei}I_i^2}{16\pi\varepsilon_0 V_z^2 B_0 r_0^2}dz = -\frac{k_{ei}I_i^2 L}{16\pi\varepsilon_0 V_z^2 B_0 r_0^2}. \quad (7)$$

Then, for the neutralization coefficient, we have

$$k_{ei} = -16\varepsilon_0\nu\frac{V_z^2 B_0 \pi r_0^2}{I_i L}. \quad (8)$$

For the specified parameters of the PROFA installation, $k_{ei} = -0.004$.

Formula (8) for the neutralization coefficient has been obtained under the assumption that the charge density is uniformly distributed over the beam cross section. Actually, the distribution of the current density and the charge is nonuniform, which would have to change the potential drop in the beam. However, because of the equipotentiality of the magnetic field lines, the potential drop in the beam is retained:

$$\Delta U = \int_0^R \frac{Q(r)}{r}dr = \int_0^{R_0}\frac{Q(r_0)}{r_0}dr_0 = \Delta U_0, \quad (9)$$

where R_0 and R are the initial and current values of the beam envelope.

For this condition to be fulfilled, the neutralization coefficient must vary as

$$k_{ei} = k_{ei0}\frac{\int_0^{R_0}\frac{Q_i(r_0)}{r_0}dr_0}{\int_0^R \frac{Q_i(r)}{r}dr}, \quad (10)$$

where k_{ei0} is the initial value of the neutralization coefficient. The variation required is provided by properly moving the electrons along the magnetic field lines.

In the presence of a magnetic field, a set of equations that describes the transport of an overneutralized ion beam has the form

$$r'' = \frac{V_\Theta^2}{rV_z^2} + \frac{e}{M}\frac{V_\Theta B_z}{V_z^2} - \frac{1}{2}\frac{e}{M}rr'\frac{V_\Theta B_z'}{V_z^2} + \frac{e}{MV_z^2}E_r, \quad (11)$$

$$V_\Theta = -\frac{eB_z}{2M}r\left[1-\frac{r_0^2 B_{z0}}{r^2 B_z}\right] + V_{\Theta 0}\frac{r_0}{r}, \quad (12)$$

$$V_z = V_0\sqrt{\frac{1-V_\Theta^2/V_0^2}{1+r'^2}}, \quad (13)$$

$$E_r = \frac{1}{2\pi\varepsilon_0}\frac{Q(r)}{r}, \quad (14)$$

$$Q(r) = k_{ei}\int_0^r 2\pi\rho_i dr. \quad (15)$$

Here, r_0 and r are the initial and current radial coordinates; V_0, V_Θ, and V_z are the total, azimuth, and longitudinal ion velocities; $V_{\Theta 0}$ is the initial azimuth ion velocity; B_{z0} is the magnetic field induction B_z at the emitter; and $Q(r)$ is the charge per unit beam length enclosed by a cylinder of radius r.

The simulation used the method of tubes of current. The partition into the tubes was performed along the radial coordinate with regard for the emission current density distribution found, as well over the radial and azimuth velocities with appropriate weighting coefficients. The initial form of the distribution function was assumed to be Maxwellian:

$$f_r(V_r) = \left(\frac{M}{2\pi k T_i}\right)^{1/2}\exp^{-\frac{MV_r^2}{2kT_i}}, \quad (16)$$

$$f_\Theta(V_\Theta) = \left(\frac{M}{2\pi k T_i}\right)^{1/2}\exp^{-\frac{MV_\Theta^2}{2kT_i}}, \quad (17)$$

where M and V_r are the ion mass and the ion radial velocity, respectively, and kT_i is the thermal energy of ions.

In the numerical simulation, it is convenient to replace the distribution function over the radial and azimuth velocities by those over the radial, α_r, and azimuth, α_Θ, angles:

$$\tan\alpha_r = \frac{V_r}{V_z}, \quad \tan\alpha_\Theta = \frac{V_\Theta}{V_z}. \quad (18)$$

The angle α_r is reckoned from the normal to the plasma surface. Then, in terms of relative units, the distribution function over the radial angles can be written as

$$f(\alpha_r) = \exp^{-\frac{\tan^2\alpha_r}{\tan^2\alpha_{HWHM}}\ln 2}, \quad (19)$$

$$f(\alpha_\Theta) = \exp^{-\frac{\tan^2\alpha_\Theta}{\tan^2\alpha_{HWHM}}\ln 2}, \quad (20)$$

where α_{HWHM} is the angle corresponding to $f = 1/2$.

As was noted, the partition into tubes of current was performed over both α_r and α_Θ. The function $Q(r)$ was recalculated at each of the integration steps with the relationship

$$Q(r) = k_{ei}\sum_{n=1}^{N}\frac{I_n}{V_{zn}}, \quad (21)$$

where I_n is the current in the tubes with a mean radius smaller than r at a given step and V_{zn} is the particle longitudinal velocity corresponding to the nth tube of current.

To find the true degree of charge neutralization and the initial distribution of the ions over the radial velocities, we calculated the radial distribution of the current density near the ballistic crossover without a magnetic field, varying the degree of charge neutralization k_{ei} and the ion temperature T_i. In addition, we took into consideration the actual geometry of the emission region boundary, which was found by equating the emission current density to the current density obtained from the Child–Langmuir law. The calculations were compared with the measurements. The best agreement was observed for $k_{ei} = 5\times10^{-4}$ and $\alpha_{HWHM} = 36.7$ mrad. The ion temperature,

$$T_i = eU_a\frac{\tan^2\alpha_{HWHM}}{\ln 2}$$

equals 40 eV. The potential well in the beam,

$$\Delta U = \frac{k_{ei}}{4\pi\varepsilon_0}\int_0^R\frac{Q(r)}{r}dr,$$

calculated from known k_{ei} agrees well with the value measured. Using the ion distribution over the radial velocities, we simulated the passage of the beam to the target in the presence of a magnetic field. Since formula (8) is an estimator, the neutralization coefficient was varied in wide limits. The initial value of α_{HWHM} was taken to be equal to 36.7 mrad. Eventually, we found the fraction of the current that reaches the target vs. neutralization coefficient k_{ei0} (Fig. 8). From this curve, it follows that the maximal current reaching the target, about 53% of the total current, is observed for $k_{ei} = -0.00075$. This value is lower than that found experimentally. The point is that the particles whose longitudinal velocity was below 25% of the total velocity, were omitted from the consideration, although some of them still could reach the target after multiple oscillations along the beam. Figure 7 shows the energy density distribution along the beam radius at the target. It is seen that the simulation and the experiment are in good agreement.

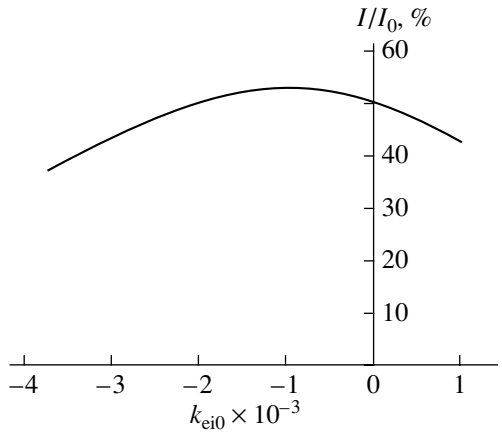

Fig. 8. Fraction of the current reaching the target vs. neutralization coefficient.

CONCLUSION

The focusing of an intense proton beam involves two stages: ballistic focusing and magnetic compression. The basic parameters of the beam (angular divergence, as well as the current density distributions at the entry to the focusing channel, near the ballistic crossover, and at the target) were studied. Data for the space charge evolution in the focusing channel were obtained, and the degree of space charge neutralization with and without an external magnetic field is determined.

The neutralization of the space charge of the beam is associated with secondary electrons emitted from the cathode grids and the target. In the absence of the magnetic field, the beam is underneutralized, the degree of underneutralization being 5×10^{-4}. In the presence of the magnetic field, the beam is overneutralized, the degree of overneutralization being $(1–4) \times 10^{-3}$. The focusing is the most efficient when the target is under a negative potential equal to or exceeding that of the second cathode grid. In this case, the maximal fraction of the current reaching the target, 70%, is observed within 10 μs after the pulse has been applied. For this time, the quasi-steady-state distribution of the space charge in the focusing channel sets up. The beam diameter on the target that was estimated from the FWHM of the energy density distribution in the beam is 11 mm. Thus, the coefficient of beam compression in terms of cross-sectional area is 1.6×10^3, which agrees with the results of simulation.

The numerical simulation of beam focusing was performed. Comparing its results with the measurements, we found the initial angular distribution of the ions, their temperature, and the degree of neutralization of the beam. The focusing efficiency and the radial distribution of the current density found by calculation are consistent with the measurements. This means that our computer model can be applied to designing installations similar to the PROFA.

In general, our experiments and simulation imply that the scheme for ion beam focusing reported in [1] offers a high efficiency.

REFERENCES

1. H. Wuerz, G. A. Viazmenova, V. S. Kuznetsov, and V. I. Engelko, Zh. Tekh. Fiz. **67** (5), 73 (1997) [Tech. Phys. **42**, 522 (1997)].
2. V. Engelko, H. Giese, and S. Schalk, in *Proceedings of the 11th International Conference on High Power Particle Beams (Beams'96), Prague, 1996*, p. 95.
3. V. Engelko, H. Giese, and S. Schalk, IEEE Trans. Plasma Sci. **25**, 722 (1997).
4. V. Engelko, H. Giese, and S. Schalk, in *Proceedings of the 11th International Conference on High Power Particle Beams (Beams'96), Prague, 1996*, p. 1111.
5. S. Schalk, *Wissenschaftliche Berichte. FZKA 6075* (Forschungszentrum, Karlsruhe, 1998).
6. M. D. Gabovich, A. A. Goncharov, and I. M. Protsenko, Zh. Tekh. Fiz. **48**, 86 (1978) [Sov. Phys. Tech. Phys. **23**, 50 (1978)].

Translated by V. Isaakyan

Technical Physics, Vol. 47, No. 3, 2002, pp. 357–360. Translated from Zhurnal Tekhnicheskoĭ Fiziki, Vol. 72, No. 3, 2002, pp. 76–79.

ELECTRON AND ION BEAMS, ACCELERATORS

Generation of Electron Beams in High-Aspect-Ratio Magnetron Guns with Secondary Emission Cathodes

N. I. Aĭzatskiĭ, A. N. Dovbnya, V. V. Zakutin, N. G. Reshetnyak, V. P. Romas'ko, Yu. Ya. Volkolupov, and M. A. Krasnogolovets

Uskoritel' Research Complex, Kharkov Institute of Physics and Technology, Ukrainian Scientific Center, Akademicheskaya ul. 1, Kharkov, 61108 Ukraine

Received May 21, 2001

Abstract—The generation of electron beams in high-aspect-ratio magnetron guns with cold metallic secondary-emission small-diameter cathodes is discussed. The parameters of the beams as functions of the electric and magnetic fields are studied for various ways of generating voltage pulses needed for the secondary emission multiplication of the electrons and the beam generation. *© 2002 MAIK "Nauka/Interperiodica".*

INTRODUCTION

Interest in magnetron guns with cold metallic cathodes operating in the secondary emission mode [1–8] is dictated by their advantages over other electron guns, such as long service time, high current density, simple design, etc. Therefore, they are promising for electron sources in accelerators and high-power reliable microwave devices [2, 9–11]. In these guns, the back bombardment of the cathode by primary electrons is employed. The bombardment causes the secondary emission multiplication of the electrons and produces an electron cloud from which an electron beam is formed [1–4, 8] in crossed electric and magnetic fields. This work studies the generation of the beams in magnetron guns with cold secondary-emission small-diameter (2–5 mm) cathodes.

EXPERIMENTAL SETUP AND TECHNIQUES

The generation of electron beams in magnetron guns with cold secondary emission cathodes was studied with a setup depicted in Fig. 1. Negative pulses (amplitude 4–100 kV, duration 4–10 μs, and repetition rate 50 Hz) from modulator *1* are applied to cathode *5* of the gun. Its anode *6* is grounded through the resistor R_3 and is connected to pulse generator *2*. Two cases of the secondary emission multiplication of electrons were used. In the former case, the multiplication of the electrons was accomplished during the trailing edge of the specially shaped voltage pulse from modulator *1*; in the latter, during the trailing edge of the voltage pulse from generator *2*.

The magnetron gun with 2-mm-diam. copper cathode and the 120-mm-long anode made of copper or stainless steel was placed in vacuum chamber *3*, evacuated to a pressure of $\leq 10^{-6}$ torr.

The magnetic field for generating and transporting the beam was produced by solenoid *4*, consisting of four separately fed sections with a total length of 550 mm. Such a configuration allows the spatial variation of the magnetic field amplitude and distribution. The beam was transported by a distance of 80–160 mm from the anode plane to the Faraday cup.

The beam current was measured with Faraday cup *7*, made in the form of a coax, and the resistor $R_4 = 12\ \Omega$ (the resistor value equals the wave impedance of the coax); the cathode voltage, with the voltage divider R_1–R_2; and the size of the beam, from its image on an X-ray film and on a molybdenum foil both placed at the end face of the coax.

RESULTS AND DISCUSSION

Beam Generation in Magnetron Guns

It has been shown [6, 8] that a magnetron gun with secondary emission cathodes forms a tubular electron beam with its inner diameter roughly equal to the diameter of the cathode. The thickness of the beam wall is usually 1.5–2.0 mm. We studied the process of beam generation and measured the beam parameters in the guns with cathode diameters of 2 and 5 mm and with anode diameters of 10, 22, 50, and 78 mm. The aspect ratio R_a/r_c (the ratio of the radius of the anode R_a to that

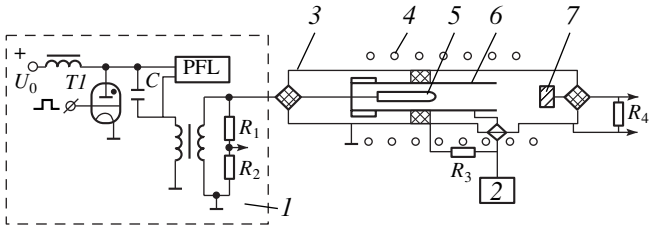

Fig. 1. Experimental setup.

1063-7842/03/4702-0357$22.00 © 2002 MAIK "Nauka/Interperiodica"

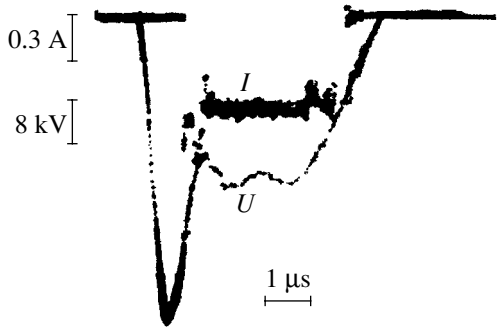

Fig. 2. Beam current and cathode voltage waveforms.

of the cathode r_c) was thus varied between 5 and 39. This range of the aspect ratio has not been considered in detail.

The interelectrode electric field needed for beam generation in the magnetron gun must have an overshoot, followed by a region where it is constant. The overshoot provides the secondary emission multiplication and the formation of the electron cloud around the cathode; in the constant field region, the secondary emission process becomes steady and the beam is generated [1, 3, 8]. The steepness and the duration of the overshoot define the beam generation stability and the stability of the formation of the beam current pulse front. The steepness providing the secondary emission multiplication must exceed 20–30 kV/μs [1, 8]. Subsequently, the top of the pulse flattens and the steady stage of the beam generation sets in. A ripple at the flat part of the top may either cause or, conversely, suppress the modulation of the beam current pulse. In addition, the ripple may lead to the generation of several electron bunches per voltage pulse [8] and also specifies the allowable energy spread in the electron beam. Therefore, when carrying out the experiments, we paid much attention to obtaining the desired time dependence of the voltage between the anode and the cathode. The desired field was provided by generating a specially shaped voltage pulse (which had a short overshoot and the long flat part) at the cathode or by simultaneously applying specially shaped field-forming voltage pulses to both electrodes.

Table

d, mm	*D*, mm	*U*, kV	*I*, A	*H*, Oe
2	50	40–55	0.8	800–1200
2	50	40–55	7	2500
2	78	40–55	1.0	700–1200
5	50	45–55	0.5	1150
5	50	45–55	1.0	1300
5	50	45–55	10	2200
5	78	26	0.5	350
5	78	26	3	1100

The Formation of the Desired Time Dependence of the Field

The first approach is to generate a cathode voltage pulse with an overshoot. In a modulator where the pulse-forming line (PFL) is completely discharged, such a pulse (having an overshoot and the flat part) can be generated with the tuning capacitor *C* (Fig. 1), connected parallel to the beam-forming line [12]. One can control the overshoot by varying the value of *C*. In this case, generator *2* is switched off. The PFL had a wave impedance of 40 Ω, and the FWHM of the pulse was 4.5 μs. Without the tuning capacitor, the modulator voltage pulse had an overshoot whose amplitude was ≈25% of that of the flat part of the pulse, which turned out to be insufficient for the beam generation. With the tuning capacitor C = 7.5 nF connected, the overshoot increased to 50% of the flat part amplitude, and for C = 15 nF, the overshoot was as high as 80%. The respective steepnesses were 25 and 40 kV/μs, and the overshoot decay time was found to be 0.6 μs. Such conditions provided the secondary emission multiplication and beam generation. The modification of this approach is the application of two voltage pulses to the common load (cathode). The first is a long flat-top pulse and the other, a short fast-decaying pulse. In this way, we obtain a voltage pulse with the shape close to that described above.

Figure 2 shows typical waveforms of the voltage pulse *U* at the cathode and of the beam current *I* at the Faraday cup that were generated with the PFL described above. The diameters of the anode and the cathode were 2 and 50 mm, respectively. For the amplitude of the flat part ≈32 kV, the beam current was 0.6 A (at a magnetic field of ≈800 Oe) and the steepness was >40 kV/μs. It is seen that the secondary emission multiplication starts when the voltage overshoots decays, while the flat part of the pulse corresponds to the steady stage of the beam generation. As follows from the waveforms, the energy of most electrons in the descending branch of the pulse exceeds their energy at the steady stage of the beam generation. This extends the energy spectrum of the beam. To diminish the spread in the particle energy and cut the rise time of the current pulse, it is necessary to cut the decay time and increase the decay steepness. This can be done with another PFL.

The second approach to obtaining the desired time dependence of the electric field in the anode–cathode gap is to apply two pulses. The first is a long flat-top pulse applied to the cathode, and the second one is a short fast-decaying pulse applied to the cathode [6]. The long flat-top voltage pulse from modulator *1* (with the capacitor *C* disconnected) is applied to the cathode of the gun. Then, generator *2* is connected to the resistor R_3 and the short fast-decaying pulse is applied to the

anode with some time delay. In the anode–cathode gap, these pulses provide the time dependence of the electric field that is necessary for the beam generation. Note that the separation of pulse application circuits allows the use of a wideband transmission line to apply the pulse from generator *2* to the anode. The decay time of the anode pulse may attain several nanoseconds; its steepness, ≈1000 kV/μs. These values provide the secondary emission multiplication and the synchronization of the beam current pulses.

Beam Parameters

We studied the parameters of the beams generated by both approaches. It was found that the beam current amplitude at the Faraday cup has a threshold dependence on the decay steepness and does not depend on the approach to secondary emission excitation. Figure 3 demonstrates the beam current (current at the Faraday cup) vs. cathode voltage for the anode diameters mentioned above. It is seen that the data points fit the Child–Langmuir law. For each of the data points, the magnetic field was evaluated from the maximal value of the beam current. For example, for the cathode diameter 2 mm, the anode diameter 50 mm, and the cathode voltage amplitude 50 kV, the beam current was found to be 7 A. This corresponds to the peak power 350 kW and the microperveance ≈0.6. The magnetic field strength in this case is 2900 Oe.

We also studied the generation of electron beams in magnetron guns with cathode diameters of 2 and 5 mm and anode diameters of 50 and 78 mm in various magnetic fields. For the cathode diameter 2 mm, the amplitude of the flat part 40–55 kV, and moderate magnetic fields (70–1200 Oe), the electron beams generated had a current ranging from 0.5 to 1.5 A (the cutoff field in this case is between ≈600 and ≈400 Oe). The outer diameter of the beam was ≈15 mm. As the magnetic field grows to 2500–3000 Oe, the beam current increases to 5–7 A. In this case, the beam had inner and outer diameters of 2 and 4 mm, respectively, at a distance of 130 mm from the anode plane for cathode and anode diameters of 2 and 50 mm. Similar results were obtained when the cathode diameter was 5 mm with the same anode diameters.

In another series of the experiments, the electron energy was 60 keV and the beam current, 10 A. The outer diameter of the beam was 5 mm. As follows from the simulation, for an energy spread in the beam from 0 to 20%, the diameter increases by no more than 20% when the beam is transported in a decaying magnetic field by a distance of 150 mm. This is consistent with the experimental data. The table lists the current I at the Faraday cup, cathode voltage U, and magnetic field strength H.

As follows from the aforesaid, the Larmor radius of the electrons is relatively large in low magnetic fields; yet, the electrons gain the energy sufficient for the secondary emission multiplication and beam generation. The electronic layer occupies a considerable part of the interelectrode space near the cathode in the transverse direction. The potential dip in the interelectrode gap, which is associated with the space charge of the electronic layer, provides the secondary emission multiplication and beam generation at the steady stage of the gun operation. At high magnetic fields, the Larmor radius decreases and the electronic layer near the cathode considerably shrinks in the transverse direction. In this case, the potential dip is larger and the electrons can gain the energy sufficient for the secondary emission multiplication to take place within a shorter distance. Also, under high magnetic fields, the space charge of the electronic layer grows; hence, the beam current increases. It appears that the high-aspect-ratio guns have a wide beam generation region (or several narrower regions), the transverse size of which (and also the beam current) varies with the magnetic field.

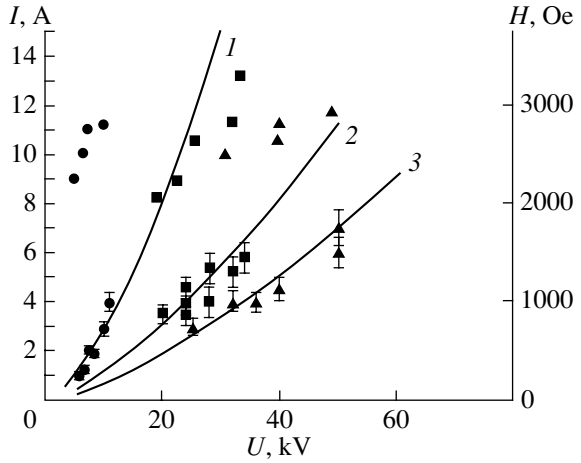

Fig. 3. Beam current vs. cathode voltage for the anode diameter (*1*) 10, (*2*) 22, and (*3*) 50 mm. The cathode diameter is 2 mm.

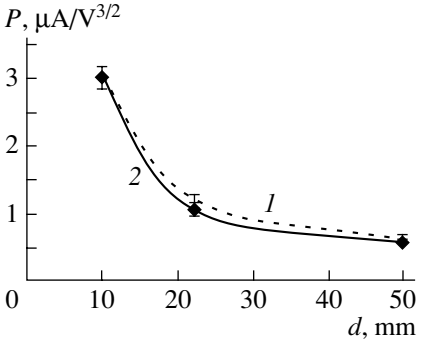

Fig. 4. Beam microperveance vs. anode diameter: (*1*) simulation and (*2*) experiment.

In Fig. 4, the microperveance of the beam formed in the magnetron gun with a cathode diameter of 2 mm is plotted against the anode diameter. The microper-

veance is seen to vary within wide limits, and the curve is well described by the perveance vs. anode diameter dependence in the form $1/(R_a - r_c)$. The point is that in an extended cylindrical diode with the constant-biased cathode and a high aspect ratio ($R_a/r_c > 5$), the electron current is inversely proportional to the anode radius (see, e.g., [13]). In this case, the current at the Faraday cup is governed by two factors. The first one is the electron density in the interelectrode space along the axis of the gun. It depends on the electric field strength at the cathode and on the anode radius. The other factor is the effect of the anode output, which serves as an electrostatic lens extracting the beam from the gun. If the cathode voltage is constant, this factor depends on the anode diameter only slightly, because the edge electric field near the axis has a large longitudinal component and the electrons gain a considerable energy before they reach the anode end, where the transverse component of the field is large. Therefore, the current amplitude at the Faraday cup will depend only on the electron concentration in the anode–cathode gap, which, in its turn, depends on the anode radius (Fig. 4).

CONCLUSION

Our study shows that the processes of secondary emission multiplication and beam generation can be triggered by various pulse-formation techniques. It is demonstrated that high-aspect-ratio magnetron guns have a wide magnetic field zone where the beams are generated. Electron beams with an outer radius of ≈4 mm and a particle energy of 5–60 keV are obtained for a magnetic field strength of ≈2500 Oe.

REFERENCES

1. V. M. Lomakin and D. V. Panchenko, Élektron. Tekh., Ser. Élektron. SVCh, No. 2, 33 (1970).
2. J. F. Skowron, Proc. IEEE **61** (3), 69 (1973).
3. S. A. Cherenshchikov, Élektron. Tekh., Ser. 1, No. 6, 20 (1973).
4. A. V. Agafonov, V. P. Tarakanov, and V. M. Fedorov, Vopr. At. Nauki Tekh., Ser. Yad.-Fiz. Issled., Nos. 2–3 (29–30), 134 (1997).
5. Y. M. Saveliev, W. Sibbett, and D. M. Parkes, Phys. Plasmas **4**, 2319 (1997).
6. A. N. Dovbnya, V. V. Zakutin, N. G. Reshetnyak, *et al.*, Vopr. At. Nauki Tekh., Ser. Yad.-Fiz. Issled., No. 4, 34 (1999).
7. N. I. Aĭzatskiĭ, A. N. Dovbnya, V. V. Zakutin, *et al.*, in *Radio Engineering: All-Ukraine Scientific and Technical Collection* (1999), Vol. 111, pp. 59–63.
8. A. N. Dovbnya, V. V. Zakutin, N. G. Reshetnyak, *et al.*, Zh. Tekh. Fiz. **71** (2), 98 (2001) [Tech. Phys. **46**, 227 (2001)].
9. G. M. Ivanov, L. A. Makhnenko, A. N. Opanasenko, and S. A. Cherenshchikov, Vopr. At. Nauki Tekh., Ser. Yad.-Fiz. Issled., Nos. 4–5 (31–32), 40 (1997).
10. V. M. Vigdorchik, V. D. Naumenko, and V. P. Timofeev, Dokl. Akad. Nauk Ukr. SSR, Ser. A: Fiz.-Mat. Tekh. Nauki, No. 7, 633 (1975).
11. V. D. Naumenko and S. A. Cherenshchikov, Izv. Vyssh. Uchebn. Zaved., Radiofiz. **27**, 250 (1984).
12. G. A. Mesyats, *Generation of High-Power Nanosecond Pulses* (Sov. Radio, Moscow, 1974).
13. V. F. Vlasov, *Electrovacuum Devices* (GIL, Moscow, 1949).

Translated by V. Isaakyan

Technical Physics, Vol. 47, No. 3, 2002, pp. 361–363. Translated from Zhurnal Tekhnicheskoĭ Fiziki, Vol. 72, No. 3, 2002, pp. 80–82.

BRIEF COMMUNICATIONS

Relation between the Expansions of an External Potential in Spherical Functions and Spheroidal Harmonics

V. A. Antonov and A. S. Baranov

Pulkovo Observatory, Russian Academy of Sciences, Pulkovskoe shosse 65, St. Petersburg, 196140 Russia

Received April 11, 2001; in final form, July 9, 2001

Abstract—Relations between the coefficients of the expansions of external potentials in spherical and spheroidal functions for finite bodies are derived. These formulas have a more compact and convenient form than those obtained by other authors. © *2002 MAIK "Nauka/Interperiodica".*

INTRODUCTION

Nowadays, the issue of relating various expansions of harmonic functions is topical for many electrostatic problems, in particular, for calculating the capacitive characteristics of systems of bodies. Similar challenges are encountered in studies of electromagnetic and acoustic waves propagating in the presence of obstacles with characteristic sizes much less than the wavelength.

From the mathematical standpoint, the same issue arises as applied to the motion of artificial celestial bodies. For functions that are harmonic in the outer space, the transition from the expansion in spheroidal functions to that in ordinary spherical harmonics (and vice versa) has apparently first been derived in [1] but in the rather awkward form. In classical books [2–4], these expansions are used separately without specifying relations between them.

The compact formulas have been given in [5] without derivation. They are also quoted in [6]. However, we will show that one of these formulas is incorrect, although the correct formula has a similar structure. One of the relations is also presented in [7] but in pass, among other similar and more general formulas. Moreover, it is difficult to use because of the unclear normalization of the function. The authors of [8–10], who were not familiar with [5], somewhat improved the transformation formulas [1]; yet, the expressions remained unwieldy. This forces us to reconsider the problem.

DERIVATION OF THE FORMULAS

As it was noted, we should consider elementary spherical and spheroidal harmonic functions:

$$U_{nk} = r^{-n-1}P_n^{|k|}(\cos\theta)e^{ik\psi}, \tag{1}$$

$$V_{nk} = q_n^{|k|}(\tau)P_n^{|k|}(t)e^{ik\psi} \quad (n = 0, 1, 2, \ldots, -n \le k \le n). \tag{2}$$

Here, P_n^k are the associated Legandre polynomials of the first kind and r, θ, and ψ are the ordinary polar coordinates in space. The spheroidal coordinates t, τ, and ψ are related to both the polar coordinates and the Cartesian ones x, y, and z by the relationships

$$r\sin\theta = \sqrt{x^2+y^2} = c\sqrt{(1-t^2)(1+\tau^2)}, \quad r\cos\theta = z = ct\tau(-1 \le t \le 1, \tau \ge 0), \tag{3}$$

where $2c$ is the focal distance in the chosen system of spheroidal coordinates (the system related to a flattened spheroid is used because of its practical importance for problems of mathematical physics).

It will suffice to consider the case $k \ge 0$, since the transition to negative k is equivalent to complex conjugation. The functions $q_n^k(\tau)$ are essentially the Legandre functions of the second kind of an imaginary argument. However, various authors give different definitions for these functions, which differ in normalizing factor. For the clearness' sake, we employ the normalization condition $q_n^k(\tau) = \tau^{-n-1} + O(\tau^{-n-3})$, since in this case both function (1) and (2) asymptotically coincide at large distances r for $c = 1$. Then, as is known,

$$\frac{q_n^k(\tau)}{(1+\tau^2)^{k/2}} = \frac{(2n+1)!!}{(n+k)!} \times \sum_{m=n}^{\infty} \frac{(m+k)!(-1)^{(n-m)/2}}{(m-n)!!(n+m+1)!!}\tau^{-m-k-1}. \tag{4}$$

On the other hand, the following formula is also well known (we represent it in terms of our normalization:

$$\frac{1}{y-x} = \sum_{m=0}^{\infty} \frac{m!}{(2m-1)!!}P_m(x)Q_m(y), \tag{5}$$

1063-7842/03/4702-0361$22.00

where $Q_m(y)$ are the Legandre functions of the second kind normalized at infinity as $Q_m(y) = y^{-m-1} + \ldots$ and x and y are arbitrary complex numbers satisfying the inequality $|x| < |y|$.

Substituting $y = iu$ into (5), we obtain

$$\frac{1}{iu - x} = \sum_{m=0}^{\infty} \frac{m!}{(2m-1)!!} P_m(x) i^{-m-1} q_m(u)$$

or

$$\frac{1}{u + ix} = \sum_{m=0}^{\infty} \frac{i^{-m} m!}{(2m-1)!!} P_m(x) q_m(u). \quad (6)$$

We should also take into account the well-known representation of the Legandre polynomial:

$$P_m(x) = \sum_{n=0}^{m}{}^{*} (-1)^{(m-n)/2} \frac{(m+n-1)!!}{n!(m-n)!!} x^n. \quad (7)$$

In (7) and further, the asterisk at the summation sign means that only the terms with the same evenness of m and n are added up. Then, relationship (6) takes the form

$$\frac{1}{u + ix} = \sum_{m=0}^{\infty} \sum_{n=0}^{m}{}^{*} i^{-m} (-1)^{(m-n)/2} \times \frac{(m+n-1)!! m!}{n!(m-n)!!(2m-1)!!} x^n q_m(u), \quad (8)$$

where u and x may be considered to be real if $u > x$.

Let us collect in both sides of (8) the terms with the same power of x^n. Then,

$$u^{-n-1} = \frac{1}{n!} \sum_{m=n}^{\infty}{}^{*} \frac{(m+n-1)!! m!}{(m-n)!!(2m-1)!!} q_m(u).$$

Differentiating this relationship k times yields

$$u^{-n-k-1} = \frac{1}{(n+k)!} \times \sum_{m=n}^{\infty}{}^{*} \frac{(m+n-1)!!(m+k)!}{(m-n)!!(2m-1)!!} \frac{q_m^k(u)}{(1+u^2)^{k/2}}. \quad (9)$$

Having found a number of auxiliary relationships, we turn to the direct construction of the coefficients α and β in the transformation formulas, which should have the form

$$U_{nk} = \sum_{m=n}^{\infty}{}^{*} \alpha_{nmk} V_{mk}, \quad V_{nk} = \sum_{m=n}^{\infty}{}^{*} \beta_{nmk} U_{mk}. \quad (10)$$

In (10), we have already taken into account the natural restrictions: the index k is not involved in the summation and the summation over m is restricted by the values of the same evenness as a given n. This follows from the symmetry considerations and was taken into account in [1, 8–10]. In order to determine α and β, it suffices to consider only points in the vicinity of the polar axis, i.e., consider an asymptotics at small θ. First of all, it is known that

$$P_n^k(\cos\theta) = 2^{-k}\{(n+k)!/[k!(n-k)!]\}\sin^k\theta + O(\sin^{k+2}\theta).$$

Correspondingly,

$$U_{nk} \approx z^{-n-1} e^{ik\psi} \frac{2^{-k}(n+k)!}{k!(n-k)!} \sin^k\theta \approx \frac{2^{-k}(n+k)!}{k!(n-k)!} \frac{(x+iy)^k}{z^{n+k+1}} \quad (11)$$

holds in the vicinity of the polar axis. A similar representation for V_{nk} may be found by going from the spheroidal coordinates to the Cartesian ones:

$$c(1-t^2)^{1/2} = [(x^2+y^2)/(1+\tau^2)]^{1/2} = \{(x^2+y^2)/[1+(z/ct)^2]\}^{1/2}.$$

Then,

$$V_{nk} \approx q_n^k\left(\frac{z}{c}\right) e^{ik\psi} 2^{-k} \frac{(n+k)!}{k!(n-k)!} \frac{(x^2+y^2)^{k/2}}{c^k\left[1+\left(\frac{z}{c}\right)^2\right]^{1/2}} = 2^{-k} \frac{(n+k)!}{k!(n-k)!} (x+iy)^k \frac{q_n^k\left(\frac{z}{c}\right)}{c^k\left[1+\left(\frac{z}{c}\right)^2\right]^{1/2}} \quad (12)$$

in the same approximation.

Substituting formulas (11) and (12) into the first relation of (10), we leave only principle terms of the order of $(x + iy)^k$ in the expansion in x and y. These terms should coincide irrespective of the other terms of higher orders of smallness. Hence, making the substitution $z/c = u$, we have

$$\frac{(n+k)!}{(n-k)!} u^{-n-k-1} = \sum_{m=n}^{\infty}{}^{*} \alpha_{nmk} \frac{(m+k)!}{(m-k)!} c^{n+1} \frac{q_m^k(u)}{(1+u^2)^{k/2}}. \quad (13)$$

Comparing (13) and (9), we arrive at

$$\alpha_{nmk} = \frac{c^{-n-1}}{(n-k)!} \frac{(m+n-1)!!(m-k)!}{(m-n)!!(2m-1)!!}. \quad (14)$$

The equality

$$\frac{(n+k)!}{(n-k)!}\frac{q_n^k(u)}{(1+u^2)^{k/2}} = \sum_{m=n}^{\infty *}\beta_{nmk}\frac{(m+k)!}{(m-k)!}c^{-m-1}u^{-m-k-1} \quad (15)$$

is found in a similar way.

From (15) and (4),

$$\beta_{nmk} = \frac{(2n+1)!!}{(n-k)!}\frac{(m-k)!(-1)^{(n-k)/2}}{(m-n)!!(n+m+1)!!}c^{m+1}. \quad (16)$$

Finally, on the basis of (14) and (16), we can write the desired formulas in the form

$$U_{nk} = \frac{c^{-n-1}}{(n-k)!}\sum_{m=n}^{\infty *}\frac{(m+n-1)!!(m-k)!}{(m-n)!!(2m-1)!!}V_{mk}, \quad (17)$$

$$V_{nk} = \frac{(2n+1)!!}{(n-k)!}\sum_{m=n}^{\infty *}\frac{(-1)^{(n-m)/2}(m-k)!c^{m+1}}{(m-n)!!(m+n+1)!!}U_{mk}. \quad (18)$$

Formula (17) coincides with that given in [5, 6] up to the normalization and notation. However, (18) differs from the corresponding one given in those works. This formula can be verified by comparing its right and left parts for a point located at the equator ($t = 0$). Then, (18) turns into the expansion $q_n^k(\tau)$ in inverse powers of $(1 + \tau^2)$ and can readily be verified.

Formulas (17) and (18) may be verified by taking into account their self-consistence: the substitution of one formula into the other should result in the identity (the sum over m is determined by the transition to the integral representation of the Euler beta function).

Recall that in the literature, various systems of spheroidal harmonic functions differing in normalization occur. However, the transition from one normalization to another in formulas (17) and (18) is quite easy, and the expressions for α and β remain rather simple monomials.

In [11], it has been proposed to use expansions related to triaxial ellipsoids. It seems that the transformation of these expansions into those in spherical functions can also be found in this case.

REFERENCES

1. M. Hotine, *Mathematical Geodesy* (Department of Commerce, Washington, DC, 1969), ESSA Monograph, No. 2.
2. E. Heine, *Handbuch der Kugelfunctionen*, Band II: *Anwendungen der Kugelfunctionen und der verwandten Functionen* (G. Reimer, Berlin, 1881).
3. E. W. Hobson, *The Theory of Spherical and Ellipsoidal Harmonics* (Cambridge Univ. Press, Cambridge, 1931; Inostrannaya Literatura, Moscow, 1952).
4. R. A. Lyttleton, *The Stability of Rotating Liquid Masses* (Cambridge Univ. Press, Cambridge, 1953).
5. V. S. Protsenko, Dokl. Akad. Nauk Ukr. SSR, Ser. A: Fiz.-Mat. Tekh. Nauki, No. 6, 32 (1984).
6. V. T. Erofeenko, *Addition Theorems* (Nauka i Tekhnika, Minsk, 1989).
7. W. Miller, Jr., *Symmetry and Separation of Variables* (Addison-Wesley, Reading, 1977; Mir, Moscow, 1981).
8. C. Jekeli, Manuscr. Geod. **13**, 106 (1988).
9. D. M. Gleason, Manuscr. Geod. **13**, 114 (1988).
10. M. S. Petrovskaya and A. N. Vershkov, Bolletino di Geodesia e Scienze Affni **59**, 57 (2000).
11. D. V. Zagrebin, *Foundations of Geometrical Geodesy* (Nauka, Leningrad, 1981).

Translated by M. Fofanov

Technical Physics, Vol. 47, No. 3, 2002, pp. 364–367. Translated from Zhurnal Tekhnicheskoĭ Fiziki, Vol. 72, No. 3, 2002, pp. 83–86.

BRIEF COMMUNICATIONS

Evolution of Short-Range, Mesoscopic, and Long-Range Orders in Magnesium–Zinc Ferrites

Z. A. Samoĭlenko*, N. N. Ivakhnenko*, V. P. Pashchenko*, O. V. Kopaev, B. K. Ostafiĭchuk**, and I. M. Gasyuk****

** Galkin Physicotechnical Institute, National Academy of Sciences of Ukraine, Donetsk, 83114 Ukraine*

*** Stefanik Carpathian State University, ul. Shevchenko 57, Ivano-Frankovsk, 76025 Ukraine*

Received April 4, 2001; in final form, June 8, 2001

Abstract—The Mössbauer and X-ray diffraction techniques are used to study the evolution of structure and chemical inhomogeneities in magnesium–zinc ferrites. These are the octahedral short-range environment of a magnetic Fe^{3+} ion, mesoscopic quasi-planar regions of size 100–200 Å (clusters) with locally changed chemical composition and crystallographic order, and the general long-range order of the ferrite matrix. In each of these three inhomogeneities, the high-temperature long-term firing of the Mg–Zn ferrite (T = 1280°C, τ = 0–8 h) induces transitions (magnetic in the short-range order, concentration in the clusters, and structural in the matrix) within the time period τ = 1–2 h. Subsequently, the structure stabilizes with the initial three-scale hierarchy retained. © *2002 MAIK "Nauka/Interperiodica".*

Magnetically soft magnesium–zinc ferrites are widely utilized in the electronic technology as a cheap alternative to expensive nickel–zinc ferrites. Most ferrites contain variable-valence cations, which lead to the formation of defects in the matrix lattice. This may cause local distortions and also break the long-range or mesoscopic order of the solid solutions. The origin of the inhomogeneities and the mechanism of their influence on the properties of commercial magnesium–zinc ferrites have been established by employing the concept of clustering and by studying changes in the fine structure of single-crystal manganous–zinc ferrites $Mn_xZn_yFe_zO_4$ [1, 2].

The atomic structure of the long-range and mesoscopic orders was analyzed with diffraction patterns taken from $Mg_{0.54}Zn_{0.46}Fe_2O_4$ (CrK_α radiation). We studied the fine structure of (1) Debye coherent scattering, (2) diffuse (coherent) scattering [3], and (3) Compton incoherent scattering. The linear size of the clusters was estimated from the diffuse peak width by the Kitaigorodsky technique [4].

In the polycrystalline samples, we studied the diffraction by different crystallographic planes of $Mg_{0.54}Zn_{0.46}Fe_2O_4$. The ferrite samples differed by the time of firing at 1280°C (from 0.5 to 8 h).

The $Mg_{0.54}Zn_{0.46}Fe_2O_4$ magnesium–zinc ferrite samples were synthesized by the ceramic technology [5] from a powder mixture of magnesium, zinc, and iron oxides. Pressed samples were sintered in air at 1280°C with subsequent free cooling.

The local magnetic order was determined from Mössbauer γ-absorption spectra for Fe^{57}. A Co^{57} gamma-ray radioactive source of activity 50 m Ci was embedded in a chromium matrix. The parameters of the Mössbauer spectra were measured with the UNIVEM computer program. Bearing in mind the spinel structure of ferrites and the relaxation character of the spectra at room temperature, we separated out the components of the spectra obtained in experiments. It turned out that the ferrite consists of several "quasi-phases," or magnetic clusters, with a certain magnetic order. Two of the quasi-phases revealed in magnesium–zinc ferrites depend on thermal treatment conditions [6]. For such inhomogeneous ferrite spinels, the Curie temperature loses its meaning, since the magnetic order changes in several stages. In terms of the modern concepts [7], localized disordered states appear in the magnetic structures. In ferrites [8], specifically, in magnesium [9] and magnesium–zinc [10] ferrites, the *A* (t, for tetra)–*B* (o, for octa) interaction dominates over the intrasublattice (*A*–*A* and *B*–*B*) interactions; therefore, account should be taken of both the local and mesoscopic (delocalized) disturbances of exchange interactions because of the different nature and scale of inhomogeneities.

The cation environment of a Fe_o^{3+} ion at octahedral sites can be represented as the Fe_o^{3+}–O^{2-}–Me_t^{2+} chain. Here, Me_t^{2+} are various closest neighbors: Mg_t^{2+} (magnesium partially occupying the tetrahedral sites because of a high temperature), Zn_t^{2+} (always at the tetrahedral sites), or Fe_t^{3+} (since Mg atoms form clusters, Fe^{3+} ions may partially appear at tetrahedral sites).

The Mössbauer spectra taken at different time instants of magnesium–zinc ferrite sintering at 1280°C do not show the α-Fe_2O_3 phase in the sextiplet even at the very beginning of sintering. This suggests that the

1063-7842/03/4702-0364$22.00 © 2002 MAIK "Nauka/Interperiodica"

samples have completely transformed to the ferrite state (i.e., to single-phase ferrite spinel) in the prefired charge before heating to the sintering temperature.

The integral intensities of the Mössbauer spectral components for the fired magnesium–zinc ferrites sintered at 1280°C are plotted in Fig. 1. Curve *A* indicates that the integral intensity S_A is constant in the entire range of firing time at 1280°C (from 0.5 to 8 h); i.e., both the concentration and ordering of Fe^{3+} remain unchanged. However, at $\tau = 2$ h, the relative contributions of the components to the integral intensity of the sextiplets change: the previously dominating S_{B1} intensity, which is associated with the exchange interaction of magnetic octahedral Fe_o^{3+} atoms with five and six nearest neighbors ($\tau < 2$ h, curve B_1) gives way to the S_{B2} intensity, which is associated with the exchange interaction of Fe_o^{3+} with the closest three and four atoms ($\tau > 2$ h, curve B_2 in Fig. 1). It is important that, at $\tau = 2$ h, both magnetic quasi-phases B_1 and B_2 coexist in equal amounts.

The heterogeneous nature of the synthesis of the magnesium–zinc ferrite shows up in the formation of structural, chemical, and magnetic inhomogeneities (Fig. 2). The integral intensities of the components of the Mössbauer absorption spectra support this character of the synthesis and imply the presence of inhomogeneous regions in the equilibrium magnesium–zinc ferrite (see curves for λ and κ in Fig. 2). Here, the κ curve reflects the monotonic growth in the concentration of the slightly inverted magnetic phase (from 0.2 to 0.4), which tends to saturate at $\tau > 4$ h.

In contrast, the concentration of the highly inverted magnetic phase (the curve λ in Fig. 2) decreases stepwise from 1 to 0.4 as the duration of the high-temperature firing increases from 0 to 8 h. The system approaches equilibrium at $\tau = 8$ h through equalizing the degrees of inversion λ and κ for both magnetic quasi-phases. These quasiphases are of a local or mesoscopic character and define the temperature dependence of the initial magnetic permeability.

For all of the samples studied, the diffraction pattern was the superposition of reflections from atomic groups of three types (Fig. 3): (1) narrow peaks from structural groups with long-range order; (2) diffuse peaks between the Debye lines from the clusters with mesoscopic atomic order; and (3) incoherent scattering (background), which increases with angle θ, from disorderly arranged atoms.

In the first two cases, we deal with coherent, while in the third case with incoherent, X-ray scattering. The Debye X-ray diffraction from the clusters obeys the law $2d\sin\theta = n\lambda$, which allowed us to identify their crystallographic structure.

With an increase in the hold time at 1280°C, the crystallographic parameters of the structural groups vary nonmonotonically in all the samples, which suggests the evolution of the atomic order. Let us consider the variations in each of the structural fractions in detail.

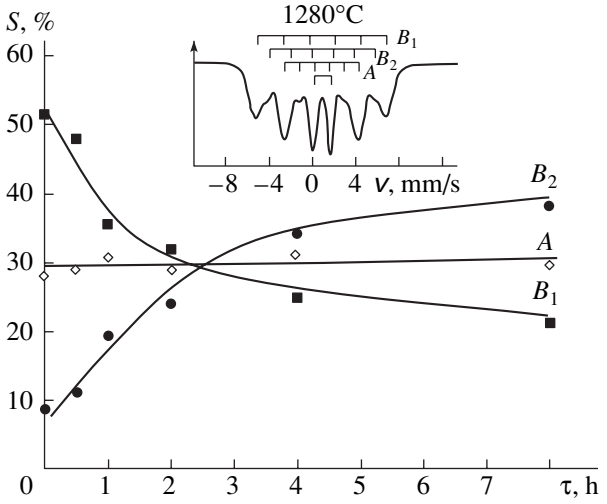

Fig. 1. Variation of the Mössbauer spectral component intensities for the $Mg_{0.54}Zn_{0.46}Fe_2O_4$ ferrite with firing time; the spectrum is shown in the inset.

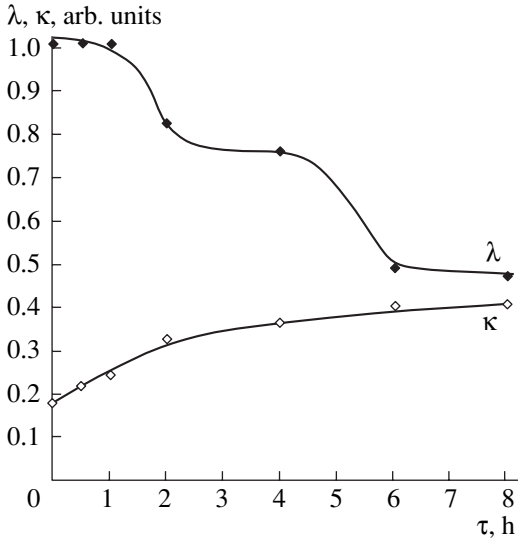

Fig. 2. Variation of the λ and κ components in the Mg–Zn ferrites sintered at 1280°C; κ and λ denote the phases with low and high degree of inversion, respectively.

The analysis of the crystallographic structure of the $Mg_{0.54}Zn_{0.46}Fe_2O_4$ matrix showed that it varies with the firing time at 1280°C (Fig. 4) as follows. Throughout the time interval, the lattice parameter differs from the tabulated value $a_{tab} = 8.414$ Å; the dependence $a = f(\tau)$ has a minimum at $\tau = 1$ h and approaches a_{tab} at $\tau = 8$ h; and two cubic sublattices with different lattice parameters coexist in the solid solution at $\tau = 2$ h, as displayed by splitting each of the diffraction lines (Fig. 3). Such a "layering" of the solid solution resembles a second-

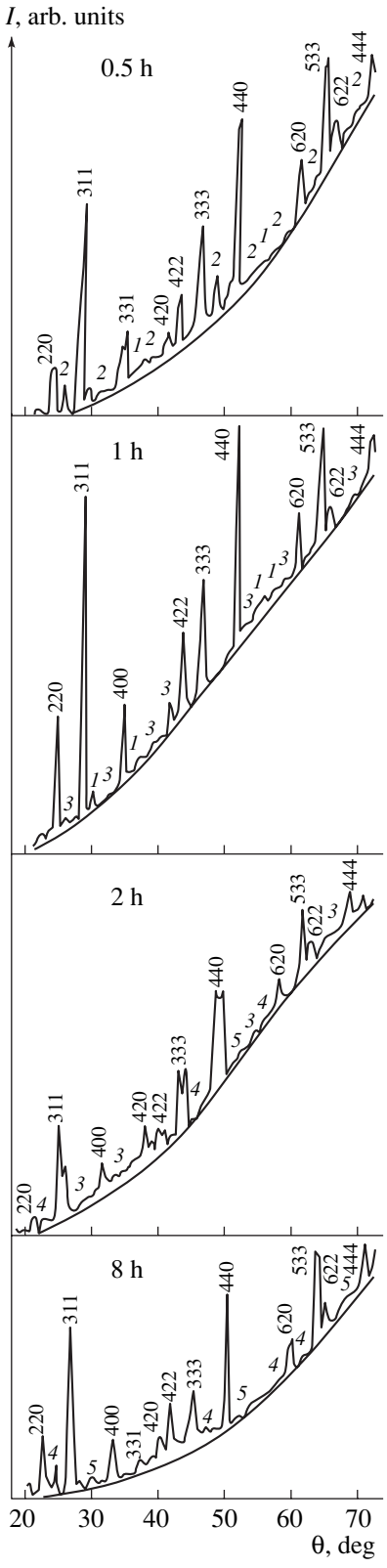

Fig. 3. Evolution of the X-ray diffraction pattern. The reflections from (*1*) ZnO, (*2*) $ZnFe_2O_4$, (*3*) Fe_2O_3, (*4*) $MgFe_2O_4$, and (*5*) MgO clusters, as well as from the associated crystallographic planes, are indicated.

order phase transition similar to ordering in the form of chemical layering and represents the metastable stage before the formation of the stable structure at $\tau = 8$ h.

The splitting of the diffraction reflections is another evidence for the coexistence in of the two phases equal amounts (the tetrahedral and octahedral environments of a Fe_o^{3+} ion at $\tau = 2$ h), which was first indicated by the Mössbauer spectra.

While the structure with long-range order changes the lattice parameter, that with mesoscopic order exhibits the changes in the chemical and phase compositions (Figs. 3, 4). At the beginning of high-temperature firing at 1280°C ($\tau = 0.5$ h), the mesoscopic structure has the ternary spinel structure $ZnO \cdot Fe_2O_3$ with individual ZnO clusters. Then, at $\tau = 1$ h, the ternary spinel breaks down into ZnO and Fe_2O_3, thus providing ordering in the cluster structure. At $\tau = 2$ h, the clusters are arranged in the spinel structure with ZnO oxide replaced by more

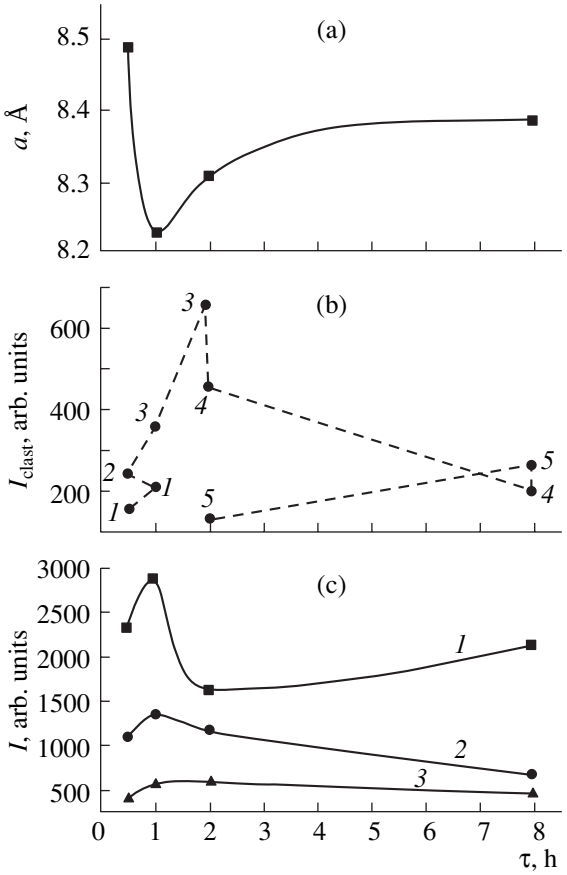

Fig. 4. (a) Experimental lattice parameter obtained from the diffraction patterns; (b) the intensity of diffuse scattering from (*1*) ZnO, (*2*) $ZnFe_2O_4$, (*3*) Fe_2O_3, (*4*) $MgFe_2O_4$, and (*5*) MgO clusters; and (c) comparison between the X-ray scattering intensities: (*1*) Debye coherent scattering, (*2*) incoherent scattering (background), and (*3*) coherent diffuse scattering from the clusters (fluctuation peaks between the lines).

stable MgO, which results in the formation of $MgFe_2O_4$ groups. However, Fe_2O_3 and MgO clusters still remain.

At $\tau = 8$ h, MgO clusters become dominant with a partial retention of $MgFe_2O_4$ spinel clusters. The changes in the X-ray intensity from the disordered structure imply that disorder decreases (Fig. 4c).

The minimum and maximum of the curves in Fig. 4 are indicative of the phase transitions in the range of $1 < \tau < 2$ h.

Thus, the X-ray intensity of coherent scattering by the matrix structure (Fig. 4c, curve *2*) and of incoherent scattering by the disordered structure peaks in the range from 1 to 2 h. This suggests that all the three structural groups responsible for the phase transitions are distorted to the maximal extent. Initially, the state of the material changes from homogeneous to inhomogeneous (the metastable state of the solid solution at $1 < \tau < 2$ h). Subsequently, the metastable phase (layered ordered solid solution) changes to the stable state (at $\tau > 2$ h). The latter corresponds to the structure of the $Mg_{0.54}Zn_{0.46}Fe_2O_4$ cubic ferrite containing a small amount (≈10%) of clusters and ions (cations and anions), the ions being strongly displaced from the crystal sites. To this atomic order, there corresponds the stabilized magnetic order where the exchange interaction with closest three and four atoms prevails.

REFERENCES

1. V. I. Arkharov, Z. A. Samoĭlenko, V. P. Pashchenko, *et al.*, Neorg. Mater. **29**, 827 (1993).
2. Z. A. Samoĭlenko, V. S. Abramov, and N. N. Ivakhnenko, Pis'ma Zh. Éksp. Teor. Fiz. **72**, 679 (2000) [JETP Lett. **72**, 472 (2000)].
3. V. D. Okunev and Z. A. Samoĭlenko, Pis'ma Zh. Éksp. Teor. Fiz. **53**, 42 (1991) [JETP Lett. **53**, 44 (1991)].
4. L. I. Kitaigorodsky, *X-ray Structure Analysis of Fine-Crystalline and Amorphous Solids* (GITTL, Moscow, 1952).
5. P. M. Bugaĭ, A. V. Kopaev, and T. S. Fedoseeva, RF Inventor's Certificate No. 1055278.
6. N. V. Pushkarev, Candidate's Dissertation (Minsk, 1987).
7. I. L. Dormann and M. I. Nogues, J. Phys.: Condens. Matter **2**, 1223 (1990).
8. J. Smit and H. P. J. Wijn, *Ferrites* (Wiley, New York, 1959; Inostrannaya Literatura, Moscow, 1962).
9. V. P. Pashchenko, G. A. Potapov, E. G. Darovskikh, *et al.*, Metallofiz. Noveĭshie Tekhnol. **18**, 48 (1996).
10. B. P. Ladgnonkar, P. N. Vosambekar, and A. S. Vaingakar, J. Magn. Magn. Mater. **210**, 289 (2000).

Translated by A. Sidorova-Biryukova

Technical Physics, Vol. 47, No. 3, 2002, pp. 368–370. Translated from Zhurnal Tekhnicheskoĭ Fiziki, Vol. 72, No. 3, 2002, pp. 87–90.

BRIEF COMMUNICATIONS

Special Features of the Structure and Properties of $La_{0.6}Sr_{0.2}Mn_{1.2-y}Cr_yO_3$ Magnetoresisitive Ceramics

Z. A. Samoĭlenko, V. P. Pashchenko, O. P. Cherenkov, and V. K. Prokopenko

Galkin Physicotechnical Institute, National Academy of Sciences of Ukraine, Donetsk, 83114 Ukraine

Received May 25, 2001; in final form, August 27, 2001.

Abstract—Atomic order and magnetoresistive parameters are studied in $La_{0.6}Sr_{0.2}Mn_{1.2-y}Cr_yO_3$ ceramics, in which Cr substituted for the above stoichiometric Mn content serves to enhance cluster formation in a solid solution. It is shown that in a range of $0.05 < y < 0.1$, $La_{0.6}Sr_{0.2}Mn_{1.2-y}Cr_yO_3$ experiences a phase transition from a partially disordered solid solution with a rhombohedral lattice ($R\bar{3}c$), in the form of planes possessing a long-range order and clusters of mesoscopic order, to a chemically microstratified solid solution, in the form of planes of an orthorhombic (*Pnma*) crystal lattice having a matrix structure and mesoscopic formations (clusters) coherently combined with a matrix of plane fragments peculiar to oxides of γ-MnO_2 type or, at $y > 0.1$, of Cr_2O_3 type. It is shown that the structural phase transition is accompanied by maximum changes of the magnetoresistive parameters in the same range of Cr concentrations, i.e., $0.05 < y < 0.10$. © *2002 MAIK "Nauka/Interperiodica".*

At the present time, the attention of researchers in physics and material science is attracted to metal oxides based on lanthanum manganite ($LaMnO_3$), in which a giant magnetoresistance is observed [1]. Of great interest are solid solutions of the composition $La_{1-x}M_xMnO_{3\pm\delta}$ (M = Ca, Sr, Ba, Pb), in which at $0 \le x \le 0.3$ a transition from antiferromagnetic to ferromagnetic order is observed accompanied by a change from semiconductor to metallic conductivity [2–7].

This work is a study of the influence on the atomic ordering of substitution of chromium ions for manganese in manganese lanthanides of composition $La_{0.6}Sr_{0.2}Mn_{1.2-y}Cr_yO_3$ ($0 \le y \le 0.2$), where chromium and oxygen form a type $R\bar{3}c$ rhombohedral structure. It was expected that the introduction of chromium would stabilize LaSrMnCrO in the rhombohedral phase because we had earlier observed that in synthesized $La_{1-x}Mn_{1+x}O_{3\pm\delta}$ lanthanides, the atomic ordering is affected by the type of crystallographic structure obtained [9].

Note should be made of the composition $La_{0.6}Sr_{0.2}Mn_{1.2-y}Cr_yO_{3\pm\delta}$, which is nonstoichiometric, with a Mn content exceeding by 0.2 the concentration of octahedral positions. Chromium was substituted for this excess Mn. It was taken into account that (i) Cr and Mn are neighbors in the periodic table; (ii) their intrinsic magnetic moments differ by a factor of 2: $4\mu_B$ for Mn^{3+} and $2\mu_B$ for Cr^{3+}; and (iii) both Mn^{3+} and Cr^{3+} can participate in high-frequency electronic exchange.

Thus, under the conditions created in the $La_{0.6}Sr_{0.2}Mn_{1.2-y}Cr_yO_{3\pm\delta}$ lanthanides studied, the magnetoresistive parameters can vary as a result of cluster formation processes in heterogeneous, although not heterophase, solid solutions, as should have been expected in accordance with [8] and our studies [9, 10]. As seen in diffraction patterns (Fig. 1), small amounts of chromium substituted for manganese tend to stabilize the type $R\bar{3}c$ rhombohedral (*R*) structure, impeding the transition to the orthorombic (*O*) type *Pnma* structure. The $R \longrightarrow O$ structural phase transition (PT) is accompanied by extreme intensity changes in the incoherent X-ray scattering, with a minimum at $0.05 < y < 0.1$ (Fig. 2). In the structure's soft mode, the rhombohedral phase appears in the form of clusters, also of the rhombohedral type, and fragments of separate families of planes with stacking faults; in most cases formation of these planes, which involves an inversion axis, occurs with the participation of planes containing volume diagonals. The orthorhombic phase in the structure's soft mode appears as orthorhombic type clusters, which, however, are represented by a binary phase from a family of planes of manganese oxide γ-MnO_2; i.e., local chemical ordering in a multicomponent system takes place. Cr in this case is found in the form of Cr_2O_3 clusters with high degree of chromium substituted for manganese ($y = 0.2$).

Changes in the structure of a multicomponent solid solution taking place in the course of the chemical-ordering type process are manifested as enhancement of the diffusion scattering within small diffraction angles ($\Theta < 20°$) at higher Cr concentrations in the samples: the high intensity of the small-angle diffuse scattering in diffraction patterns from samples with $y = 0.05$

1063-7842/03/4702-0368$22.00 © 2002 MAIK "Nauka/Interperiodica"

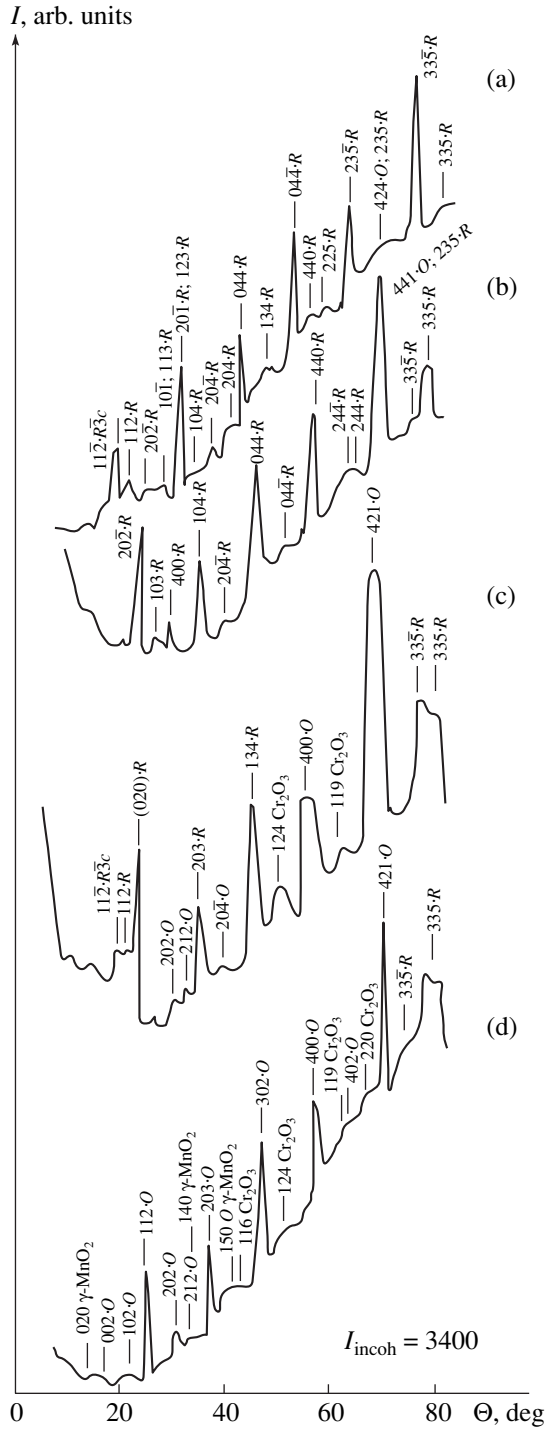

Fig. 1. Diffraction patterns of samples with *y*: (a) 0; (b) 0.05; (c) 0.1; (d) 0.2.

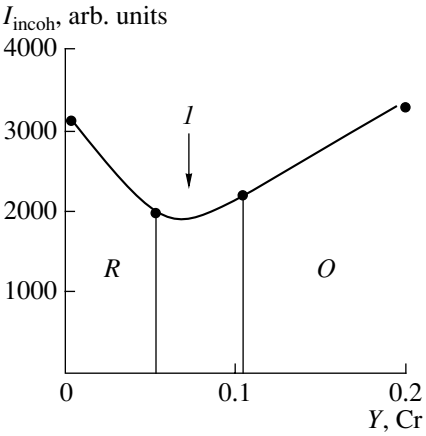

Fig. 2. Incoherent X-ray scattering intensity as a function of *y*. (*1*) $R \longrightarrow O$ phase transition.

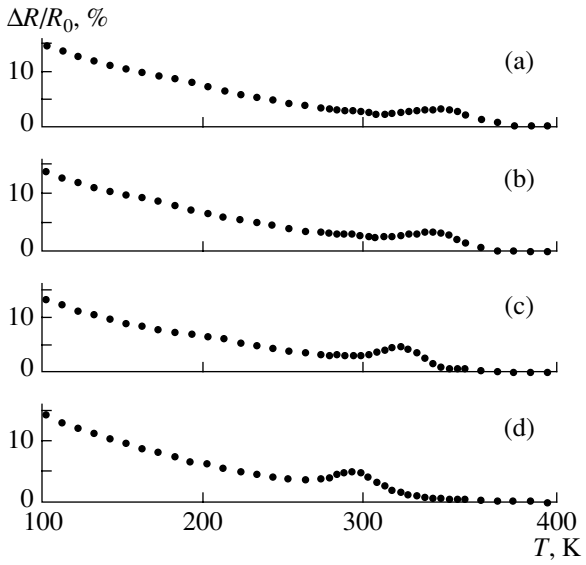

Fig. 3. Temperature dependences of the magnetoresistive effect in the samples. (a–d) Same as in Fig. 1.

and 0.1 (curves in Figs. 1b, 1c) and weak scattering for $y = 0$ (curves in Figs. 1a, 1d). Higher intensity at small angles is characteristic of the second kind of phase transitions [8]; in this sample group, it is the ordering of the solid solution analogous to chemical microstratification. This process leads to the emergence of nonuniformity of the composition over the bulk of solid solution and of thermodynamically stable quasi-binary formations (clusters) coherently coupled to the matrix structure. Every cluster type in this multicomponent solid solution consists of only one kind of cationic element of the entire set and of oxygen anions (Fig. 1).

In the entire chromium concentration range studied, the conductivity is metallic up to a temperature corresponding to the maximum resistance $T(R_{max})$ (Fig. 3). Above $T(R_{max})$ the conductivity is of the semiconductor type. With *y* increasing from 0 to 0.2, the phase transition temperature varies from 370 to 300 K. The maximum value of the resistance normalized to the value at 273 K ($R_{max}/R(273\ K)$) drops with increasing concentration of chromium ions (see table).

The magnetoresistive effect ($\Delta R/R_0 = (R_0 - R_H)/R_0$) measured in a field of $H = 5$ kOe is demonstrated in

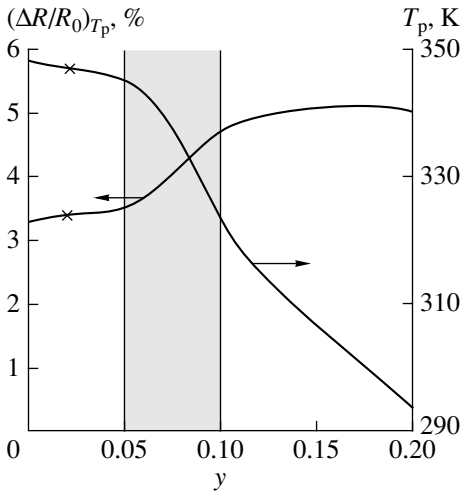

Fig. 4. Variation with y of the magnetoresistivity peak temperature and maximum values of $\Delta R/R_0$.

Fig. 3. With increasing Cr concentration, the magnetoresistivity peak temperature (T_p) decreases monotonically, as is the case with the resistance maximum temperature (see table). The magnetoresistive effect at T_p also increases by about 50% at $y = 0.2$. According to the experimental data in Fig. 4, with increasing chromium concentration, the magnetoresistance peak in manganite–lanthanum–strontium grows and T_p decreases. The range of composition where the most significant variations of these parameters occur is $0.05 < y < 0.1$; curves of $\Delta R/R_0 = f(y)$ and $T_p = f(y)$ have an intersection point at about $y = 0.085$. This result is in agreement with the character of the structural changes (Figs. 1 and 2), causing the transition from the rhombohedral to orthorombic phase for the same concentration composition.

Transport properties of ceramic samples

y	$T_{R_{max}}$, K	R_{max}/R (273 K)
0	367	1.45
0.02	365	1.42
0.05	362	1.40
0.1	334	1.38
0.2	302	1.20

CONCLUSIONS

The $R \longrightarrow O$ structural phase transition uncovered in $La_{0.6}Sr_{0.2}Mn_{1.2-y}O_3$ for compositions of $0.05 < y < 0.1$ and the results of studies on their magnetoresistive parameters testify that the variation of magnetic properties in this system is due to considerable rearrangement of the atomic structure. With increasing chromium content in LaSrMnCrO, the concentration volume of the ferromagnetic phase having an $R\bar{3}c$ rhombohedral lattice is gradually replaced by an antiferromagnetic phase having a *Pnma* orhtorombic lattice. This condition is known as transformation of a two-phase magnetic structure in the form of "diamagnetic drops in a ferromagnetic medium" into a structural state in the form of "ferromagnetic drops in a diamagnetic medium" [1]. Near such a structural magnetic and resistive transition, a maximum in the magnetoresistance is observed. With increasing chromium content, the magnetoresistive effect becomes stronger and the phase transition temperature of the $La_{0.6}Sr_{0.2}Mn_{1.2-y}Cr_yO_3$ solid solutions under study diminishes.

REFERENCES

1. É. L. Nagaev, Usp. Fiz. Nauk **166**, 833 (1996) [Phys. Usp. **39**, 781 (1996)].
2. H. Y. Hwang, S.-W. Cheong, P. G. Radaelli, *et al.*, Phys. Rev. Lett. **75**, 914 (1995).
3. S. de Brion, G. Chouteau, and P. Leday, Czech. J. Phys. **46**, 2123 (1996).
4. J. F. Mitchell, D. N. Argyrion, C. D. Petter, *et al.*, Phys. Rev. B **54**, 6172 (1996).
5. A. Urushibara, Y. Moritomo, T. Arima, *et al.*, Phys. Rev. B **51**, 14103 (1995).
6. Y. Tokura, Y. Tomioka, H. Kuwahara, *et al.*, J. Appl. Phys. **79**, 5288 (1996).
7. A. Anane, C. Dupas, K. Le Dang, *et al.*, J. Phys.: Condens. Matter **7**, 7015 (1995).
8. M. A. Krivoglaz, *Electron Structure and Electron Properties of Metals and Alloys: Collection of Scientific Works* (Naukova Dumka, Kiev, 1988), pp. 3–39.
9. P. V. Pashchenko, S. I. Khartsev, O. P. Cherenkov, *et al.*, Neorg. Mater. **35**, 1509 (1999).
10. V. P. Pashchenko, A. A. Shemyakov, V. K. Prokopenko, *et al.*, J. Magn. Magn. Mater. **220**, 52 (2000).

Translated by B. Kalinin

Technical Physics, Vol. 47, No. 3, 2002, pp. 371–373. Translated from Zhurnal Tekhnicheskoĭ Fiziki, Vol. 72, No. 3, 2002, pp. 91–94.

BRIEF COMMUNICATIONS

Impurity Diffusion in a Gas Flow in a Channel

F. G. Baksht and V. G. Ivanov

Ioffe Physicotechnical Institute, Russian Academy of Sciences, Politekhnicheskaya ul. 26, St. Petersburg, 194021 Russia

Received June 15, 2001

Abstract—The impurity concentration N in a gas flow in a channel is approximately calculated. In a number of cases, the wall losses of impurities in the channel can be taken into account by introducing an effective lifetime τ that describes the diffusion drift of the impurity from the flow toward the walls. © *2002 MAIK "Nauka/Interperiodica".*

(1) For definiteness, we consider the flow of a molecular gas in a channel. The gas contains a small portion of vibrationally excited (for example, to the first level) molecules. Schematically, the flow is shown in Fig. 1: the gas flows through discharge chamber I, where the initial concentration of excited molecules is generated and enters two-dimensional channel II. During the flow through the channel, the excited molecules are lost due to vibrational (V–t) relaxation in the volume and adsorption on the channel walls (see, for example, [1, 2]).

(2) To determine the lifetime τ of the excited molecules, consider the initial zone of the flow in the channel. The distribution of the concentration of the excited molecules along the length x and across the section (in the direction y) of the channel can be found from the convective diffusion equation

$$\mathbf{V}_0 \cdot \nabla N - D\nabla^2 N = -N/\tau_{vt}, \tag{1}$$

where $\mathbf{V}_0$ is the flow velocity along the x axis within the initial zone of the flow, which is assumed to be constant; D is the self-diffusion coefficient of the molecules (in the general case, the diffusion coefficient of the impurities in the gas); τ_{vt} is the time of (V–t) relaxation; and ∇ is the del operator.

At the walls of the channel, the boundary conditions for Eq. (1) have the form [3]

$$D\frac{\partial N(x, y)}{\partial y} = \pm\frac{1}{2}N(x, y)\bar{\nu}\frac{\gamma}{2-\gamma} \quad \left(y = \mp\frac{L}{2}\right), \tag{2}$$

where $\bar{\nu} = \sqrt{8T/\pi M}$ is the average thermal velocity of the molecules and $\gamma(\theta) = 1 - r(\theta)$ is the coefficient of sticking the vibrationally excited molecules to the surface (r is the reflection coefficient).

The quantity γ depends on the surface coverage θ by adsorbed atoms and on the potential barrier for the surface adsorption of the molecules. The height of this barrier varies in a wide range from small ones (for example, for Pd) to those that significantly exceed T (for example, for Cu) [4, 5]. At the channel entrance ($x = 0$, $-L/2 \le y \le L/2$), the initial distribution of the concentration of the excited molecules $N(0, y)$ is set.

The solution of Eq. (1) is the sum of its particular solutions that one finds by the method of separation of variables [6]. Then, the general solution can be written in the form

$$N(x, y) = \sum_{k=1}^{\infty} A_k \cos(\mu_k y/R) \times \exp\{-[\sqrt{1 + \vartheta^2(\mu_k^2 + R^2/D\tau_{vt})} - 1]x/\vartheta R\}. \tag{3}$$

Here, $\vartheta = 2D/RV_0$; $R = L/2$; μ_k are the positive roots of the equation $\cot\mu = \mu/B$ ($k = 1, 2, 3, \ldots$), where $B = (R\bar{\nu}/2D)\gamma/(2\gamma)$; and

$$A_k = \frac{\mu_k}{\mu_k + \sin\mu_k\cos\mu_k}\frac{1}{R}\int_{-R}^{R} N(0, y)\cos(\mu_k y/R)dy \tag{4}$$

are the Fourier expansion coefficients for the initial distribution of the concentration $N(0, y)$.

By order of magnitude, the parameter ϑ is equal to the ratio of the terms

$$-D\frac{\partial^2 N}{\partial x^2} \quad \text{and} \quad V_0\frac{\partial N}{\partial x},$$

entering into (1); i.e., it defines the ratio of longitudinal diffusion to convection. At $\vartheta \gg 1$, the convective term in Eq. (1) is insignificant. In this case, the distribution of the impurity concentration in the channel is governed solely by diffusion and, as follows from (3), has the form

$$N(x, y) = \sum_{k=1}^{\infty} A_k \cos(\mu_k y/R) \times \exp\left\{-\frac{x}{R}\sqrt{\mu_k^2 + R^2/D\tau_{vt}}\right\}. \tag{5}$$

1063-7842/03/4702-0371$22.00

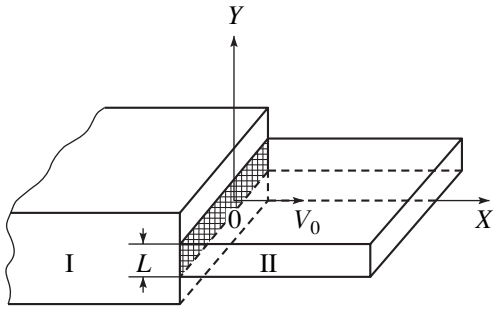

Fig. 1. Scheme of the flow: I, discharge chamber; II, channel; and V_0, gas flow velocity at the channel entrance. The cross section of the entering flow ($x = 0$) is hatched.

The flux density Γ of the excited molecules entering the channel is given by

$$\langle \Gamma(0, y)\rangle \equiv -D\frac{\partial \langle N(x, y)\rangle}{\partial x}\bigg|_{x=0} = \frac{D}{R}\sum_{k=1}^{\infty} A_k \frac{\sin\mu_k}{\mu_k}\sqrt{\mu_k^2 + \frac{R^2}{D\tau_{vt}}}. \quad (6)$$

In (6), the symbol $\langle\ldots\rangle$ means averaging over the cross section of the channel. It is seen that, at $R \ll \sqrt{D\tau_{vt}}$, the characteristic diffusion length of the impurities along the channel is $\approx R$; otherwise, it is on the order $\sqrt{D\tau_{vt}}$. The total flux of the impurity molecules that enters the channel is equal to the product of $\langle\Gamma(0, y)\rangle$ and the cross-sectional area S of the channel.

(3) Now we consider the other limiting case when $\vartheta \ll 1$ and, as a result, the longitudinal diffusion is negligible. Then, the term $-D(\partial^2 N/\partial x^2)$ in (1) can be neglected and the impurities along the channel are transported only by convection, while across the channel, exclusively by diffusion (it is this situation that has been considered in [1, 2]). In our case, in the time it takes for the impurity to diffuse across the channel over a distance $\approx R$, it travels a path x along the channel that is greater than R: $x/R \sim 1/\vartheta$. Under these conditions, it is appropriate to describe the losses of the impurity molecules in the channel, which are associated with volume (v–t)-relaxation and drift to the channel walls, with the help of the effective lifetime τ_0. To determine τ_0, we consider the concentration $\langle N(x, y)\rangle$ averaged over the cross section of the channel. Assuming that $\vartheta \ll 1$ in (3) and averaging the result over y, we obtain

$$\langle N(x, y)\rangle = F(\xi)\exp\{-x/V_0\tau_{vt}\}, \quad (7)$$

where

$$F(\xi) = \sum_{k=1}^{\infty} A_k \frac{\sin\mu_k}{\mu_k}\exp\left\{-\frac{4\mu_k^2}{\pi^2}\xi\right\}. \quad (8)$$

Here, $\xi = x/V_0\tau_d$ and $\tau_d = \Lambda^2/D$ and $\Lambda = L/\pi$ are the time and the length of the transverse diffusion of the impurities. Let the effective lifetime of impurity particles be given by

$$\frac{d\langle\Gamma(x, y)\rangle}{dx} = -\frac{\langle N(x, y)\rangle}{\tau_0(x)}. \quad (9)$$

Here, $\langle\Gamma(x, y)\rangle = V_0\langle N(x, y)\rangle$ is the flux density of the impurities along the channel after averaging over its cross section. Using (7) and (9), we find

$$1/\tau_0 = \frac{1}{\tau_{vt}} + \frac{1}{\tau},$$

where

$$\frac{1}{\tau(\xi)} = \frac{1}{\tau_d}\frac{d}{d\xi}\ln F(\xi). \quad (10)$$

The total losses of the impurity molecules per unit length of the channel are equal to $-S\langle N(x, y)\rangle/\tau_0$. The parameter τ in (10) specifies the loss rate of the excited molecules due to their lateral diffusion from the flow toward the walls. The lifetime τ thus introduced virtually coincides with the lifetime that arises in the problem on the temporal evolution of the impurity concentration $n(t, y)$ in discharge afterglow ($t \geq 0$) [7].[1] This is associated with the fact that Eq. (1), in which the term

$$-D\frac{\partial^2 N(x, y)}{\partial x^2}$$

is omitted, coincides with the corresponding equation for $n(t, y)$ when t is replaced by x/V_0. The solutions for $n(t, y)$ and $N(x, y)$ are similar only at $\vartheta \ll 1$, when the order of Eq. (1) in x can be lowered. In the general case (i.e., when ϑ is arbitrary), such a similarity is absent and it is necessary to use the solution of Eq. (1) in form (3). In this case, the wall losses in the channel can no longer be described with the effective diffusion lifetime τ.

(4) In calculating τ with expression (10), one usually leaves only the first term in sum (8). The resulting value of τ (below, it is denoted τ_1) is equal to

$$\tau_1 = \tau_d(\pi/2\mu_1)^2, \quad (11)$$

where $\mu_1(B)$ is the least positive root of the equation $\cot\mu = \mu/B$. Such an approach is *a fortiori* valid for $\xi \gg 1$, when the terms with $k \geq 2$ make a small contribution to (8). Below, we will show that actually the applicability domain of expression (11) is considerably wider. The replacement of τ by τ_1 leads to the exact solution also at $\xi = 1$, as well as in a sufficiently wide range of ξ at $\xi < 1$.

[1] Expression (10) for τ obtained in our work differs from the corresponding expression in [7] in that averaging over the cross section of the channel was not performed in [7] and the problem was solved for the cylindrical geometry.

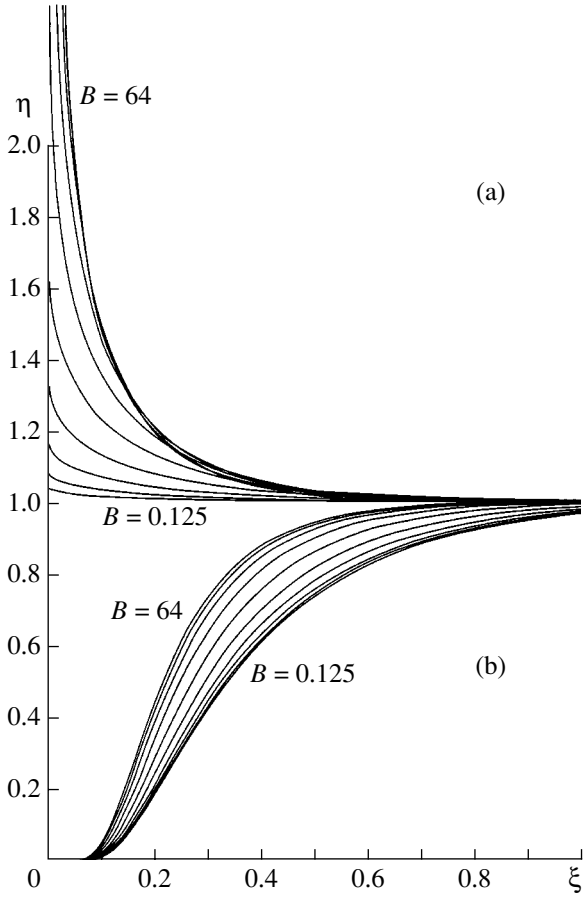

Fig. 2. Distribution of $\eta(\xi)$ along the channel. For neighboring curves, the parameter B differs by a factor of 2, varying from 0.125 to 64. (a) Impurity is uniformly distributed over the channel entrance and (b) impurity is concentrated at the center of the channel entrance.

In the limiting cases $B \gg 1$ ($\mu_1 \simeq \pi/2$) and $B \ll 1$ ($\mu_1 \simeq \sqrt{B}$), expression (11) yields $\tau_1 = \tau_d$ and $\tau_1 = (L/\bar{v})(2 - \gamma)/\gamma$, respectively. The former value corresponds to the conditions when the sticking coefficient γ is not too small and the drift time of the molecules depends on the time τ_d of their lateral diffusion to the walls. Then, boundary condition (2) is changed to $N(x, \pm L/2) \simeq 0$. The latter is obtained when $\gamma \ll 1$ and is so small that $\tau \gg \tau_d$. In this case, the concentration N of the impurities is nearly uniformly distributed over the cross section of the channel and the flux density of molecules escaping the gas and being adsorbed on the surface equals $\simeq(\gamma/4)N\bar{v}$. For intermediate values of B, expression (11) is closely approximated by the formula $\tau_1 = \tau_d + (L/\bar{v})(2-\gamma)/\gamma$ [7]. The accuracy of calculation that can be achieved when the approximate value of τ_1 is used instead of τ is illustrated in Fig. 2. Here, for the two opposite cases, $\eta(\xi) = \tau_1(\xi)/\tau(\xi)$ is plotted as a function of distance ξ from the channel entrance. In Fig. 2a, it is assumed that, at the entrance ($x = 0$), the impurities are uniformly distributed over the cross section of the channel: $N(0, y) = N_0$, where N_0 is the concentration of the impurities at the entrance. In this case,

$$F(\xi) = N_0 \sum_{k=1}^{\infty} \frac{2\sin^2\mu_k}{\mu_k(\mu_k + \sin\mu_k\cos\mu_k)} \exp\left\{-\frac{4\mu_k^2}{\pi^2}\xi\right\}. \quad (12)$$

In Fig. 2b, we assume that, at $x = 0$, the impurities are totally concentrated at the channel center $N(0, y) = (L\tilde{N}_0/S)\delta(y)$, where $\tilde{N}_0$ is the number of the particles per unit length of the channel at $x = 0$. Then,

$$F(\xi) = \frac{2\tilde{N}_0}{S} \sum_{k=1}^{\infty} \frac{\sin\mu_k}{\mu_k + \sin\mu_k\cos\mu_k} \exp\left\{-\frac{4\mu_k^2}{\pi^2}\xi\right\}. \quad (13)$$

At $\xi \geq 1$, we have the same asymptotic distribution in both cases:

$$N(x, y) = A_1\cos(\mu_1 y/R) \times \exp\{-[x/V_0\tau_{vt} + (4/\pi^2)\mu_1^2\xi]\}. \quad (14)$$

In Fig. 2a (showing the most often observed situation, which is of utmost interest), as the gas flows through the channel, the concentration profile $N(y)$ narrows because of the adsorption of the impurities on the walls. It is seen that, even in the worst case, i.e., at $B \gg 1$, the effective lifetime τ_1 can be used instead of τ with an accuracy no worse than 0.1 for $\xi \geq 0.3$. The initial distribution $N(0, y) \sim \delta(y)$ in Fig. 2b is hypothetical and the worst for using approximate expression (11). However, even here in the worst case $B \ll 1$, the effective lifetime τ_1 can be used with an accuracy no worse than 0.1 at $\xi \geq 0.8$.

ACKNOWLEDGMENTS

We are grateful to Yu.Z. Ionikh who called our attention to his study [7].

REFERENCES

1. F. G. Baksht and V. G. Ivanov, Zh. Tekh. Fiz. **68** (10), 10 (1998) [Tech. Phys. **43**, 1145 (1998)].
2. F. G. Baksht and V. G. Ivanov, Zh. Tekh. Fiz. **69** (6), 15 (1999) [Tech. Phys. **44**, 621 (1999)].
3. F. G. Baksht, V. G. Ivanov, A. B. Rybakov, and V. G. Yur'ev, Preprint No. 946, FTI AN SSSR (Physicotechnical Institute, USSR Academy of Sciences, Leningrad, 1985); F. G. Baksht and A. B. Rybakov, Zh. Tekh. Fiz. **56**, 297 (1986) [Sov. Phys. Tech. Phys. **31**, 181 (1986)].
4. P. L. Andrew and A. A. Haasz, J. Appl. Phys. **72**, 2749 (1992).
5. C. T. Rettner, H. A. Michelsen, and D. J. Auerbach, J. Chem. Phys. **102**, 4625 (1995).
6. A. V. Lykov, *Theory of Heat Conduction* (GITTL, Moscow, 1952).
7. Yu. Z. Ionikh, Opt. Spektrosk. **51**, 76 (1981) [Opt. Spectrosc. **51**, 39 (1981)].

Translated by Yu. Vishnyakov